

UNICAMP

UNIVERSIDADE ESTADUAL DE
CAMPINAS

Instituto de Física Gleb Wataghin

THAÍS VICTA TREVISAN

Exotic phenomena in low-dimensional systems

**Fenômenos exóticos em sistemas de baixa
dimensionalidade**

Campinas

2019

Thaís Victa Trevisan

Exotic phenomena in low-dimensional systems

Fenômenos exóticos em sistemas de baixa dimensionalidade

Tese apresentada ao Instituto de Física Gleb Wataghin da Universidade Estadual de Campinas como parte dos requisitos exigidos para a obtenção do título de Doutora em Ciências.

Thesis presented to the Gleb Wataghin Institute of Physics of the University of Campinas in partial fulfillment of the requirements for the degree of Doctor of Science.

Supervisor: Amir Ordacgi Caldeira

Este exemplar corresponde à versão final da Tese defendida pela aluna Thaís Victa Trevisan e orientada pelo Prof. Dr. Amir Ordacgi Caldeira.

Campinas

2019

Ficha catalográfica
Universidade Estadual de Campinas
Biblioteca do Instituto de Física Gleb Wataghin
Lucimeire de Oliveira Silva da Rocha - CRB 8/9174

T729e Trevisan, Thaís Victa, 1991-
Exotic phenomena in low-dimensional systems / Thaís Victa Trevisan. –
Campinas, SP : [s.n.], 2019.

Orientador: Amir Ordacgi Caldeira.
Tese (doutorado) – Universidade Estadual de Campinas, Instituto de Física
Gleb Wataghin.

1. Correntes persistentes. 2. Benzeno. 3. Supercondutividade. 4. Lifshitz,
Transição de. 5. Sistemas desordenados. I. Caldeira, Amir Ordacgi, 1950-. II.
Universidade Estadual de Campinas. Instituto de Física Gleb Wataghin. III.
Título.

Informações para Biblioteca Digital

Título em outro idioma: Fenômenos exóticos em sistemas de baixa dimensionalidade

Palavras-chave em inglês:

Persistent currents

Benzene

Superconductivity

Lifshitz transition

Disordered systems

Área de concentração: Física

Titulação: Doutora em Ciências

Banca examinadora:

Amir Ordacgi Caldeira

Pascoal José Giglio Pagliuso

Eduardo Miranda

Mucio Amado Continentino

Álvaro Ferraz Filho

Data de defesa: 11-09-2019

Programa de Pós-Graduação: Física

Identificação e informações acadêmicas do(a) aluno(a)

- ORCID do autor: <https://orcid.org/0000-0001-6912-6347>

- Currículo Lattes do autor: <http://lattes.cnpq.br/8526560666304076>



MEMBROS DA COMISSÃO JULGADORA DA TESE DE DOUTORADO DE **THAÍS VICTA TREVISAN – RA 093064** APRESENTADA E APROVADA AO INSTITUTO DE FÍSICA “GLEB WATAGHIN”, DA UNIVERSIDADE ESTADUAL DE CAMPINAS, EM 11 / 09 / 2019.

COMISSÃO JULGADORA:

- Prof. Dr. Amir Ordacgi Caldeira – Orientador – DFMC/IFGW/UNICAMP
- Prof. Dr. Pascoal José Giglio Pagliuso – DEQ/IFGW/UNICAMP
- Prof. Dr. Eduardo Miranda – DFMC/IFGW/UNICAMP
- Prof. Dr. Mucio Amado Continentino – CBPF
- Prof. Dr. Álvaro Ferraz Filho - IIF/UFRN

OBS.: Informo que as assinaturas dos respectivos professores membros da banca constam na ata de defesa já juntada no processo vida acadêmica da aluna.

CAMPINAS
2019

Aos meus pais Ana Maria V. Trevisan e Pedro H. Z. Trevisan e ao meu irmão Paulo V. Trevisan.

Acknowledgements

I would like to express my heartiest gratitude to my parents Ana Maria Victa Trevisan and Pedro H. Z. Trevisan, as well as to my brother Paulo Victa Trevisan for their unconditional support over all these years. I dedicate this work to you. Thank you for always supporting my professional choices, even though they took me away from you for a while. Thank you for always recognizing the importance of education and Science. I want you to know that my accomplishments are also yours.

I am also thankful to my parents and my godparents Maria Flavia A. B. Trevisan and José Junior Trevisan for supporting my education. I hope I can always make you proud.

I am sincerely thankful to Professors Alberto Saa, Eduardo Miranda, Amir Caldeira, Marcus Aguiar, Kyoko Furuya (who unfortunately is no longer between us) José Brum, Peter Schulz, and Carola Dobrigkeit Chinellato for the amazing classes during undergrad and grad school. I will be inspired by you when the time comes for me to prepare classes myself.

I would also like to express my deepest gratitude for my advisor Professor Amir Caldeira for all the years we worked together and for the opportunities he gave me. I also thank Gustavo Monteiro, Amir's postdoc, for the collaborations.

I owe a deep sense of gratitude for Professor Rafael Fernandes, who was my advisor during my one-year scholarship at University of Minnesota, in Minneapolis, United States. Rafael, thank you very much for involving me in two fantastic research projects which are bearing fruits. Thank you for having always been available to answer my questions and for your guidance. It was an amazing experience to work with you!

In addition, I am deeply thankful to Michael Schütt, with whom I collaborated during my stay at University of Minnesota. It was also an amazing experience to work with you, Michael. I appreciate all of our long discussions and your patience. I learned a lot from you. I can say that if I know how to make proper use of Wolfram Mathematica resources, it is mostly thanks to you. Besides, I'm sincerely thankful to you and to your family for kindly welcoming me to Minneapolis.

I also thank my friends Rene Alvares Donado, Mário Malcoms, Pedro Bortolin, Leandra Martinez, Carolina Arruda, Victor Quito, Pedro Lopes, Jéssica Rego, Bárbara Peluzo, Morten Christenses, Maria Navarro Gastiasoro, Helder Faria, Danilo Elias, Arthur Faria, Gabriel Weiderpass, Gustavo Ceolin Bortolo, Raul Guidolini Cecato Lucca Maia Bollani, Beatriz Sechin Zazulla, Larissa Saemi Ganaha, Henrique Antonio Stelari, Carlos

Eduardo Millani, Julia Cabral d'Avilla, Adriano Grigolo, Vanessa Rodrigues, Gustavo Monteiro e Débora Príncipe for all the good moments we shared. A special thanks to Rene, Mário and Carol for the friendship over the years and the support through difficult times. I also would like to express my sincere gratitude to Rene for making me company every time I needed to stay at work until late.

A special thanks also go to Pedro Bortolin, who in addition to being a dear friend, was also my Cello teacher. Pedro, I'm deeply thankful for your support and your amazing lessons. Thank you for helping me to realize my dream of learning to play a musical instrument and for supporting my music arrangements. It was invaluable for me to achieve a balance between my work and personal life. I also thank my ensemble mates Marcus, Leandro, Elizeu and Amaury for their friendship and for the memorable rehearsals on the Monday evenings.

Another special thanks goes to my friend Victor Quito for joining me at Ames' coffee shops during the weekends, where most of the suggested modifications to this thesis were implemented.

This work was supported by São Paulo Research Foundation (Fapesp) through processes number 2015/21349-7 and BEPE 2016/12874-3 and by CNPq through process number 141176/2015-6.

Agradecimentos

Agradeço aos meus pais, Ana Maria Victa Trevisan e Pedro H. Z. Trevisan e ao meu irmão, Paulo Victa Trevisan, pelo apoio incondicional. À vocês dedico esse trabalho. Muito obrigada por sempre apoiarem minhas escolhas profissionais, ainda que elas me levem pra longe de vocês. Obrigada por sempre reconhecerem a importância da educação e, em particular, da ciência. Saibam que minhas conquistas são igualmente suas.

Aos meus pais e também aos meus padrinhos Maria Flávia Trevisan e José Junior Trevisan, agradeço per todo o investimento em minha educação. Eu nunca teria chegado até aqui se não fosse pelo apoio de vocês e espero sempre ser capaz de deixá-los orgulhosos.

Aos Professores Alberto Saa, Eduardo Miranda, Amir Caldeira, Marcus Aguiar, Kyoko Furuya (que infelizmente não está mais entre nós) José Brum, Peter Schulz, and Carola Dobrigkeit Chinellato, agradeço pelas suas aulas incríveis durante a graduação, mestrado edoutorado. Me inspirarei em vocês quando for a minha vez de preparar um curso.

Deixo um agradecimento especial ao meu orientador Professor Amir Caldeira por todos esses anos que trabalhamos juntos. Obrigada pelas várias discussões, pela orientação e pelas oportunidades que você me proporcionou durante esses anos. Também agradeço ao Gustavo Monteiro, pós-doc do Amir, pela colaboração nos trabalhos.

Também agradeço especialmente ao Professor Rafael Fernandes, meu orientador durante o intercâmbio de um ano na Universidade de Minnesota, Minneapolis, Estados Unidos. Rafael, muito obrigada por me envolver em dois projetos incríveis que estão rendendo muitos frutos. Muito obrigada por estar sempre disponível pra me ajudar com as minhas dúvidas e pela sua orientação impecável. Trabalhar com você foi uma experiência incrível!

Outra pessoa que foi muito importante durante o ano que passei em Minneapolis foi o Michael Schütt. Michael, trabalhar com você também foi uma experiência incrível. Não sei sem como agradecer por todas as nossas longas e produtivas discussões. Além disso, se hoje eu sei usar os recursos que o Wolfram Mathematica tem a oferecer é em grande parte graças a você. Sou profundamente grata a você e à sua família por terem me recebido tão bem em Minneapolis.

Aos meus amigos Rene Alvares Donado, Mário Malcoms, Pedro Bortolin, Leandra Martinez, Carolina Arruda, Victor Quito, Pedro Lopes, Jéssica Rego, Bárbara Peluzo, Helder Faria, Danilo Elias, Arthur Faria, Gabriel Weiderpass, Gustavo Ceolin

Bortolo, Raul Guidolini Cecato Lucca Maia Bollani, Beatriz Sechin Zazulla, Larissa Saemi Ganaha, Henrique Antonio Stelari, Carlos Eduardo Millani, Julia Cabral d'Avilla, Adriano Grigolo, Vanessa Rodrigues, Gustavo Monteiro e Débora Príncipe, agradeço por todos os bons momentos que compartilhamos. Em especial, gostaria de agradecer à Carol, René e Mário por todos os anos de amizade e apoio nos momentos difíceis. Ao René agradeço ainda pela companhia no trabalho até tarde da noite sempre que tínhamos um prazo mais apertado, ou quando tínhamos uma conta que não conseguíamos resolver, um "bug" nos algoritmos, ou só por diversão mesmo porque estávamos empolgados com a pesquisa.

Deixo um agradecimento especial também ao Pedro Bortolin, que além de ser um querido amigo, foi também meu professor de violoncelo. Obrigada pelo seu apoio e pelas suas aulas maravilhosas. Pedro, muito obrigada por me ajudar a realizar o sonho de aprender a tocar um instrumento musical e por me encorajar com meus arranjos. Isso foi fundamental para que eu alcançasse um equilíbrio entre a minha vida pessoal e profissional. Agradeço ainda aos meus companheiros de ensemble Pedro, Marcus, Leandro e Elizeu, pela amizade pelos memoráveis ensaios às segundas-feiras.

Também agradeço especialmente ao meu amigo Victor Quito pela sua companhia nos cafés de Ames, onde implementei a maior parte das correções na tese que foram sugeridas pela banca examinadora.

Agradeço à Fundação de Amparo à Pesquisa do Estado de São Paulo por apoiar esse trabalho através dos processos de número:

- 2015/21349-7 - Doutorado, fluxo contínuo.
- 2016/12874-3 - Bolsa de Estágio em Pesquisa no Exterior (BEPE)

Agradeço ao Conselho Nacional de Desenvolvimento Científico e Tecnológico (CNPq) por apoiar esse trabalho através do processo de número 141176/2015-6.

“Remember to look up at the stars and not down at your feet. Try to make sense of what you see and wonder about what makes the Universe exist. Be curious. And however difficult life may seem, there is always something you can do and succeed at. It matters that you don’t just give up.” - Stephen Hawking

Resumo

Essa tese é composta de dois grandes blocos, onde abordamos dois distintos fenômenos exóticos em sistemas eletrônicos interagentes de baixa dimensionalidade. Na primeira parte da tese, estudamos a anisotropia magnética observada experimentalmente nas moléculas aromáticas. Nosso objetivo é formular um modelo microscópico mínimo capaz de descrever a física desse curioso fenômeno que é alvo de muitas controvérsias na literatura. Mostramos que, ao contrário do que diz o modelo RCM (do inglês *Ring Current Model*), apenas os graus de liberdade dos elétrons π - ou seja, aqueles que ocupam os orbitais p_z do anel aromático - não são suficientes para uma descrição completa das propriedades magnética desses sistemas. Derivamos, então, usando uma aproximação *semelhante* à aproximação de Born-Oppenheimer, uma extensão do modelo de Hubbard onde uma interação efetiva atrativa e do tipo momento-momento entre os elétrons π é mediada por excitações virtuais dos elétrons mais localizados (porém não congelados) que compõem as ligações σ no plano molecular.

Já na segunda metade da tese, estudamos a supressão da supercondutividade em um supercondutor de duas bandas no regime onde uma delas é incipiente, ou seja, quando uma das bandas está logo acima (ou logo abaixo) do nível de Fermi. Num supercondutor de muitas bandas mais de uma banda de condução pode cruzar o nível de Fermi simultaneamente, dando origem, para temperaturas abaixo da temperatura de transição supercondutora (T_c), a um estado com múltiplos gaps supercondutores. A ocupação das bandas, por sua vez, é controlada pela densidade de portadores de carga (n) presentes no sistema. Suponhamos, por exemplo, que um determinado material supercondutor apresente duas bandas de condução não degeneradas e que, inicialmente, apenas uma delas cruze o nível de Fermi. Ao aumentarmos n , o que pode ser feito, por exemplo, através de dopagem química, aumentamos a ocupação da banda de menor energia até que atingimos o fundo da segunda banda que então começará a ser populada. Nesse caso, uma nova folha da superfície de Fermi emerge, caracterizando uma *transição de Lifshitz*.

Uma transição de Lifshitz deixa uma assinatura no comportamento de T_c em função de n . Curiosamente, ao contrário do que se esperava, foi observado em experimentos recentes que T_c de dois exemplos paradigmáticos de supercondutores de muitas bandas - o SrTiO₃ (STO) e a interface LaAlO₃/SrTiO₃ (LAO/STO) - sofre uma redução nas vizinhanças da transição de Lifshitz. Utilizando uma teoria de campo médio, nós explicamos esse comportamento não intuitivo como um efeito de impurezas não magnéticas presentes no sistema. Mostramos que nas vizinhanças da transição de Lifshitz há uma competição entre dois efeitos opostos: de um lado, T_c tende a aumentar como resultado da amplificação da densidade de estados decorrente do aparecimento da nova banda. De outro lado,

espalhamentos de elétrons entre as bandas devido às impurezas quebram os pares de Cooper, prejudicando a fase supercondutora. Quando as impurezas são fortes o suficiente, o segundo efeito vence e, como resultado, T_c é suprimida. Nosso modelo aponta para uma natureza não convencional do estado supercondutor em ambos STO e interface LAO/STO, uma questão ainda em aberto na literatura. Além disso, também predizemos uma mudança de simetria do estado supercondutor, de s^{+-} para s^{++} , em função da densidade eletrônica, o que pode ser verificado experimentalmente. Esse trabalho foi feito na Universidade de Minnesota, sob orientação do Prof. Rafael Fernandes e em colaboração com o pós-doc Michael Schütt, durante um estágio de um ano financiado pelo projeto BEPE 2019/12874-3 concedido pela Fapesp.

Palavras-chave: Moléculas aromáticas. Correntes Persistentes. Anisotropia Magnética. Diamagnetismo. Supercondutores de muitas bandas. Supercondutividade não convencional. Desordem. Transição de Lifshitz.

Abstract

This thesis is organized in two big blocks, where we investigate two distinct exotic phenomena in low-dimensional systems of interacting electrons. In the first half of this thesis, we address the experimentally observed magnetic anisotropy of aromatic molecules. Our goal is to formulate a microscopic minimal model to describe the fundamental physics behind this curious and controversial phenomenon. We argue that, on the contrary of the main idea of the Ring Current Model, the degrees of freedom of the π -electrons (i.e., those occupying the p_z orbitals of the aromatic ring) are not enough to properly describe the magnetic properties of aromatic molecules. We derive an extension of the Hubbard model where a *momentum-momentum effective attractive interaction* between the π -electrons is mediated by virtual excitations of the σ -electrons (i.e., those occupying the sp_2 hybridized orbitals in the molecule's plane).

In the second half of this thesis, we investigate the suppression of superconductivity in a two-band superconductor in a regime where one of the bands is incipient, i.e., in the limit where its bottom is just above (or below) the Fermi level. In a multiband superconductor, multiple conduction bands can cross the Fermi level simultaneously, originating, at a temperature below the superconducting transition temperature (T_c), multiple superconducting gaps, one in each of the bands. By increasing the system's electronic density (n), such that a new band becomes populated, another Fermi pocket emerges in the Fermi surface, signaling a *Lifshitz transition*. Such a transition leaves a signature in the behavior of $T_c(n)$. Contrary to what is expected, it was recently observed a suppression of T_c close to a Lifshitz transition in two paradigmatic examples of multiband superconductors, the SrTiO₃ (STO) and the LaAlO₃/SrTiO₃ (LAO/STO) interfaces. Using a mean-field approach, we explained this counter-intuitive result as an effect of non-magnetic impurities, which, as evidenced by resistivity data, cannot be neglected in these systems. We show that there is a competition between two opposite effects in the vicinity of the Lifshitz transition of a two-band superconductor with dominant intraband pairing interaction and subleading interband pairing interaction: on the one hand, T_c tends to increase as a result of the enhancement of the system's density of states as the second band appears. On the other hand, interband electronic scattering processes due to the presence of disorder start to happen as the second band becomes populated, which breaks the Cooper pairs and, therefore, has a detrimental effect on superconductivity. When disorder is strong enough, the second effect wins, resulting in a suppression of T_c . Our model also suggests an unconventional nature for superconductivity in both STO and LAO/STO interfaces, a topic that remains open and highly debated in the literature. Furthermore, our model also predicts a change in the symmetry, from s^{+-} to s^{++} , of the superconducting state as a function of n , which can be experimentally verified. This

work was done at the University of Minnesota, under the supervision of Professor Rafael Fernandes and in collaboration with the Postdoctoral researcher Michael Schütt, during the one-year scholarship supported by Fapesp BEPE fellowship No. 2016/12874-3.

Keywords: Aromatic molecules. Persistent currents. Magnetic anisotropy. Diamagnetism. Multiband superconductors. Unconventional superconductivity. Disorder. Lifshitz transition.

Contents

1	INTRODUCTION	17
2	THE MAGNETIC ANISOTROPY OF AROMATIC MOLECULES	24
2.1	Prototypes of aromatic molecules	24
2.2	Single-band Hubbard model and Hückel model	27
2.2.1	Energy spectrum	29
2.2.2	Persistent currents and magnetic susceptibility	33
2.3	Extended Hubbard model	41
2.3.1	Generalized Born-Oppenheimer approximation	42
2.3.2	Effective interaction in first quantization	47
2.3.3	Effective interaction in second quantization	49
2.3.4	Results and discussion	53
2.4	Hubbard Hamiltonian for the σ-electrons	58
2.5	Conclusions - Part I	64
3	THE SUPPRESSION OF SUPERCONDUCTIVITY NEAR A LIF-SHITZ TRANSITION	66
3.1	Clean Multiband Superconductors	66
3.1.1	Asymptotic solution of the gap equation	72
3.2	Dirty Multiband Superconductors	75
3.2.1	Asymptotic solution in the high-density limit	85
3.2.2	Asymptotic solution in the dilute regime	90
3.3	Conclusions - part II	95
	Bibliography	97
	APPENDIX	101
	APPENDIX A – DERIVATION OF THE HUBBARD HAMILTONIAN	102
A.1	Single-band Hubbard Hamiltonian	102
A.1.1	Complete energy spectrum	105
A.2	Multiband Hubbard Hamiltonian	105
	APPENDIX B – ESTIMATION OF THE ON-SITE COULOMB RE-PULSION	110

	APPENDIX C – MATRIX ELEMENT OF P IN THE SITE BASIS	115
	APPENDIX D – BREIT-DARWIN HAMILTONIAN IN SECOND QUANTIZATION	116
D.1	Estimation of $\overleftrightarrow{T}^{(i)}$	120
	APPENDIX E – MATSUBARA SUMS FOR THE CLEAN CASE	. 123
	APPENDIX F – MATSUBARA SUMS FOR THE DIRTY CASE	. 126

1 Introduction

In Condensed Matter Physics, there are several phenomena in which exotic electronic states, with unique physical properties, arise as a consequence of either low-dimensionality, strong inter-electronic interactions, or a combination of both. A few paradigmatic examples [1] of such exotic phenomena are the unconventional superconductivity in the cuprates, where it is generally accepted that the fundamental physics is described by that of a copper oxide plane (effective 2D system), the fractional Quantum Hall effect, where the Hall resistance is quantized in non-integers multiples of h/e^2 , and the recently observed correlated phases in twisted bilayer graphene, which compose a very active research line nowadays [2, 3, 4].

In this thesis, we investigate two distinct exotic phenomena in low-dimensional systems of interacting electrons: (a) the anisotropic magnetic response of aromatic molecules (chapter 2) and (b) the suppression of superconductivity across the Lifshitz transition in 2D two-band superconductors (chapter 3).

Aromaticity is a very delicate concept that lies at the heart of chemistry since the discovery of the benzene molecule by Michael Faraday [5] in 1825. It is generally accepted that aromatic molecules are composed of a planar cyclic arrangement of carbon atoms. In this configuration, each carbon atom has four valence orbitals: one p_z orbital and three sp_2 orbitals, which originate from the hybridization of the s , p_x and p_y orbitals. The electrons occupying the p_z orbitals show large delocalization, being able to hop from one atom to its closest neighbor, conferring extra stability to the molecule [6]. However, up to this date, no smoking gun evidence could tell us if a given molecule is aromatic. In other words, there is no single property which can be related to an unequivocal measure of aromaticity [7, 8, 9]. On the contrary, along the years different criteria for aromaticity were proposed, and, among them, one which became very popular is the *magnetic criteria for aromaticity* [7].

In the decade of 1930s, it was experimentally verified that aromatic molecules have a peculiar magnetic property: when a magnetic field is applied perpendicularly to their planes, the induced magnetic moment is such that its component parallel to the field is much more intense than the perpendicular components, reflecting in an anisotropy of the molecules' magnetic susceptibility (which we hereafter denote by $\Delta\chi$) [10]. As pointed by Linus Pauling "*the susceptibility ellipsoids of the aromatic molecules are found to be approximately prolate ellipsoids of revolution, with the long axis normal to the plane of the ring system*" [11].

To explain this phenomenon, Linus Pauling [11], Fritz London [12, 13, 14] and

Kathleen Lonsdale [15] developed a model known as *Ring Current Model* (RCM for short). Although there are some differences in the formulation proposed by each of them [7], they agree that the abnormally large induced magnetic momentum in the direction of the external field has its origin in the high mobility of the electrons occupying the p_z orbitals of the aromatic ring, which are denominated π -electrons. The basic idea is as follows: the π -electrons can move almost freely through the aromatic ring. Therefore, when a magnetic field is applied perpendicularly to the molecular plane, they acquire a component of momentum in the angular direction, which defines an *electric current loop* along the aromatic ring. Such loop current, in turn, generates a magnetic momentum that naturally points in the same direction of the field.

To understand the origin of the delocalization of the π -electrons, let's take a look into the didactic example of a benzene molecule. The overlap of the p_z orbitals forms three π -bonds between pairs of adjacent carbon atoms. There are two possible configurations for such π -bonds, as shown in Fig. 1, and the molecule's ground state correspond to a linear combination of them, which make the π -electrons wave functions extended in space [16].

Although the RCM model provides a very intuitive qualitative picture of the physics behind the magnetic properties of the aromatic molecules, its original conception is rooted in a series of unjustified hypothesis which originated several misunderstandings and controversies along the years [7]. One of the major misunderstandings has to do with the nature of the current loop that establishes in the aromatic ring: London called it a "*supracurrent*" to emphasize that this loop current experiences no electric resistance [12, 13, 14]. Over the years, this term evolved to "*supercurrent*" [17, 18, 19], leading some people to believe that the current loops in aromatic molecules were essentially the same phenomena as the superconducting currents in a superconducting ring, but this is absolutely false!

The persistent currents in aromatic molecules and the supercurrents in a

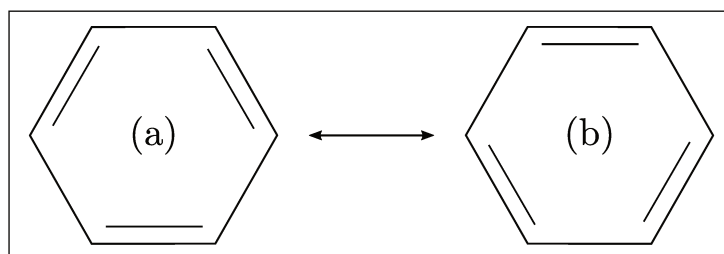


Figure 1 – **Resonating Kekulé structures for benzene.** Illustration of the two different distribution of the π -bonds between pairs of carbon atoms in a benzene molecule. The double line represents double covalent bonds, composed by one π -bond, due to the overlap of the p_z orbitals, and one σ -bond, due to the overlap of neighboring sp_2 orbitals. The single lines represent a single σ -bond.

superconductor are completely different physical phenomena. When one thinks about superconductivity, maybe the first thing that comes to mind is its perfect conductivity (although it is not the most fundamental physical property of a superconductor¹), but dissipationless currents are also found in non-superconducting states. At the time that the RCM model was formulated, it was not known that a *normal metal ring* supports a persistent electric current, as long as it is small enough, clean enough, and is kept at low temperatures. Such persistent current is an *equilibrium phenomenon*, resulting from the quantum coherent motion of the electrons along the ring [20]. This is the type of current we encounter in the aromatic molecules [21]. Hereafter, every time we say persistent current, we mean the equilibrium dissipationless currents that are observed in normal metal micro/mesoscopic rings.

Conversely, in a superconductor, the current-carrying states are not equilibrium states of the system, but rather metastable states with a very long life-time [1]. There are two more key differences between persistent current in normal metal rings and supercurrents in superconductors:

- The persistent current ceases to exist once the external magnetic field is removed.
- A supercurrent is always diamagnetic, while the direction of the persistent current is very sensitive to the number of electrons present in the system [9].

We mentioned above that there are some unjustified hypothesis in the foundation of the RCM model [7]. One of them is that the σ -electrons - i.e., those in the hybridized sp_2 orbitals oriented in the molecular plane, see Fig. 4 - *do not contribute* to the enhancement of the molecule's induced magnetic moment in the direction of the external magnetic field. We can wonder: *is it really true that the degrees of freedom of the π -electrons alone can account for the magnetic anisotropy of the aromatic molecules?* We argue that the answer is no!

As we show in Sec. 2.2, if we use a single-band Hubbard model (only one p_z orbital per atom of the aromatic ring) to describe the π electrons of a benzene molecule, we obtain a $\Delta\chi$ smaller than the experimental value. Even if we completely neglect the inter-electronic interactions, so the aforementioned Hubbard model reduces to the Hückel model (which is actually the model used in London's conception of the RCM model), we obtain a $\Delta\chi$ which is *not* in good agreement with the experimental result.

We argue that it is necessary to take into account the degrees of freedom of the σ -electrons for a proper description of the magnetic properties of the aromatic molecules. In Sec. 2.3 we derive a possible minimal model that does it. Note that if the

¹One cannot derive, from the perfect conductivity another fundamental property of the superconductors, which is its perfect diamagnetism. But the contrary is true.

sigma-electrons are kept static, frozen in the molecule's σ -bonds, the only role they play in the dynamics of the π -electrons, is the generation of a static charge density in the bonds, which composes the periodic potential felt by the π -electrons. If, on the other hand, we allow virtual excitations of the σ -electrons to happen, they modify the charge density in the bonds and, consequently, the potential felt by the π -electrons as they move along the ring. We show that such virtual excitations of the σ -electrons mediate an *effective attractive momentum-momentum interaction between the π -electrons*, which promotes an enhancement of the magnetic response of the aromatic rings. In the specific case of the benzene molecule, the experimental value of $\Delta\chi$ is recovered.

The second half of this thesis is dedicated to another exotic physical phenomenon, which is unrelated to the magnetic anisotropy of aromatic molecules: the suppression of superconductivity across the Lifshitz transition in a multiband superconductor.

In the opinion of this author, superconductivity is one of the most fascinating topics of modern Physics. It was first observed by Kamerlingh Onnes, in 1911, while he was studying the resistivity, as function of temperature, of a sample of mercury. Onnes saw that, below a critical temperature (the superconducting transition temperature T_c), the material's resistivity suddenly dropped to zero, signaling a *perfect conductance*. It took more than 50 years after the discovery of superconductivity for the development of the first microscopical model that successfully describes this phenomenon: the BCS model, named after John Bardeen, Leon Cooper, e John Robert Schrieffer.

Briefly speaking, the BCS model tells us that electrons in an underlying crystal lattice experience an effective attractive interaction mediated by the phonons [22, 23]. Such attraction causes an instability in the system and promotes the formation of pairs of electrons, denominated *Cooper pairs*, which condense in a state that becomes macroscopically occupied. Over the years, new superconductors were discovered, with increasing values of T_c , where the aforementioned phononic mechanism could no longer account for their physical properties. These superconductors are generically called *unconventional superconductors*.

It remains an exciting open problem to elucidate the origin of superconductivity in the unconventional superconductors: although it is generally accepted that in these systems the electrons also bind in Cooper pairs, there is no consensus about the "glue" that keeps them together. It might be the case that the microscopic mechanism for superconductivity is different for each of the distinct families of unconventional superconductors (such as the cuprates, iron pnictides, organic superconductors, heavy fermions and so on).

Moreover, the phase diagram of unconventional superconductors is incredibly rich. One often finds a plethora of different phases in the vicinity of superconductivity, which can compete with the superconducting state or enhance it. These systems are a

playground to study highly correlated phases of matter.

A particularly interesting class of superconductors are the multiband ones. In these materials the underlying crystal structure is such that multiple conduction bands can cross the Fermi levels simultaneously, which originates, below T_c , multiple superconducting (SC) gaps. For instance, multiband superconductivity should be common among materials in which multiple electronic d orbitals are occupied. Examples of multiband superconductors can be found among either conventional superconductors (MgB₂ [24], NbSn₃ [25], and NbSe₂ [26]) and unconventional superconductors (such as BaFe₂As₂ [27], Sr₂RuO₄ [28], and CeCoIn₅ [29]).

Recent experiments also reveal multiband superconductivity in bulk SrTiO₃ (STO for short) [30, 31]. It was the first oxide discovered to be superconductor, and, until today, the nature and origin of its superconducting state remain an unsettled puzzle. STO has three concentric conduction electron-like bands centered at the center of the Brillouin zone, which originate from the t_{2g} orbitals of the Ti atoms. Furthermore, the degeneracy of these bands is lifted by a combination of spin-orbit interaction and crystal field [32].

The superconducting state in STO is established upon electron doping, which increases the density (n) of charge carriers in the system. It can be done, for instance, by replacing some of the titanium atoms by niobium (SrTi_{1-x}Nb_xO₃) or by removing some of the oxygen atoms (SrTiO_{3-δ}). Curiously, superconductivity was found to persist over a wide range of electron doping - see Fig. 2(a) - even when a tiny amount of electrons is present in the system, which makes STO an example of a *dilute superconductor*.

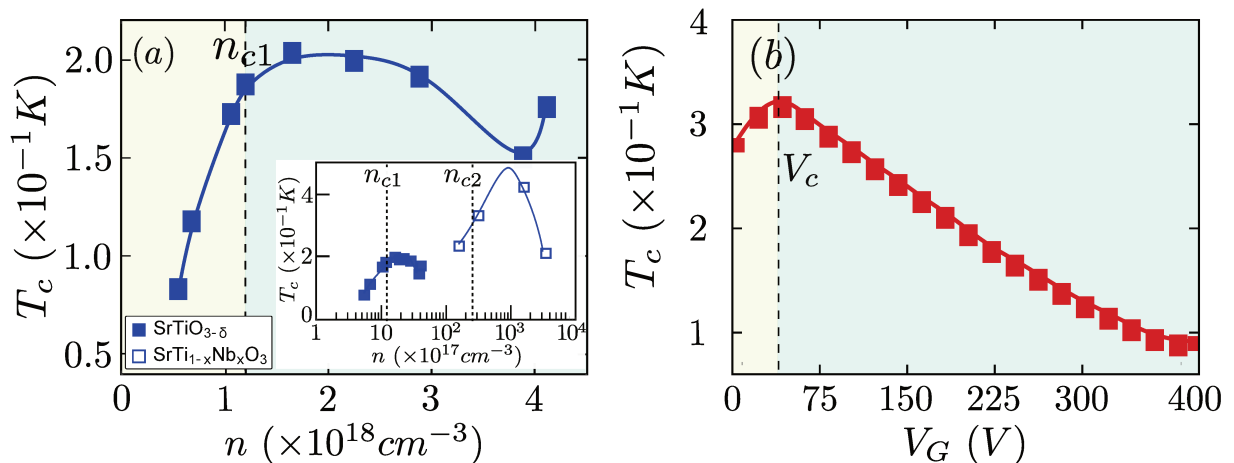


Figure 2 – **Experimental phase diagram of SrTiO₃ and LaAlO₃/STO** faces Panels (a) and (b) reproduce the experimental T_c reports and [33], respectively. In bulk STO (a), the carrier concentration is controlled by chemical doping, and Lifshitz transitions take place at the carrier densities n_{c1} and n_{c2} (see inset). In LAO/STO (b), the carrier concentration is controlled by the gate voltage V_G and a Lifshitz transition happens at V_c .

The multiband character of STO manifests in its phase diagram[31] - i.e., T_c as a function of n - which exhibits a double dome shape, as shown in the inset in Fig. 2(a). When n is smaller than a critical value $n_{c,1}$, only the lower band is occupied and its Fermi surface is (approximately) a small sphere. In this case, we are in the regime of *single-band superconductivity*. As we increase n , T_c monotonically increases as a consequence of the increasing density of states of the system. When n equals a critical value $n_{c,1}$, we are at the bottom of the second band, which now becomes populated, signaling a *Lifshitz transition* (LT). In general, a LT is any change in a system's Fermi surface as function of the electronic density (or, equivalently, chemical potential), but in the specific context of multiband superconductivity, it is characterized by the appearance of a new Fermi pocket at the Fermi surface as a new band becomes populated.

For $n > n_{c,1}$, the two lower bands are occupied and we are in the regime of *two-band superconductivity*. If we continue increasing n , at $n = n_{c,2}$ we reach the bottom of the third band and the system undergoes another Lifshitz transition. Finally, for $n > n_{c,2}$, we enter in the regime of *three-band superconductivity*. It is important to say that $n_{c,1}$ and $n_{c,2}$ were measured for the first time through quantum oscillation experiments in 2014 [31].

Interestingly, if we focus on the low-density region of the phase diagram of STO (region of the first SC dome in the inset in Fig.2(a)), we see that the maximum of the superconducting dome coincides with the critical density $n_{c,1}$ where the Lifshitz transition takes place. This is unexpected and counter-intuitive. Since the system's density of states increases across the LT, we would expect T_c follow the same trend. As shown in Fig. 2(b), the same non-monotonic behavior of T_c is observed in another multiband superconductor, the LaAlO₃/SrTiO₃ interface[33], which, as a matter of fact, shows several similarities with bulk STO.

Moreover, residual resistivity data [31, 34] reveals that STO and LAO/STO interfaces are dirty systems: we show in Sec. 3.2 that such transport data allow us to estimate the impurity scattering rate (τ^{-1}) for both STO and LAO/STO interfaces, yielding $\tau^{-1} \approx 10T_c$. Such a large scattering rate in comparison with T_c tells us that the role of disorder cannot be neglected in the description of the physical properties of these materials. Motivated by the aforementioned experimental results, in the second half of this thesis we study the evolution of T_c of a dirty two-band superconductor, as a function of the chemical potential, across the LT.

In this work, we take into account only non-magnetic disorder and we show that interband scattering processes are strongly pair-breaking if the interband superconducting pairing interaction is *repulsive*. Actually, in the vicinity of the Lifshitz transition, our model reveals the competition between the tendency of increase of T_c , promoted by the enhancement of the system's density of states and the detrimental effects of the interband scattering processes. Therefore, when disorder is strong enough, the second effect wins,

resulting in a suppression of superconductivity across the Lifshitz transition in agreement with the experimental phase diagrams of Fig. 2.

As explain in Sec.3.2, another two important outcomes of our model are (a) evidence of an unconventional nature of superconductivity for both STO and LAO/STO interfaces and (b) a prediction of crossover in the symmetry of the superconductor state, which might explain why some recent experiments performed in STO showed signatures of single-band superconductivity even in a doping region where it is known that multiple bands crosses the Fermi level.

In this thesis, we focus on 2D bands, since this is the case where an analytic calculation of $T_c(\mu)$ can be done, but we emphasize that the same qualitative behavior holds for 3D conduction bands, as shown in Refs. [35, 36].

The order of the sections is outlined at the beginning of each of the subsequent chapters. We emphasize that chapters 2 and 3 are independent, so the reader should feel free to choose the order he/she prefers to read. This material was written with the purpose to be accessible for a more general audience than Condensed Matter physicists. Therefore, this thesis is made to be self-contained and fundamental concepts used here are presented in detail. To not make the reading tedious for those who are already familiarized with the formalism we use here, we provide a set of six appendices which complement the body of the main text.

2 The magnetic anisotropy of aromatic molecules

In this chapter, we propose a minimal microscopic model (Eq.(2.91)) to describe the exotic magnetic anisotropic response of the aromatic molecules. Our model consists of an extension of the Hubbard model for the π -electrons (i.e., those occupying the p_z orbitals of the aromatic ring, as explained in Sec. 2.1), in which an *effective attractive momentum-momentum interaction* between them is mediated by virtual fluctuations of the σ -electrons (i.e., those occupying the hybridized sp_2 orbitals in the plane of the aromatic molecule).

A description of the discrete microscopic rings we use as prototypes of aromatic molecules is given in Sec. 2.1. In the subsequent Sec. 2.2, we motivate the need for an extension of the Hubbard model by showing, explicitly, that the degrees of freedom of the π -electrons alone cannot account for the anisotropy of the magnetic susceptibility measured in the benzene molecule. We derive our model in Sec.2.3, where all the assumptions and approximations are carefully discussed. In Sec.2.4, two key assumptions of our model are justified. Our most important results are summarized in Sec. 2.5.

A set of appendices (Appendix A to Appendix D) complements the body of this chapter. Going through these appendices is not required to understand the ideas presented in the main body of the thesis. Therefore they can be skipped if the reader wishes so.

2.1 Prototypes of aromatic molecules

The systems we study in this chapter are *small discrete rings*, i.e., discrete 1D lattices that obey *periodic boundary conditions*. We denote by N the number of sites of the ring and by a its lattice spacing, so the ring's length is simply $L = Na$. These discrete rings are sometimes called in the literature *Hubbard rings*[37], since their electronic degrees of freedom are modeled by the Hubbard model or some extension of it, as is the case in this thesis.

If we think of each of the ring's sites as a carbon atom, we can interpret them as prototypes of aromatic rings of real aromatic molecules¹. On the contrary of real-life molecules, however, *we impose the sites to be always static*. That is because in this work

¹Here, we refer to aromatic molecules whose rings are composed solely by carbon atoms.

we focus solely on *orbital electronic properties* and, thus, we do not investigate effects related to the ionic degrees of freedom, such as the molecular vibrational levels.

Recall that a neutral carbon atom has a total of six electrons, two of them in the $1s$ shell, strongly bound to the atom's nuclei, while the remaining four electrons are in the outermost $2s$ and $2p$ orbitals. In the ring configuration, the $2s$, $2p_x$ and $2p_y$ orbitals, whose wave functions are expressed by [38]

$$\langle r\theta\phi | s_j \rangle = f_s(j)Y_0^0(\theta_j, \phi_j) , \quad (2.1)$$

$$\langle r\theta\phi | p_{x,j} \rangle = \frac{f_{p_x}(j)}{\sqrt{2}} [Y_1^{-1}(\theta_j, \phi_j) - Y_1^1(\theta_j, \phi_j)] , \quad (2.2)$$

$$\langle r\theta\phi | p_{y,j} \rangle = \frac{f_{p_y}(j)}{\sqrt{2}} [Y_1^{-1}(\theta_j, \phi_j) + Y_1^1(\theta_j, \phi_j)] , \quad (2.3)$$

hybridize. It defines *three orthonormal sp_2 orbitals* [16]:

$$|sp_{2,j}^{(I)}\rangle = \frac{1}{\sqrt{3}} |s_j\rangle + \frac{2}{\sqrt{3}} |p_{x,j}\rangle , \quad (2.4)$$

$$|sp_{2,j}^{(II)}\rangle = \frac{1}{\sqrt{3}} |s_j\rangle - \frac{1}{\sqrt{6}} |p_{x,j}\rangle + \frac{1}{\sqrt{2}} |p_{y,j}\rangle , \quad (2.5)$$

$$|sp_{2,j}^{(III)}\rangle = \frac{1}{\sqrt{3}} |s_j\rangle - \frac{1}{\sqrt{6}} |p_{x,j}\rangle - \frac{1}{\sqrt{2}} |p_{y,j}\rangle . \quad (2.6)$$

The p_z orbitals, on the other hand,

$$\langle r\theta\phi | p_{z,j} \rangle = f_{p_z}(j)Y_1^0(\theta, \phi) , \quad (2.7)$$

remains unchanged. In the previous equations $Y_l^m(\theta, \phi)$ denotes the spherical harmonics². Besides $\mathbf{j} \equiv \mathbf{r} - \mathcal{R}_j$, are vector positions centered at the j -th site of the ring, with associates polar and azimuthal angles $0 \leq \theta_j \leq \pi$, $0 \leq \phi_j \leq 2\pi$, respectively. Illustrations of the s , p and hybridized sp orbitals are provided in Fig. 3. The vector \mathcal{R}_j is the position of the j -th site of the ring, which we discuss in more details below. Moreover, the specific functional form of the radial component of the orbitals, $f_s(j)$, $f_{p_x}(j)$, $f_{p_y}(j)$ and $f_{p_z}(j)$ are discussed in the Appendix A.

It is important to note that the sp_2 orbitals are oriented along the ring's plane in such a way that there is an angular spacing of $2\pi/3$ between them (see Fig. 3 (b) and Fig. 4 (c)). The p_z orbitals, on the other hand, are oriented perpendicularly to the ring's plane, as illustrated in Fig. 4 (b). The overlap between the sp_2 orbitals of two adjacent carbon atoms - as well as the overlap between an sp_2 orbital of a carbon atom and the

²In our notation, $Y_l^m(\theta, \phi) = (-1)^m \sqrt{\frac{(2l+1)(l-m)!}{4\pi(l+m)!}} P_{lm}(\cos\theta) e^{im\phi}$, where $P_{lm}(x)$ are the associated Legendre Polynomials, with $l = 0, 1, 2, \dots$ and $m = -l, -l+1, \dots, l-1, l$.

s orbital of a hydrogen atom in the specific case of the benzene molecule, see Fig. 4(a) - forms *covalent bonds* known as σ -bonds. Moreover, the overlap between neighboring p_z orbitals forms the so-called π -bonds, a weaker type of covalent bond. Briefly speaking, the π -bonds are weaker than the σ -bonds because the overlap between adjacent p_z orbitals are much smaller than that of neighboring sp_2 orbitals. Following the usual nomenclature, we hereafter denominate the electrons at the sp_2 orbitals by σ -electrons, while those occupying the p_z orbitals are called π -electrons.

Along this chapter, we focus on microscopic rings with a small number of sites, $3 \leq N \leq 6$, essentially because in these cases where we are able to perform an exact diagonalization of the Hamiltonians we study in the subsequent sections. However, the extended Hubbard model we derive in Sec. 2.3, which is one of the most important results of this chapter, holds for any number of sites N and can also be extended to a 2D carbon

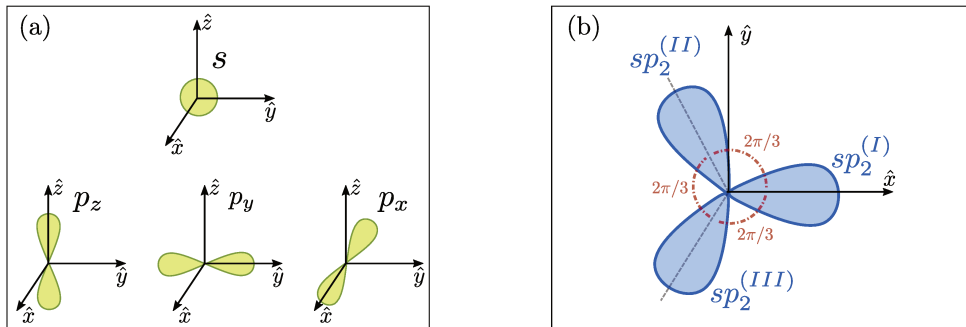


Figure 3 – **Carbon atom's valence orbitals.** Panel (a) illustrates the angular dependence of the $2s$, $2p_x$, $2p_y$ and $2p_z$ carbon's orbitals. Panel (b) illustrates the three sp_2 orbitals resulting from the hybridization of the $2s$, $2p_x$ and $2p_y$ orbitals. The sp_2 orbitals are oriented in the xy plane with an angular spacing of $2\pi/3$ between them.

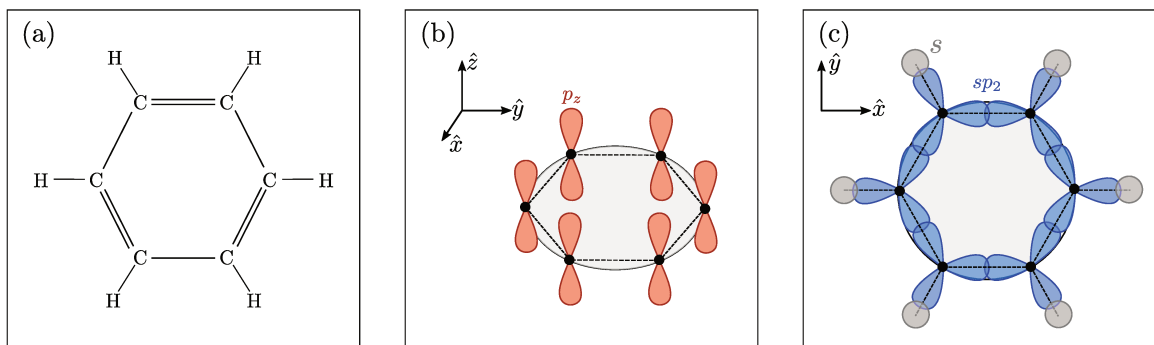


Figure 4 – **Benzene molecule (C_6H_6).** The panel (a) brings an illustration of the chemical structure of the benzene molecule, where the single (double) lines represent single (double) chemical bonds. Panels (b) and (c) show a didactic sketch of the (b) p_z orbitals, perpendicular to the molecular plane, and (c) hybridized sp_2 orbitals oriented in the molecule's plane. Panel (c) also show the s orbitals of the hydrogen atoms.

lattice, as the graphene. Such generalization, however, is beyond the scope of this thesis and is left for a future project.

We choose the rings' plane coinciding with the xy plane, adopting the center of the ring as the origin of the coordinate system. In this configuration, the position of the j -th site of the ring is given by

$$\mathcal{R}_j = \frac{a}{\sqrt{2(1 - \cos(2\pi/N))}} [\cos \alpha_j \hat{x} + \sin \alpha_j \hat{y}] , \quad (2.8)$$

with $j = 1, 2, \dots, N$. Here, $\alpha_j = (j - 1)2\pi/N$ denotes the site's angular position, and a is the lattice spacing. In analogy, to the real aromatic molecules, we consider *three orbitals per ring's site*: one p_z orbital two sp_2 orbitals. The third sp_2 orbital on a given site, which binds it to another atom (such as the hydrogen atom in the case of the benzene molecule) is considered frozen, as explained in Appendix A.2, and therefore incorporated in the ring's sites. An illustration is shown in Fig. 5.

2.2 Single-band Hubbard model and Hückel model

The RCM model provides a simple qualitative scenario to understand the magnetic anisotropy of aromatic molecules, where the loop current created by the delocalized π -electrons is the origin of its exotic magnetic response. However, turning to a microscopic point of view, *is it really true that the π -electrons alone can account for this curious*

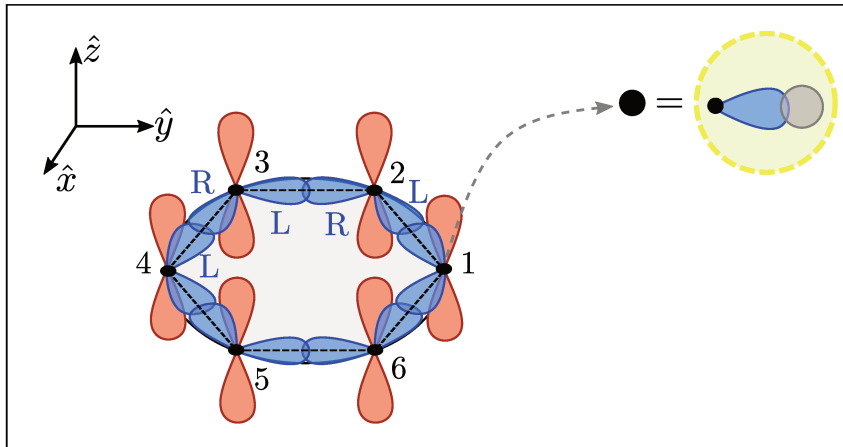


Figure 5 – **Three-band model.** Illustration of the orbital structure of the rings we consider in this thesis. Each of the N sites of the rings ($N = 6$ in this figure) contains one p_z orbital and two sp_2 orbitals, which we denominate *left* sp_2 orbital (L) and *right* sp_2 orbital (R) according to the right-hand rule. The sites are always enumerated in increasing order in the counter-clockwise direction. The degrees of freedom of the third sp_2 orbital of each site, as well as those of the valence orbitals of another atom that might bond with it are frozen and absorbed in the ring's sites.

magnetic property of aromatic molecules? To answer this question let's take a step back and investigate the magnetic properties of discrete rings with N sites, N_e electrons, and, following the ideas of the RCM model, with *only one p_z orbital per site*. In other words, in this section we *freeze* the degrees of freedom of the σ -electrons, which are incorporated at the ring's sites (see Fig. 6), and thus contribute to the dynamics of the π -electrons only though the the generation of a *static charge density at the σ -bonds* encoded in the ring's periodic potential - see Eq.(A.1). We emphasize that the ring with $N = N_e = 6$ is the prototype of the benzene molecule.

The simplest model that describes the degrees of freedom of N_e itinerant and *interacting* electrons in a single-orbital N -site lattice is the standard³ single-band Hubbard model[39],

$$\hat{H}_0 = -t \sum_{j=1}^N \sum_{\sigma} \left(c_{j\sigma}^{\dagger} c_{j+1\sigma} + \text{h.c.} \right) + U \sum_{j=1}^N \hat{n}_{j\uparrow} \hat{n}_{j\downarrow}, \quad (2.9)$$

where the operator $c_{j\sigma}^{\dagger}$ ($c_{j,\sigma}$) creates (annihilates) a electron with spin⁴ σ at the p_z orbital of the j -th site of the ring, and $\hat{n}_{j\sigma} = c_{j\sigma}^{\dagger} c_{j\sigma}$ is the number operator. Such Hamiltonian essentially tells us that, in a lattice, electrons can hop from site i to site j with a probability amplitude t_{ij} - which depends both on the overlap between the orbitals centered on these sites and on the periodic potential generated by the lattice ions together with its

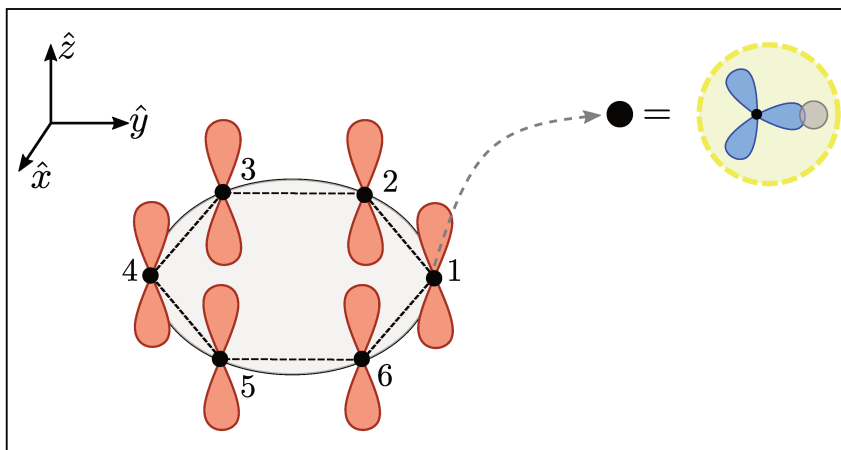


Figure 6 – **Single-band model.** Illustration of the orbital structure of the rings we consider in Sec. 2.2. Each of the N sites of the rings ($N = 6$ in this figure) contains *only one p_z* . The degrees of freedom of the sp_2 orbitals, as well as those of the valence orbitals of another atom that might bond with it are frozen and absorbed in the ring's sites. The ring's sites are always enumerated in a crescent order in the counter-clockwise direction.

³Along this thesis, by *standard Hubbard model* we mean the Hubbard Hamiltonian composed solely by a hopping term and the on-site repulsion, as defined in Eq.(2.9) i.e., no second-neighbor hopping or next-neighbor Coulomb repulsion.

⁴Note that σ are the eigenvalues of the projection of the spin operator in the z axis. Therefore, here $\sigma = \uparrow$ denotes a spin up, while $\sigma = \downarrow$ denotes a spin down.

core electrons - and interact with each other through the Coulomb repulsion, which is approximated to a purely *local* interaction U , called *on-site Coulomb repulsion*.

Here, we approximate t_{ij} by the first-neighbor hopping [39]: $t_{ij} = -t(\delta_{j,i+1} + \delta_{j,i-1})$, with $\delta_{i,j}$ denoting the usual Kronecker delta, and

$$t = - \int d\mathbf{r} \varphi_i^*(\mathbf{r}) \left[-\frac{\hbar^2}{2m} \nabla^2 + V_c(\mathbf{r}) \right] \varphi_j(\mathbf{r}) , \quad (2.10)$$

where $\varphi_i(\mathbf{r})$ is the Wannier wave function of an electron in the p_z orbital of site i , and $V_c(\mathbf{r})$. We emphasize that, although the hopping between second-neighbor sites (and even more distant sites) can in principle happen, they are much smaller than t , since the overlap between p_z orbitals at different sites significantly decreases as the sites are more separated.

Furthermore, in terms of the aforementioned Wannier wave functions, the on-site Coulomb repulsion takes the form

$$U = e^2 \int d\mathbf{r} \int d\mathbf{r}' \frac{|\varphi_i(\mathbf{r})|^2 |\varphi_i(\mathbf{r}')|^2}{|\mathbf{r} - \mathbf{r}'|} , \quad (2.11)$$

where $e \approx 1.602 \times 10^{-19} C$ ($\approx 8.542 \times 10^{-2}$, dimensionless in Natural Units⁵) is the elementary charge⁶. If we set $U = 0$, Eq.(2.9) reduces to a purely tight-binding Hamiltonian known as *Hückel Hamiltonian*. For self-consistency purposes of this thesis, we provide a careful derivation of Eq.(2.9) in Appendix A.

Note that, up to this point, we did not specify the functional forms of $\varphi_j(\mathbf{r})$ and $V_c(\mathbf{r})$. The specific angular and radial dependence of $\varphi_j(\mathbf{r})$ is important to calculate the numerical values for the parameters t and U . An estimation of these parameters is provided in Appendix B for the specific case of the prototype of benzene. Here, it is enough to keep in mind that the deeper $V_c(\mathbf{r})$ is at the site positions, the larger is the tendency of the electrons to localize around those sites and, therefore, the smaller is the hopping amplitude. Bottom line is that, for now, we do not need to worry about neither $V_c(\mathbf{r})$ nor $\varphi_j(\mathbf{r})$, since in the calculations performed in this chapter, except when explicitly mentioned otherwise, all physical quantities are given in units of t and/or U/t .

2.2.1 Energy spectrum

In the case of the Hückel model (Eq.(2.9) with $U = 0$), we can easily determine the energy levels and correspondent eigenstates of a generic ring with N sites and N_e

⁵The Natural Units are defined by $\hbar = c = 4\pi\epsilon_0 = 1$ and the remaining units are given in terms of electron-volt. For instance, length and time have dimension of inverse of energy ($1/eV$), and electric charge is dimensionless. Therefore, in this unit system the electric current has dimension of energy.

⁶Notice that every time e appears in this thesis' equations, we mean $e > 0$. The negative sign of the electronic charge is always explicitly included.

independent electrons. We only need to apply the Fourier transform to the electronic creation and annihilation operators,

$$c_{k\sigma}^\dagger = \frac{1}{\sqrt{N}} \sum_{j=1}^N e^{i2\pi kj/N} c_{j\sigma}^\dagger, \quad (2.12)$$

$$c_{k\sigma} = \frac{1}{\sqrt{N}} \sum_{j=1}^N e^{-i2\pi kj/N} c_{j\sigma}, \quad (2.13)$$

where $c_{k\sigma}^\dagger$ ($c_{k\sigma}$) creates (annihilates) a electron with spin σ and quasi-momentum k (with $k = 0, 1, \dots, N-1$). This way, we obtain the Hückel Hamiltonian in the *Bloch basis*

$$\hat{H}_{\text{Hückel}} = -2t \sum_{k=1}^{N-1} \sum_{\sigma=\uparrow,\downarrow} \cos\left(\frac{2\pi k}{N}\right) c_{k\sigma}^\dagger c_{k\sigma} = \sum_{k,\sigma} \varepsilon_k \hat{n}_{k,\sigma}, \quad (2.14)$$

where $\hat{n}_{k\sigma} = c_{k\sigma}^\dagger c_{k\sigma}$ is the number operator in Bloch basis and

$$\varepsilon_k \equiv -2t \cos\left(\frac{2\pi k}{N}\right) \quad (2.15)$$

denote its N *single-particle energy levels*⁷.

Therefore, in order to calculate the many-body ground state energy of a ring with N sites and N_e independent electrons, among which $N_{e\uparrow}$ have spin up and $N_{e\downarrow}$ have spin down, we just need to fill the levels k obeying the Pauli exclusion principle. The corresponding ground state wave function is simply the Slater determinant of the single-particle wave functions $|k, \sigma\rangle \equiv c_{k\sigma}^\dagger |0\rangle$ (with $|0\rangle$ denoting the electronic *vacuum*) of each level k . It means that the many-body ground state and the corresponding energy are given by

$$|\phi_0^{(H)}\rangle = \prod_{k=0}^{N_{e\uparrow}-1} \prod_{q=0}^{N_{e\downarrow}-1} c_{k\uparrow}^\dagger c_{q\downarrow}^\dagger |0\rangle, \quad (2.16)$$

and

$$E_0^{(H)} = \sum_{k=0}^{N_{e\uparrow}-1} \varepsilon_k + \sum_{q=0}^{N_{e\downarrow}-1} \varepsilon_q = 2 \sum_{k=0}^{N_e^{(-)}-1} \varepsilon_k + \sum_{N_e^{(-)}}^{N_e^{(+)}-1} \varepsilon_k, \quad (2.17)$$

respectively. We define $N_e^{(-)} \equiv \min\{N_{e\uparrow}, N_{e\downarrow}\}$ and $N_e^{(+)} \equiv \max\{N_{e\uparrow}, N_{e\downarrow}\}$. The elementary excitations of this model are usual particle-hole pairs, obtained by promoting an electron from the level k to another previously unoccupied level q .

⁷Note that in order to derive Eq. (2.14), we used the sum rule that defines the Kronecker delta, $\delta_{k,q} \equiv \frac{1}{N} \sum_{j=1}^N e^{i2\pi(j(k-q))/N}$.

Unfortunately, such a simple picture does not hold for $U \neq 0$. Since the kinetic and the interaction parts of the Hubbard Hamiltonian Eq.(2.9) do not commute, there is no basis where both are simultaneously diagonal. Consequently, apart from very particular cases, such as a ring with $N = 3$ sites and $N_e = 2$ electrons, in which we can calculate analytic expressions for the eigenvalues and eigenvectors of \hat{H}_0 , our only hope to determine its exact energy spectrum and corresponding states relies on numerical diagonalization.

However, this is not a trivial task, since the dimension $d \equiv 2N!/[(2N - N_e)!N_e!]$ of the the Fock space where \hat{H}_0 is defined grows exponentially with the number of sites and electrons in the ring. For instance, in the case of the prototype of benzene ($N = N_e = 6$), $d = 924$. It is important to note that, when dealing with large d (and we will encounter $d > 924$ in subsequent sections), it is advisable to make use of the Hamiltonian's symmetry in order to rewrite it in a block-diagonal form, which reduces computational costs of the diagonalization procedure. For instance, the spin operator

$$\hat{S}_z = \sum_{j=1}^N (\hat{n}_{j\uparrow} - \hat{n}_{j\downarrow}) \quad (2.18)$$

commutes with \hat{H}_0 , meaning that the z -component of the *total* spin of the system (s_z) is a conserved quantity. In other words, each eigenstate of the Hubbard Hamiltonian has a well defined value of s_z , and the matrix element of \hat{H}_0 between two eigenstates of \hat{S}_z with different values of s_z is identically zero. Consequently, in the basis spanned by the eigenstates of Eq.(2.18), the Hubbard Hamiltonian acquires a block-diagonal form, and we only need to diagonalize each block separately.

Hereafter, as a matter of personal taste, we choose to work in the *site basis*, rather than in the Bloch basis. The former is spanned by

$$\mathcal{B}_0 = \left\{ |n_{1\uparrow}n_{1\downarrow} \cdots n_{N\uparrow}n_{N\downarrow}\rangle / \sum_{j,\sigma} n_{j\sigma} = N_e \text{ and } n_{j\sigma} = 0 \text{ or } 1 \right\}, \quad (2.19)$$

where[16] $|n_{1\uparrow}n_{1\downarrow} \cdots n_{N\uparrow}n_{N\downarrow}\rangle = c_{N\downarrow}^\dagger \cdots c_{1\downarrow}^\dagger c_{1\uparrow}^\dagger |0\rangle$.

Fig. 7 shows some of the energy levels, as function of U/t , obtained through numerical diagonalization of Eq.(2.9) for rings with (a) $N = 3$, (b) $N = 4$, (c) $N = 5$ and (d) $N = 6$ sites. These energy spectra were calculated for the rings in the *half-filling regime*, where $N = N_e$. This choice is motivated by the electronic configuration of the benzene molecule, where we have a total of six π -electrons occupying the the six p_z orbitals of the aromatic ring. Moreover panels (b)-(d) show just a few of the low-lying energy levels of the systems. That is because their complete energy spectra are very large, and including all the curves in the same panel results in quite confusing figures. For completeness, though, the full energy spectra as function of U/t can be found in Fig. 34 at Appendix A.

We verified that although in some of the rings the on-site Coulomb repulsion can break some of the levels degeneracy, such as the ring with $N = N_e = 3$, the ground state can remain degenerate (with a degeneracy four in the case of $N = N_e = 3$) even for finite U/t .

Interestingly, as already observed by other authors [37], the physical properties of these discrete microscopic rings are very sensitive to either the number of sites and electrons of the system. Actually, we can classify the rings in three distinct families, with the components of each family (at half-filling) showing similar properties:

- **Rings with $N = 2n + 1$, $n \in \mathbb{N}$ and $n \geq 1$.** As we see in the next subsection, in the presence of an external magnetic field, the rings of this family show a periodicity of half of a flux quanta in their equilibrium physical properties. The rings of the other two families below, on the other hand, show a periodicity of an integer flux quanta [37].

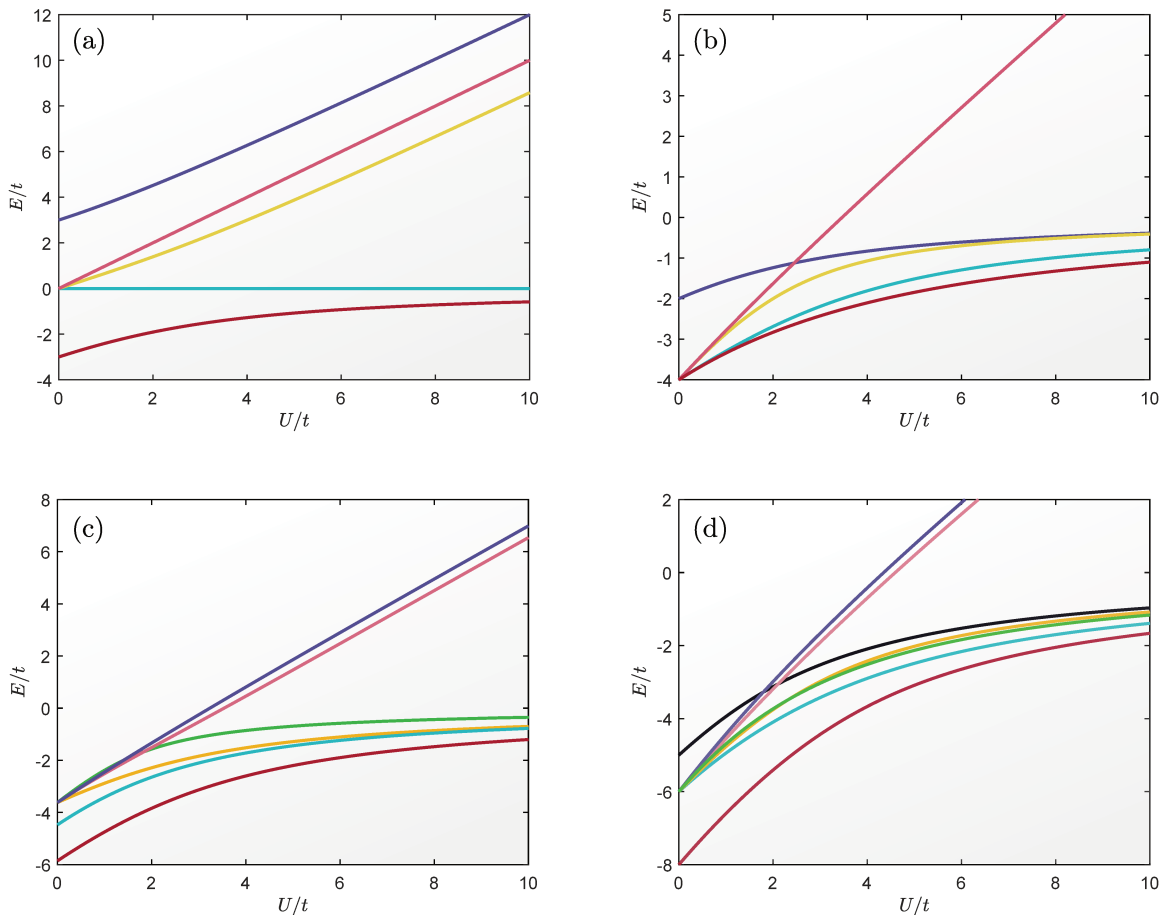


Figure 7 – **Energy spectrum of the Hubbard Hamiltonian.** The panels show the energy levels, as function of U/t for rings with (a) $N = 3$ sites, (b) $N = 4$ sites, (c) $N = 5$ sites and (d) $N = 6$ sites at the half-filling regime, i.e., $N = N_e$. In the panels (b) to (d), only a few of the low-lying energy levels are plotted. The corresponding complete spectrum can be found in Appendix A.

- **Rings with $N = 4n$, $n \in \mathbb{N}$ and $n \geq 1$.** The rings of this family show a paramagnetic persistent current in the ground state.
- **Rings with $N = 4n + 2$, $n \in \mathbb{N}$ and $n \geq 1$.** The prototype of the benzene molecule belongs to this family. It is the only family of microscopic rings for which the ground state is non-degenerate at half-filling. Moreover, in the presence of an external magnetic field, they show a diamagnetic persistent current in their ground state.

2.2.2 Persistent currents and magnetic susceptibility

What about the magnetic properties of the rings described by Eq.(2.9)? To answer this question, let's imagine the following set up: keeping the ring in the xy plane, we apply a magnetic field \mathbf{B} along the z -axis passing through its center, but *without touching its perimeter*. Such a field can be produced, for instance, by a thin infinitely-long solenoid. In this case, we can neglect the contribution of the Zeeman term - which describes the coupling between the electrons total spin and the magnetic field - to the system's total Hamiltonian. As a consequence, the magnetic properties calculated within this setup are a result of the *orbital degree of freedom* of the valence electrons solely.

In the presence of the field \mathbf{B} , due to the minimal coupling $\mathbf{P} \rightarrow \mathbf{P} + e\mathbf{A}/c$, where $\mathbf{B} \equiv \nabla \times \mathbf{A}$ is the vector potential associated with the magnetic field, e is the elementary charge, and c is the speed of light, each electron acquires a component in its momentum in the angular direction, which, in turn, induces a current loop around the ring.

The aforementioned minimal coupling is expressed, in the language of second quantization, as a local Gauge transformation in the electronic creation and annihilation operators[41, 20],

$$c_{j\sigma}^\dagger \rightarrow e^{-i2\pi f/N} c_{j\sigma}^\dagger, \quad (2.20)$$

$$c_{j\sigma} \rightarrow e^{i2\pi f/N} c_{j\sigma}. \quad (2.21)$$

Here $f \equiv \phi/\phi_0$ represents the dimensionless magnetic flux that pierces the ring, and $\phi_0 = 2\pi\hbar c/e$ is the magnetic flux quantum. Plugging Eqs.(2.20) and (2.21) into Eq.(2.9), we readily obtain the Hubbard Hamiltonian in an external magnetic field,

$$\hat{H}_{0,(mag)} = -t \sum_{j=1}^N \sum_{\sigma=\uparrow,\downarrow} \left(e^{i2\pi f/N} c_{j\sigma}^\dagger c_{j+1\sigma} + \text{h.c.} \right) + U \sum_{j=1}^N \hat{n}_{j\uparrow} \hat{n}_{j\downarrow}. \quad (2.22)$$

Note that f shifts the single-particle energy levels defined in Eq.(2.15), which now take the form

$$\varepsilon_k(f) = -2t \cos \left(\frac{2\pi(k+f)}{N} \right). \quad (2.23)$$

This is precisely the origin of the aforementioned periodicity of the equilibrium properties, such as ground state energy, persistent current and magnetic susceptibility, of our microscopic rings.

Fig. 8, shows the many-body ground state energy (E_0), obtained through exact diagonalization of Eq.(2.22), as a function of the dimensionless magnetic flux f that pierces a ring with (a) $N = 3$, (b) $N = 4$, (c) $N = 5$ and (d) $N = 6$ sites. The different color curves in each panel refers to different values of the ratio U/t , as indicated in the legend of panel (a). Note that the periodicity of $E_0(f)$, as anticipated in Sec. 2.2.1, is $1/2$ (corresponding to a half flux quantum, $\phi_0/2$) for rings with an odd number of sites, and 1 (corresponding to an integer flux quantum) for those with *even* number of sites. We verified, in agreement with Ref.[37], that going away from the half-filling, the ground state energy periodicity is always 1, independent of the number of sites in the ring.

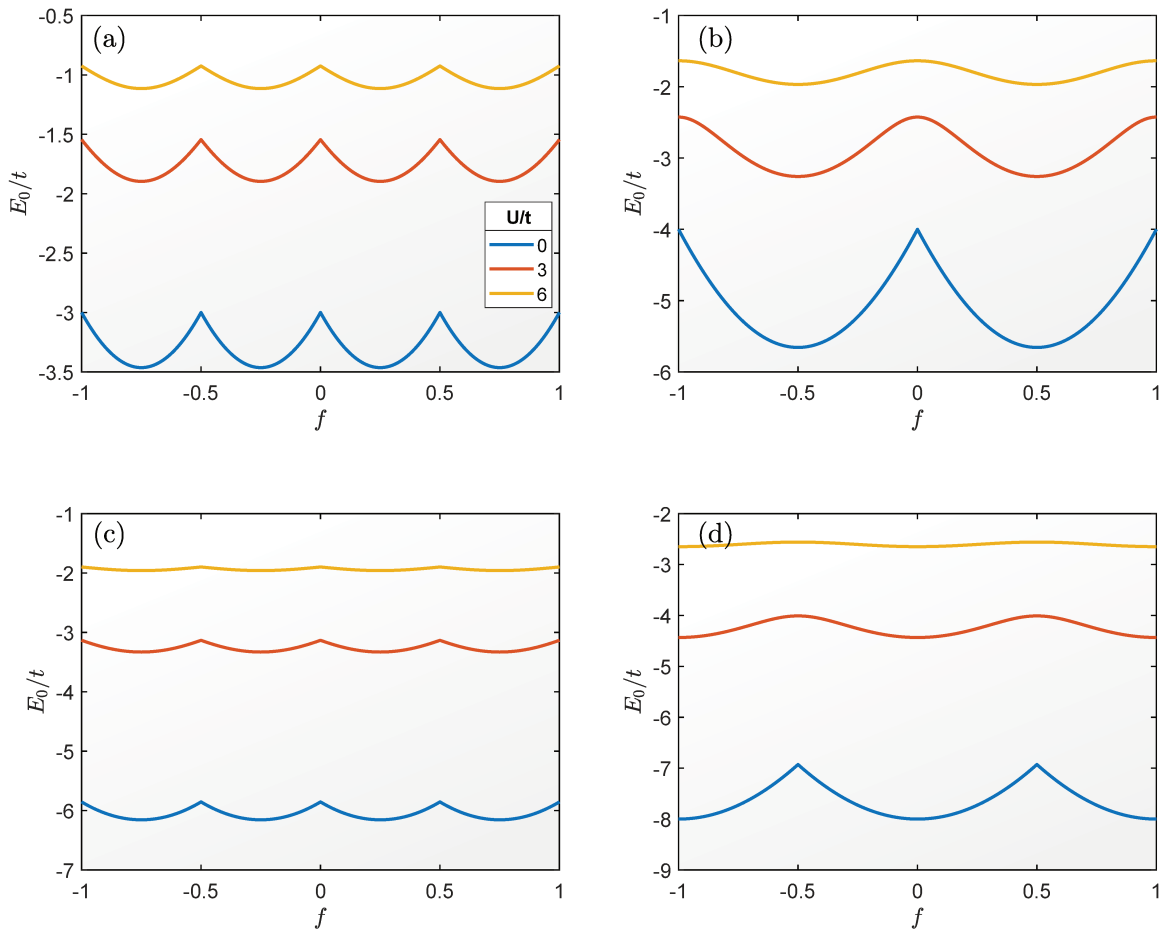


Figure 8 – **Ground state energy as function of magnetic flux.** The panels show the the ground state energy (E_0) of a ring with (a) $N = 3$ sites, (b) $N = 4$ sites, (c) $N = 5$ sites and (d) $N = 6$ sites, as function of the dimensionless magnetic flux that pierces it ($f = \phi/\phi_0$) and for different values of the ratio U/t , as indicated at the legend in panel (a). As in Fig. 7, all the rings are in the half-filling regime ($N_e = N$). The legend in panel (a) also apply for the panels (b)-(d).

Interestingly, Fig. 8 also shows that the amplitude of the oscillations of $E_0(f)$ get significantly reduced as we increase U/t . This is a manifestation of the tendency of localization of the electrons at the ring's sites: as U increases, an increasingly amount of energy is required to promote double occupation of the sites - which inevitably happens as the electrons move around in the half-filling regime.

Note that the value of the magnetic field we need to apply to the rings in order to observe the periodicity of its ground state energy is ridiculously large. For instance, for a ring with three sites and a lattice spacing of the order of 1\AA , the magnitude of the magnetic field we would need to apply in order to have a flux quantum piercing its area would be of $B \approx 5.8 \times 10^5 T$, impossible to achieve in a laboratory. But we do not need to worry about it, since here we are mostly interested in the low field response of the rings.

Another way to rationalize the periodicity of the equilibrium properties of the ring is through band theory. Actually, there is a one-to-one correspondence between the boundary conditions satisfied by the Bloch wave functions of an electron moving in an external potential with periodicity $2\pi/\phi_0$ and the boundary condition imposed by the phase $e^{i2\pi f/N}$ in the Hamiltonian, meaning that the magnetic field creates micro-bands in the single-particle spectrum. An electron in each of these micro-bands has a group velocity which is proportional to the curvature of the band, and the sum of the contributions of all the electrons in the system gives rise to a finite current along the ring. At zero-temperature ($T = 0$), it is given (in Natural Units) by

$$I_0(f) = -\frac{e}{2\pi} \frac{\partial E_0(f)}{\partial f}, \quad (2.24)$$

where E_0 is the many-body ground-state energy. We emphasize that such an electric current is *persistent* in the sense that it does not suffer the effect of dissipation, but it vanishes if we turn off the magnetic field. Moreover it is an *equilibrium property of the ring*, and should not be confused with the supercurrents in a superconducting loop, as explained in Sec. 1.

It is worth saying that we can also express $I_0(f)$ as the expectation value, in the ring's (many-body) ground state, here denoted by $|\phi_0(f)\rangle$, of an *electric current operator*, i.e., $I_0(f) \equiv \langle \phi_0(f) | \hat{J}_0 | \phi_0(f) \rangle$. With the help of the Feynman-Hellman theorem, we can write

$$\begin{aligned} \frac{\partial E_0(f)}{\partial f} &= \left\langle \phi_0(f) \left| \frac{\partial \hat{H}_{0,\text{mag}}}{\partial f} \right| \phi_0(f) \right\rangle \\ &= -\frac{i2\pi t}{N} \left\langle \phi_0(f) \left| \sum_{j,\sigma} \left(e^{i2\pi f/N} c_{j\sigma}^\dagger c_{j+1\sigma} - \text{h.c.} \right) \right| \phi_0(f) \right\rangle. \end{aligned} \quad (2.25)$$

Therefore, substituting Eq.(2.25) into Eq.(2.24), we readily identify

$$\hat{J}_0 = \frac{iet}{N} \sum_{j=1}^N \sum_{\sigma=\uparrow,\downarrow} \left(e^{i2\pi f/N} c_{j\sigma}^\dagger c_{j+1\sigma} - \text{h.c.} \right) . \quad (2.26)$$

Equivalently, the expression for \hat{J}_0 can also be derived using the continuity equation,

$$(-e)\dot{\hat{n}}_{i\sigma} + \hat{j}_{i\sigma} - \hat{j}_{i-1\sigma} = 0 , \quad (2.27)$$

as discussed in details in Ref.[41]. Here, $\hat{j}_{i\sigma}$ defines the electric current per lattice site per spin, and $\dot{\hat{n}}_{i\sigma} = i \left[\hat{H}_{0,mag}, \hat{n}_{i\sigma} \right]$.

Fig.9 shows the persistent current, as function of f , which establishes in the ground state of a ring with (a) $N = 3$, (b) $N = 4$, (c) $N = 5$ and (d) $N = 6$ sites. The

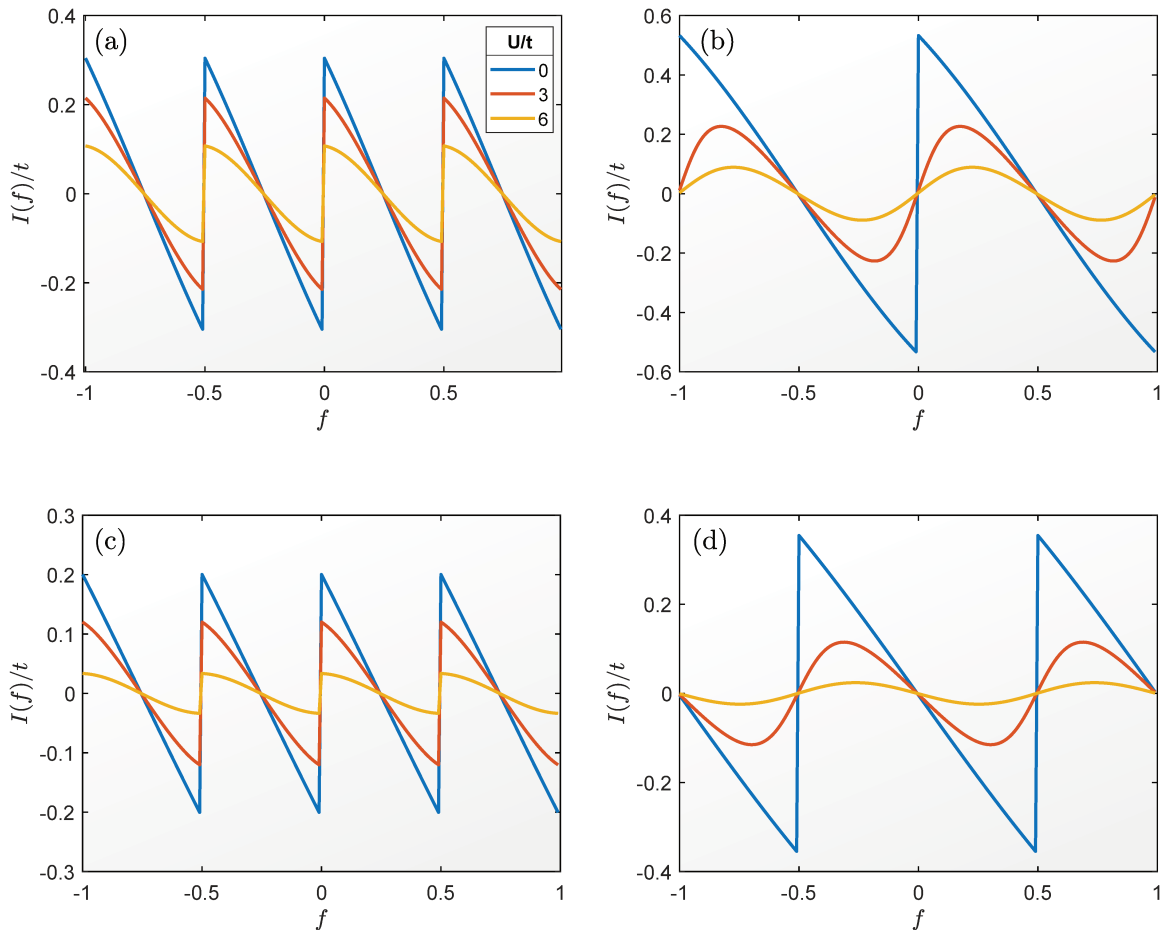


Figure 9 – **Persistent current as function of magnetic flux.** The panels show persistent current (I_0) that establishes in the ground state of the ring with (a) $N = 3$ sites, (b) $N = 4$ sites, (c) $N = 5$ sites and (d) $N = 6$ sites, as function of the dimensionless magnetic flux that pierces it ($f = \phi/\phi_0$) and for different values of the ratio U/t , as indicated at the legend in panel (a). As in Fig. 8, all the rings are in the half-filling regime ($N_e = N$). The legend in panel (a) also apply for the panels (b)-(d).

periodicity of $I_0(f)$ is, of course, the same as that of $E_0(f)$ shown in Fig. 8. Moreover, the magnitude of $I_0(f)$ decreases with increasing U/t , signaling once again the tendency of localization of the π -electrons at the ring's sites.

The discontinuities in the curves $I_0(f)$ at certain f indicates the existence of degeneracy of the ring's ground state at these values of flux: if the ground state is degenerate (with a degeneracy, let's say, g_0), then any linear combination of these g_0 orthonormal eigenstates is also a ground state of the systems. Moreover, each different linear combinations can lead to different results for $\langle \phi_0(f) | \hat{J}_0 | \phi_0(f) \rangle$. As soon as the magnetic field breaks the ground state degeneracy (when $f > 0$ in panels (a), (b) and (c) from Fig. 9, for instance), $I_0(f)$ assumes a unique well defined value. In Fig. 9(a) and 9(c), we note that the discontinuities of $I_0(f)$ at $f = 0$ persist even when $U/t \neq 0$, which evidences that, as mentioned before, in these cases the on-site Coulomb repulsion does not break the ground state's degeneracy.

Differentiating $I_0(f)$ with respect to f and taking the limit $f \rightarrow 0$ gives us the system's response to the external field, i.e., its *magnetic susceptibility*,

$$\chi_{(mol)} = \gamma (Na)^4 \left. \frac{\partial I_0(f)}{\partial f} \right|_{f \rightarrow 0}, \quad (2.28)$$

here expressed in units of cm^3/mol . The quantity $\gamma \equiv 10^6 \mu_0 N_A e / (128\pi^4)$ is a numerical constant, where N_A denotes Avogadro number, and μ_0 is the magnetic permeability.

We emphasize that $\chi_{(mol)}$ corresponds to a theoretical calculation of the magnetic anisotropy of our prototypes of aromatic molecules, since Eq. (2.28) gives only the contribution of the current loop to the system's magnetic response. Recall that, as explained at the begging of Sec. 2.2.2, we neglected the Zeeman splitting, so no spin response is included in Eq. (2.28)! Therefore $\chi_{(mol)}$ and $\Delta\chi$ can be used interchangeably along this chapter. Moreover, $\chi_{(mol)} > 0$ means that the current circulates in a direction such that it generates a magnetic momentum in the *same direction* of \mathbf{B} , and the ring is called *paramagnetic*. Conversely, if $\chi_{(mol)} < 0$ the magnetic momentum generated by the current loop opposes the external field, and the ring is denominated *diamagnetic*.

Fig. 10 shows $\chi_{(mol)}$ as function of U/t for rings with (a) $N = 3$, (b) $N = 4$, (c) $N = 5$ sites and (d) $N = 6$ sites at half-filling. Note that the magnetic responses of the ring with three and five sites are very similar, which is expected since they belong to the same family, as discussed in Sec. 2.2.1. Moreover, all of these rings are diamagnetic when $U = 0$. This can be easily understood if we use once more the Feynman-Hellman theorem

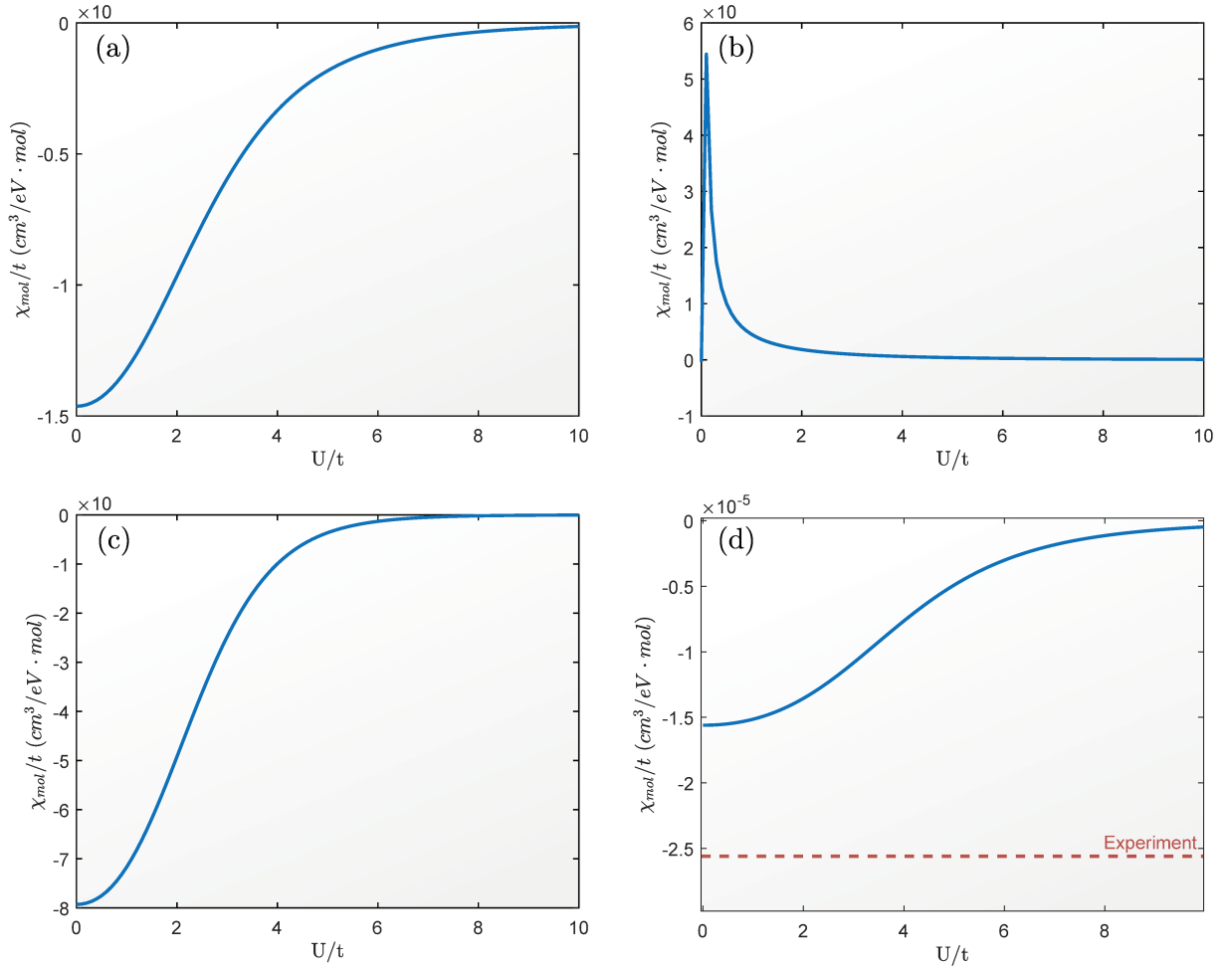


Figure 10 – **Magnetic susceptibility as function of U/t .** The panels show the magnetic susceptibility at low field ($f \rightarrow 0$) as function of the ratio U/t for rings with (a) $N = 3$ sites, (b) $N = 4$, (c) $N = 5$ and (d) $N = 6$ sites, all of them in the half-filling regime ($N_e = N$). In panel (d) the red dashed line correspond to the experimental value of the anisotropy of the magnetic susceptibility of benzene.

to write

$$\begin{aligned} \frac{\partial I_0(f)}{\partial f} &= \left\langle \phi_0(f) \left| \frac{\partial \hat{J}_0}{\partial f} \right| \phi_0(f) \right\rangle \\ &= -\frac{2\pi e t}{N^2} \left\langle \phi_0(f) \left| \sum_{j,\sigma} \left(e^{i2\pi f/N} c_{j\sigma}^\dagger c_{j+1\sigma} + \text{h.c.} \right) \right| \phi_0(f) \right\rangle, \end{aligned} \quad (2.29)$$

thus, when $f \rightarrow 0$,

$$\chi_{(mol)} = 2\pi e \gamma N^2 a^4 \left\langle \phi_0 \left| \hat{H}_{\text{Hückel}} \right| \phi_0 \right\rangle = 2\pi e \gamma N^2 a^4 E_0^{(H)}. \quad (2.30)$$

Recall that $E_0^{(H)}$ is the Hückel model ground state energy defined in Eq.(2.17), which, as we can see from Fig. 7, is always negative.

When $U > 0$, on the other hand, the diamagnetic responses of the rings with $N = 3$ and $N = 5$ rings is suppressed, while a paramagnetic response is induced in the ring with $N = 4$ sites.

Now, let's return to the prototype of the benzene molecule ($N = N_e = 6$). In Ref. [42], the authors estimated $t \approx 2.54eV$ and $U \approx 10.1eV$ for this molecule by looking at its experimental low-energy excitation spectrum. Moreover, the Coulomb interaction between electrons in first-neighbor sites ($V \sum_{i,j} \hat{n}_i \hat{n}_j$) is not negligible in benzene. However, we can still use the Hamiltonian defined in Eq.(2.9): in Ref. [40], the authors show that the nearest-neighbor interaction V has the effect of suppressing the on-site Coulomb repulsion U . They thus derived an effective $U/t \approx 1.2$ for benzene, which gives $U \approx 3.05eV$ if we use $t = 2.54eV$. These are the values we adopt hereafter for the prototype of benzene.

Fig. 10(d) shows $\chi_{(mol)}$ (normalized by t) for the prototype of benzene as a function of U/t . Note that $U/t = 1.2$ yields $\chi_{(mol)} \approx -3.79 \times 10^{-5} cm^3/mol$, which is roughly 3/5 of experimental result of $\Delta\chi = -6.49 \times 10^{-5} cm^3/mol$ reported in Ref.[43]. Even if we completely neglect the inter-electronic interactions (returning, therefore, to the Hückel model), this scenario does not get better: in this case we obtain $\chi_{(mol)} \approx -3.96 \times 10^{-5} cm^3/mol$, still smaller than $\Delta\chi$.

Another thing we can do is fix $U = 3.05eV$ and calculate $\chi_{(mol)}$ as function of

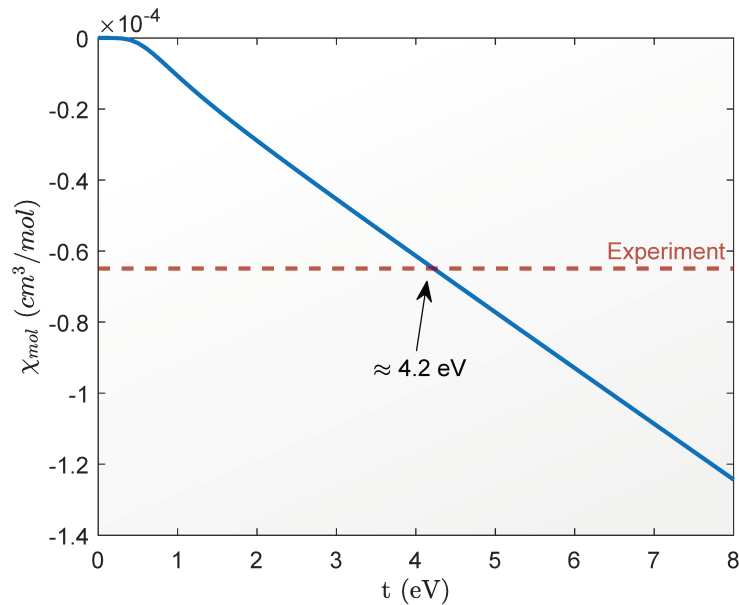


Figure 11 – **Magnetic susceptibility for the prototype of a benzene molecule.** Magnetic molar susceptibility for a ring with $N = 6$ sites and $N_e = 6$ electrons as function of t and with $U = 3.048eV$ fixed. The red dashed line show the experimental value for the magnetic susceptibility of benzene ($\Delta\chi = -6.49 \times 10^{-5}$). The theoretical and experimental values agree for $t \approx 4.2eV$.

t , as shown in Fig. 11. In this case, we conclude that $\chi_{(mol)}$ equals the experimental result for a hopping parameter of $t \approx 4.2eV$, which is unrealistic for benzene. This is the reason why we argue that a description of the physics of the benzene molecule - and by extension, that of larger aromatic molecules - through a single-band Hubbard model as defined in Eq.(2.9) is not complete.

What could be missing in Eq.(2.9)? We argue that the dynamics of the σ -electrons is the missing key! In the next section we show that, even if we want an effective model only for the π -electrons, the effects of the *local excitation of the binding electrons* must be taken into account. Imagine the following: suppose that we have a $N = 6$ ring, now with the sp_2 orbitals unfrozen - see Fig. 5. Besides, let's forget, for now, the π -electron and focus on the two σ -electrons per bond, which gives us a total $N_e^{(\sigma)} = 12$ electrons in the ring's hybridized sp_2 orbitals. We can imagine, for an illustrative picture, each of the six σ -bonds as a two-level system, independent of each other. So, the many-body ground state, here denoted by $|\varphi_0^{(\sigma)}\rangle$, corresponds to two σ -electrons, with opposite spins, in the lowest level of each bond. It defines a charge density in the bonds

$$\rho_0(\mathbf{r}) = -e \sum_{\alpha=\uparrow,\downarrow} \left\langle \varphi_0^{(\sigma)} \left| \hat{\psi}_\alpha^{(\sigma)\dagger}(\mathbf{r}) \hat{\psi}_\alpha^{(\sigma)}(\mathbf{r}) \right| \varphi_0^{(\sigma)} \right\rangle, \quad (2.31)$$

where $\hat{\psi}_\alpha^{(\sigma)\dagger}(\mathbf{r})$ ($\hat{\psi}_\alpha^{(\sigma)}(\mathbf{r})$) is the creation (annihilation) field operator that creates (annihilates) a σ -electrons with spin α at the position \mathbf{r} of the space. Following the notation introduced in Appendix A it takes the form

$$\hat{\psi}_\alpha^{(\sigma)\dagger}(\mathbf{r}) = \sum_{j=1}^N \sum_{\kappa=1,2} W_{j,\kappa}^*(\mathbf{r}) d_{j\kappa;\alpha}, \quad (2.32)$$

where the function $W_{j,\kappa}(\mathbf{r})$ denotes the Wannier wave function correspondent to the κ sp_2 orbital ($\kappa = 1$ for the *right* orbital and $\kappa = 2$ for the *left orbital* - see Fig. 5) centered in the site j .

The charge density in Eq.(2.31), in turn, renormalizes the periodic potential due to the ring's site,

$$\bar{V}_c^{(0)}(\mathbf{r}) = V_c(\mathbf{r}) + \int d\mathbf{r}' \frac{\rho_0(\mathbf{r}')}{|\mathbf{r} - \mathbf{r}'|}. \quad (2.33)$$

Now, we introduce $N_e^{(\pi)}$ π -electrons in the ring's p_z orbitals, so we have a total of $N_e = N_e^{(\pi)} + N_e^{(\sigma)}$ electrons in the ring. Due to the Coulomb repulsion, these extra π -electrons disturb the charge distribution in the σ -bonds, modifying the density (2.31). In other words, the π -electrons induce excitations of the σ -electrons, which now can be promoted to their first excited state $|\varphi_1^{(\sigma)}\rangle$. According to the simplified picture where each bond can be approximated by a two-level system, such state would correspond to a configuration where five of the bonds have two electrons in its ground state, while in

one of them one electron is promoted to the second energy-level. In this case, the charge density in the bonds would change to

$$\rho_1(\mathbf{r}) = -e \sum_{\alpha=\uparrow,\downarrow} \left\langle \varphi_1^{(\sigma)} \left| \hat{\psi}_\alpha^{(\sigma)\dagger}(\mathbf{r}) \hat{\psi}_\alpha^{(\sigma)}(\mathbf{r}) \right| \varphi_1^{(\sigma)} \right\rangle, \quad (2.34)$$

and, consequently, the π -electrons would feel a different external potential

$$\bar{V}_c^{(1)}(\mathbf{r}) = V_c(\mathbf{r}) + \int d\mathbf{r}' \frac{\rho_1(\mathbf{r}')}{|\mathbf{r} - \mathbf{r}'|}, \quad (2.35)$$

which in turn defines a different hopping amplitude, so the σ -electrons excitations can directly affect the dynamics of the π -electrons.

It does not seem absurd to think that such change in the external potential could give rise to an effective interaction between the π -electrons, in a similar way as in a conventional superconductor, the deviation of the ions from their equilibrium position, due to an electron that just passed by, attracts another nearby electron, resulting in an effective inter-electronic attraction mediated by phonons. We are not saying that a Cooper pair will form in the ring, though!

If an effective interaction between the π -electrons, *mediated by the σ -electrons* indeed exists, *what would be its form? Would it be attractive or repulsive? And how would it affect the magnetic properties of the rings?* These are exactly the questions we address in the next section.

2.3 Extended Hubbard model

The scenario we explored in the last paragraphs of Sec. 2.2.2 suggests a *separation of energy scales in the system*. Because the σ electrons are localized in the ring's bonds, we expect that it would cost more energy to promote them to their first excited state in comparison to the amount of energy needed to excite the π -electrons. In other words, the energy scale separating the ground state and the first excited state of the σ -electrons (let's denote it by Λ) is expected to be larger than the typical excitation energy of the π -electrons, which is set by the hopping parameter t defined in Eq.(2.10). Therefore, recalling the uncertainty principle $\Delta E \Delta t \geq \hbar/2$, it implies that the σ -electrons excitations happen in a much faster time scale than that associated with the motion of the π -electrons around the ring.

We can thus think of two different "*types*" of electrons in the ring: the σ -electrons are the *fast* electrons, whereas the π -electrons are the *slow* ones. This scenario resembles the well-known *Born-Oppenheimer approximation*, introduced in several text-books - see, for instance Ref. [16] - to decouple the nucleonic and the electronic degrees of freedom of a molecule. Briefly speaking, due to the huge mass difference between the atomic nuclei

and the electrons, the former moves around their equilibrium position much more slowly than the time scale of the electronic motion. Then, the standard Born-Oppenheimer approximation tells us that the electronic dynamics happens as if they were placed in a *static periodic potential* generated by the nuclei in a particular frozen arrangement. For each nuclei arrangement, we are then able to calculate the electronic eigenvalues which, in turn, define an external potential for the nuclei themselves, and can be used to determine the molecule's vibrational levels.

Here, inspired by the energy scale separation between the σ -electrons and the π -electrons, we use a perturbation approach which we call *generalized Born-Oppenheimer approximation*, in the sense that in our case the degrees of freedom of the σ -electrons and the π -electron are those to be decoupled. It is fundamental to note that, in our approximation, contrary to the standard Born-Oppenheimer approximation, *the ring's sites remain static all the time. No ionic degrees of freedom are addressed in our calculations!*

2.3.1 Generalized Born-Oppenheimer approximation

Here, it is more convenient to return to first quantization where the *complete* Hamiltonian of a ring with N sites and $N_e = N_e^{(\pi)} + N_e^{(\sigma)}$ electrons is given by $\mathcal{H} = \mathcal{H}_p + \mathcal{H}_b$, where

$$\mathcal{H}_p = \sum_{i=1}^{N_e^{(\pi)}} \left(\frac{\mathbf{P}_i^2}{2m} + \tilde{V}_c(\mathbf{R}_i) \right) + \frac{1}{2} \sum_{i \neq j} U(\mathbf{R}_i - \mathbf{R}_j) \quad (2.36)$$

describes the $N_e^{(\pi)}$ π -electrons, with momenta and positions denoted by \mathbf{R}_i and \mathbf{P}_i , respectively ($i = 1, 2, \dots, N_e^{(\pi)}$). In this equation, $U(\mathbf{r}, \mathbf{r}') = e^2/|\mathbf{r} - \mathbf{r}'|$ is the standard Coulomb repulsion. Moreover, the Hamiltonian

$$\mathcal{H}_b = \sum_{\alpha=1}^{N_e^{(\sigma)}} \left(\frac{\mathbf{P}_\alpha^2}{2m} + \tilde{V}_c(\mathbf{r}_\alpha) \right) + \frac{1}{2} \sum_{\alpha \neq \beta} U(\mathbf{r}_\alpha - \mathbf{r}_\beta) + \sum_{i,\alpha} U(\mathbf{r}_\alpha - \mathbf{R}_i) \quad (2.37)$$

accounts for either the degrees of freedom of the $N_e^{(\sigma)}$ σ -electrons, with momenta and positions denoted by \mathbf{r}_α and \mathbf{p}_α , respectively ($\alpha = 1, 2, \dots, N_e^{(\sigma)}$), as the coupling between them and the π -electrons. Hereafter, we reserve Roman (Greek) characters as indexes for quantities referring to π -electrons (σ -electrons). It is important to note that the periodic potential $\tilde{V}_c(\mathbf{r})$ that appears in Eqs.(2.36) and (2.37) is not the same as $V_c(\mathbf{r})$ defined in Eq.(2.10): while $V_c(\mathbf{r})$ is generated by the ring's sites with both its core electrons and the *frozen σ -electrons in the bonds*, $\tilde{V}_c(\mathbf{r})$, on the other hand, does not include any contribution of the σ -electrons. In other words, recalling our discussion at the end Sec. 2.2.2, $V_c(\mathbf{r})$ is essentially $\tilde{V}_c(\mathbf{r})$ renormalized by the the static charge density in the bonds generated by the σ -electrons in their many-body ground state.

In this section, we denote by $\psi(\mathbf{r}, \mathbf{R})$ the total many-body wave function, where \mathbf{r} stands for the entire set of positions of the σ -electrons $\{\mathbf{r}_1, \mathbf{r}_2, \dots, \mathbf{r}_{N_e^{(\sigma)}}\}$, while

\mathbf{R} denotes the set of positions of the π -electrons, $\{\mathbf{R}_1, \mathbf{R}_2, \dots, \mathbf{R}_{N_e^{(\pi)}}\}$. Our *generalized Born-Oppenheimer approximation* consists in assuming that the total wave function has the following separable form:

$$\psi(\mathbf{r}, \mathbf{R}) = \sum_{\nu} \phi_{\nu}(\mathbf{R}) \varphi_{\nu}(\mathbf{r}, \mathbf{R}) , \quad (2.38)$$

where $\phi_{\nu}(\mathbf{R})$ refers to the π -electrons wave functions, and $\varphi_{\nu}(\mathbf{r}, \mathbf{R})$ denotes the σ -electrons wave functions for a **frozen configuration of π -electrons** (fixed \mathbf{R}). The later obeys the following Schrödinger equation:

$$\mathcal{H}_b(\mathbf{R})\varphi_{\nu}(\mathbf{r}, \mathbf{R}) = \lambda_{\nu}(\mathbf{R})\varphi_{\nu}(\mathbf{r}, \mathbf{R}) . \quad (2.39)$$

We emphasize that \mathbf{R} in Eq.(2.39) is an external parameter rather than a dynamical variable. For each \mathbf{R} , the Schrödinger equation (2.39) determines the σ -electrons eigenvalues $\lambda_{\nu}(\mathbf{R})$ (with quantum numbers $\nu = 0, 1, 2, \dots$), which, as it will shortly become clear, act as extra external potentials for the π -electrons.

Substituting the ansatz (2.38) into the full time-independent Schrödinger equation $\mathcal{H}\psi = E\psi$ and using Eq.(2.39), we find that the π -electrons wave function must obey

$$E \sum_{\nu} \phi_{\nu}(\mathbf{R})\varphi_{\nu}(\mathbf{r}, \mathbf{R}) = \sum_{\nu} \left\{ [\mathcal{H}_p\phi_{\nu}(\mathbf{R}) + \lambda_{\nu}(\mathbf{R})\phi_{\nu}(\mathbf{R})] \varphi_{\nu}(\mathbf{r}, \mathbf{R}) + \frac{1}{2m} \sum_{j=1}^{N_e^{(\pi)}} [\mathbf{P}_j^2 \varphi_{\nu}(\mathbf{r}, \mathbf{R}) + 2(\mathbf{P}_j \varphi_{\nu}(\mathbf{r}, \mathbf{R})) \cdot \mathbf{P}_j] \phi_{\nu}(\mathbf{R}) \right\} . \quad (2.40)$$

Now, multiplying Eq.(2.40) on the left by $\varphi_{\mu}^*(\mathbf{r}, \mathbf{R})$, integrating over the σ -electron positions, and using the fact that $\varphi_{\mu}(\mathbf{r}, \mathbf{R})$ defines an orthonormal basis, i.e.,

$$\langle \varphi_{\mu} | \varphi_{\nu} \rangle_{\mathbf{r}} = \int d\mathbf{r} \varphi_{\mu}^*(\mathbf{r}, \mathbf{R})\varphi_{\nu}(\mathbf{r}, \mathbf{R}) = \delta_{\mu,\nu} , \quad (2.41)$$

we rewrite Eq.(2.40) as the following set of coupled equations

$$[\mathcal{H}_p + \lambda_{\nu}(\mathbf{R})] \phi_{\nu}(\mathbf{R}) + \sum_{\mu} \mathcal{A}_{\nu\mu} \phi_{\mu}(\mathbf{R}) = E\phi_{\nu}(\mathbf{R}) . \quad (2.42)$$

Note that, contrary to Eq.(2.39), \mathbf{R} is now a dynamical variable. Moreover, the operator $\mathcal{A}_{\nu\mu}$ is responsible for coupling the π -electron wave functions with different μ and ν , and it has the form

$$\mathcal{A}_{\nu\mu} = f_{\nu\mu}(\mathbf{R}) + \sum_{j=1}^{N_e^{(\pi)}} \mathbf{g}_{\nu\mu}^{(j)}(\mathbf{R}) \cdot \mathbf{P}_j , \quad (2.43)$$

with

$$f_{\nu\mu}(\mathbf{R}) \equiv -\frac{\hbar^2}{2m} \sum_{j=1}^{N_e^{(\pi)}} \langle \varphi_\nu | \nabla_j^2 | \varphi_\mu \rangle_{\mathbf{r}} = -\sum_{j=1}^{N_e^{(\pi)}} \frac{\hbar^2}{2m} \int d\mathbf{r} \varphi_\nu^*(\mathbf{r}, \mathbf{R}) \nabla_j^2 \varphi_\mu(\mathbf{r}, \mathbf{R}) , \quad (2.44)$$

$$\mathbf{g}_{\nu\mu}^{(j)}(\mathbf{R}) \equiv -\frac{i\hbar}{m} \langle \varphi_\nu | \nabla_j | \varphi_\mu \rangle_{\mathbf{r}} = -\frac{i\hbar}{m} \int d\mathbf{r} \varphi_\nu^*(\mathbf{r}, \mathbf{R}) \nabla_j \varphi_\mu(\mathbf{r}, \mathbf{R}) . \quad (2.45)$$

Here ∇_j denotes the gradient with respect to the position of the j -th π -electron (\mathbf{R}_j) of the system.

In order to develop a more intuitive picture of the meaning of Eqs.(2.39) and (2.42) let's make a sketch of $\lambda_\nu(\mathbf{R})$. Fig. 12(a) shows an illustration of three of these eigenvalues as if they were a 1D function, in analogy with the standard Born-Oppenheimer approximation, which we are more used to. In reality, of course $\lambda_\nu(\mathbf{R})$ defines a hypersurface in the space configuration of the π -electrons. Hereafter, since we want to derive a *low-energy effective model for the π -electrons*, we focus only on the ground state and the first excited state of the σ -electrons, as illustrated in Fig. 12(b), i.e., we truncate the sum in Eq.(2.38) at $\nu = 1$. In this case, Eq.(2.42) simplifies to a set of two coupled equations,

$$\mathcal{H}_0 \phi_{0,n}(\mathbf{R}) + A_{01} \phi_{1,n}(\mathbf{R}) = E_n \phi_{0,n}(\mathbf{R}) , \quad (2.46)$$

$$\mathcal{H}_1 \phi_{1,n}(\mathbf{R}) + A_{10} \phi_{0,n}(\mathbf{R}) = E_n \phi_{1,n}(\mathbf{R}) , \quad (2.47)$$

where the index n labels the quantum numbers which characterizes the system's energy levels. Besides, we define $\mathcal{H}_0 \equiv \mathcal{H}_p + \lambda_0(\mathbf{R}) + \mathcal{A}_{00}$ and $\mathcal{H}_1 \equiv \mathcal{H}_p + \lambda_1(\mathbf{R}) + \mathcal{A}_{11}$. We emphasize

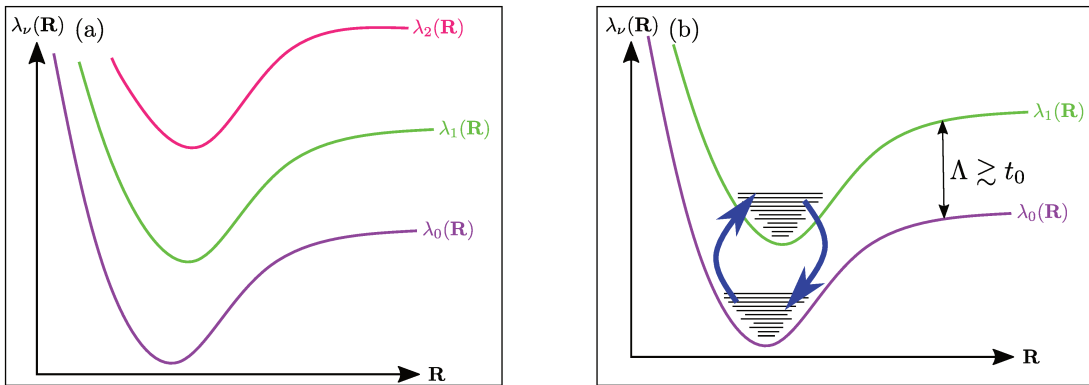


Figure 12 – **Energy "surfaces" of the σ -electrons.** Illustration of the energy levels of the σ -electrons as function of the π -electrons configuration $\lambda_\nu(\mathbf{R})$ as if they were 1D function of \mathbf{R} , in analogy to the simpler standard Born-Oppenheimer approximation. Panel (a) represents the first three low-lying $\lambda_\nu(\mathbf{R})$. Panel (b) focus only in the first two σ -electrons energy levels. In each of them, the π -electron Hubbard spectrum is represented by the horizontal black lines. The blue arrows indicates virtual excitations that can happen in the system if the energy separation (Λ) between the two σ -electron surfaces is comparable with the π -electrons hopping amplitude.

that in the language of second quantization, \mathcal{H}_0 is a single-band Hubbard Hamiltonian with a renormalized hopping amplitude t_0 . Similarly, \mathcal{H}_1 is a Hubbard Hamiltonian with another hopping parameter t_1 .

In the limit that $\lambda_0(\mathbf{R})$ and $\lambda_1(\mathbf{R})$ are too far apart, energetically ($\Lambda_{1,0}(\mathbf{R}) \equiv \lambda_1(\mathbf{R}) - \lambda_0(\mathbf{R}) \gg t_0$), $\mathcal{A}_{\nu\mu}$ becomes negligible. Consequently, Eqs.(2.46) and (2.47) decouple and the system's energy levels are just the set composed by the union of the eigenvalues of \mathcal{H}_0 and \mathcal{H}_1 , illustrated by the horizontal black lines in Fig. 12(b). Note that, in this limit, the low-lying energy states of the systems are those of \mathcal{H}_0 , which means that the π -electrons move along the ring as if the σ -electrons were actually frozen in their ground state $\lambda_0(\mathbf{R})$, recovering the standard Hubbard model we described in Sec.2.2. The interesting limit is when $\Lambda_{1,0}(\mathbf{R})$ is still larger than t_0 , but they are of the *same order* ($\Lambda_{1,0}(\mathbf{R}) \gtrsim t_0$). This is exactly the case of our rings, as we show in Sec.2.4, and in this limit $\mathcal{A}_{\nu\mu}$ cannot be neglected. Actually, this operator mixes the eigenstates of \mathcal{H}_0 and \mathcal{H}_1 . Let's explore this scenario in more details in the next paragraphs.

Isolating $\phi_{1,n}(\mathbf{R})$ in Eq.(2.47) and substituting it in Eq.(2.46), we obtain an effective Schrödinger equation for $\phi_{0,n}(\mathbf{R})$,

$$[\mathcal{H}_0 + \mathcal{A}_{01} (E_n - \mathcal{H}_1)^{-1} \mathcal{A}_{10}] \phi_{0,n}(\mathbf{R}) = E_n \phi_{0,n}(\mathbf{R}) . \quad (2.48)$$

Note that

$$\mathcal{W}_{eff}(\mathbf{P}, \mathbf{R}) = \mathcal{A}_{01} (E_n - \mathcal{H}_1)^{-1} \mathcal{A}_{10} , \quad (2.49)$$

which in general depends on both momenta and positions, defines an *effective interaction* between the π -electrons, which carries information about the virtual excitations of the σ -electrons. Moreover, Eq.(2.48) is a self-consistent equation, since the potential defined in Eq.(2.49) itself depends of the energy levels E_n we want to calculate. However, hope is not lost, since we can approach Eq.(2.48) using perturbation theory, more specifically, *Wigner-Brillouin perturbation theory* [44].

Let's denote by $\zeta_{0,n}(\mathbf{R})$ and $\varepsilon_n^{(0)}$ ($\zeta_{1,n}(\mathbf{R})$ and $\varepsilon_n^{(1)}$) the eigenstates and correspondent eigenvalues of the Hubbard-like Hamiltonian \mathcal{H}_0 (\mathcal{H}_1). Both $\zeta_{0,n}(\mathbf{R})$ and $\zeta_{1,n}(\mathbf{R})$ span an orthonormal basis, i.e.

$$\sum_n |\zeta_{\nu,n}\rangle \langle \zeta_{\nu,n}| = \mathbb{1} , \quad (2.50)$$

$$\langle \zeta_{\nu,n} | \zeta_{\nu,m} \rangle = \int d\mathbf{R} \zeta_{\nu,n}^*(\mathbf{R}) \zeta_{\nu,m}(\mathbf{R}) = \delta_{n,m} , \quad (2.51)$$

with $\nu = 0, 1$ and $\langle \zeta_{0,n} | \zeta_{1,m} \rangle \neq \delta_{m,n}$. Wigner-Brillouin Perturbation Theory tells us that

$\phi_{0,n}(\mathbf{R})$ and $\zeta_{0,n}(\mathbf{R})$, as well as E_n and ε_n are related through

$$\phi_{0,n}(\mathbf{R}) = \zeta_{0,n}(\mathbf{R}) + \sum_{m \neq n} \frac{\langle \zeta_{0,m} | \mathcal{W}_{eff} | \zeta_{0,n} \rangle}{E_n - \varepsilon_m^{(0)}} \zeta_{0,m}(\mathbf{R}) + \mathcal{O}(\mathcal{W}_{eff}^2), \quad (2.52)$$

$$E_n = \varepsilon_n + \langle \zeta_{0,n} | \mathcal{W}_{eff} | \zeta_{0,n} \rangle + \mathcal{O}(\mathcal{W}_{eff}^2), \quad (2.53)$$

with

$$\langle \zeta_{0,m} | \mathcal{W}_{eff} | \zeta_{0,n} \rangle = \int d\mathbf{R} \zeta_{0,m}^*(\mathbf{R}) \mathcal{W}_{eff}(\mathbf{P}, \mathbf{R}) \zeta_{0,n}(\mathbf{R}) \quad (2.54)$$

being the matrix element of the effective interaction (2.49) in the basis spanned by the $\zeta_{0,n}(\mathbf{R})$ states.

In zeroth order perturbation theory for the energy ($E_n \approx \varepsilon_n^{(0)}$), and neglecting quadratic or higher orders of \mathcal{W}_{eff} in the perturbation expression for the eigenstates, we obtain

$$\phi_{0,n}(\mathbf{R}) \approx \zeta_{0,n}(\mathbf{R}) + \sum_{m \neq n} \frac{1}{\varepsilon_n^{(0)} - \varepsilon_m^{(0)}} \langle \zeta_{0,m} | \mathcal{A}_{01} (\varepsilon_n^{(0)} - \mathcal{H}_1)^{-1} \mathcal{A}_{10} | \zeta_{0,n} \rangle \zeta_{0,m}(\mathbf{R}), \quad (2.55)$$

from which it is clear that the matrix element defined in Eq.(2.54) simplifies to

$$\langle \zeta_{0,m} | \mathcal{W}_{eff} | \zeta_{0,n} \rangle \approx -\frac{1}{\Lambda} \langle \zeta_{0,m} | \mathcal{A}_{01} \mathcal{O}_n \mathcal{A}_{10} | \zeta_{0,n} \rangle, \quad (2.56)$$

where \mathcal{O}_n is a complicated many-body operator defined as

$$\mathcal{O}_n \equiv \left[\sum_m \left(1 - \frac{\varepsilon_n^{(0)} - \varepsilon_m^{(0)}}{\Lambda} \right) |\zeta_{1,m}\rangle \langle \zeta_{1,m}| \right]^{-1}. \quad (2.57)$$

To derive Eqs.(2.56) and (2.57), we use the closure relation in Eq.(2.50) to rewrite $\varepsilon_n^{(0)} - \mathcal{H}_1$ in Eq.(2.55) as

$$\varepsilon_n^{(0)} \mathbb{1} - \sum_m \varepsilon_m^{(1)} |\zeta_{1,m}\rangle \langle \zeta_{1,m}| = \sum_m (\varepsilon_n^{(0)} - \varepsilon_m^{(1)}) |\zeta_{1,m}\rangle \langle \zeta_{1,m}|. \quad (2.58)$$

Besides, we approximate the energy levels of \mathcal{H}_1 as those of \mathcal{H}_0 displaced by the energy separation between the two σ -electrons energy surfaces, i.e.

$$\varepsilon_m^{(1)} \approx \varepsilon_m^{(0)} + \Lambda_{1,0}(\mathbf{R}). \quad (2.59)$$

Recall that we previously defined $\Lambda_{1,0}(\mathbf{R}) \equiv \lambda_1(\mathbf{R}) - \lambda_0(\mathbf{R})$. Interestingly, in Sec.2.4 we show that such energy spacing between the σ -electrons energy surface depend weakly on \mathbf{R} , so it is reasonable to approximate it by a constant, $\Lambda_{1,0}(\mathbf{R}) \approx \Lambda > 0$, consistently with the notation we have been using since the beginning of this section.

Unfortunately, even after the aforementioned approximations, the effective interaction is still very complicated and, specially because we need to invert a many-body operator in Eq.(2.57), it does not seem possible for us to derive an analytic expression for \mathcal{W}_{eff} at this point. To proceed we need further simplifications, which are described in detail in the subsequent subsection.

2.3.2 Effective interaction in first quantization

The first thing we need to do is return to the expression of $A_{\nu\mu}$ defined in Eqs.(2.43)-(2.45) and find an approximate expression for it. Let's start by studying $\mathbf{g}_{\nu\mu}^{(j)}(\mathbf{R})$.

Note that taking the gradient of Eq.(2.39) with respect to the position of the j -th π -electron, multiplying the resulting, at the left, by $\varphi_\nu^*(\mathbf{r}, \mathbf{R})$, and integrating over the positions of the σ -electrons, we obtain

$$\int d\mathbf{r} \varphi_\nu^*(\mathbf{r}, \mathbf{R}) \nabla_j \varphi_\mu(\mathbf{r}, \mathbf{R}) = \frac{1}{\lambda_\mu(\mathbf{R}) - \lambda_\nu(\mathbf{R})} \int d\mathbf{r} \varphi_\nu^*(\mathbf{r}, \mathbf{R}) (\nabla_j \mathcal{H}_b) \varphi_\mu(\mathbf{r}, \mathbf{R}) . \quad (2.60)$$

Recall that \mathbf{R} is merely an external parameter for \mathcal{H}_b , and it appears only in the Coulomb repulsion term - see Eq.(2.37) - therefore, it follows that

$$\nabla_j \mathcal{H}_b(\mathbf{R}) = e^2 \sum_{\alpha=1}^{N_e^{(\sigma)}} \frac{\mathbf{r}_\alpha - \mathbf{R}_j}{|\mathbf{r}_\alpha - \mathbf{R}_j|^3} . \quad (2.61)$$

Our task now is to calculate the the integral over the positions of the σ -electrons. Since we have a term $|\mathbf{r}_\alpha - \mathbf{R}_j|^3$ in the denominator of the integrand, the σ -electrons which are closer to the j -th π -electron are those who give the largest contribution to the right-hand side of Eq.(2.60). Furthermore, as discussed in Sec. 2.1, we have two σ -electrons per bond. Consequently, for each π -electron localized at a given ring site, there are four nearest neighbors σ -electrons, here labeled by 1 to 4 for simplicity, that dominate the sum in Eq.(2.61), which we can approximate as

$$\begin{aligned} & \int d\mathbf{r} \varphi_\nu^*(\mathbf{r}, \mathbf{R}) (\nabla_j \mathcal{H}_b) \varphi_\mu(\mathbf{r}, \mathbf{R}) \approx \\ & e^2 \hat{d}_j^{(L)} \int d\mathbf{r} \varphi_\nu^*(\mathbf{r}, \mathbf{R}) \left(\frac{1}{|\mathbf{r}_1 - \mathbf{R}_j|^2} + \frac{1}{|\mathbf{r}_2 - \mathbf{R}_j|^2} \right) \varphi_\mu(\mathbf{r}, \mathbf{R}) + \\ & e^2 \hat{d}_j^{(R)} \int d\mathbf{r} \varphi_\nu^*(\mathbf{r}, \mathbf{R}) \left(\frac{1}{|\mathbf{r}_3 - \mathbf{R}_j|^2} + \frac{1}{|\mathbf{r}_4 - \mathbf{R}_j|^2} \right) \varphi_\mu^{(\sigma)}(\mathbf{r}, \mathbf{R}) , \end{aligned} \quad (2.62)$$

where we define

$$\hat{d}_j^{(R)} \equiv \frac{1}{a} (\mathcal{R}_{j+1} - \mathcal{R}_j) \quad (2.63)$$

as the versor in the direction of the *right* σ -bond, between the sites j and $j+1$. Recall that \mathcal{R}_j is the position of site j defined in Eq.(2.8). On the other hand, $\hat{d}_j^{(L)}$ denotes the versor in the direction of the *left* σ -bond and it is related with Eq.(2.63) through $\hat{d}_j^{(L)} = -\hat{d}_{j-1}^{(R)}$.

Concerning the remaining integrals on the right-hand side of Eq.(2.62), if we had $|\mathbf{r}_\alpha - \mathbf{R}_j|$ in the denominator, they would be of the order of the on-site Coulomb repulsion between π -electrons and σ -electrons, which, as we show in Appendix B, is of the same order of the on-site repulsion (U) between the π -electrons. Moreover, it follows

from the discussion in previous paragraph that $|\mathbf{r}_\alpha - \mathbf{R}_j|$ is of order of the lattice spacing. Consequently, we can roughly estimate

$$e^2 \int d\mathbf{r} [\varphi_\nu(\mathbf{r}, \mathbf{R})]^* \frac{1}{|\mathbf{r}_1 - \mathbf{R}_j|^2} \varphi_\mu(\mathbf{r}, \mathbf{R}) \sim \frac{U}{a}, \quad (2.64)$$

and similarly for the other integrals involving \mathbf{r}_2 , \mathbf{r}_3 and \mathbf{r}_4 . Therefore, Eq.(2.62) results in

$$\int d\mathbf{r} [\varphi_\nu(\mathbf{r}, \mathbf{R})]^* (\nabla_j \mathcal{H}_b) \varphi_\mu(\mathbf{r}, \mathbf{R}) \approx 2 \frac{U}{a} \left(\hat{d}_j^{(R)} - \hat{d}_{j-1}^{(R)} \right) = 2g_N \frac{U}{a} \hat{n}_j. \quad (2.65)$$

Here \hat{n}_j is the versor in the direction of the position of the site where the π -electron is localized at, but pointing inwards and g_N is the numerical factor

$$g_N = \sqrt{2(1 + \cos(2\pi/N))}. \quad (2.66)$$

Substituting Eq.(2.65) into Eq.(2.60) and comparing it with (2.45) we readily identify

$$\mathbf{g}_{\nu\mu}^{(j)}(\mathbf{R}) \approx -\frac{i\hbar}{am} \frac{2U}{\lambda_\mu(\mathbf{R}) - \lambda_\nu(\mathbf{R})} \left(\hat{d}_j^{(R)} - \hat{d}_{j-1}^{(R)} \right). \quad (2.67)$$

Besides, we neglect $f_{\nu\mu}(\mathbf{R})$, since this term doesn't involve the π -electrons momenta and, therefore, when included in Eq.(2.56) gives rise, in first order perturbation theory, to a one-body term that can be incorporated in the hopping parameter. Therefore, from Eq.(2.67) and, as in the previous section, assuming $\lambda_1(\mathbf{R}) - \lambda_0(\mathbf{R}) \approx \Lambda > 0$ (constant), we can approximate \mathcal{A}_{01} and \mathcal{A}_{10} by a simple one-body operator

$$A_{01} \approx -\frac{2i\hbar U g_N}{ma\Lambda} \sum_{j=1}^{N_e^{(\pi)}} \hat{n}_j \cdot \mathbf{P}_j, \quad (2.68)$$

$$A_{10} \approx \frac{2i\hbar U g_N}{ma\Lambda} \sum_{j=1}^{N_e^{(\pi)}} \hat{n}_j \cdot \mathbf{P}_j. \quad (2.69)$$

At this point, we have almost everything we need we need to derive a simplified expression for \mathcal{W}_{eff} in first quantization. Now, we need to come back to Eq.(2.57). If \mathcal{O}_n were a constant, it would generate a \mathcal{W}_{eff} which would be just the product of two one-body operators, and thus not a true two-body operator. The simplest assumption we can make about Eq.(2.57) is that it has a two-body component which can correlate the momentum operators that appear in Eqs.(2.68) and (2.69). In this case, we can write

$$\mathcal{W}_{eff} \approx -\frac{1}{\Lambda^3} \left(\frac{2\hbar U g_N}{ma} \right)^2 \sum_{i,j=1}^{N_e^{(\pi)}} \mathbf{P}_i \cdot \hat{n}_i \mathcal{O}(\mathbf{R}_i, \mathbf{R}_j) \hat{n}_j \cdot \mathbf{P}_j, \quad (2.70)$$

which is genuinely a two-body operator. Note that since \hat{n}_j is a simple versor rather than an operator, we can freely interchange it with the momentum operator, i.e. $\hat{n}_j \cdot \mathbf{P}_j = \mathbf{P}_j \cdot \hat{n}_j$,

and, therefore, define a tensor

$$\overleftrightarrow{T}(\mathbf{R}_i, \mathbf{R}_j) \equiv \hat{n}_i \mathcal{O}(\mathbf{R}_i, \mathbf{R}_j) \hat{n}_j, \quad (2.71)$$

which encodes the information about the ring's σ -bonds orientation through the versors \hat{n}_i .

An effective momentum-momentum interaction with a similar form of Eq.(2.70) already appeared in the literature some decades ago, when Bohm and Pines wrote the seminal series of papers about the electron gas [45, 46, 47]. They were able to show that there is an effective inter-electronic potential mediated by plasmons, which they recognized as a Biot-Savart interaction. However, they argue that such interaction is negligible because of screening effects. In our case, on the other hand, since we are dealing with a few body system, screening effects are not strong enough to suppress this kind of interaction.

Furthermore Eq.(2.70) also resembles the form of the Breit-Darwin (or current-current) interaction \hat{H}_{BD} . In appendix D we show how to derive the second-quantized expression for the Breit-Darwin Hamiltonian and, comparing Eq.(2.70) with Eq.(D.47), we note that \hat{W}_{eff} contains two of the processes that appear in the Breit-Darwin Hamiltonian. However, these terms appear with different relative signs in \hat{H}_{BD} and \hat{W}_{eff} .

It worth noting that there is a crucial difference between our effective potential and the Breit-Darwin Hamiltonian: while the later is a relativistic correction to the Coulomb repulsion, \hat{W}_{eff} is a much more intense interaction.

2.3.3 Effective interaction in second quantization

In the previous section we showed that virtual excitations of the σ -electrons mediate an effective momentum-momentum attraction between the π -electrons, which, in first quantization, is given by Eq.(2.70). Here, we derive its expression in the language of second quantization. By adding the second-quantized W_{eff} to Eq.(2.9), we derive an extended Hubbard Hamiltonian for the degrees of freedom of the π -electrons alone, but which takes into account the effects of the σ -electrons in their dynamics. It is important to note that in this section \mathbf{r} no longer denotes the set of positions of the σ -electrons, but rather a generic position in space.

Since W_{eff} in Eq.(2.70) is a two-body operator, the standard procedure to determine its second-quantized expression is [22, 16]

$$\hat{W}_{eff} = \frac{1}{2} \sum_{\sigma, \sigma'} \int \int d\mathbf{r} d\mathbf{r}' \hat{\psi}_{\sigma}^{\dagger}(\mathbf{r}) \hat{\psi}_{\sigma'}^{\dagger}(\mathbf{r}') \mathbf{P} \cdot \overleftrightarrow{T}(\mathbf{r}, \mathbf{r}') \cdot \mathbf{P}' \hat{\psi}_{\sigma'}(\mathbf{r}') \hat{\psi}_{\sigma}(\mathbf{r}), \quad (2.72)$$

where, in coordinate representation, $\mathbf{P} = -i\hbar\nabla$ and $\mathbf{P}' = -i\hbar\nabla'$, with ∇' denoting the gradient with respect to \mathbf{r}' . Besides $\hat{\psi}_{\sigma}^{\dagger}(\mathbf{r})$ ($\hat{\psi}_{\sigma}(\mathbf{r})$) is the field operator that creates

(annihilates) an electron with spin σ at the position \mathbf{r} . Since we are deriving an effective model for the π -electrons alone, such field operator is defined only in terms of the Wannier wave functions for the p_z orbitals ($\varphi_j(\mathbf{r})$), as shown in Eq.(A.5). Here the reader should be warned not to confuse $\varphi_j(\mathbf{r})$ with the σ -electrons wave functions $\varphi_\nu(\mathbf{r}, \mathbf{R})$ we defined in Sec. 2.3.1.

Substituting Eq.(A.5) into Eq.(2.72) we find the second-quantized effective interaction in the *site basis*,

$$\hat{\mathcal{W}}_{eff} = -\frac{1}{2\Lambda^3} \left(\frac{2\hbar U g_N}{ma} \right)^2 \sum_{i,j,k,l=1}^N \sum_{\sigma,\sigma'} w_{ijkl} c_{i\sigma}^\dagger c_{j\sigma'}^\dagger c_{k\sigma'} c_{l\sigma} , \quad (2.73)$$

where w_{ijkl} is the matrix element

$$w_{ijkl} \equiv \langle ij | \mathbf{P} \cdot \overleftrightarrow{\mathbf{T}} \cdot \mathbf{P}' | lk \rangle = -\hbar^2 \int \int d\mathbf{r} d\mathbf{r}' \varphi_i^*(\mathbf{r}) \varphi_j^*(\mathbf{r}') \nabla \cdot \overleftrightarrow{\mathbf{T}}(\mathbf{r}, \mathbf{r}') \cdot \nabla' \varphi_k(\mathbf{r}') \varphi_l(\mathbf{r}) , \quad (2.74)$$

which we study in detail henceforth.

To start with, we apply two closure identities,

$$\mathbb{1} = \sum_{i,j=1}^N |ij\rangle \langle ij| , \quad (2.75)$$

between the momentum operators and the tensor $\overleftrightarrow{\mathbf{T}}$, which give us

$$w_{ijkl} = \sum_{i_1, i_2} \sum_{j_1, j_2} \langle ij | \mathbf{P} | i_1 i_2 \rangle \cdot \langle i_1 i_2 | \overleftrightarrow{\mathbf{T}} | j_1 j_2 \rangle \cdot \langle j_1 j_2 | \mathbf{P}' | lk \rangle . \quad (2.76)$$

Note that \mathbf{P} acts only on the *first* entry of a ket $|ij\rangle$, i.e.

$$\langle \mathbf{r}\mathbf{r}' | \mathbf{P} | ij \rangle = \langle \mathbf{r} | \mathbf{P} | i \rangle \langle \mathbf{r}' | j \rangle . \quad (2.77)$$

Similarly, \mathbf{P}' acts only on the second entry of $|ij\rangle$. Therefore

$$\langle ij | \mathbf{P} | i_1 i_2 \rangle = \langle i | \mathbf{P} | i_1 \rangle \langle j | i_2 \rangle = \langle i | \mathbf{P} | i_1 \rangle \delta_{j, i_2} , \quad (2.78)$$

$$\langle j_1 j_2 | \mathbf{P}' | lk \rangle = \langle j_2 | \mathbf{P}' | k \rangle \langle j_1 | l \rangle = \langle j_2 | \mathbf{P}' | k \rangle \delta_{j_1, l} , \quad (2.79)$$

and, as a consequence of the orthonormality of the Wannier wave functions, Eq.(2.76) becomes

$$w_{ijkl} = \sum_{i_1, j_2=1}^N \sum \langle i | \mathbf{P} | i_1 \rangle \cdot \langle i_1 j | \overleftrightarrow{\mathbf{T}} | l j_2 \rangle \cdot \langle j_2 | \mathbf{P}' | k \rangle . \quad (2.80)$$

Now, consistently with the standard approximations we used in appendix A to derive single-band Hubbard Hamiltonian, we can show (see Appendix C) that momentum

matrices elements appearing in Eq.(2.80) can be approximated by a term connecting only nearest neighbor sites,

$$\langle i | \mathbf{P} | j \rangle \approx \frac{imt}{\hbar} (\mathcal{R}_i - \mathcal{R}_j) \delta_{j,i\pm 1} . \quad (2.81)$$

Recall that \mathcal{R}_i is the position of the i -th site of the ring given by Eq.(2.8), t is the hopping parameter between two neighboring p_z orbital, and m is the electron mass. Therefore, substituting Eq.(2.81) into Eq.(2.80) we obtain four contributions for w_{ijkl} :

$$\begin{aligned} w_{ijkl} \approx & - \left(\frac{mt}{\hbar} \right)^2 \left[(\mathcal{R}_i - \mathcal{R}_{i+1}) \cdot \langle i+1 \ j | \overleftrightarrow{T} | l \ k+1 \rangle \cdot (\mathcal{R}_{k+1} - \mathcal{R}_k) \right. \\ & + (\mathcal{R}_i - \mathcal{R}_{i+1}) \cdot \langle i+1 \ j | \overleftrightarrow{T} | l \ k-1 \rangle \cdot (\mathcal{R}_{k-1} - \mathcal{R}_k) \\ & + (\mathcal{R}_i - \mathcal{R}_{i-1}) \cdot \langle i-1 \ j | \overleftrightarrow{T} | l \ k+1 \rangle \cdot (\mathcal{R}_{k+1} - \mathcal{R}_k) \\ & \left. + (\mathcal{R}_i - \mathcal{R}_{i-1}) \cdot \langle i-1 \ j | \overleftrightarrow{T} | l \ k-1 \rangle \cdot (\mathcal{R}_{k-1} - \mathcal{R}_k) \right] . \quad (2.82) \end{aligned}$$

Concerning the matrix element of the tensor \overleftrightarrow{T} , we assume, as it is done with the Coulomb repulsion matrix elements in the standard Hubbard model (see Appendix A), that its leading contributions come from the on site terms. Mathematically, this means

$$\langle ij | \overleftrightarrow{T} | lk \rangle \approx \overleftrightarrow{T}_i \delta_{j,i} \delta_{k,i} \delta_{l,i} , \quad (2.83)$$

where we define $\overleftrightarrow{T}_i \equiv \langle ii | \overleftrightarrow{T} | ii \rangle$. As it will soon become clearer (see Eq.(2.85)), \overleftrightarrow{T}_i depends on the specific i -th site of the ring.

Returning to the definition of \overleftrightarrow{T} in Eq.(2.71), we can write

$$\overleftrightarrow{T}_i = \int \int d\mathbf{r} d\mathbf{r}' \varphi_i^*(\mathbf{r}) \varphi_i^*(\mathbf{r}') \hat{n} \mathcal{O}(\mathbf{r}, \mathbf{r}') \hat{n}' \varphi_i(\mathbf{r}') \varphi_i(\mathbf{r}) , \quad (2.84)$$

with $\hat{n} \equiv \mathbf{r}/r$ and $\hat{n}' \equiv \mathbf{r}'/r'$. Moreover, since the Wannier wave functions are localized at the ring's sites,

$$\begin{aligned} \overleftrightarrow{T}_i &= \hat{\mathcal{R}}_i \left[\int \int d\mathbf{r} d\mathbf{r}' \varphi_i^*(\mathbf{r}) \varphi_i^*(\mathbf{r}') \mathcal{O}(\mathbf{r}, \mathbf{r}') \varphi_i(\mathbf{r}') \varphi_i(\mathbf{r}) \right] \hat{\mathcal{R}}_i \\ &= \hat{\mathcal{R}}_i \langle ii | \mathcal{O} | ii \rangle \hat{\mathcal{R}}_i \end{aligned} \quad (2.85)$$

with $\hat{\mathcal{R}}_i = \mathcal{R}_i/|\mathcal{R}_i|$. Assuming, for simplicity, that the matrix element of $\mathcal{O}(\mathbf{r}, \mathbf{r})$ is homogeneous, i.e. $\langle ii | \mathcal{O} | ii \rangle = \mathcal{O}_0$ is *site independent*, where \mathcal{O}_0 is a scalar presumably of

order one, we rewrite Eq.(2.82) as

$$\begin{aligned}
w_{ijkl} \approx - \left(\frac{mt}{\hbar} \right)^2 \mathcal{O}_0 & \left[(\mathcal{R}_i - \mathcal{R}_{i+1}) \cdot \hat{\mathcal{R}}_{i+1} (\mathcal{R}_{i+1} - \mathcal{R}_i) \cdot \hat{\mathcal{R}}_{i+1} \delta_{j,i+1} \delta_{l,i+1} \delta_{k,i} \right. \\
& + (\mathcal{R}_i - \mathcal{R}_{i+1}) \cdot \hat{\mathcal{R}}_{i+1} (\mathcal{R}_{i+1} - \mathcal{R}_{i+2}) \cdot \hat{\mathcal{R}}_{i+1} \delta_{j,i+1} \delta_{l,i+1} \delta_{k,i+2} \\
& + (\mathcal{R}_i - \mathcal{R}_{i-1}) \cdot \hat{\mathcal{R}}_{i-1} (\mathcal{R}_{i-1} - \mathcal{R}_{i-2}) \cdot \hat{\mathcal{R}}_{i-1} \delta_{j,i-1} \delta_{l,i-1} \delta_{k,i-2} \\
& \left. + (\mathcal{R}_i - \mathcal{R}_{i-1}) \cdot \hat{\mathcal{R}}_{i-1} (\mathcal{R}_{i-1} - \mathcal{R}_i) \cdot \hat{\mathcal{R}}_{i-1} \delta_{j,i-1} \delta_{l,i-1} \delta_{k,i} \right] . \quad (2.86)
\end{aligned}$$

Now, note that

$$\mathcal{R}_i \cdot \hat{\mathcal{R}}_i = \frac{a}{\sqrt{2(1 - \cos(2\pi/N))}} , \quad (2.87)$$

$$\mathcal{R}_{i\pm 1} \cdot \hat{\mathcal{R}}_i = \frac{a}{\sqrt{2(1 - \cos(2\pi/N))}} \cos\left(\frac{2\pi}{N}\right) , \quad (2.88)$$

recalling that a is the system's lattice spacing. Therefore, Eq.(2.86) simplifies to

$$\begin{aligned}
w_{ijkl} \approx \left(\frac{mt}{\hbar} \right)^2 \frac{a^2 \mathcal{O}_0 (1 - \cos(2\pi/N))}{2} & \left[\delta_{j,i+1} \delta_{l,i+1} \delta_{k,i} + \delta_{j,i+1} \delta_{l,i+1} \delta_{k,i+2} \right. \\
& \left. + \delta_{j,i-1} \delta_{l,i-1} \delta_{k,i-2} + \delta_{j,i-1} \delta_{l,i-1} \delta_{k,i} \right] . \quad (2.89)
\end{aligned}$$

Substituting Eq.(2.89) into Eq.(2.73) we find, after a few changes of variables,

$$\begin{aligned}
\hat{W}_{eff} = - \frac{(tU)^2}{\Lambda^3} 2\mathcal{O}_0 (1 - \cos^2(2\pi/N)) & \sum_{j=1}^N \sum_{\sigma, \sigma'} \left[\left(c_{j\sigma}^\dagger c_{j+1\sigma'}^\dagger c_{j\sigma'} c_{j+1\sigma} + \text{h.c.} \right) \right. \\
& \left. + \left(c_{j\sigma}^\dagger c_{j-1\sigma'}^\dagger c_{j-2\sigma'} c_{j-1\sigma} + \text{h.c.} \right) \right] . \quad (2.90)
\end{aligned}$$

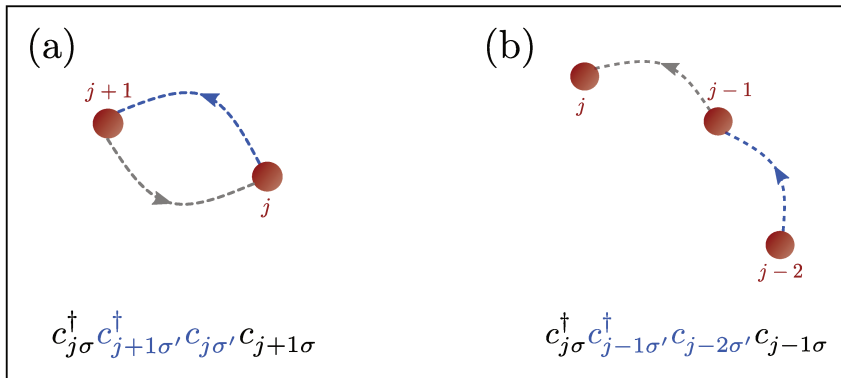


Figure 13 – **Effective interaction.** Illustration of two types of two-body processes that appear in the effective interaction Eq.(2.90). (a) is the "Bubble term", while (b) is the extended term that favors the electron delocalization. The Hermitian conjugates of (a) and (b) just reverse the direction of the arrows.

The effective interaction Eq.(2.90) involves two types of processes, which we illustrate in Fig. 13. The first one $\propto c_{j\sigma}^\dagger c_{j+1\sigma'}^\dagger c_{j\sigma'} c_{j+1\sigma}$ is what we called "bubble term", since it destroys an electron in the site j and creates it in the site $j+1$, but also destroys another electron in the same $j+1$ site and creates it in the site j . Thus, such term restricts the electronic movement between two neighboring sites of the ring. The second term $\propto c_{j\sigma}^\dagger c_{j-1\sigma'}^\dagger c_{j-2\sigma'} c_{j-1\sigma}$, on the other hand, involves two neighboring sites and *favours the electron delocalization*.

Combining Eq.(2.90) with Eq.(2.9), we find the following extended Hubbard model for the π -electrons:

$$\begin{aligned} \hat{H} = & -t \sum_{j=1}^N \sum_{\sigma} \left(c_{j\sigma}^\dagger c_{j+1\sigma} + \text{h.c.} \right) + U \sum_{j=1}^N \hat{n}_{j\uparrow} \hat{n}_{j\downarrow} \\ & - \lambda_N \left(\frac{U}{t} \right)^2 \sum_{j=1}^N \sum_{\sigma, \sigma'} \left[\left(c_{j\sigma}^\dagger c_{j+1\sigma'}^\dagger c_{j\sigma'} c_{j+1\sigma} + \text{h.c.} \right) + \left(c_{j\sigma}^\dagger c_{j-1\sigma'}^\dagger c_{j-2\sigma'} c_{j-1\sigma} + \text{h.c.} \right) \right], \end{aligned} \quad (2.91)$$

where we define the coupling constant

$$\lambda_N \equiv 2 \frac{t^4}{\Lambda^3} \mathcal{O}_0 (1 - \cos^2(2\pi/N)) . \quad (2.92)$$

Recall that $\Lambda > 0$ is the energy scale of the separation between the ground state and the first excited state of the σ -electrons, which we approximate by a constant, i.e., independent of the π -electron configuration. It is important to say that it is the relation between the parameters t and Λ that will set the energy scale of the coupling λ_N . Hereafter, we set $2\mathcal{O}_0(1 - \cos^2(2\pi/N)) \sim 1$ and, then, replace the coupling constant λ_N by simply $\lambda \equiv t^4/\Lambda^3 < 1$.

Eq. (2.91) is the central result of this chapter, and next we investigate the physical properties arising from our model.

2.3.4 Results and discussion

Through exact diagonalization of the Hamiltonian in Eq.(2.91), similarly to what we did in Sec. 2.2.1, we obtain its energy spectrum as function of U/t for a fixed λ/t . For the results shown in Fig. 14, we choose $\lambda/t = 0.1$. As in Fig. 7, we show only a few of the low-lying energy levels rather than the full energy spectrum.

Comparing the new energy spectrum with that of the standard Hubbard model (shown in dashed lines in the panels of Fig. 14), we can readily see that the effective interaction significantly reduces the ground state energy of the rings as U becomes larger. Interestingly, if we look closer at the spectrum of the ring with $N = 3$ sites in panel (a), we note that E_0 first increase with U , and starts to decrease only for $U/t > 4$. Such behavior - which is also observed in the spectrum of the larger rings as long as we use smaller values

for λ - reflects a competition between the the on-site Coulomb repulsion and the effective interaction \mathcal{W}_{eff} : on the one hand, the on-site Coulomb repulsion helps the electron to localize at the ring's sites, avoiding double occupancy. The effective momentum-momentum attraction, on the other hand, favors the electron delocalization. Both of these interactions depend on U . However, while the on-site Coulomb interaction has a linear dependence on U , \mathcal{W}_{eff} depends quadratically on this parameter, via λU^2 . Therefore, for small U , the linear term wins, but it is overcome by the quadratic term as U increases.

In the presence of an external magnetic field, again perpendicular to the ring's

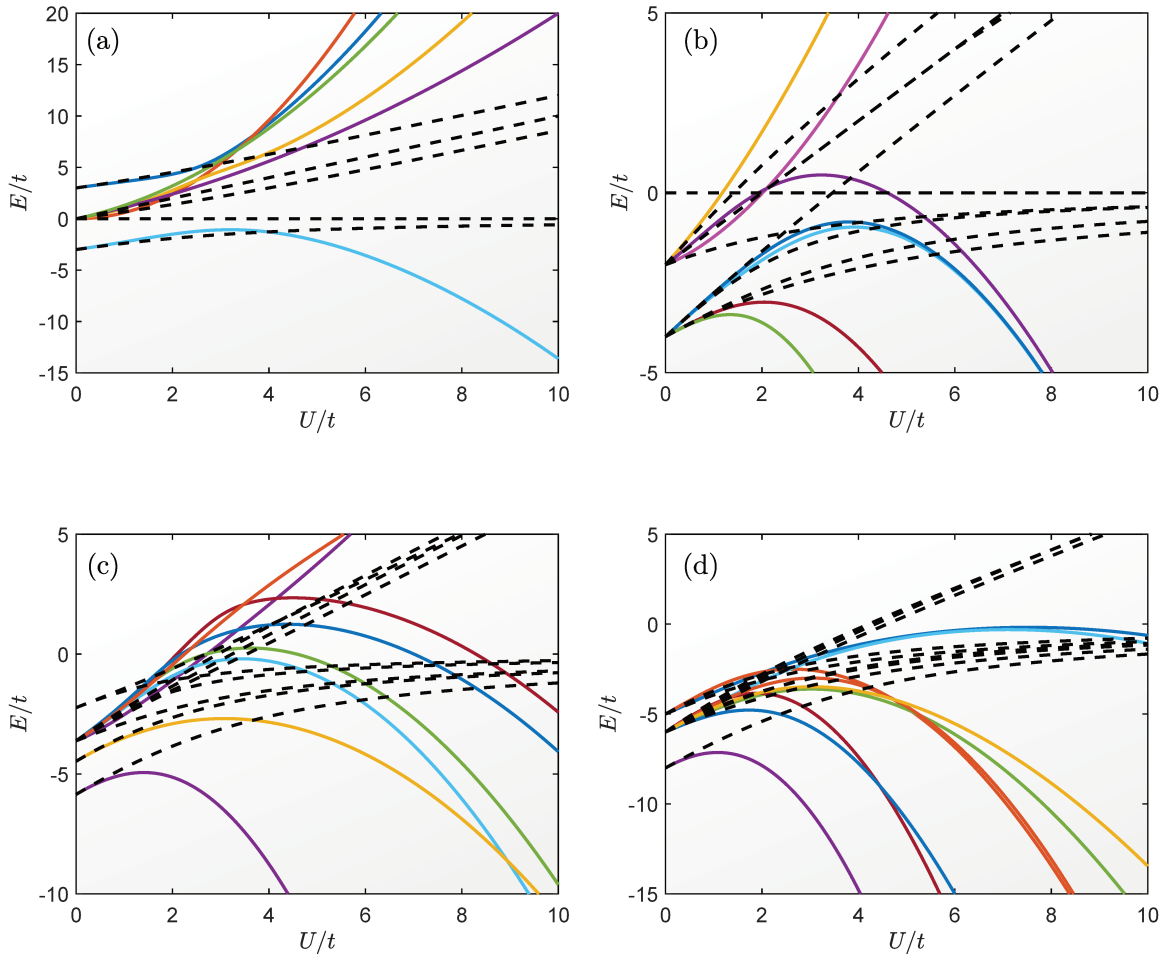


Figure 14 – **Energy spectrum of the extended Hubbard Hamiltonian.** The panels show the energy levels of Eq.(2.91), as function of U/t for rings with (a) $N = 3$ sites, (b) $N = 4$ sites, (c) $N = 5$ sites and (d) $N = 6$ sites at half-filling regime ($N = N_e$) and with $\lambda/t = 0.1$. In the panels (b) to (d), only a few of the low-lying energy levels are plotted. The dashed lines correspond $\lambda = 0$, i.e., the spectrum of the standard Hubbard model defined in Eq.(2.9).

plane, Eq.(2.91) needs to be modified accordingly,

$$\hat{H}_{mag} = -t \sum_{j=1}^N \sum_{\sigma} \left(e^{i2\pi f/N} c_{j\sigma}^{\dagger} c_{j+1\sigma} + \text{h.c.} \right) + U \sum_{j=1}^N \hat{n}_{j\uparrow} \hat{n}_{j\downarrow} - \lambda \left(\frac{U}{t} \right)^2 \sum_{j=1}^N \sum_{\sigma, \sigma'} \left[\left(c_{j\sigma}^{\dagger} c_{j+1\sigma'}^{\dagger} c_{j\sigma'} c_{j+1\sigma} + \text{h.c.} \right) + \left(e^{-i4\pi f/N} c_{j\sigma}^{\dagger} c_{j-1\sigma'}^{\dagger} c_{j-2\sigma'} c_{j-1\sigma} + \text{h.c.} \right) \right], \quad (2.93)$$

as explained in Sec. 2.2.2. Once again, the ground state energy of the ring and its persistent current are periodic with the magnetic flux, as we can see from Fig. 15 and Fig. 16, respectively. In these two figures, the different color curves refer to different values of the ratio λ/t , as indicated in the figures' labels and both follow the same color code. Moreover,

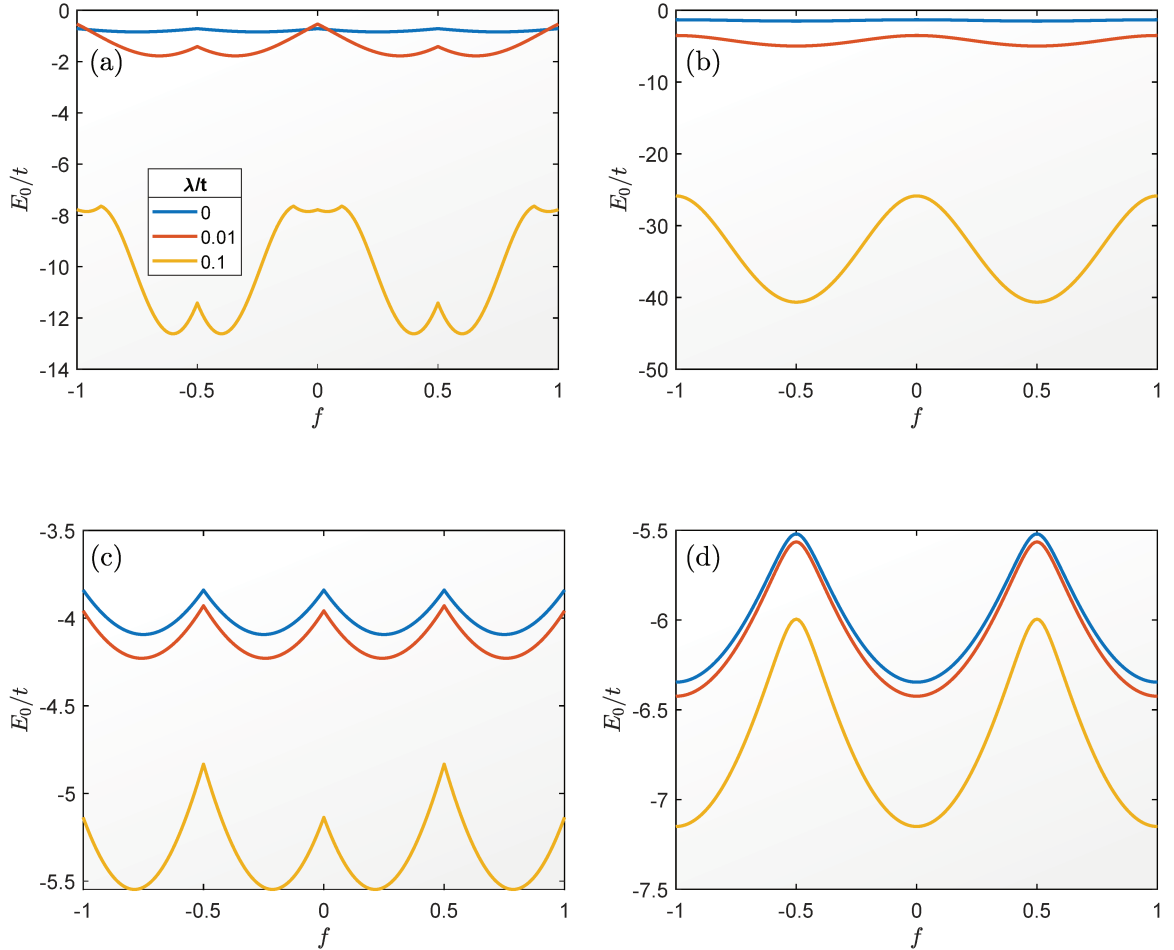


Figure 15 – **Ground state energy as function of the magnetic flux.** The panels show the the ground state energy (E_0) of a ring with (a) $N = 3$ sites, (b) $N = 4$ sites, (c) $N = 5$ sites and (d) $N = 6$ sites all in the half-filling regime, as function of the dimensionless magnetic flux that pierces it ($f = \phi/\phi_0$) and for different values of the ratio λ/t , as indicated at the legend in panel (a). The parameter U is fixed. In each of the panels we have, (a) $U/t = 8$, (b) $U/t = 8$, (c) $U/t = 2$ and (d) $U/t = 1.2$.

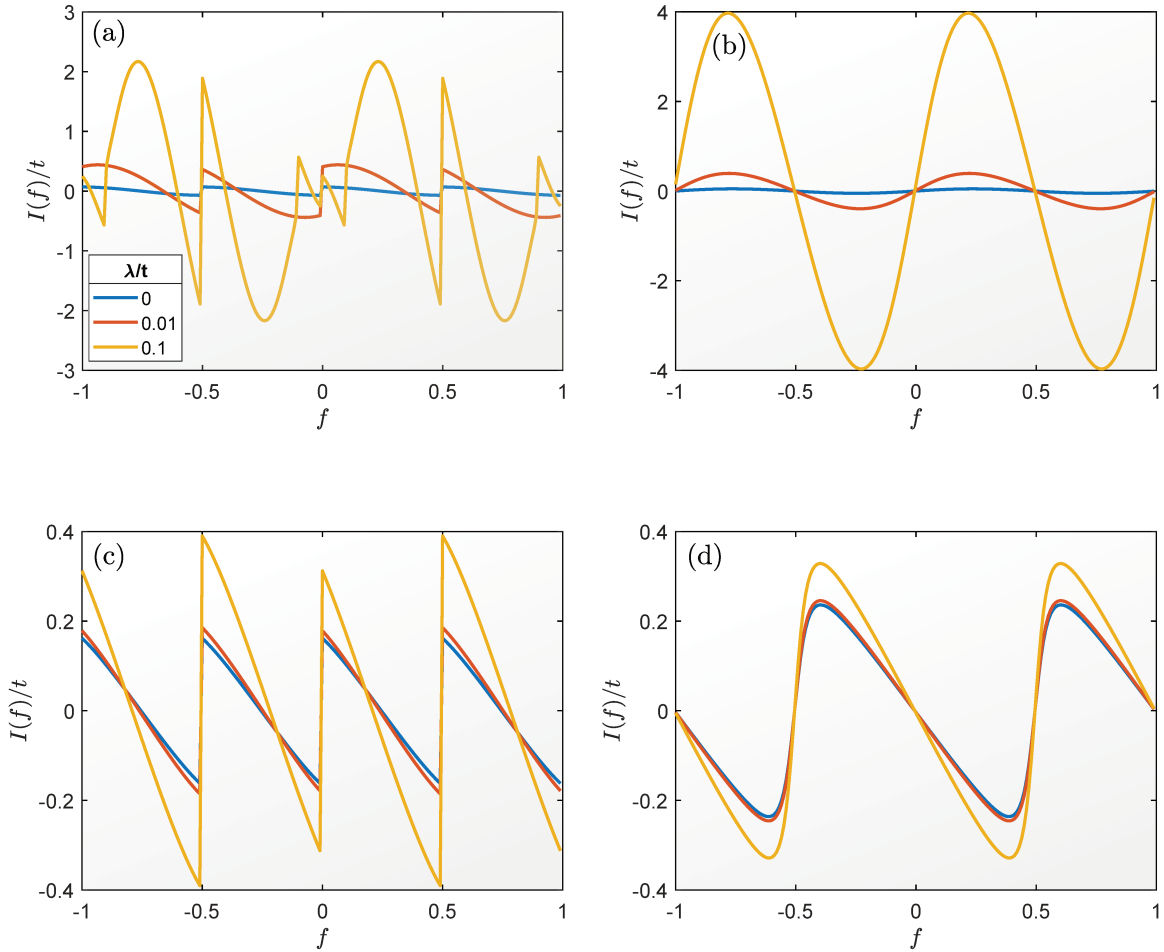


Figure 16 – **Persistent current as function of the magnetic flux.** The panels show persistent current (I_0) that establishes in the ground state of the ring with (a) $N = 3$ sites, (b) $N = 4$ sites, (c) $N = 5$ sites and (d) $N = 6$ sites, as function of the dimensionless magnetic flux that pierces it ($f = \phi/\phi_0$) and for different values of the ratio λ/t , as indicated at the legend in panel (a). The values of U/t in each panel are the same as in Fig. 8.

the ratio U/t is fixed in each panel, as described in the legend.

In each panel of Fig. 15 U/t was chosen in such a way to guarantee that, for the largest ratio of λ/t considered in these plots ($\lambda/t = 0.1$ corresponding to the yellow curves), the effects of \mathcal{W}_{eff} overcome those of the on-site Coulomb repulsion. This way, we can verify once more that our effective momentum-momentum interaction has the effect of lowering significantly the ring's ground state energy. Moreover, we note a significant difference in the periodicity of $E_0(f)$ in comparison with our results of Sec. 2.2.2. While in the standard Hubbard model $E_0(f)$ (and by extension $I_0(f)$) has the periodicity of half of a flux quantum for rings with an even number of sites (in the half-filling regime), here \mathcal{W}_{eff} imposes a periodicity of an integer number of flux quanta - see Fig. 15(a) and (c).

Furthermore, as we can see in Fig. 16, \mathcal{W}_{eff} amplifies the persistent current in the rings, and, as a consequence, enhances their magnetic responses. Fig. 17 shows the

magnetic susceptibility, as function of U/t for rings with (a) $N = 3$, (b) $N = 4$, (c) $N = 5$ and (d) $N = 6$ sites, all of them in the half-filling regime. We can see that for large enough λ/t , our effective interaction favors diamagnetism for all the rings but the one with $N = 4$ sites, where paramagnetism is enhanced. Such result reinforces the sensitivity of the ring's properties on its number of sites and electrons.

Most importantly, for our prototype of the benzene molecule, we recover the experimental $\Delta\chi$ if we choose $\lambda/t \approx 0.18$, as shown in Fig. 18. Recalling that $\lambda = t^4/\Lambda^3$ and using $t = 2.54\text{eV}$, a ratio $\lambda/t \approx 0.18$ sets the energy scale of the separation between the two low-lying energy levels of the σ -electrons in $\Lambda \approx 4.5\text{eV}$. It agrees with Λ estimated

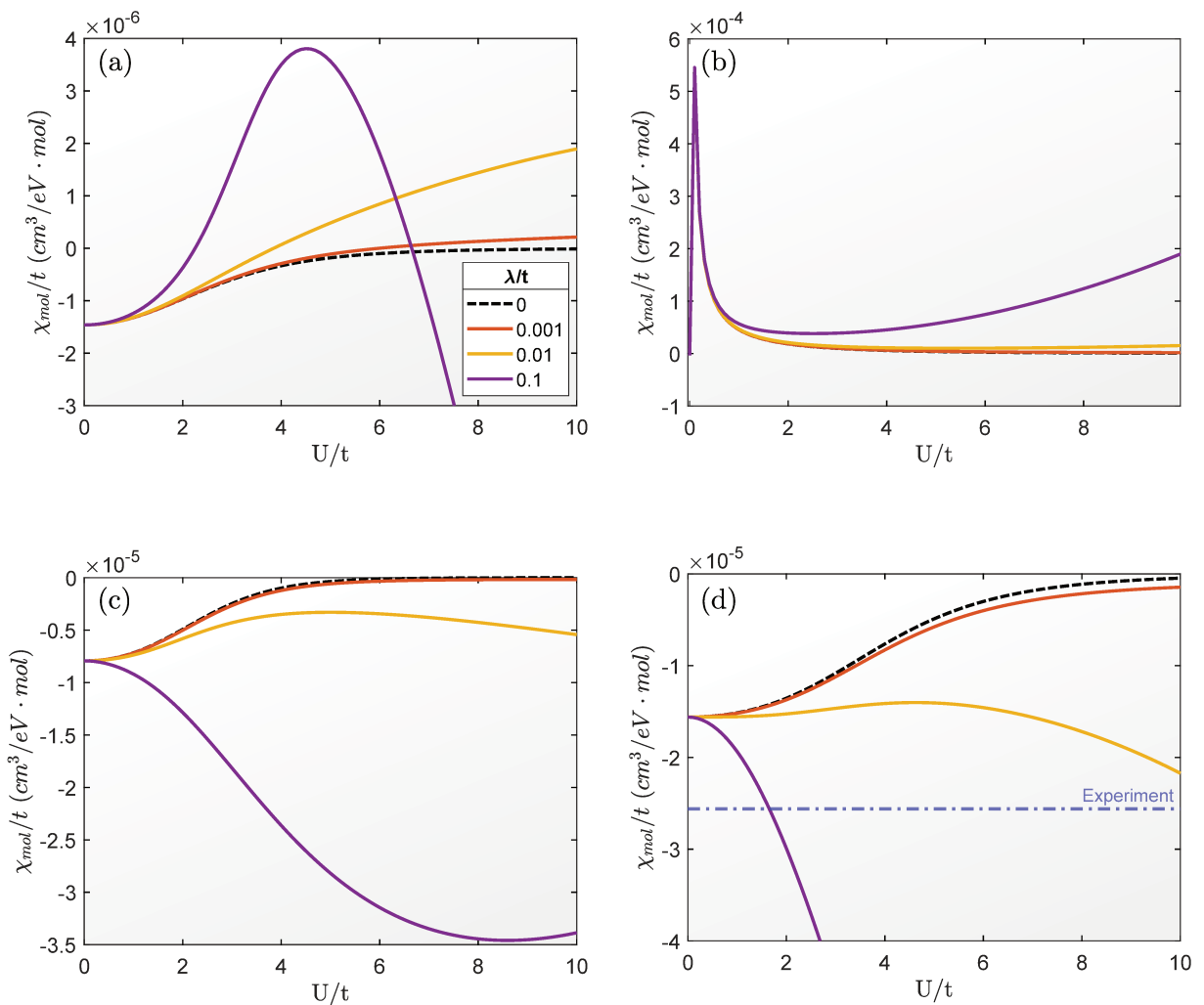


Figure 17 – **Magnetic susceptibility as function of U/t .** The panels show the magnetic susceptibility at low field ($f \rightarrow 0$) as a function of the ratio U/t for rings with (a) $N = 3$ sites, (b) $N = 4$, (c) $N = 5$ and (d) $N = 6$ sites, all of them in the half-filling regime ($N_e = N$). The different color curves in each panel refer to different values of λ/t , as indicated in the legend of panel (a). The blue dashed line in panel (d) mark the experimental value of the anisotropy of the magnetic susceptibility of benzene.

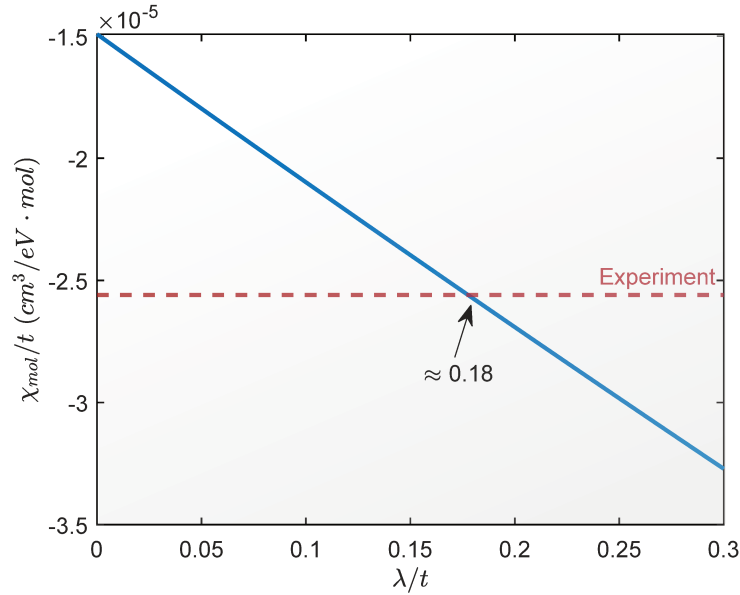


Figure 18 – **Magnetic susceptibility for the prototype of a benzene molecule.** Magnetic molar susceptibility for a ring with $N = 6$ sites and $N_e = 6$ electrons as function of λ/t and with $U = 3.048eV$ fixed. The red dashed line show the experimental value for the magnetic susceptibility of benzene ($\Delta\chi = -6.49 \times 10^{-5}$ notmalized by $t = 2.54eV$). The theoretical and experimental values agree for $\lambda/t \approx 0.18$.

in Sec. 2.4, evidencing that the approximations we used to derive Eq.(2.91) are consistent.

2.4 Hubbard Hamiltonian for the σ -electrons

In Sec. 2.3 we used the natural energy scale separation of our system to derive, via a generalized Born-Oppenheimer approximation, an effective interaction between the π -electrons mediated by virtual excitations of the σ -electrons. Conversely, we could derive a three-band Hubbard model for our rings, obtaining a Hamiltonian that accounts for the degrees of freedom of these two types of electrons on equal footing.

As carefully derived in Appendix A, such three-band Hubbard Hamiltonian has the form $\hat{H} = \hat{H}_p + \hat{H}_{sp} + \hat{H}_c$, where \hat{H}_p is the Hamiltonian for the degrees of freedom of the π -electrons *only*, which has the same form as in Eq.(2.9). We emphasize that similarly to Sec. 2.3, the charge density in the bonds generated by the σ -electrons do not contribute to the hopping parameter in \hat{H}_p . Additionally,

$$\hat{H}_{sp} = -\tilde{t} \sum_{j=1}^N \sum_{\sigma} \left(d_{j,1\sigma}^{\dagger} d_{j+1,2\sigma} + d_{j,2\sigma}^{\dagger} d_{j-1,1\sigma} \right) + \sum_{j=1}^N \left[\tilde{U}_1 \sum_{\kappa} \hat{n}_{j,\kappa\uparrow} \hat{n}_{j,\kappa\downarrow} + \tilde{U}_2 \sum_{\sigma,\sigma'} \hat{n}_{j,1\sigma} \hat{n}_{j,2\sigma'} \right] \quad (2.94)$$

is the Hubbard Hamiltonian of the σ -electrons, where $d_{j,\kappa\sigma}^{\dagger}$ ($d_{j,\kappa\sigma}$) creates (annihilates) an electron with spin σ in the κ sp_2 orbital centered in the j -th site of the ring ($\kappa = 1$ for the

right orbital and $\kappa = 2$ for the *left* orbital - see Fig. 5).

In Eq. (2.94), the parameter \tilde{t} denotes the hopping amplitude (a) between the *right* sp_2 orbital of the site j and the *left* sp_2 orbital of site $j + 1$ and (b) between the the *left* sp_2 orbital of site j and the *right* sp_2 of site $j - 1$. Moreover, \tilde{U}_1 is the **intra-orbital on-site repulsion**, associated with the Coulomb repulsion between two electrons in the **same** sp_2 orbital of site j , while the parameter \tilde{U}_2 is the **inter-orbital on-site repulsion** and describes the Coulomb repulsion between two electrons at **different** sp_2 orbitals of the same site j of the ring. See Fig. 19 for an illustrative picture.

Lastly,

$$\hat{H}_c = U_c \sum_{j=1}^N \sum_{\sigma, \sigma'} \hat{n}_{j\sigma} (\hat{n}_{j,1\sigma'} + \hat{n}_{j,2\sigma'}) \quad (2.95)$$

accounts for the density-density coupling between the σ -electrons and the π -electrons. In Eqs.(2.94) and (2.95) $\hat{n}_{j,\kappa\sigma} = d_{j,\kappa\sigma}^\dagger d_{j,\kappa\sigma}$ is the number operator associated with the sp_2 orbitals.

Defining new *bond* fermionic operators

$$a_{j\sigma}^\dagger \equiv \frac{1}{\sqrt{2}} \left(d_{j,1\sigma}^\dagger + d_{j+1,2\sigma}^\dagger \right) , \quad (2.96)$$

$$b_{j\sigma}^\dagger \equiv \frac{1}{\sqrt{2}} \left(d_{j,1\sigma}^\dagger - d_{j+1,2\sigma}^\dagger \right) , \quad (2.97)$$

which creates, respectively, an electron with spin σ in a symmetric and anti-symmetric

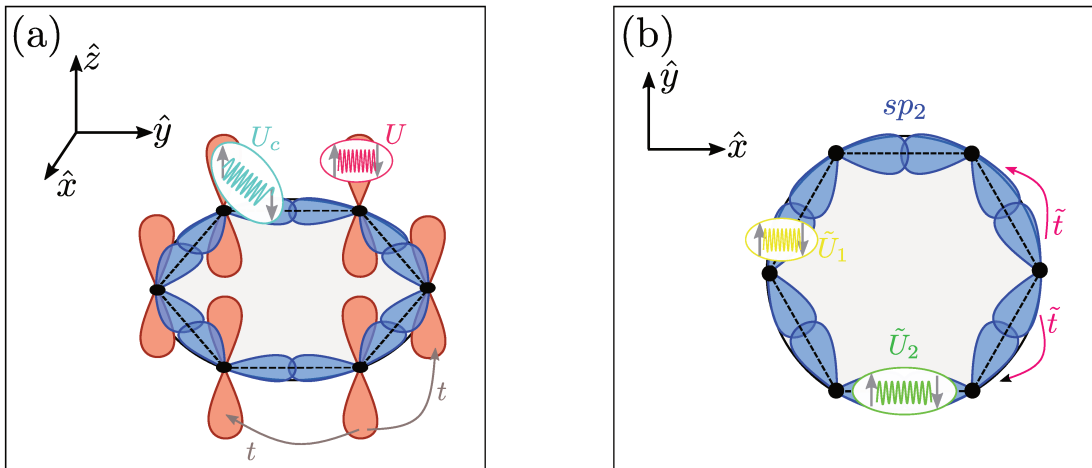


Figure 19 – **Illustration of the parameters in the multiband Hubbard model.** In panel (a) we illustrate the hopping between p_z orbitals (t), the on-site repulsion between π -electrons (U) and the coupling between π -electrons and σ -electrons (U_c). In panel (b), we illustrate the hopping between sp_2 orbitals (\tilde{t}), as well as the intra-orbital (\tilde{U}_1) and inter-orbital (\tilde{U}_2) on-site repulsion between the σ -electrons.

combinations of the sp_2 orbitals of two neighboring ring's sites, we can rewrite Eq.(2.94) as

$$\begin{aligned} \hat{H}_{sp_2} = & \sum_{j=1}^N \tilde{t} \left(\hat{N}_{a,j} - \hat{N}_{b,j} \right) + \frac{\tilde{U}_1}{4} \sum_{j=1}^N \left[\left(\hat{N}_{a,j} + \hat{N}_{b,j} - 1 \right)^2 + \hat{X}_j^2 - 1 \right] \\ & + \frac{\tilde{U}_2}{4} \sum_{j=1}^N \left[\left(\hat{N}_{a,j} + \hat{N}_{b,j} + \hat{X}_j \right) \left(\hat{N}_{a,j-1} + \hat{N}_{b,j-1} - \hat{X}_{j-1} \right) \right] . \end{aligned} \quad (2.98)$$

Here we define the number operators

$$\hat{N}_{a,j} \equiv \sum_{\sigma} a_{j\sigma}^{\dagger} a_{j\sigma} , \quad (2.99)$$

$$\hat{N}_{b,j} \equiv \sum_{\sigma} b_{j\sigma}^{\dagger} b_{j\sigma} . \quad (2.100)$$

Additionally,

$$\hat{X}_j = \sum_{\sigma=\uparrow,\downarrow} \left(a_{j\sigma}^{\dagger} b_{j\sigma} + h.c. \right) . \quad (2.101)$$

Using the fermionic anti-commutation relations - see Eqs.(A.11)-(A.12) and Eqs.(A.15)-(A.17) - we show that $\hat{N}_{j,a} + \hat{N}_{j,b}$ commutes with \hat{H} . It means that *the total number of σ -electrons per bond is a conserved quantity*. In other words, we can look for the eigenstates and eigenvalues of the three-band Hubbard Hamiltonian in a subspace with a fixed number of σ -electrons per bond, and, once again inspired by the benzene molecule, hereafter we consider the subspace of **two σ -electrons per bond**, where Eq.(2.98) simplifies to

$$\hat{H}_{sp} = \sum_{j=1}^N \left[\tilde{t} \left(\hat{N}_{a,j} - \hat{N}_{b,j} \right) + \frac{\tilde{U}_1}{4} \hat{X}_j^2 \right] + \frac{\tilde{U}_2}{4} \sum_{j=1}^N \left[\left(2 + \hat{X}_j \right) \left(2 - \hat{X}_{j-1} \right) \right] . \quad (2.102)$$

However, such three-band model brings some complications. In the first place, the dimension of the Fock space where \hat{H} is defined (let's call it d) is huge! Since we are considering σ -electrons and π -electrons as distinguishable particles, d is the product of the dimension of the Fock space of the π -electrons (d_{π}) and the σ -electrons (d_{σ}). As discussed Sec. 2.2.1, $d_{\pi} = (2N)! / (N_e! (2N - N_e^{(\pi)})!)$, with $N_e^{(\pi)}$ denoting the total number of the π -electrons in the rings, while $d_{\sigma} = 6^N$, as a consequence of having only two electrons per bond⁸. For instance, for the prototype of the benzene molecule d is of order of 10^7 , so an exact diagonalization of the complete \hat{H} does not seem possible even for the small rings we consider here.

Furthermore, even if the exact diagonalization is feasible, it is not clear how to derive an effective Hamiltonian for the π -electrons from \hat{H} . That is why the generalized Born-Oppenheimer approximation we introduce in Sec. 2.3.1 seems to be the most convenient approach for the purposes of this thesis.

⁸Therefore, the number of σ -electrons in the rings is $N_{\sigma} = 2N$. The total number of electrons in the ring is thus $N_e = N_e^{(\pi)} + N_e^{(\sigma)}$.

However, we can use the aforementioned three-band model to verify the validity of two important assumptions we made in Sec. 2.3.1, at which our central result Eq.(2.70) relies on:

- **Assumption 1:** the energy separation between the ground state and first excited state of the σ -electrons, denoted by Λ , is not much larger than the π -electrons hopping amplitude, i.e., $\Lambda \gtrsim t$. Recall that if, on the other hand, $\Lambda \gg t$, the dynamics of the π -electrons would happen as if the σ -electrons were frozen in their ground state and we would recover the usual single-band Hubbard Hamiltonian discussed in Sec. 2.2.
- **Assumption 2:** Λ depends weakly on the configuration of the electrons in the π -orbitals. Recalling our discussion in Sec. 2.3.1, such energy scale is actually dependent on the π -electrons configurations: $\Lambda = \Lambda_{1,0}(\mathbf{R}) = \lambda_1(\mathbf{R}) - \lambda_0(\mathbf{R})$, where $\lambda_\nu(\mathbf{R})$ are the eigenvalues of Eq.(2.37) for a fixed set of positions of π -electrons, $\mathbf{R} = \{\mathbf{R}_1 \cdots, \mathbf{R}_{N_e(\pi)}\}$. However, along our calculations in Sec. 2.3.1, we approximate it by a constant.

To test the validity of the assumptions listed above, we perform an exact diagonalization of $\hat{H} = \hat{H}_p + \hat{H}_{sp} + \hat{H}_c$ for fixed configurations of π -electrons and study its resulting eigenvalues. In this case, since the π -electrons are kept static at a chosen configuration, the hopping term of \hat{H}_p vanishes and the number operators $\hat{n}_{j\sigma} = c_{j\sigma}^\dagger c_{j\sigma}$ must be replaced by scalars $n_{j\sigma}$, which can assume the values zero or one. Therefore, the on-site Coulomb repulsion term of \hat{H}_p turns into a *configuration-dependent constant*

$$f(\mathcal{C}) = U \sum_{j=1}^N n_{j\uparrow} n_{j\downarrow} , \quad (2.103)$$

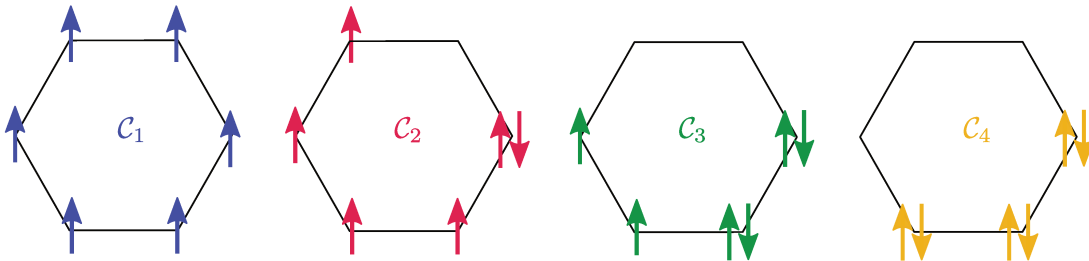


Figure 20 – **Different configurations of six π electrons in a six site ring.** Illustration with four of the many possible configurations of six π -electrons occupying the p_z orbitals of the prototype of the benzene molecule. The configuration \mathcal{C}_1 , with $\{n_{1\uparrow} n_{1\downarrow} \cdots n_{N\uparrow} n_{N\downarrow}\} = \{1, 0, 1, 0, 1, 0, 1, 0, 1, 0, 1, 0\}$ has no double occupation of orbitals, while \mathcal{C}_2 , with $\{1, 1, 0, 0, 1, 0, 1, 0, 1, 0, 1, 0\}$ has one double occupation, \mathcal{C}_3 , with $\{1, 1, 0, 0, 0, 0, 1, 0, 1, 0, 1, 1\}$ has two double occupations and \mathcal{C}_4 , with $\{1, 1, 0, 0, 0, 0, 0, 0, 1, 1, 1, 1\}$ has three double occupations.

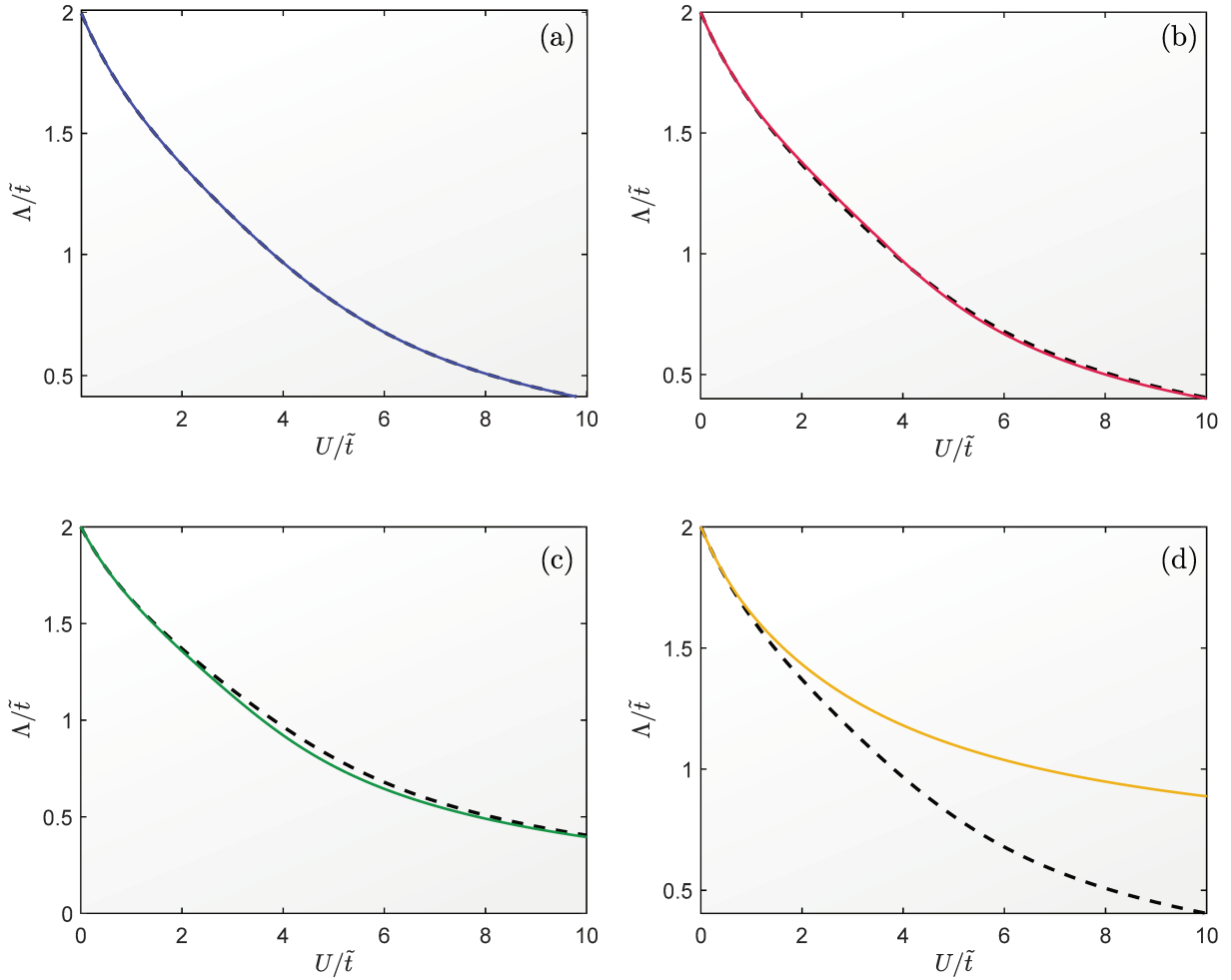


Figure 21 – **Excitation energy of the σ -electrons as function of U for the prototype of benzene.** We show the energy difference (Λ) between the first excited state of $\hat{H}(\mathcal{C})$ defined in Eq.(2.105) and its ground state as a function of the on-site Coulomb repulsion U for four distinct configurations of the six π -electrons in a six site ring: configuration \mathcal{C}_1 in panel (a), \mathcal{C}_2 in panel (b), \mathcal{C}_3 in panel (c), and \mathcal{C}_4 in panel (d). These configurations are illustrated in Fig. 20. In all the panels, the dashed black lines corresponds to Λ in the absence of π -electrons. Here we set $\tilde{U}_1 = \tilde{U}_2 = U_c = U$. Besides, both Λ and U are normalized by the hopping between sp_2 orbitals, \tilde{t} .

while Eq.(2.95) simplifies to

$$\hat{H}_c(\mathcal{C}) = \frac{U_c}{2} \sum_{j=1}^N \sum_{\sigma} n_{j\sigma} \left[4 + \hat{X}_j - \hat{X}_{j-1} \right]. \quad (2.104)$$

We emphasize that in Eqs.(2.103) and (2.104) \mathcal{C} labels the specific configuration of π -electrons we taken into account, which is parametrized by the set $\{n_{1\uparrow}n_{1\downarrow} \cdots n_{N\uparrow}n_{N\downarrow}\}$ of zeros and ones. The resulting configuration-dependent Hamiltonian for the σ -electrons is

readily obtained:

$$\hat{H}(\mathcal{C}) = \sum_{j=1}^N \left[\tilde{t} \left(\hat{N}_{a,j} - \hat{N}_{b,j} \right) + \frac{\tilde{U}_1}{4} \hat{X}_j^2 - \frac{\tilde{U}_2}{4} \hat{X}_j \hat{X}_{j-1} + V_j(\mathcal{C}) \left(\hat{X}_j - \hat{X}_{j-1} \right) \right] + K(\mathcal{C}) , \quad (2.105)$$

with

$$V_j(\mathcal{C}) = \tilde{U}_2 + U_c \sum_{\sigma} n_{j\sigma} , \quad (2.106)$$

$$K(\mathcal{C}) = f(\mathcal{C}) - \tilde{U}_2 + 2 \sum_{j=1}^N V_j(\mathcal{C}) . \quad (2.107)$$

Fig. 20 illustrates four possible families of π -electrons configurations for the prototype of the benzene molecule. It is important to note that $V_j(\mathcal{C})$ and $\mathcal{K}(\mathcal{C})$ are invariant by global spin flip, so all configurations obtained from those shown in Fig. 20 by reversing all the spins results in the same $\hat{H}_{\mathcal{C}}$ and are, therefore, equivalent. Moreover, the configurations obtained by applying the benzene's point group symmetry to Fig. 20 are also equivalent. However, we emphasize that Fig. 20 does not present all the possible π -electron configurations, a lot of them are omitted for simplicity.

In the remaining part of this section, we study Eq.(2.105) for the prototype of the benzene molecule. For simplicity, we set $\tilde{U}_1 = \tilde{U}_2 = U_c = U$. This is justified by our estimation of these parameters in Appendix B: there, using an approximation of localized orbitals we show that the aforementioned interaction parameters are indeed very close to each other.

Fig. 21 shows Λ (normalized by the hopping \tilde{t} between sp_2 orbitals) as a function of U/\tilde{t} for each of the π -electrons configurations shown in Fig. 20 (the same color code is used in both figures). For comparison purposes, in each panel we also show $\Lambda(U)$ when no π -electron is present in the ring (black dashed lines), i.e., the excitation energy of the σ -electrons alone.

The first thing we should notice is that for small U/\tilde{t} , $\Lambda/\tilde{t} \approx 1.5$, i.e., Λ is of the same order as \tilde{t} , which is surely larger than the p_z orbital hopping t (although not much larger than that), so we are safe to assume that $\Lambda \gtrsim t$.

Furthermore, except for Fig. 21(d), the curves $\Lambda(U)$ with (solid line) and without (dashed line) π -electrons show an astonishing agreement, pointing out that Λ indeed doesn't depend much on the π -electron configuration. Concerning the panel (d) of the same figure, we see that the deviation between the lines becomes considerable as we increase U/\tilde{t} . But, for benzene, recalling the estimations of the authors in Ref. [40], $U/\tilde{t} < U/t = 1.2$, where the agreement between the solid and dashed lines is still quite good. Therefore we are also safe to approximate Λ by a constant.

The same qualitative results hold for the other configurations omitted in Fig. 20 and for rings with $N \neq 6$.

2.5 Conclusions - Part I

In this chapter, we study the physical properties of rings with $3 \leq N \leq 6$ sites, N_e electrons, and three orbitals per site, which we interpret as prototypes of aromatic molecules. In particular, we focus on their energy spectrum, and their magnetic response in the presence of an external magnetic field applied perpendicularly to their plane.

The magnetic field induces a persistent current in the ring's ground state, which in turn, generates a magnetic moment in the same direction of the field. It is accepted that this is the physics happening in the aromatic rings of real-life aromatic molecules: the persistent current that establishes in the aromatic ring is the origin of the experimentally observed magnetic anisotropy in these molecules. Let us emphasize here that such persistent current is an equilibrium property of the system and ceases to exist if the field is removed. Therefore it should not be confused with a superconducting current in a superconducting ring.

The question which remains is *which electrons contribute to the above mentioned persistent current?* According to the RCM model, the answer would be the π -electrons alone, since they are highly delocalized, while the σ -electrons, localized in the σ -bonds, are considered frozen. However, we show, by describing these π -electron through the standard Hubbard model, that for realistic values of the hopping ($t \approx 2.54eV$) and on-site repulsion ($U \approx 3.05eV$) [40] the calculated anisotropy in the magnetic susceptibility ($\Delta\chi$) is only 3/5 of the experimental value. We, therefore, argue that a minimal model to explain the magnetic properties of the aromatic molecules should also include the degrees of freedom of the σ -electrons.

Although it is true that the σ -electrons are more localized than the π -electrons, they can undergo local excitations in the σ -bonds, which, in turn, modify the electron charge density in the bonds and, therefore modify the periodic potential felt by the π -electrons. We show that if we allow excitations of the σ -electrons to happen, they mediate an attractive momentum-momentum effective interaction between the π -electrons \hat{W}_{eff} defined in Eq.(2.70), which bears some similarities with the Breit-Darwin interaction and with the Biot-Savart interaction derived by Pines and Bohm.

We obtain such effective momentum-momentum interaction through a generalized Born-Oppenheimer approximation, which, motivated by a natural energy scale separation between the σ -electrons and the π -electrons, allow us to decouple their degrees of freedom in a wave function ansatz similar to that used in the usual text-book Born-Oppenheimer approximation.

The central result of this chapter is our minimal effective model for the π -electrons, which corresponds to an extended Hubbard model where \hat{W}_{eff} is added to Eq.(2.9). We verified that the main effect of our effective momentum-momentum interaction is to amplify the magnetic response of the rings. In particular, for the prototype of the benzene molecule ($N = N_e^{(\pi)} = 6$), \mathcal{W}_{eff} favors diamagnetism and recover the experimental $\Delta\chi$ if we choose a coupling constant of $\lambda/t \approx 0.18$, consistent with the approximations we used in Sec. 2.3.1 to derive \mathcal{W}_{eff} .

Although it is beyond the scope of this thesis, we emphasize that microscopic model we propose holds for any number of sites N and can also be extended to more complex systems, such as the graphene.

3 The Suppression of Superconductivity near a Lifshitz Transition

In this chapter, we study the effect of non-magnetic impurities in a two-band superconductor in the regime where the second band is incipient, i.e., when its bottom is just below (or just above) the Fermi level. In particular, we investigate the evolution of the superconducting transition temperature (T_c) as a function of the chemical potential (μ) as we go through a Lifshitz transition characterized here by the appearance of a new Fermi pocket in the Fermi surface when the second band becomes populated.

In Sec. 3.1 we review some results already known about $T_c(\mu)$ of a two-band *clean* superconductor. We show how to derive its coupled self-consistent gap equations and how to analytically solve them in the particular case of 2D bands. In Sec. 3.2, we calculate $T_c(\mu)$ for the same two-band superconductor but, this time, in the presence of randomly distributed non-magnetic impurities. We show that, in the vicinity of the Lifshitz transition, there is a competition between two effects: on the one hand, T_c tends to increase because of the enhancement of the electronic density of states promoted by the appearance of the second Fermi pocket. On the other hand, the *interband scattering* processes induced by disorder break the Cooper pairs and suppress superconductivity. When disorder is strong enough, the second effect wins and $T_c(\mu)$ decreases, in agreement with the experimental results of two paradigmatic examples of multiband superconductors: SrTiO₃ and the LaAlO₃/SrTiO₃ interface. Finally, in Sec. 3.3 we summarize our principal results.

As in Chapter 2, the body of the text is complemented with Appendices. The results presented in this chapter were recently published in Physical Review Letters [35] and Physical Review B [36], and the order of the sections here follows that of Ref. [36].

3.1 Clean Multiband Superconductors

In a multiband superconductor, more than one conduction band crosses the Fermi levels simultaneously. These bands can be either electron-like, hole-like or a mixture of these two types. Here we focus on the case of a superconductor with two *parabolic* and *concentric* electron-like bands. Its effective Hamiltonian, similarly to Ref. [48], is given by

$$H_0 = \sum_{\mathbf{k}, i, \sigma} \xi_{i, \mathbf{k}} c_{i, \mathbf{k} \sigma}^\dagger c_{i, \mathbf{k} \sigma} + \sum_{\mathbf{k}, \mathbf{k}', i, j} V_{ij} c_{i, \mathbf{k} \uparrow}^\dagger c_{i, -\mathbf{k} \downarrow}^\dagger c_{j, -\mathbf{k}' \downarrow} c_{j, \mathbf{k}' \uparrow} . \quad (3.1)$$

Here $c_{i,\mathbf{k}\sigma}^\dagger$ ($c_{i,\mathbf{k}\sigma}$) creates (annihilates) an electron with momentum \mathbf{k} and spin σ in band i (with $i = 1, 2$), which has dispersion $\xi_{i,\mathbf{k}} = k^2/2m_i + W_i$, as illustrated in Fig. 22(a). The bottom of the bands are separated by an energy scale $\varepsilon_0 > 0$. Hereafter, we denote by $W_1 \equiv -\mu$ the bottom of band 1, and by $W_2 \equiv -\mu + \varepsilon_0$ the bottom of band 2, where $\mu > 0$ is the chemical potential, which controls occupation of the bands.

For $\mu < \varepsilon_0$, only the lower band is occupied and we have a simple single-band superconductor. By increasing the density of electrons in the system, μ increases, until it reaches the bottom of the second band. At this point the system undergoes a so called *Lifshitz transition* (LT), which, in the context of multiband superconductivity, is characterized by the appearance of a new Fermi pocket at the FS as a new band becomes populated. Note that, in the case of our parabolic bands, as μ goes across ε_0 the FS changes from a single sphere ($\mu < \varepsilon_0$) to two concentric spheres ($\mu > \varepsilon_0$), as illustrated in Fig. 22(b). We can wonder: *Is there any signature of the Lifshitz transition in the system's phase diagram (which corresponds to the superconducting transition temperature (T_c) as function of the μ)?* As we will shortly see, the answer is yes!

In Eq.(3.1) V_{ij} describes the pairing interaction matrix: V_{11} and V_{22} are the *intra*band pairing interactions, while $V_{12} = V_{21}$ are the *inter*band pairing interactions. Regarding the sign of the pairing interactions, we consider $V_{11} > 0$ and $V_{22} > 0$ always *attractive*, otherwise we would not find superconductivity when only band 1 is occupied ($\mu < \varepsilon_0$). The interband pairing, on the other hand, can be either attractive or repulsive,

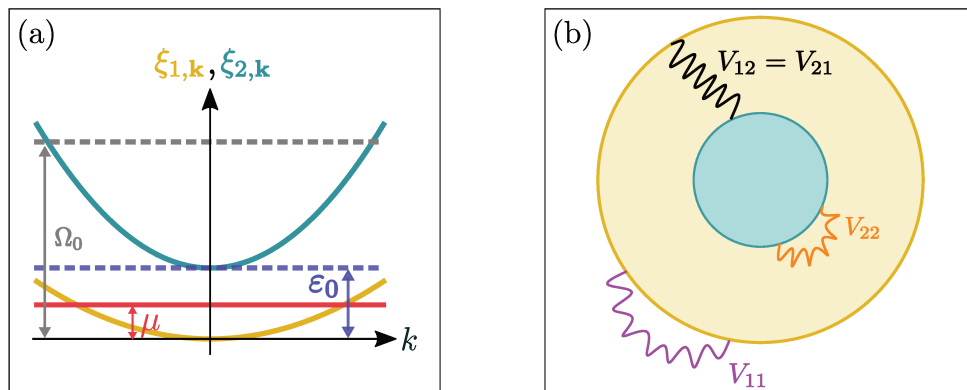


Figure 22 – **Two-band superconductor.** (a) Illustration of two electron-like parabolic and concentric bands displaced by an energy $\varepsilon_0 > 0$. Their occupations are controlled by the chemical potential $\mu > 0$. When μ becomes larger than ε_0 , the second band becomes populated, signaling a Lifshitz transition (LT). $\Omega_0 \gg \varepsilon_0$ is the pairing interaction energy cutoff, which plays a similar role as the Debye frequency in conventional superconductors. (b) Illustration of the pairing interactions we consider in our model. $V_{11} > 0$ and $V_{22} > 0$ are intra-band pairing interactions, while $V_{12} = V_{21}$ are inter-band pairing interactions. The later can be either attractive or repulsive. The yellow sphere corresponds to the Fermi pocket of band 1, while the green one is the Fermi pocket of band 2.

which gives rise to different superconducting states, as will be explained later in this chapter. Note that we are considering momentum-independent pairing interactions, which leads to isotropic superconducting gaps (*s*-wave superconductivity). A discussion about the microscopic origin of V_{ij} is beyond the scope of this thesis.

How do we calculate T_c of a multiband superconductor? Within a mean-field approach, it is actually not a complicated task. There will be some complications arising from the fact that we are close to the bottom of the bands, but we will get there. We start by decoupling (3.1) in the Cooper channel, in a similar way it is done in a single-band superconductor. It corresponds to replace $c_{j,-\mathbf{k}\downarrow}c_{j,\mathbf{k}\uparrow}$ in Eq.(3.1) by its expectation value $\langle c_{j,-\mathbf{k}\downarrow}c_{j,\mathbf{k}\uparrow} \rangle$ plus fluctuations. Neglecting terms that are quadratic or higher orders in the fluctuations, we thus obtain

$$H_0 = \sum_{\mathbf{k},i,\sigma} \xi_{i,\mathbf{k}} c_{i,\mathbf{k}\sigma}^\dagger c_{i,\mathbf{k}\sigma} - \sum_{\mathbf{k},i} \left(\Delta_i c_{i,\mathbf{k}\uparrow}^\dagger c_{i,-\mathbf{k}\downarrow}^\dagger + h.c. \right), \quad (3.2)$$

where

$$\Delta_i = - \sum_{\mathbf{k},j} V_{ij} \langle c_{j,-\mathbf{k}\downarrow} c_{j,\mathbf{k}\uparrow} \rangle. \quad (3.3)$$

is the *isotropic* superconducting gap in band i .

There are several ways to derive the self-consistent equations for the gaps Δ_i - see for instance a review on Ref.[49]. Here, it is more convenient to work with Green's function in Nambu space, since this formalism proves to very useful in Sec. 3.2, when we introduce disorder in the system. Defining the Nambu spinor $\hat{\psi}_{\mathbf{k}}^\dagger = \left(c_{1,\mathbf{k}\uparrow}^\dagger c_{1,-\mathbf{k}\downarrow} c_{2,\mathbf{k}\uparrow}^\dagger c_{2,-\mathbf{k}\downarrow} \right)$, we can rewrite Eq.(3.2) in a matrix form

$$H_0 = \sum_{\mathbf{k}} \hat{\psi}_{\mathbf{k}}^\dagger \bar{\xi}_{\mathbf{k}} \hat{\psi}_{\mathbf{k}}, \quad (3.4)$$

where

$$\bar{\xi}_{\mathbf{k}} = \begin{pmatrix} \xi_{1,\mathbf{k}} & -\Delta_1 & 0 & 0 \\ -\Delta_1 & -\xi_{1,\mathbf{k}} & 0 & 0 \\ 0 & 0 & \xi_{2,\mathbf{k}} & -\Delta_2 \\ 0 & 0 & -\Delta_2 & -\xi_{2,\mathbf{k}} \end{pmatrix}, \quad (3.5)$$

and, from Eq. (3.4), we can readily calculate the system's bare Green's function [22, 56]: $\hat{\mathcal{G}}_0(\mathbf{k}, \omega_n) = (i\omega_n \mathbb{1} - \bar{\xi}_{\mathbf{k}})^{-1}$, where $\omega = (2n + 1)\pi T$ (with $n \in \mathbb{N}$) are the usual Matsubara frequencies and $\mathbb{1}$ is the identity matrix in Nambu space. Performing a simple matrix inversion, we obtain

$$\hat{\mathcal{G}}_0(\mathbf{k}, \omega_n) = \begin{pmatrix} \mathcal{G}_{1,0} & \mathcal{F}_{1,0} & 0 & 0 \\ \mathcal{F}_{1,0} & -\mathcal{G}_{1,0}^* & 0 & 0 \\ 0 & 0 & \mathcal{G}_{2,0} & \mathcal{F}_{2,0} \\ 0 & 0 & \mathcal{F}_{2,0} & -\mathcal{G}_{2,0}^* \end{pmatrix}, \quad (3.6)$$

where

$$\mathcal{G}_{i,0}(\mathbf{k}, \omega_n) = -\frac{i\omega_n + \xi_{i,\mathbf{k}}}{\omega_n^2 + \xi_{i,\mathbf{k}}^2 + \Delta_i^2}, \quad (3.7)$$

and

$$\mathcal{F}_{i,0}(\mathbf{k}, \omega_n) = \frac{\Delta_i}{\omega_n^2 + \xi_{i,\mathbf{k}}^2 + \Delta_i^2} \quad (3.8)$$

are, respectively, the *normal* and the *anomalous* components of the Green's function.

Note that it is the anomalous Green's function which gives us information about the superconducting gap: since $\langle c_{i,-\mathbf{k}\downarrow} c_{i,\mathbf{k}\uparrow} \rangle = T \sum_n \mathcal{F}_{i,0}(\mathbf{k}, \omega_n)$, when combining Eqs. (3.3) and (3.8) we find the self-consistent gap equations:

$$\Delta_i = \pi T \sum_{j,n} \lambda_{ij} \Delta_j \left\langle \frac{1}{\omega_n^2 + \xi^2 + \Delta_j^2} \right\rangle_j^{\Omega_0}. \quad (3.9)$$

Here, in order to shorten the notation, we define

$$\langle \mathcal{O}(\xi) \rangle_i^{\xi_c} \equiv \frac{1}{\pi \rho_{i,0}} \int_{W_i}^{\xi_c} d\xi \rho_i(\xi) \mathcal{O}(\xi), \quad (3.10)$$

with $\mathcal{O}(\xi)$ denoting an arbitrary function of energy, and ξ_c denoting the upper cutoff for the integral. We also define the *dimensionless coupling constants* $\lambda_{ij} = -\rho_{j,0} V_{ij}$. It is important to note that in our notation $\lambda_{ij} < 0$ means a *repulsive* interaction, while $\lambda_{ij} > 0$ means an *attractive* interaction. Besides, $\rho_i(\xi)$ corresponds to the density of states *per spin* of band i , while $\rho_{i,0} \equiv \rho_i(W_i + \varepsilon_0)$ is the density of states at an energy ε_0 above the bottom of the band. In the particular case of parabolic 2D bands, the density of states is a constant: $\rho_i(\xi) = \rho_{i,0} = m_i/(2\pi)$. Finally, Ω_0 is the energy scale of the pairing interactions, which plays a similar role as the Debye frequency in the standard BCS superconductors.

Before proceeding, let's take a closer look at the self-consistency equations and highlight their major differences with that of a usual BCS single-band superconductor. In the usual BCS approach, what is often done in integrals such as Eq.(3.10) is to approximate the density of states by a constant (which is its value at the Fermi level) and calculate the remaining integral between $\pm\infty$. That is essentially because the Fermi energy is much larger than the pairing interaction cutoff. Here, on the other hand, since we are in the vicinity of the bottom of the bands the Fermi energy is much smaller than Ω_0 (also $\varepsilon_0 \ll \Omega_0$). In this regime, which is called *dilute superconductivity*, we cannot make the aforementioned approximations: $\rho_i(\xi)$ must be kept in the integrand and the limits of the integral carry information about the bottom of the band through W_i . Luckily, for 2D bands we can still analytically evaluate the energy integrals that appear in the model, because the density of states is already a constant in this case.

Close to T_c , Δ_i are very small. Consequently, we can expand the right-hand side of Eq.(3.9) in powers of Δ_i . Neglecting quadratic and higher orders, we obtain the *linearized* gap equations, which written in a matrix form, become

$$\begin{pmatrix} \Delta_1 \\ \Delta_2 \end{pmatrix} = \begin{pmatrix} \lambda_{11} & \lambda_{12} \\ \lambda_{21} & \lambda_{22} \end{pmatrix} \hat{A}_{\text{clean}}(\mu, T_c) \begin{pmatrix} \Delta_1 \\ \Delta_2 \end{pmatrix}. \quad (3.11)$$

The matrix elements of \hat{A}_{clean} are functions of μ and T_c , and carry information about the bottom of the bands:

$$\left(\hat{A}_{\text{clean}}\right)_{ij} = \delta_{ij} \pi T_c \sum_n \left\langle \frac{1}{\omega_n^2 + \xi^2} \right\rangle_i^{\Omega_0} = \delta_{ij} \frac{\pi}{2} \left\langle \frac{1}{\xi} \tanh\left(\frac{\xi}{2T_c}\right) \right\rangle_i^{\Omega_0}. \quad (3.12)$$

To obtain the second equality on the right-hand side of Eq.(3.12), we need to calculate the Matsubara sum¹

$$T_c \sum_n \frac{1}{[(2n+1)\pi T_c]^2 + \xi^2} = \frac{1}{2\xi} \tanh\left(\frac{\xi}{2T_c}\right). \quad (3.13)$$

From Eq.(3.11), it is evident that the the self-consistent gap equations are coupled through λ_{12} and λ_{21} , which are equal only if the density of states of the two bands coincide: recall that from our definition of the dimensionless coupling constants it follows that $\lambda_{21}/\lambda_{12} = \rho_{1,0}/\rho_{2,0}$. However, they *have the same sign*, which is set by the sign of $V_{12} = V_{21}$.

Still looking at Eq.(3.11), it is also evident that finding its solution corresponds to solving an eigenvalue problem: $T_c(\mu)$ is determined when the *largest eigenvalue* of $\hat{\lambda} \hat{A}_{\text{clean}}$ equals one, i.e.

$$\prod_{i=1,2} \left[\left(\hat{A}_{\text{clean}}\right)_{ii} \det(\hat{\lambda}) - \lambda_{\bar{i}\bar{i}} \right] = \lambda_{12} \lambda_{21}, \quad (3.14)$$

as long as $\det(\hat{\lambda}) = \lambda_{11} \lambda_{22} - \lambda_{12} \lambda_{21} \neq 0$. Here $\hat{\lambda}$ is the coupling matrix, with matrix elements $(\hat{\lambda})_{ij} = \lambda_{ij}$. Besides, we define $\bar{i} = 1$ ($\bar{i} = 2$) for $i = 2$ ($i = 1$). Furthermore, Eq.(3.11) tells us that the behavior of $T_c(\mu)$, for a *clean two-band SC* is *independent of the sign of the interband pairing interaction*, since Eq.(3.14) depends on them only through $\lambda_{12} \lambda_{21}$.

The sign of λ_{12} sets the relative sign of the SC gaps, and, consequently, the symmetry of the superconducting state:

¹In this chapter, every time we write a Matsubara sum with unspecified limits $\left(\sum_n\right)$, we mean $n \in \mathbb{N}$ ranging from $-\infty$ to ∞ .

- For an attractive interband coupling ($\lambda_{12} > 0$), the eigenvector of $\hat{\lambda}\hat{A}_{\text{clean}}$ is such that Δ_1 and Δ_2 have the *same sign*. Such superconductor state is denominated s^{++} state.
- For a repulsive interband coupling ($\lambda_{12} < 0$), on the other hand, Δ_1 and Δ_2 acquire opposite signs, which corresponds to an *unconventional* s^{+-} superconducting state.

Another important detail is that the chemical potential that appears in Eq.(3.11) is also a function of the superconducting temperature $\mu(T_c)$ and, as shown in Ref.[50], in the proximity of a Lifshitz transition $\mu(T_c)$ does not coincide with the chemical potential at zero temperature. To solve this issue, we express T_c as function of the total number of electrons in the system, hereafter denote by N , which is determined by the normal components of the Green's function Eq.(3.6): recall that we can write

$$N = \sum_{\mathbf{k}, i, \sigma} \langle c_{i, \mathbf{k}\sigma}^\dagger c_{i, \mathbf{k}\sigma} \rangle = \sum_{i, \mathbf{k}} \left(1 - \langle c_{i, \mathbf{k}\uparrow} c_{i, \mathbf{k}\uparrow}^\dagger \rangle + \langle c_{i, -\mathbf{k}\downarrow}^\dagger c_{i, -\mathbf{k}\downarrow} \rangle \right), \quad (3.15)$$

and since $\langle c_{i, \mathbf{k}\sigma} c_{i, \mathbf{k}\sigma}^\dagger \rangle = -T \sum_n \mathcal{G}_{i,0}(\mathbf{k}, \omega_n)$, and $\langle c_{i, -\mathbf{k}\sigma}^\dagger c_{i, \mathbf{k}\sigma} \rangle = T \sum_n \mathcal{G}_{i,0}^*(\mathbf{k}, \omega_n)$, it follows that

$$N = 2 \sum_{\mathbf{k}} \left[1 - T_c \sum_{j,n} \frac{\xi_{j,\mathbf{k}}}{\omega_n^2 + \xi_{j,\mathbf{k}}^2} \right] = 2\pi \mathcal{A} \sum_{j=1}^2 \rho_{j,0} \left\langle \frac{1}{1 + e^{\xi/T_c}} \right\rangle_j, \quad (3.16)$$

where \mathcal{A} denotes the total area of the system².

The simultaneous numeric solution of Eqs.(3.14) and (3.16) yields $T_c(N)$ shown in Fig. 23(a), from which we can see that $T_c(N)$ is *enhanced* across the Lifshitz transition (which, in our notation, happens at $N = N_c$). That is because as we go across the LT, the system's density of states sharply increases due to the appearance of the new Fermi pocket. Therefore, more electronic states contributes to the superconducting condensate, which makes T_c go up. Moreover in agreement with Ref. [48], the larger is $|\lambda_{12}|$, the sharper is the enhancement of T_c .

As mentioned before, for the particular case of 2D bands we can solve Eq.(3.14) analytically. That is what we do in Sec. 3.1.1, which is specially important to set the stage for the calculations we perform in Sec. 3.2.1 and Sec. 3.2.2, where the analytic investigation provides valuable insights about the physics of dirty multiband superconductors. Furthermore, since the behavior of $T_c(N)$ is not dramatically different than the behavior of $T_c(\mu)$ in the vicinity of the Lifshitz transition, as shown in Fig. 23 (b), for simplicity we focus on an analytic expression for T_c as function of the chemical potential, rather than as function of the total number of electrons in the system.

²For the case of 3D bands, $\mathcal{A} \rightarrow \mathcal{V}$ is the total volume of the system - see Ref. [36].

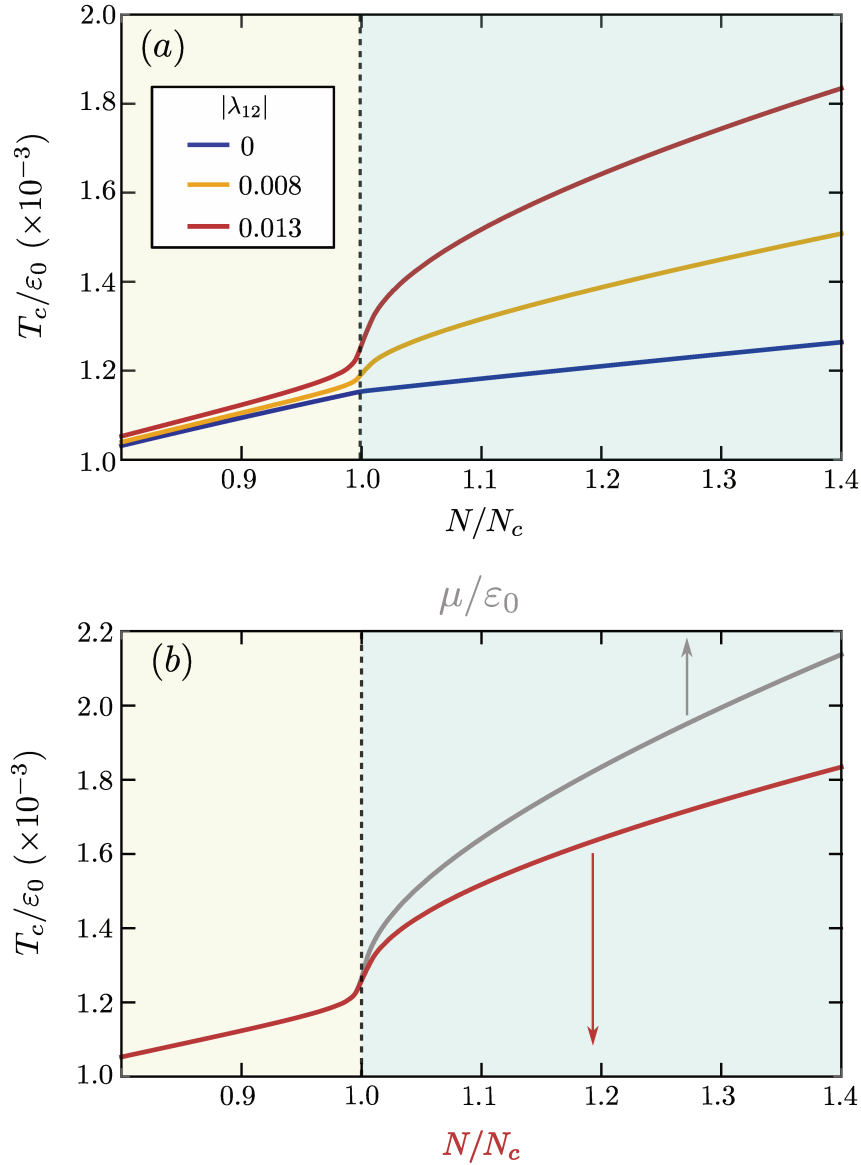


Figure 23 – **Phase diagram of the clean two-band superconductor with 2D bands.** Panel (a) shows T_c as function of the occupation number N for several values of the parameter λ_{12} . In panel (b), we compare T_c as a function of N with T_c as a function of the chemical potential $\mu(T_c)$ with $|\lambda_{12}| = 0.013$. In both panels, $\lambda_{11} = \lambda_{22} = 0.13$ and $\rho_{2,0} = \rho_{1,0}$. Note that T_c is normalized by the energy displacement between the bands ε_0 and N is normalized by the critical occupation number N_c at which the Lifshitz transition takes place.

3.1.1 Asymptotic solution of the gap equation

Let's return to Eq.(3.12). First, note that if we are in the high-density limit, in which the Fermi energy is much larger than Ω_0 ($\mu \gg \Omega_0$) then

$$\int_{W_i}^{\Omega_0} d\xi \rho_i(\xi) \frac{1}{2\xi} \tanh\left(\frac{\xi}{2T_c}\right) = \rho_{i,F} \int_0^{\Omega_0/T_c} dy \frac{1}{y} \tanh\left(\frac{y}{2}\right) = \rho_{i,F} \ln\left(\frac{\kappa\Omega_0}{T_c}\right) \quad (3.17)$$

and we recover the usual BCS solution:

$$\left(\hat{A}_{\text{clean}}\right)_{ij} = \delta_{ij} \left(\frac{\rho_{i,F}}{\rho_{i,0}}\right) \ln \left(\frac{\kappa\Omega_0}{T_c}\right). \quad (3.18)$$

Here, $\kappa = 2e^\gamma/\pi \approx 1.13$, with γ denoting Euler's constant, and $\rho_{i,F}$ is the density of states of band i at the Fermi level.

In the-low density regime, on the other hand, in order to capture the behavior of $T_c(\mu)$ across the Lifshitz transition, we calculate the energy integral in Eq.(3.12) *before* the Matsubara sum, obtaining

$$\left(\hat{A}_{\text{clean}}\right)_{ii} = T_c \sum_n \frac{1}{\omega_n} \left[\arctan \left(\frac{\Omega_0}{\omega_n}\right) - \arctan \left(\frac{W_i}{\omega_n}\right) \right]. \quad (3.19)$$

Regarding the Matsubara sums in Eq.(3.19), there are two asymptotic regimes, for each band, where we can calculate them analytically: $|W_i| \ll T_c$ and $|W_i| \gg T_c$, but still $|W_i| \ll \Omega_0$. It defines four different regions in the system's phase diagram, as illustrated in Fig. 24, at which we can find analytic expressions for (3.19):

- In region I, we have $-W_1 < T_c$ and $W_2 > T_c$, which corresponds to μ ranging from zero to a critical μ_1^* , such that $\mu_1^* \sim T_c(\mu_1^*)$.
- In region II, we have $-W_1 > T_c$ and $W_2 > T_c$, which corresponds to $\mu_1^* < \mu < \mu_2^*$. Here $\mu_2^* \sim \varepsilon_0 - T_c(\mu_2^*)$.

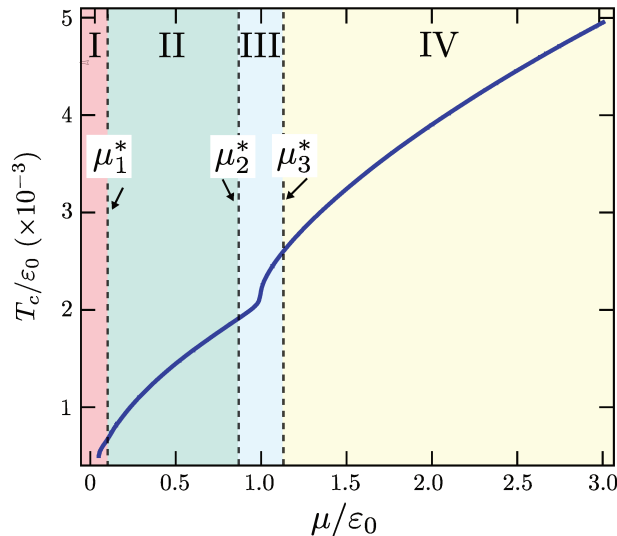


Figure 24 – **Regions of the phase diagram for the asymptotic studies.** Illustration of the regions of the (μ, T) phase diagram of a two-band superconductor for the calculation of the asymptotic behavior of $T_c(\mu)$ in the clean and dirty regimes. The size of the regions are exaggerated for schematic purposes. The precise definition of each region is given in the main text.

- In region III, we have $-W_1 > T_c$ and $|W_2| < T_c$. This region corresponds to $\mu_2^* < \mu < \mu_3^*$, with $\mu_3^* \sim \varepsilon_0 + T_c(\mu_3^*)$.
- In region IV, we have $-W_1 > T_c$ and $-W_2 > T_c$. This region corresponds to $\mu > \mu_3^*$.

As we show in Appendix E, by expanding the summand of Eq.(3.19) in Taylor series in

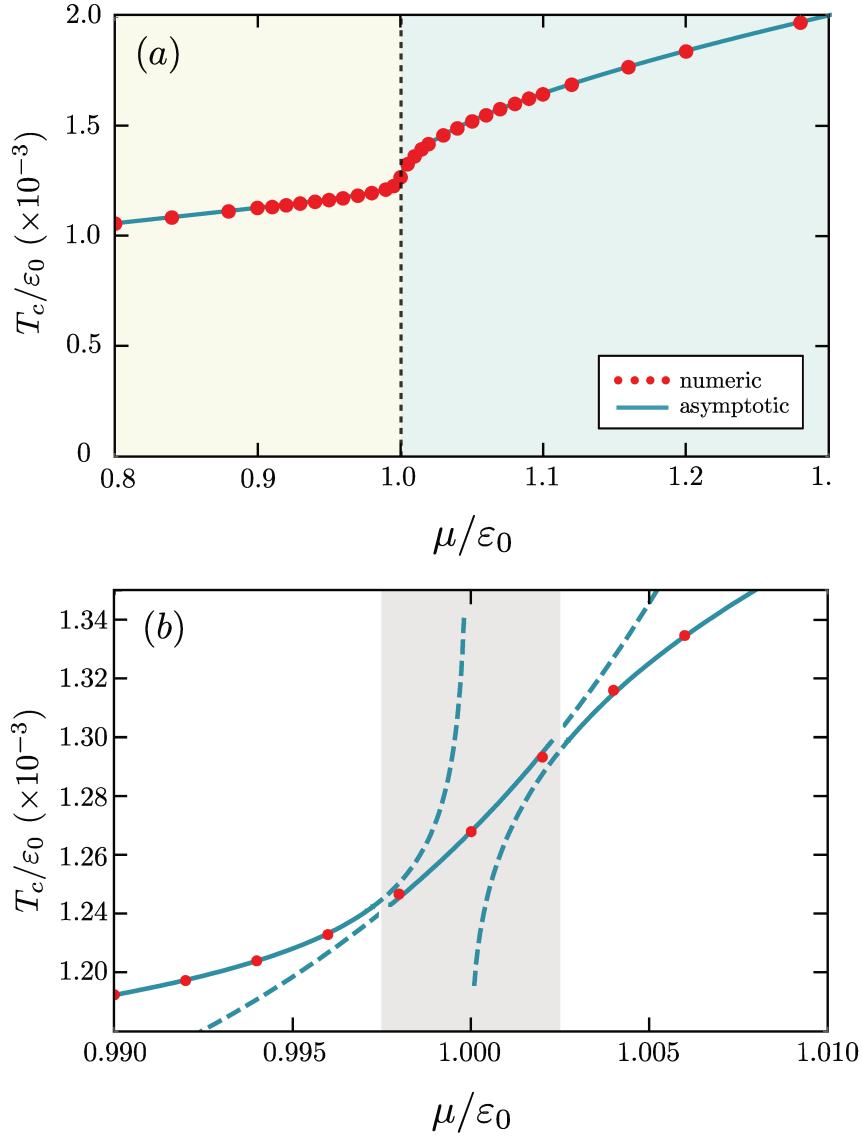


Figure 25 – Comparison between the numerical (symbols) and asymptotic analytical results (solid curve) for T_c , as function of the chemical potential μ , for the 2D clean system across the Lifshitz transition at $\mu = \varepsilon_0$. Panel (b) is a zoom of panel (a) that highlights the very narrow range of μ for which the asymptotic solutions start to fail (gray dashed area). The parameters used here are the same as in Fig. 23(b).

each region of Fig. 24, we obtain

$$\left(\hat{A}_{\text{clean}}\right)_{11} \sim \frac{1}{2} \begin{cases} \ln\left(\frac{\kappa\Omega_0}{T_c}\right) + \frac{\mu}{2T_c}, & \text{region I} \\ \ln\left(\frac{\kappa^2\Omega_0\mu}{T_c^2}\right), & \text{otherwise} \end{cases}, \quad (3.20)$$

and

$$\left(\hat{A}_{\text{clean}}\right)_{22} \sim \frac{1}{2} \begin{cases} \ln\left(\frac{\Omega_0}{\varepsilon_0 - \mu}\right), & \text{regions I and II} \\ \ln\left(\frac{\kappa\Omega_0}{T_c}\right) + \frac{(\mu - \varepsilon_0)}{2T_c}, & \text{region III} \\ \ln\left(\frac{\kappa^2\Omega_0(\mu - \varepsilon_0)}{T_c^2}\right), & \text{region IV} \end{cases}. \quad (3.21)$$

Now that we have an analytic expression for $\left(\hat{A}_{\text{clean}}\right)_{ij}$, solving Eq.(3.14) simplifies to finding a solution of a transcendental equation, which results in an asymptotic $T_c(\mu)$ in each of the four regions of Fig. 24. Note that it is in contrast with the full numerical solution, which involves the numerical calculation of either the Matsubara sum or the energy integral in Eq.(3.12).

Fig. 25(a) shows a comparison between the analytic and the numeric solutions of the coupled gap equations. We can see that our asymptotic analysis captures the behavior of $T_c(\mu)$ across the Lifshitz transition with great accuracy. A zoom-in in the vicinity of the Lifshitz transition shown in Fig. 25(b) reveals that the asymptotic $T_c(\mu)$ is not continuous across the boundaries of the different regions of Fig. 24, which has to do with the own nature of the asymptotic method. Furthermore, as highlighted in the same figure, some of the asymptotic solutions show diverging behavior near the boundaries. However, the ranges of μ for which the asymptotic solutions do not behave well are very small - too small to be shown in the scale of panel (a), and are thus omitted in that plot.

3.2 Dirty Multiband Superconductors

Resistivity measurements elucidate the importance of disorder in both STO and LAO/STO interfaces. The low-temperature electric resistivity, when extrapolated to zero-temperature, results in a constant called *residual resistivity* (ρ_0). From the residual resistivity, together with the electron density (n) obtained from Hall resistivity measurements, we can *estimate* the impurity scattering rate (i.e. the average number of electron-impurity collisions per unit time) using the Drude formula:

$$\tau^{-1} = \frac{\rho_0 n e^2}{m_e}. \quad (3.22)$$

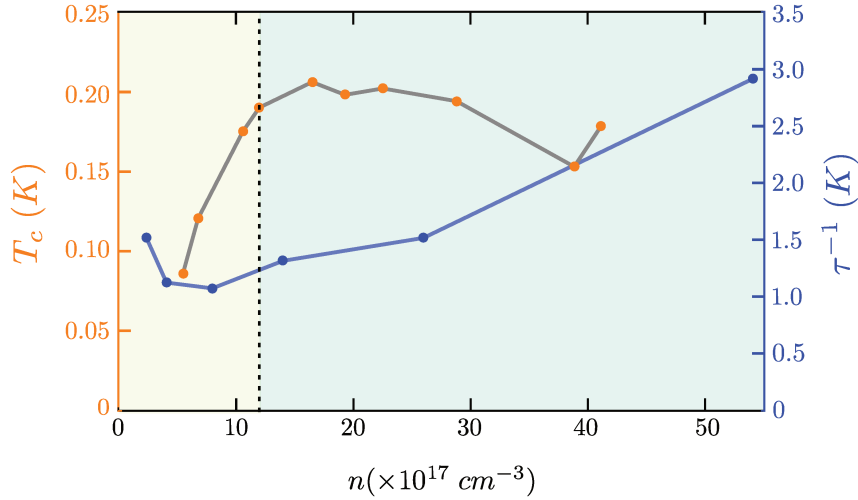


Figure 26 – **Impurity scattering rate across the Lifshitz transition.** We show the impurity scattering rate (τ^{-1}) as a function of the electronic density (n) for STO in the low-density regime (blue points). It was estimated from residual resistivity data taken from Ref. [34]. For comparison purpose, in the same panel we show the experimental $T_c(n)$ for STO (orange points) according to Ref. [31]. The units system was chosen such that both T_c and τ^{-1} are expressed in Kelvin.

Here e is the electron charge and m_e is its rest mass. Figure 26 shows τ^{-1} , as a function of n , for STO in the low-density region of its phase diagram, where we plugged into Eq.(3.22) ρ_0 and n reported in Ref. [34]. Note that the units were chosen such that both T_c and τ^{-1} could be expressed in Kelvin³.

For comparison purposes, also in Fig. 26 we show the experimental T_c as a function of n for bulk STO from Ref. [31]. There are two important features to be observed in this figure: in the first place, note that the scattering rate is much larger than T_c , roughly $\tau^{-1} \sim 10T_c$ for the density range considered. It tells us that disorder plays an important role in the system and, therefore, cannot be neglected.

Secondly, although τ^{-1} shows a strong density dependence in the two-band regime of the phase diagram (green region in Fig. 26), it does not vary much in the vicinity of the Lifshitz transition, which is emphasized by the dashed vertical black line in Fig. 26. Therefore, since we are mostly interested in the physics of a multiband superconductor in the vicinity of a Lifshitz transition, we approximate the impurity scattering rate by a constant in this chapter. We also emphasize that a similar calculation of $\tau^{-1}(n)$ can be done for LAO/STO interfaces [51], yielding the same qualitative behavior of Fig. 26.

Once experimental data evidences the importance of disorder in two important examples of multiband superconductor, we ask ourselves the following generic questions:

³ τ^{-1} has dimensions of the inverse of time, which corresponds to Electron-Volt in the Natural Units system. Besides, Electron-Volt and Kelvin are related by the Boltzmann constant.

how does the behavior of $T_c(N)$ - and also that of $T_c(\mu)$ - change if we include **non-magnetic** disorder in the system? Does it change at all? At first glance, we could think that the answer is no, since there is a theorem named after the physicist Philip Anderson [52], which tells us that a superconductor with an isotropic gap is insensitive to non-magnetic disorder - see also Ref. [49]. However, multiband superconductors exhibit novel physical phenomena in comparison to their single-band counterparts, and their response to disorder is no exception.

As we will see in Sec. 3.2.1, in a two-band superconductor Anderson's theorem only applies when the SC gap in both bands are equal $\Delta_1 = \Delta_2$, which only occurs in the high-density limit and for specific choices of the coupling constants and density of states. Interestingly, it was shown [53, 61] that there is a similarity between multiband superconductors, with different superconducting gaps in each of the bands, and a *anisotropic single-band superconductor*, where the Anderson theorem loses its validity: the larger is the difference between Δ_1 and Δ_2 , the larger is the impact of disorder in T_c .

Here we show that the suppression of T_c is much stronger if we have a repulsive interband interaction. It shows us that studying the effects of disorder in a given superconductor is an powerful tool to investigate the nature of the superconducting state: if the phase diagram is sensitive to non-magnetic disorder, odds are that the superconductor belongs to the family of unconventional superconductors.

We include disorder in our model by adding to Eq.(3.1) the following impurity Hamiltonian

$$H_{\text{imp}} = \sum_{\mathbf{k}, \mathbf{k}', \sigma} \sum_{\alpha, \beta} W_{\alpha\beta}(\mathbf{k} - \mathbf{k}') c_{\alpha, \mathbf{k}\sigma}^\dagger c_{\beta, \mathbf{k}'\sigma} , \quad (3.23)$$

where $W_{\alpha\beta}(\mathbf{q})$ denotes the impurity potential, which works as an external potential for the electrons. Since we are in the vicinity of the bottom of the bands, and, consequently, we have a small Fermi surface, we can focus on small-momentum impurity scattering. Hereafter, we denote by $v \equiv W_{11}(0) = W_{22}(0)$ the *intradband impurity potential*, which scatters electrons within the same band, and by $u \equiv W_{12}(0) = W_{21}(0)$ the *interband impurity potential*, which scatters electrons between the bands. Note that, for simplicity we choose equal interband scattering potentials and equal intraband scattering potentials. However, we emphasize that the qualitative behavior of $T_c(\mu)$ we describe below *does not depend* on this assumption.

The impurity potential also depends on the set of positions of each impurity, here denoted by $\{\mathbf{R}\} \equiv \{\mathbf{R}_1, \mathbf{R}_2, \dots, \mathbf{R}_{N_{\text{imp}}}\}$, where $N_{\text{imp}} \gg 1$ the total number of impurities, and since we are dealing with random disorder, \mathbf{R}_j are random variables. Therefore, the impurities define a configuration-dependent external potential for the electrons, which *breaks the translational symmetry of the system*. As a consequence, the impurity self-energy not only depends parametrically on $\{\mathbf{R}\}$ but also is a function of two momentum variables:

$\hat{\Sigma}(\mathbf{k}, \mathbf{k}', \omega_n; \{\mathbf{R}\})$. The same is true for the system's total Green's function, which obeys the Dyson's equation

$$\hat{\mathcal{G}}^{-1}(\mathbf{k}, \mathbf{k}', \omega_n; \{\mathbf{R}\}) = \hat{\mathcal{G}}_0^{-1}(\mathbf{k}, \omega_n) - \hat{\Sigma}(\mathbf{k}, \mathbf{k}', \omega_n; \{\mathbf{R}\}) . \quad (3.24)$$

However, since we want to calculate T_c , which is a thermodynamical property of the system, instead of studying the local effects of disorder, we can take an average of $W_{\alpha\beta}$, $\hat{\Sigma}$ and $\hat{\mathcal{G}}$ over all possible impurity configurations, which have equal probabilities since, as we said before, the impurities are randomly distributed in the system. This is a well known procedure called *self-averaging* and it restores the translational symmetry of the system [57, 23].

The self-averaged self-energy is

$$\hat{\Sigma}(\mathbf{k}, \omega_n) \equiv \left\langle \hat{\Sigma}(\mathbf{k}, \mathbf{k}', \omega_n; \{\mathbf{R}\}) \right\rangle_{imp} = \int \prod_{j=1}^{N_{imp}} \frac{d\mathbf{R}_j}{\mathcal{A}} \hat{\Sigma}(\mathbf{k}, \mathbf{k}', \omega_n; \mathbf{R}_1, \dots, \mathbf{R}_{N_{imp}}) , \quad (3.25)$$

where \mathcal{A} is the total area of the system. A similar expression holds for the self-averaged Green's function, and the Dyson equation simplifies

$$\hat{\mathcal{G}}^{-1}(\mathbf{k}, \omega_n) = \hat{\mathcal{G}}_0^{-1}(\mathbf{k}, \omega_n) - \hat{\Sigma}(\mathbf{k}, \omega_n) , \quad (3.26)$$

as usual in translational invariant systems. Hereafter, every time we write $\hat{\mathcal{G}}$, $\hat{\Sigma}$ and $W_{\alpha\beta}$, we mean the correspondent self-averaged quantities.

The self-averaged self-energy is represented diagrammatically in Fig. 27(a). Among the diagrams, those that, like the first, contain only one dashed line emerging from an impurity circle, can be renormalized away by introducing a constant in the Hamiltonian and hence they can be neglected. Furthermore, the diagrams with more than two dashed lines per impurity circle represent processes of multiple scattering per impurity and we also neglect them, since we are dealing with weak impurities.

The dominant diagrams are then those with two dashed lines per impurity circle. Among them, those that contains crossing lines, like the fifth diagram of Fig.27(a), are subleading and also neglected. This is called *non-crossing approximation* [23]. As a result, only the family of diagrams shown in Fig. 27(b) contributes to the impurity self-energy, which becomes

$$\hat{\Sigma}(\mathbf{k}, \omega_n) = n_{imp} \int \frac{d^d k'}{(2\pi)^d} \hat{W}_{\mathbf{k}'-\mathbf{k}} \hat{\mathcal{G}}(\mathbf{k}', \omega_n) \hat{W}_{\mathbf{k}-\mathbf{k}'} , \quad (3.27)$$

with

$$\hat{W}_{\mathbf{k}, \mathbf{k}'} = \begin{pmatrix} v & 0 & u & 0 \\ 0 & -v & 0 & -u \\ u & 0 & v & 0 \\ 0 & -u & 0 & -v \end{pmatrix} . \quad (3.28)$$

Note that Fig.27(b) contains a sum over infinite diagrams. Therefore, the self-energy depends on the total Green's functions, and the Dyson's equation Eq.(3.26), which is represented diagrammatically in Fig. 27(c), needs to be solved self-consistently. This is the reason why the method just described is called *self-consistent Born approximation*.

To proceed, we parametrize $\hat{\mathcal{G}}$ by the same matrix structure than $\hat{\mathcal{G}}_0$ in Eq. (3.6), but replacing ω_n , $\xi_{i,\mathbf{k}}$ and Δ_i by renormalized Matsubara frequencies $\tilde{\omega}_{n,j}$, energy dispersion $\tilde{\xi}_{j,\mathbf{k}} \equiv \xi_{j,\mathbf{k}} + h_{n,j}$ and superconducting gaps $\tilde{\Delta}_j$. Substituting such \mathcal{G} into Eq.(3.27) and plugging the resulting expression into Eq. (3.26), we find a set of self-consistent equations

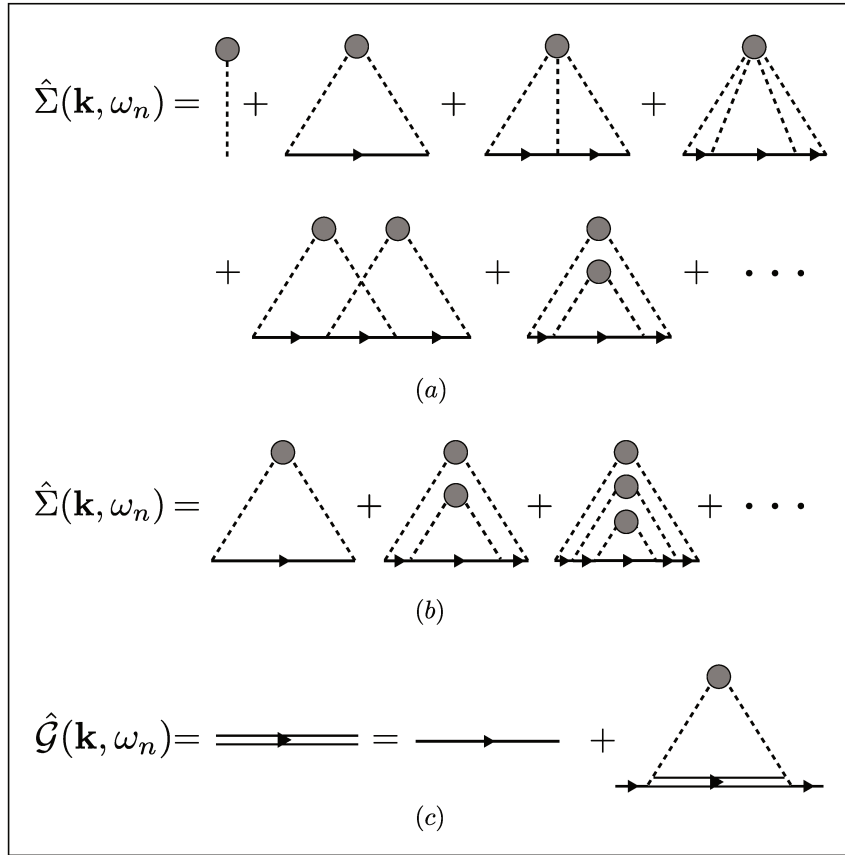


Figure 27 – **Diagrammatic expansion of the self-averaged self-energy and Green's function.** In panel (a) some of the diagrams that contribute to the self-energy summation are shown. In panel (b) we show the diagrammatic expansion for the self-energy in the self-consistent Born approximation and in (c) the Dyson equation for the total Green's function is shown according to the self-consistent Born approximation. The solid single lines represent the bare Green's function \mathcal{G}_0 , while the dashed lines refer to the impurity potential in Nambu space $\hat{W}_{\mathbf{k}-\mathbf{k}'}$ and the gray circle represent the impurity concentration $n_{imp} = N_{imp}/\mathcal{A}$.

for the aforementioned renormalized quantities:

$$\tilde{\omega}_{n,i} = \omega_n + \sum_j \frac{\tau_{ij}^{-1} \tilde{\omega}_{n,j}}{2} \left\langle \frac{1}{\tilde{\omega}_{n,j}^2 + (\xi + h_{n,j})^2 + \tilde{\Delta}_j^2} \right\rangle_j^\Lambda, \quad (3.29)$$

$$\tilde{\Delta}_i = \Delta_i + \sum_j \frac{\tau_{ij}^{-1} \tilde{\Delta}_j}{2} \left\langle \frac{1}{\tilde{\omega}_{n,j}^2 + (\xi + h_{n,j})^2 + \tilde{\Delta}_j^2} \right\rangle_j^\Lambda, \quad (3.30)$$

$$h_{n,i} = - \sum_j \frac{\tau_{ij}^{-1}}{2} \left\langle \frac{\xi + h_{n,j}}{\tilde{\omega}_{n,j}^2 + (\xi + h_{n,j})^2 + \tilde{\Delta}_j^2} \right\rangle_j^\Lambda. \quad (3.31)$$

Here, Λ is the band width, which we consider to be the same for both bands and, hereafter, equal to the pairing interaction cutoff ($\Lambda = \Omega_0$). Besides, τ_{ij}^{-1} denotes the impurity scattering rates, which we define as

$$\tau_{ij}^{-1} = 2\pi n_{\text{imp}} \rho_{j,0} (|v|^2 \delta_{i,j} + |u|^2 \delta_{\bar{i},j}). \quad (3.32)$$

Once again we use the notation $\bar{i} = 1(2)$ if $i = 2(1)$. Note that τ_{11} and τ_{22} (τ_{12} and τ_{21}) define the *intra*band (*inter*band) impurity scattering rates.

At T_c we can linearize Eqs.(3.29)-(3.31), similarly as we did with the gap equations in Sec. 3.1. In this case, we can readily see that Eq.(3.30) decouples from Eqs. (3.29) and (3.31). The former, written in a matrix form, becomes

$$\begin{pmatrix} \tilde{\Delta}_1 \\ \tilde{\Delta}_2 \end{pmatrix} = \begin{pmatrix} \Delta_1 \\ \Delta_2 \end{pmatrix} + \frac{1}{2} \begin{pmatrix} \tau_{11}^{-1} B_1^{(n)} & \tau_{12}^{-1} B_2^{(n)} \\ \tau_{21}^{-1} B_1^{(n)} & \tau_{22}^{-1} B_2^{(n)} \end{pmatrix} \begin{pmatrix} \tilde{\Delta}_1 \\ \tilde{\Delta}_2 \end{pmatrix}, \quad (3.33)$$

where we define

$$B_i^{(n)} \equiv \left\langle \frac{1}{\tilde{\omega}_{n,i}^2 + (\xi + h_{n,i})^2} \right\rangle_i^{\Omega_0}. \quad (3.34)$$

Besides, performing a simple two-by-two matrix inversion, we can rewrite Eq.(3.33) as

$$\begin{pmatrix} \tilde{\Delta}_1 \\ \tilde{\Delta}_2 \end{pmatrix} = \frac{1}{D_n} \hat{M}_n \begin{pmatrix} \Delta_1 \\ \Delta_2 \end{pmatrix}, \quad (3.35)$$

where the matrix elements of \hat{M}_n are given by

$$\left(\hat{M}_n \right)_{ij} = \left(1 - \frac{\tau_{\bar{i}\bar{i}}^{-1}}{2} \left\langle \frac{1}{\tilde{\omega}_{n,\bar{i}}^2 + (\xi + h_{n,\bar{i}})^2} \right\rangle_{\bar{i}}^\Lambda \right) \delta_{i,j} + \frac{\tau_{ij}^{-1}}{2} \left\langle \frac{1}{\tilde{\omega}_{n,j}^2 + (\xi + h_{n,j})^2} \right\rangle_j^\Lambda \delta_{\bar{i},j}, \quad (3.36)$$

while

$$D_n = 1 - \sum_i \frac{\tau_{\bar{i}\bar{i}}^{-1}}{2} \left\langle \frac{1}{\tilde{\omega}_{n,\bar{i}}^2 + (\xi + h_{n,\bar{i}})^2} \right\rangle_{\bar{i}}^\Lambda + \frac{\det(\hat{\tau}^{-1})}{4} \prod_i \left\langle \frac{1}{\tilde{\omega}_{n,i}^2 + (\xi + h_{n,i})^2} \right\rangle_i^\Lambda. \quad (3.37)$$

denotes its determinant. Here, to shorten the notation we define the scattering rate matrix $(\hat{\tau}^{-1})_{ij} \equiv \tau_{ij}^{-1}$.

Note that Eq. (3.35) is not the self-consistency equation for the superconducting gaps yet! Similarly as we did in Sec. 3.1, using the anomalous part of the total Green's function to calculate the expected values that appear in Eq.(3.3), we obtain

$$\begin{pmatrix} \Delta_1 \\ \Delta_2 \end{pmatrix} = \begin{pmatrix} \lambda_{11} & \lambda_{12} \\ \lambda_{21} & \lambda_{22} \end{pmatrix} \begin{pmatrix} B_1^{(n)} & 0 \\ 0 & B_2^{(n)} \end{pmatrix} \begin{pmatrix} \tilde{\Delta}_1 \\ \tilde{\Delta}_2 \end{pmatrix}. \quad (3.38)$$

The self-consistent gap equations for a dirty two-band superconductor are determined when we combine Eqs.(3.35) and (3.38), which gives us an eigenvalue problem with same form as Eq.(3.11), but with the matrix \hat{A}_{clean} replaced by \hat{A}_{dirty} , which has more complex matrices elements:

$$\left(\hat{A}_{\text{dirty}}\right)_{ij} = \pi T_c \sum_n \frac{B_i^{(n)}}{D_n} \left(\delta_{ij} + C_{ij}^{(n)}\right), \quad (3.39)$$

with $B_i^{(n)}$ defined in Eq.(3.34), and

$$C_{ij}^{(n)} = -\delta_{i,j} \frac{\tau_{ii}^{-1}}{2} \left\langle \frac{1}{\tilde{\omega}_{n,i}^2 + (\xi + h_{n,i})^2} \right\rangle_{\bar{i}}^{\Lambda} + \delta_{\bar{i},j} \frac{\tau_{ij}^{-1}}{2} \left\langle \frac{1}{\tilde{\omega}_{n,j}^2 + (\xi + h_{n,j})^2} \right\rangle_j^{\Lambda}. \quad (3.40)$$

In contrast to \hat{A}_{clean} , \hat{A}_{dirty} is a non-diagonal matrix. Moreover, it carries information about either the bottom of the bands, through its dependence of W_i , and about disorder, though its dependence on the scattering rates τ_{ij}^{-1} .

Furthermore, the equation that gives the total number of electrons in the systems also changes in order to incorporate the effects of disorder. Through the same procedure we described in Sec. 3.1 to derive Eq.(3.16), here we obtain

$$N = 2 \sum_{\mathbf{k}} \left[1 - T_c \sum_{j,n} \frac{(\xi_{j,\mathbf{k}} + h_{n,j})}{\tilde{\omega}_{n,j}^2 + (\xi_{j,\mathbf{k}} + h_{n,j})^2} \right]. \quad (3.41)$$

Therefore, in the case of dirty multiband superconductors, we need to simultaneously solve Eq.(3.11) with $\hat{A}_{\text{clean}} \rightarrow \hat{A}_{\text{dirty}}$, and Eqs.(3.29) (3.31), Eq.(3.41) to calculate T_c as function of N . Similarly to Sec. 3.1, we can achieve this goal numerically or analytically, through an asymptotic study. Below we show and compare the results in both cases.

Let's start by the full numerical solution. Fig. 28 shows the phase diagram ($T_c(N)$) for a two-band superconductor with (a) repulsive interband coupling ($\lambda_{12} < 0$) and (b) attractive interband coupling ($\lambda_{12} > 0$). The different color lines refers to different values of the impurity scattering rates, as indicated in the label of panel (b). For simplicity, in these figures we choose the same value for the interband and intraband scattering rates $\tau_{ii}^{-1} = \tau_{12}^{-1} = \tau_{21}^{-1}$ (*point-like impurities*), as well as a dominant intraband pairing

interaction $\lambda_{11} = \lambda_{22} = 0.13$ and subleading interband pairing interaction. However, the results are qualitatively the same for other values of τ_{ij}^{-1} , as long as the interband scattering rate remains finite and $|\lambda_{12}| \ll \lambda_{1,1}, \lambda_{2,2}$.

We can clearly see that non-magnetic impurities reduces T_c (specially in the vicinity of the Lifshitz transition) in both the attractive and repulsive interband coupling cases. Moreover, the larger is τ^{-1} , the sharper is the suppression of superconductivity across the Lifshitz transition.

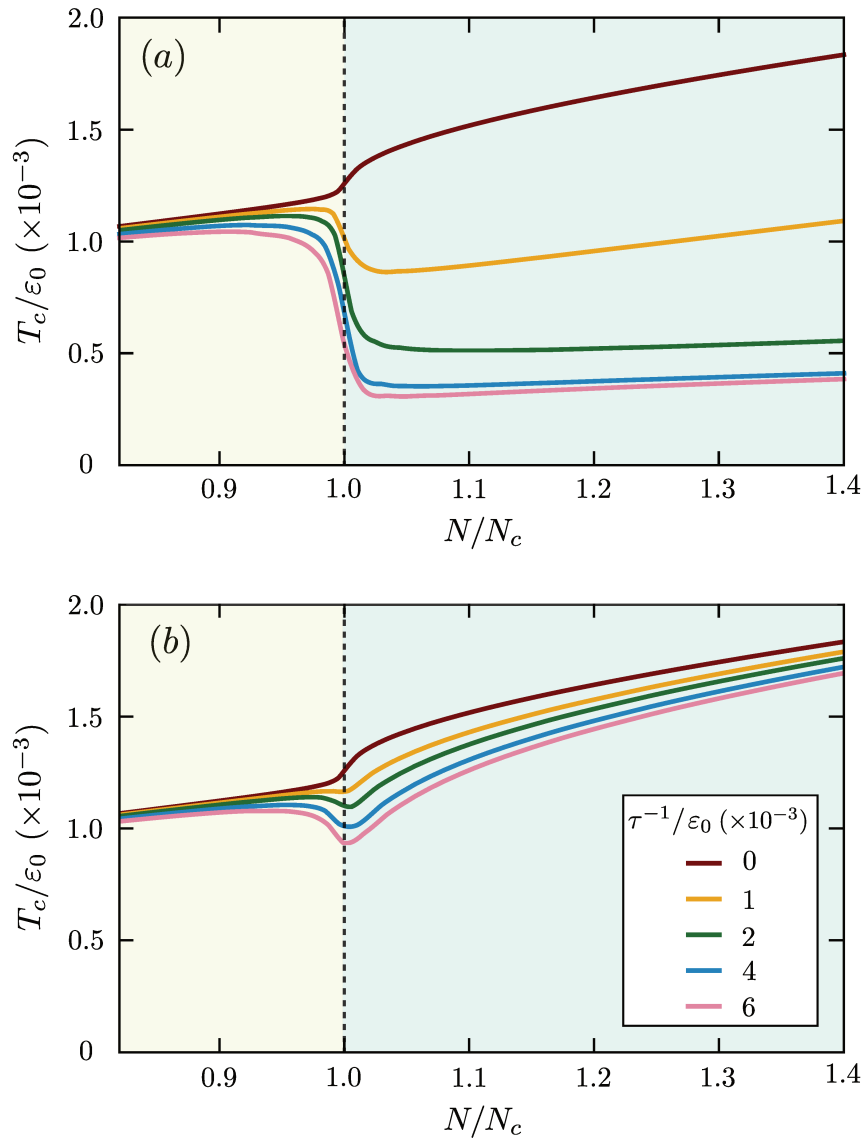


Figure 28 – **Superconducting transition temperature T_c as function of the occupation number N for 2D bands.** A Lifshitz transition takes place at N_c . Different point-like impurity scattering rates τ^{-1} are shown for an interband pairing interaction λ_{12} that is either (a) repulsive or (b) attractive. In these figures we used dominant attractive intraband pairing $\lambda_{11} = \lambda_{22} = 0.13$ and subleading interband pairing interaction $|\lambda_{12}| = 0.013$. We also set $\rho_{1,0} = \rho_{2,0}$ and $\Omega_0/\epsilon_0 = 5$.

Comparing panels (a) and (b) in Fig. 28, we conclude that the effect of disorder is stronger when the *interband pairing interaction* is repulsive. It can be rationalized in terms of Anderson's theorem: the differences between Δ_1 and Δ_2 are larger when $\lambda_{12} < 0$, and, as in an anisotropic single-band superconductor, the effects of non-magnetic disorder are more significant. Conversely, if $\Delta_1 = \Delta_2$, which happens in the high-density limit if the interband pairing interaction is attractive, Anderson's theorem is recovered and $T_c(N)$ no longer changes if we increase or reduce disorder. That's why we see the curves of Fig. 28(b) collapsing into the same line as N increases.

If we perform the full numerical calculations with $\tau_{12}^{-1} = \tau_{21}^{-1} = 0$, we find, independently of the values we choose for intraband scattering rates, the same qualitative behavior of Fig. 23(a). In other words, we verified that the effect of intraband scattering on $T_c(N)$ is minor, which is, once again, a consequence of Anderson's theorem. The interband scattering processes, on the other hand, are the responsible for breaking the Cooper pairs and, consequently, suppress superconductivity. Our results show that what happens in a dirty multiband superconductor is a competition between two opposite effects in the vicinity of the Lifshitz transition: on the one hand, T_c tends to increase as the second band becomes populated as a consequence of the enhancement of the system's density of states. On the other hand, when the second band appears, impurities can scatter electron from band 1 to band 2 and vice-versa, which breaks the Cooper pairs and therefore is detrimental to superconductivity. When disorder are strong enough, the second effect wins and T_c gets reduce.

Importantly, as explained in Ref. [35], we also did the full numerical calculations for 3D bands, where the same qualitative behavior of Fig. 28 was found, with the difference that the suppression of T_c is smoother for 3D bands as a consequence of a vanishing density of states in the bottom of the bands. Moreover, our theoretical phase diagrams (for both 2D and 3D) for a repulsive interband pairing exhibit a great qualitative agreement with the experimental phase diagrams of STO [31] and LAO/STO interfaces [33] - compare Fig. 2 with Fig. 28. It suggests an *unconventional nature for superconductivity in these two materials*, a topic highly debated in the literature.

Looking at the eigenvectors⁴ $\hat{\Delta}$ of the coupled gap equation $\hat{\Delta} = \hat{\lambda} \hat{A}_{\text{dirty}} \hat{\Delta}$, we find another important result. In Sec. 3.1 we explained that the sign of the interband pairing interaction λ_{12} and λ_{21} sets the relative sign of the superconducting gaps in each of the bands. Recall that, there, an attractive inter-band pairing leads to a s^{++} superconducting state, where Δ_1 and Δ_2 have the same sign, while a repulsive interband interaction leads to an unconventional s^{+-} state, characterized by opposite sign gaps. When disorder comes in play, this scenario changes a bit: while in the attractive interband pairing situation the state is always s^{++} , a crossover $s^{+-} \rightarrow s^{++}$ can happen when the interband pairing

⁴We denote by $\hat{\Delta}$ the vector such that $(\hat{\Delta})_i = \Delta_i$, with $i = 1, 2$.

interaction is repulsive.

Such a crossover is shown in Fig. 29, where we plot $2\arctan(\Delta_1/\Delta_2)/\pi \pmod{\pi}$ to deal with the freedom in choosing the global sign of $\hat{\Delta}$ as function of N/N_c (recalling that N_c is the critical number of electrons at which the Lifshitz transition takes place). When $\text{sign}(\Delta_1) = \text{sign}(\Delta_2)$, $\arctan(\Delta_1/\Delta_2) < \pi/2$, which corresponds to the blue region in Fig. 29. Conversely, when $\text{sign}(\Delta_1) = -\text{sign}(\Delta_2)$, $\arctan(\Delta_1/\Delta_2) > \pi/2$, and we are in the red region of the same figure. We can see that for weak disorder we never leave the red region as N increases, meaning that the symmetry of the remains s^{+-} with the evolution of N . For strong disorder, on the other hand, we go from the red to the blue region as N increases after the Lifshitz transition, signaling the crossover $s^{+-} \rightarrow s^{++}$ as function of N .

A crossover from a superconducting s^{+-} state to a s^{++} state was previously observed [55], but as a function of the impurity strength rather than as a function of the electron density with a fixed disorder strength, as is our case. Interestingly, such crossover can leave signatures in the system's spectroscopic and thermodynamic properties. For electronic densities close to that where the crossover takes place, the gap in the incipient band (Δ_2) is very small and, as a consequence, it could be not identified by some probes. As a result, a signal consistent with single-band superconductivity would be measured. As a matter of fact, recent optical conductivity data for doped STO showed a signature of single-band superconductivity in a doping region where it is known that more than one conduction band crosses the Fermi level [58].

As we mentioned before, the detrimental effects of interband scattering to

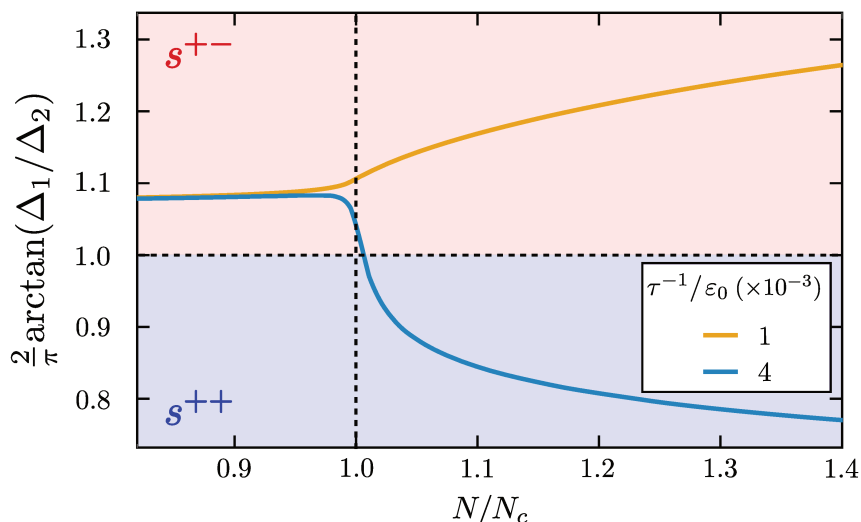


Figure 29 – **Ratio between the two isotropic SC gaps in bands 1 and 2 (Δ_1 and Δ_2 , respectively) across the Lifshitz transition at $N = N_c$.** This plot refers to the 2D bands case shown in Fig. 28. For sufficiently large impurity scattering rate, the relative sign of the two SC gaps change for $N > N_c$, signaling a crossover from an s^{+-} SC state to an s^{++} one.

superconductivity are stronger in two-band superconductors with a dominant attractive intraband pairing and subleading repulsive interband superconducting pairing. In the next subsections we see how this result appears in an asymptotic study of the coupled gap equations $\hat{\Delta} = \hat{\lambda}\hat{A}_{\text{dirty}}\hat{\Delta}$ and the self-consistent Eqs.(3.29) and (3.31). Note that to avoid cumbersome notations, hereafter we denote by $T_c(\hat{\tau}^{-1} = 0) \equiv T_{c,0}$ the superconducting transition temperature in the absence of disorder. Besides, $\hat{A}_{\text{dirty}} \equiv \hat{A}_d$, and $\hat{A}_{\text{clean}} = \hat{A}_c$

3.2.1 Asymptotic solution in the high-density limit

In the remaining part of this chapter, let's look for analytic expressions for the matrix elements of \hat{A}_d . Besides, since the general function for $T_c(\hat{\tau}^{-1})$ has no analytic form, hereafter we focus on the behavior for weak disorder and compute $\partial T_c / \partial \tau_{ij}^{-1}$.

A very convenient way of calculating $\partial T_c / \partial \tau_{ij}^{-1}$ is making use of the Feynman-Hellmann theorem - see for instance Refs. [59, 60]. Denoting by $\alpha(T)$ the largest eigenvalue of $(\hat{\lambda}\hat{A}_d)$ for a given temperature T and by $\alpha_0(T)$ the largest eigenvalue of $(\hat{\lambda}\hat{A}_c)$, with correspondent left and right eigenvectors $\langle \alpha_L^{(0)} |$ and $| \alpha_R^{(0)} \rangle$, respectively, the Feynman-Hellmann theorem tells us that that

$$\left. \frac{\partial \alpha}{\partial \tau_{ij}^{-1}} \right|_{\tau_{ij}^{-1}=0} = \frac{\langle \alpha_L^{(0)} | \frac{\partial(\hat{\lambda}\hat{A}_d)}{\partial \tau_{ij}^{-1}} | \alpha_R^{(0)} \rangle}{\langle \alpha_L^{(0)} | \alpha_R^{(0)} \rangle}. \quad (3.42)$$

It is important to emphasize that here we need both the left and right eigenvectors of $\hat{\lambda}\hat{A}_c$ and $\hat{\lambda}\hat{A}_d$ because these matrices are nonsymmetric. Now, recalling that at each fixed value of the chemical potential μ the SC transition temperature is given by $\alpha(T_c) = 1$, we find, using the Maxwell relations, that

$$\left. \frac{\partial T_c}{\partial \tau_{ij}^{-1}} \right|_{\tau_{ij}^{-1}=0} = - \frac{\langle \alpha_L^{(0)} | \frac{\partial(\hat{\lambda}\hat{A}_d)}{\partial \tau_{ij}^{-1}} | \alpha_R^{(0)} \rangle}{\langle \alpha_L^{(0)} | \alpha_R^{(0)} \rangle} \frac{1}{(\partial \alpha_0 / \partial T)|_{T=T_c}}. \quad (3.43)$$

This is the general formalism we use in this and in the next subsection.

It is enlightening to start by the high-density regime, where the role of the interband scattering is highlighted. In this case, $\mu \gg \{\Omega_0, \varepsilon_0\}$ and we recover the standard BCS approximation (for both 2D and 3D bands, the results of this subsection are the same!): the density of states appearing inside the energy integrals like Eq.(3.10) can be approximated by its value at the Fermi surface ($\rho_{i,F}$) and the integration limits become symmetric:

$$\langle \mathcal{O}(\xi) \rangle_i^{\xi_c} \equiv \frac{\rho_{i,F}}{\pi \rho_{i,0}} \int_{-\xi_c}^{\xi_c} d\xi \mathcal{O}(\xi). \quad (3.44)$$

Note that the energy cutoff ξ_c can assume the values Ω_0 or Λ depending on what we are calculating. For instance, when we calculate $B_i^{(n)}$ defined in Eq.(3.34), $\xi_c = \Omega_0$. When calculating $C_i^{(n)}$ defined in Eq.(3.40), on the other hand, $\xi_c = \Lambda$.

Since $\{\Lambda, \Omega\} \gg T_c$, $\xi_c/T_c \rightarrow \infty$, so the energy integration are performed from $-\infty$ to ∞ , which give us simple expressions

$$\left\langle \frac{1}{\tilde{\omega}_{n,i}^2 + \xi^2} \right\rangle_i^{\Omega_0} = \left\langle \frac{1}{\tilde{\omega}_{n,i}^2 + \xi^2} \right\rangle_i^{\Lambda} = \frac{\rho_{i,F}}{\rho_{i,0}|\tilde{\omega}_{n,i}|}. \quad (3.45)$$

Now, substituting Eq.(3.45) into Eq.(3.29), we find

$$|\tilde{\omega}_{n,i}| = |\omega_n| + \frac{1}{2} \sum_j \tau_{ij}^{-1}, \quad (3.46)$$

where we incorporate the ratios $\rho_{i,F}/\rho_{i,0}$ in the definitions of the pairing couplings and impurity scattering rates ⁵ ($\frac{\rho_{i,F}}{\rho_{i,0}} \tau_{ij}^{-1} \rightarrow \tau_{ij}^{-1}$ and $\frac{\rho_{i,F}}{\rho_{i,0}} \lambda_{ij} \rightarrow \lambda_{ij}$). Moreover, in the high-density limit, the renormalization in the bands' dispersion vanishes $h_{n,i} \rightarrow 0$.

Therefore, substituting Eq.(3.46) into Eqs.(3.34), (3.37) and (3.40), we obtain the following results:

$$\frac{B_i^{(n)}}{D_n} = \frac{\left(|\omega_n| + \frac{1}{2} \sum_j \tau_{ij}^{-1} \right)}{|\omega_n| \left(|\omega_n| + \frac{1}{2} \sum_j \tau_{jj}^{-1} \right)} \quad (3.47)$$

$$\frac{B_i^{(n)}}{D_n} C_{ij}^{(n)} = \frac{(-\delta_{i,j} \tau_{ii}^{-1} + \delta_{i,j} \tau_{ii}^{-1})}{2 |\omega_n| \left(|\omega_n| + \frac{1}{2} \sum_j \tau_{jj}^{-1} \right)}, \quad (3.48)$$

and

$$D_n = \frac{|\omega_n| \left(|\omega_n| + \frac{1}{2} \sum_j \tau_{jj}^{-1} \right)}{\prod_i \left(|\omega_n| + \frac{1}{2} \sum_j \tau_{ij}^{-1} \right)}. \quad (3.49)$$

which, after some simple algebra, can be rearranged into

$$\left(\hat{A}_d \right)_{ij} = \delta_{i,j} P_i + \delta_{i,j} Q_i \quad (3.50)$$

with

⁵Note that it corresponds to using the density of states at the Fermi level $\rho_{i,F}$, instead of $\rho_{i,0}$, in the the definitions of the pairing couplings and impurity scattering rates, i.e. $\lambda_{ij} = -\rho_{j,F} V_{ij}$ and $\tau_{ij}^{-1} = 2\pi n_{\text{imp}} \rho_{j,F} (|v|^2 \delta_{i,j} + |u|^2 \delta_{i,j})$.

$$P_i = \ln \left(\frac{\kappa \Omega_0}{T_c} \right) - \frac{\rho_{i,F}^-}{\rho_{1,F} + \rho_{2,F}} \left[\psi \left(\frac{1}{2} + \frac{\tau_{\text{inter}}^{-1}}{2\pi T_c} \right) - \psi \left(\frac{1}{2} \right) \right], \quad (3.51)$$

$$Q_i = \frac{\rho_{i,F}^-}{\rho_{1,F} + \rho_{2,F}} \left[\psi \left(\frac{1}{2} + \frac{\tau_{\text{inter}}^{-1}}{2\pi T_c} \right) - \psi \left(\frac{1}{2} \right) \right]. \quad (3.52)$$

Here, there are two important details. First, we can see that the dependence of Eqs.(3.47)-(3.49) with the *intraband* scattering rates is such that they exactly cancel out when plugged into the expression for \hat{A}_d , which then becomes a function only of the interband scattering rates, $\tau_{\text{inter}}^{-1} \equiv \frac{1}{2} (\tau_{12}^{-1} + \tau_{21}^{-1})$. It means that in the high-density limit the impact of disorder in T_c comes solely from the interband scattering processes.

Second, in order to derive Eqs.(3.51) and (3.52), we use the result (see Appendix E)

$$\sum_n \frac{1}{|\omega_n| + x} \approx \frac{1}{\pi T_c} \left[\ln \left(\frac{\Gamma_c}{2\pi T_c} \right) - \psi \left(\frac{1}{2} + \frac{x}{2\pi T_c} \right) \right], \quad (3.53)$$

where Γ_c is the upper cutoff of the Matsubara sum, needed for convergence ($\Gamma_c = \Omega_0 \gg T_c$ for the $B_i^{(n)}$ terms), and $\psi(x)$ is the digamma function.

As in Sec. 3.1.1, once we have the analytic expression for the matrix elements \hat{A}_d , solving the coupled gap equations $\hat{\Delta} = \hat{\lambda} \hat{A}_d \hat{\Delta}$ corresponds to solve a set of transcendental equations, which, in this case, give us T_c as function of τ_{inter}^{-1} .

Instead of calculating $T_c(\tau_{\text{inter}}^{-1})$, let's investigate the behavior of $\partial T_c / \partial \tau_{\text{inter}}^{-1}$ using Eq.(3.43). First of all, substituting Eq.(3.45) into Eq.(3.12), it is straightforward to derive that the largest eigenvalue of $\hat{\lambda} \hat{A}_c$ is

$$\alpha_0 = \lambda_+ \ln \left(\frac{\kappa \Omega_0}{T_c} \right), \quad (3.54)$$

with

$$\lambda_+ = \lambda_0 + \sqrt{\delta \lambda^2 + \frac{1}{r} \lambda_{12}^2}, \quad (3.55)$$

while its correspondent right and left eigenvectors are given by, respectively

$$|\alpha_R^{(0)}\rangle = \begin{pmatrix} \delta \lambda + \sqrt{\delta \lambda^2 + \frac{1}{r} \lambda_{12}^2} \\ \frac{1}{r} \lambda_{12} \end{pmatrix}, \quad (3.56)$$

and

$$\langle \alpha_L^{(0)} | = \begin{pmatrix} \delta \lambda + \sqrt{\delta \lambda^2 + \frac{1}{r} \lambda_{12}^2} \\ \lambda_{12} \end{pmatrix}^T. \quad (3.57)$$

In Eqs.(3.54)-(3.57), we introduce the following definitions: $\lambda_{12}/\lambda_{21} = \tau_{12}^{-1}/\tau_{21}^{-1} = r$, $\lambda_0 = \frac{1}{2}(\lambda_{11} + \lambda_{22})$ and $\delta\lambda = \frac{1}{2}(\lambda_{11} - \lambda_{22})$. Furthermore, noting that $\hat{\Delta}$ is proportional to $|\alpha_R^{(0)}\rangle$, we can clearly see from Eq.(3.57) that $\text{sgn}(\Delta_1/\Delta_2) = \text{sgn}(\lambda_{12})$, so an attractive λ_{12} promotes equal sign gaps, while a repulsive λ_{12} promote opposite sign gaps, as we explained in Sec. 3.1.

Secondly, from Eq.(3.50), we readily find

$$\left. \frac{\partial (\hat{\lambda} \hat{A}_d)}{\partial \tau_{\text{inter}}^{-1}} \right|_{\tau_{\text{inter}}^{-1}=0} = \frac{1}{(1+r)} \frac{\pi}{4T_{c,0}} \begin{pmatrix} \lambda_{12} - r\lambda_{11} & -\lambda_{12} + r\lambda_{11} \\ \lambda_{22} - \lambda_{12} & -\lambda_{22} + \lambda_{12} \end{pmatrix}. \quad (3.58)$$

So, substituting Eqs.(3.54)-(3.58) into Eq.(3.43), we finally find, if we set $r = 1$ i.e., if $\lambda_{12} = \lambda_{21}$ and $\tau_{12}^{-1} = \tau_{21}^{-1}$, which in turn is achieved if we assume equal density of states for both bands,

$$\left. \frac{\partial T_c}{\partial \tau_{\text{inter}}^{-1}} \right|_{\tau_{\text{inter}}^{-1}=0} = -\frac{\pi}{8} \left[1 - \frac{\text{sgn}(\lambda_{12})}{\sqrt{\left(\frac{\lambda_{11}-\lambda_{22}}{2\lambda_{12}}\right)^2 + 1}} \right]. \quad (3.59)$$

This expression reveals important properties of impurity scattering in multiband superconductors. The first thing we should notice is that non-magnetic disorder affects both s^{+-} and s^{++} superconducting states! Although the effect is much stronger in s^{+-} states ($\lambda_{12} < 0$), Fig. 30(a) shows that T_c of an s^{++} superconducting state is suppressed as long as $\lambda_{11} \neq \lambda_{22}$. We can understand why that is returning to Eq. (3.56): there, we can see that $\lambda_{11} = \lambda_{22}$ (and therefore $\delta\lambda = 0$) leads to $\Delta_1 = \Delta_2$. In this case, as we said before, Anderson's theorem holds and T_c becomes insensitive to non-magnetic disorder.

Returning to the $\lambda_{12} < 0$ case, we can compare the role of non-magnetic disorder in multiband superconductors with the role of *magnetic disorder in single-band superconductors*. For a single-band s -wave superconductor with magnetic disorder characterized by a scattering rate τ_{mag}^{-1} ,

$$\left(\frac{\partial T_c}{\partial \tau_{\text{mag}}^{-1}} \right)_{\text{AG}} = -\frac{\pi}{4}. \quad (3.60)$$

This is known as *Abrikosov-Gor'kov result* - see Ref. [49]. Comparing Eqs.(3.59) and (3.60), we conclude that for a two-band superconductor, in the high-density regime and with repulsive interband pairing interaction, $\left| \frac{\partial T_c}{\partial \tau_{\text{inter}}^{-1}} \right| \leq \left| \frac{\partial T_c}{\partial \tau_{\text{mag}}^{-1}} \right|$, as evidenced in Fig. 30(a).

Alternatively, we can calculate $\partial T_c / \partial \tau_{\text{inter}}^{-1}$ as function of r by setting $\lambda_{11} = \lambda_{22}$ in Eq.(3.58). We thus obtain

$$\left. \frac{\partial T_c}{\partial \tau_{\text{inter}}^{-1}} \right|_{\tau_{\text{inter}}^{-1}=0} = -\frac{\pi}{8} \left[1 - \frac{2\sqrt{r} \text{sgn}(\lambda_{12})}{1+r} \right], \quad (3.61)$$

from which we can see that the difference between the density of states of the bands plays a similar role as the asymmetry between the intraband pairing interactions $\lambda_{11} - \lambda_{22}$. Fig. 30(b) shows that the suppression of T_c is zero (maximum) when $r = 1$ for a superconductor with attractive (repulsive) interband pairing. Our results are in agreement with previous works such as Refs. [61, 55, 62].

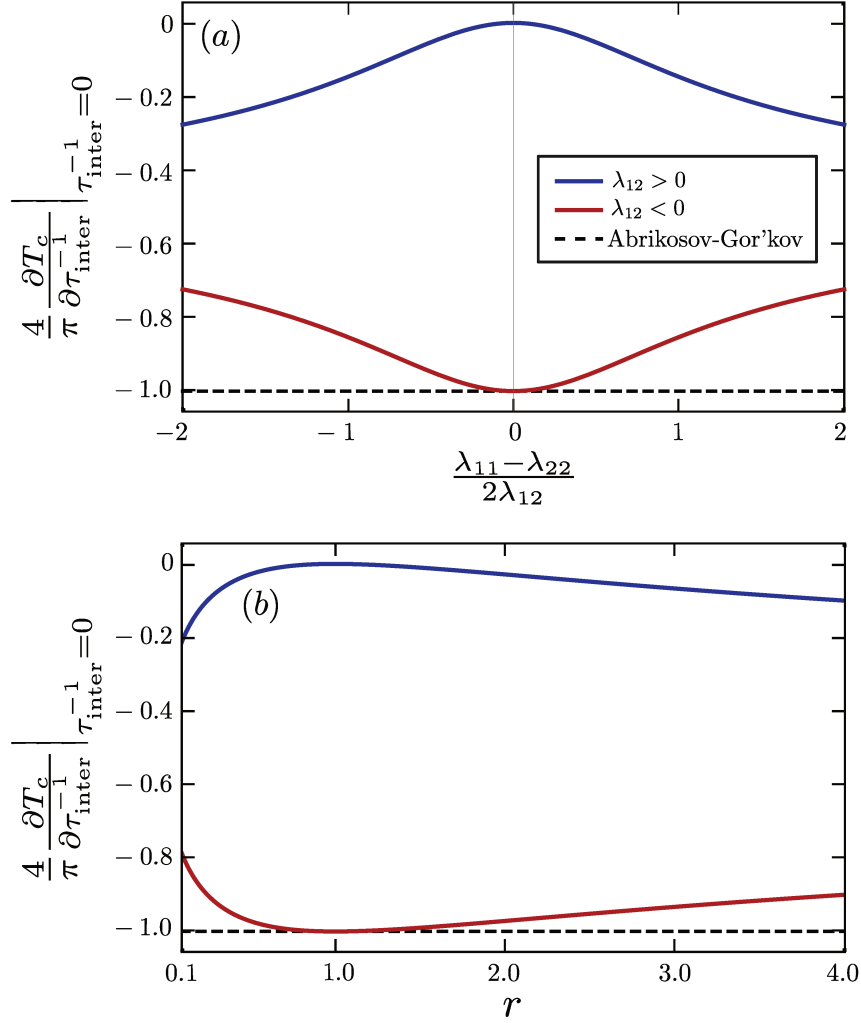


Figure 30 – The rate of suppression of T_c by interband non-magnetic impurity

scattering $\tau_{\text{inter}}^{-1}, \frac{\partial T_c}{\partial \tau_{\text{inter}}^{-1}} \Big|_{\tau_{\text{inter}}^{-1}=0}$. These figures account for repulsive ($\lambda_{12} < 0$,

red curves) and attractive ($\lambda_{12} > 0$, blue curves) interband pairing interactions, in the high-density regime. In panel (a), the density of states of the two bands are set to be the same, but the intraband pairing interactions of the two bands, λ_{11} and λ_{22} , are allowed to be different. In panel (b), λ_{11} is set to be the same as λ_{22} , but the two density of states are allowed to be different, with $r = \rho_{2,F}/\rho_{1,F}$. In both panels, the suppression rates are normalized by the magnitude of the Abrikosov-Gor'kov value of $-\pi/4$ corresponding to the suppression rate of T_c of a single-band superconductor by magnetic impurity scattering.

3.2.2 Asymptotic solution in the dilute regime

Let's now return to the low-density regime, where $\mu \ll \Omega_0$. Here, unfortunately, the energy integrals appearing in Eqs.(3.29)-(3.31) and Eq.(3.39) are not so simple as Eqs.(3.45), but we can still solve the gap equations and the self-consistent equations for the renormalized Matsubara frequencies, bands dispersion, and superconducting gaps *in the limit of weak disorder*.

As in Sec. 3.1.1, we investigate T_c as a function of μ , rather than a function of N . Here, motivated by the result of Sec. 3.2.1, we neglect the intraband scattering rates by setting $\tau_{11}^{-1} = \tau_{22}^{-1} = 0$. Moreover, for simplicity, we also set $h_{n,i} = 0$. In the end, we can compare our analytic $T_c(\mu)$ with our numeric results to conclude if these are indeed good approximations.

Expanding Eq.(3.29) up to linear order in the interband scattering rates, we find

$$\tilde{\omega}_{n,i} = \omega_n \left(1 + \frac{1}{2\pi} \tau_{\bar{i}}^{-1} f_{n,\bar{i}} \right), \quad (3.62)$$

where we defined the function

$$f_{n,i} \equiv \frac{1}{\omega_n} \left[\arctan \left(\frac{\Omega_0}{\omega_n} \right) - \arctan \left(\frac{W_i}{\omega_n} \right) \right], \quad (3.63)$$

which came from the result of the energy integration. Recall that $\bar{i} = 1(2)$ for $i = 2(1)$. Moreover, evaluating the energy integrals in Eq.(3.39) and also expanding the resulting expression in linear order in $\tau_{\bar{i}}^{-1}$ yields

$$\hat{A}_d = \hat{A}_c + \tau_{\text{inter}}^{-1} \delta \hat{A}, \quad (3.64)$$

where \hat{A}_c is the clean-case diagonal matrix defined in Eq.(3.12), and, once more, $\tau_{\text{inter}}^{-1} \equiv \frac{1}{2} (\tau_{12}^{-1} + \tau_{21}^{-1})$ denotes the average interband impurity scattering. The matrix elements of $\delta \hat{A}$ carries complicated Matsubara sums:

$$\left(\delta \hat{A} \right)_{ij} = \frac{1}{2\pi} \left[R_i \delta_{ij} + S (-\delta_{i,j} + \delta_{\bar{i},j}) \right], \quad (3.65)$$

with

$$R_i = -T_c \sum_n \left(\frac{\Lambda}{\Lambda^2 + \omega_n^2} - \frac{W_i}{W_i^2 + \omega_n^2} \right) f_{n,\bar{i}}, \quad (3.66)$$

$$S = T_c \sum_n f_{n,1} f_{n,2}. \quad (3.67)$$

To derive Eqs.(3.66) and Eqs.(3.67) we made two simplifications: we set the density of states of the two bands to be equal, $\rho_{1,0} = \rho_{2,0}$, and considered $\Omega_0 = \Lambda$. It

is important to emphasize that the main results presented here do not rely on these simplifications.

To determine analytic asymptotic expressions for the matrix elements of \hat{A}_d , we follow the same asymptotic procedure explained in Sec. 3.1.1. The calculation is straightforward and, as shown in Appendix F, it results in long expressions for R_1 , R_2 , and S .

Recalling that $\alpha(T)$, denotes the largest eigenvalue of $\hat{\lambda}\hat{A}_d$, where \hat{A}_d is defined in Eq.(3.64), it follows that, similarly to Sec.3.1.1, finding $T_c(\mu)$ involves solving a transcendental algebraic equation $\alpha = 1$, with:

$$\alpha = \frac{1}{2} \left[a_{11} + a_{22} + \sqrt{(a_{11} - a_{22})^2 + 4a_{12}a_{21}} \right], \quad (3.68)$$

where we defined, in terms of the analytic expressions for R_i and S calculated in Appendix F:

$$\begin{aligned} a_{11} &= \lambda_{11} \left[A_1 + \frac{\tau_{\text{inter}}^{-1}}{2\pi} (R_1 - S) \right] + \frac{\tau_{\text{inter}}^{-1}}{2\pi} \lambda_{12} S \\ a_{12} &= \lambda_{12} \left[A_2 + \frac{\tau_{\text{inter}}^{-1}}{2\pi} (R_2 - S) \right] + \frac{\tau_{\text{inter}}^{-1}}{2\pi} \lambda_{11} S \\ a_{21} &= \lambda_{12} \left[A_1 + \frac{\tau_{\text{inter}}^{-1}}{2\pi} (R_1 - S) \right] + \frac{\tau_{\text{inter}}^{-1}}{2\pi} \lambda_{22} S \\ a_{22} &= \lambda_{22} \left[A_2 + \frac{\tau_{\text{inter}}^{-1}}{2\pi} (R_2 - S) \right] + \frac{\tau_{\text{inter}}^{-1}}{2\pi} \lambda_{12} S, \end{aligned} \quad (3.69)$$

with $A_1 = \left(\hat{A}_c \right)_{11}$ and $A_2 = \left(\hat{A}_c \right)_{22}$.

A comparison between the analytic and numeric $T_c(\mu)$ is presented in Fig. 31, for the cases of attractive and repulsive interband pairing interactions. As in the clean case, we can see an excellent agreement the two methods, except in very narrow regions where the asymptotic approximation fails. Similarly to Fig. 25, these regions are too narrow compared to the scale of the plots and are thus not shown in the plots. Moreover, the agreement between the asymptotic solution and the numerical results near the Lifshitz transition improves as the scattering rates becomes smaller, which makes sense since, as we said in the beginning of this subsection, our asymptotic study holds for weak disorder.

As in Sec. 3.2.1, here we are also interested in the behavior of $\partial T_c / \partial \tau_{\text{inter}}^{-1}$ obtained through Eq.(3.43). It is straightforward to calculate, in terms of the functions R_1 , R_2 and S ,

$$\begin{aligned} \left\langle \alpha_L^{(0)} \left| \frac{\partial(\hat{\lambda}\hat{A}_d)}{\partial \tau_{\text{inter}}^{-1}} \right| \alpha_R^{(0)} \right\rangle &= \left\{ (1 - \lambda_{11}A_2) \left[(R_1 - S)(\lambda_{11} - \lambda_{11}^2A_2 + \lambda_{12}^2A_2) + \lambda_{12}S(1 + \lambda_{11}A_1) \right] \right. \\ &\quad \left. + \lambda_{12}^2A_1(R_2 - S + \lambda_{12}SA_2) \right\} \frac{1}{2\pi}, \end{aligned} \quad (3.70)$$

and

$$\left. \frac{\partial \alpha_0}{\partial T} \right|_{T=T_c} = \frac{1}{2 - \lambda_{11}(A_1 + A_2)} \sum_{j=1}^2 (\lambda_{11} - \lambda_{11}^2 A_j + \lambda_{12}^2 A_j) \left. \frac{\partial A_j}{\partial T} \right|_{T=T_c}, \quad (3.71)$$

as well as

$$\langle \alpha_L^{(0)} | \alpha_R^{(0)} \rangle = (1 - \lambda_{11} A_2)^2 + \lambda_{12}^2 A_1 A_2, \quad (3.72)$$

which we can substitute in Eq.(3.43) and determine $\partial T_c / \partial \tau_{\text{inter}}^{-1}$ in each of the four regions

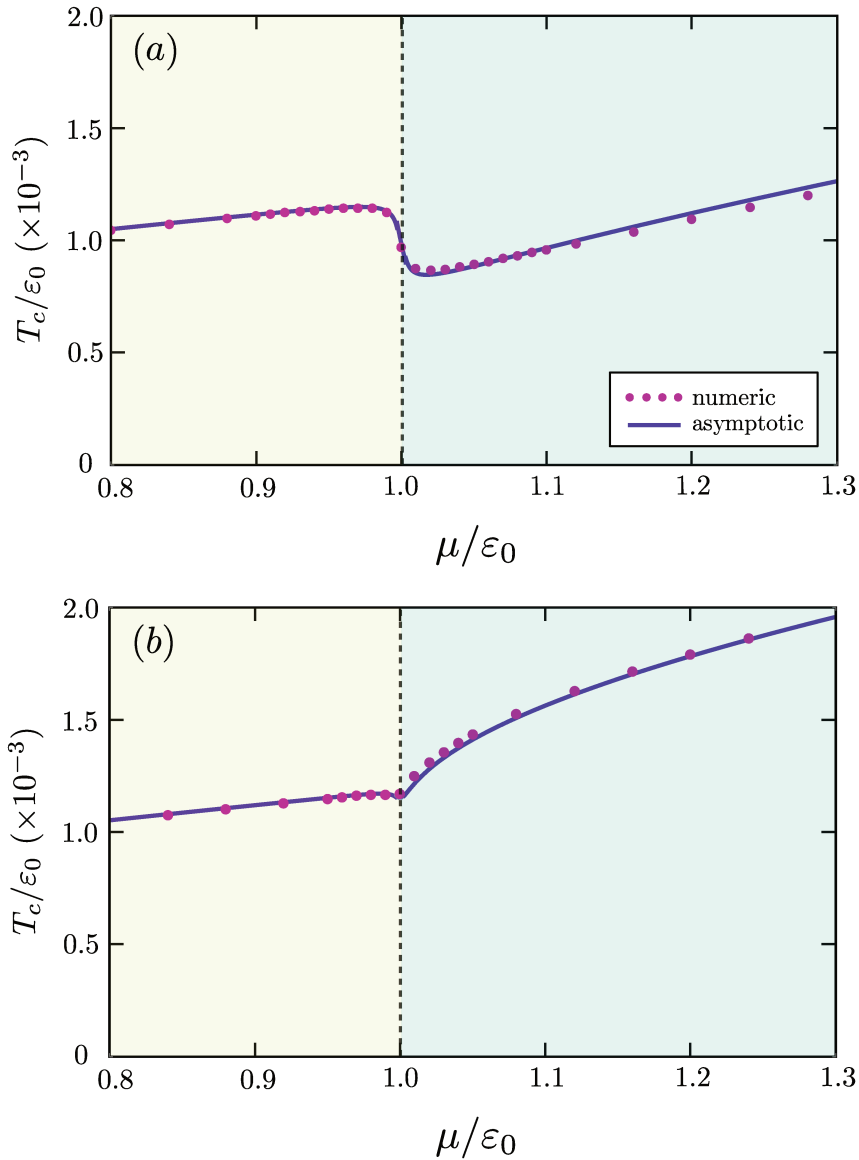


Figure 31 – Comparison between the numerical (symbols) and asymptotic analytical results (solid curves) for T_c , as function of the chemical potential μ , for the 2D dirty system across the Lifshitz transition at $\mu = \epsilon_0$. Here we set $\rho_{1,0} = \rho_{2,0}$, $\lambda_{11} = \lambda_{22} = 0.13$, and $|\lambda_{12}| = 0.013$, with $\lambda_{12} < 0$ (repulsive interband pairing interaction) in panel (a) and $\lambda_{12} > 0$ (attractive interband pairing interaction) in panel (b). The interband impurity scattering τ_{inter}^{-1} is set to $\tau_{\text{inter}}^{-1}/\epsilon_0 = 10^{-3}$.

of the phase diagram in Fig. 24. This result, as function of the chemical potential, is shown in Fig. 32 for the case of a two-band superconductor with (a) attractive, and (b) repulsive interband pairing interaction.

In Fig. 32, we normalize $\partial T_c / \partial \tau_{\text{inter}}^{-1}$ by the Abrikosov-Gor'kov suppression rate $-\pi/4$. Moreover, the insets in each panel display zooms of the behaviors of the asymptotic solutions near the Lifshitz transition, where, similarly as the clean case in Sec. 3.1.1, the asymptotic solutions show discontinuities across the boundaries of the regions of Fig. 24.

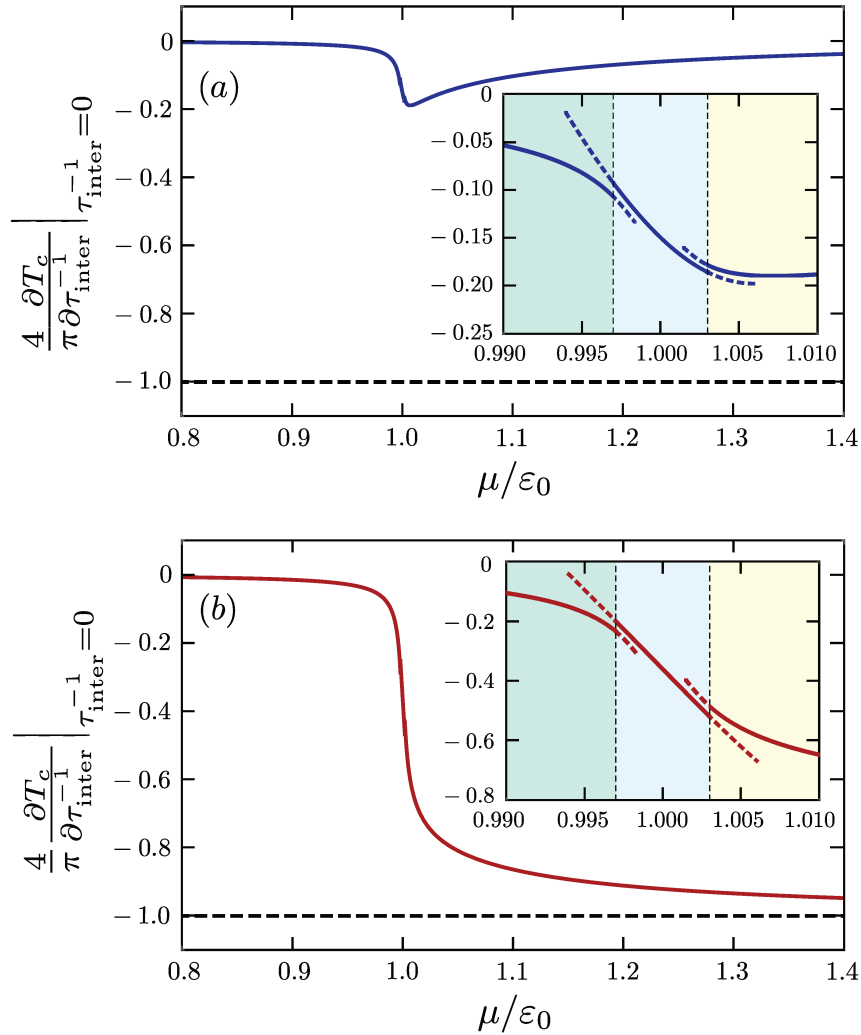


Figure 32 – **The rate of suppression of T_c by interband impurity scattering,** $\frac{\partial T_c}{\partial \tau_{\text{inter}}^{-1}} \Big|_{\tau_{\text{inter}}^{-1}=0}$. These figures account for attractive ($\lambda_{12} > 0$, panel (a)) and repulsive ($\lambda_{12} < 0$, panel (b)) interband pairing interactions, in the dilute regime. The insets highlight the asymptotic behaviors across the boundaries of regions II, III, and IV of Fig. 24. In both panels, the suppression rates are normalized by the absolute value of the Abrikosov-Gor'kov suppression rate of $-\pi/4$, corresponding to the case of a single-band superconductor by magnetic impurity scattering. The parameters used here are $\rho_{1,0} = \rho_{2,0}$, $\lambda_{11} = \lambda_{22} = 0.13$, and $\lambda_{12} = \lambda_{21}$, with $|\lambda_{12}| = 0.013$.

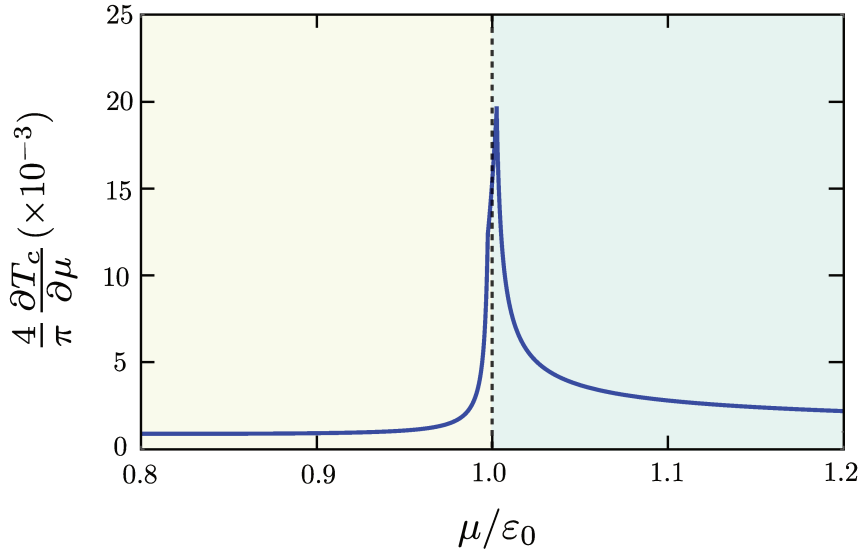


Figure 33 – **Rate of enhancement of T_c by changes in the chemical potential, $\frac{\partial T_c}{\partial \mu}$, for the clean 2D system.** The parameters are the same as those used in Fig. 32. To make the comparison with that figure more transparent, we also normalize the rate of change of T_c by $\pi/4$.

The results far from the Lifshitz transition are not surprising: before the Lifshitz transition, when only one band is present, $\partial T_c / \partial \tau_{\text{inter}}^{-1}$ is very small, since the second band is sunk below the Fermi level. After the Lifshitz transition, when the second band is no longer incipient, we approach the high-density limit and, consequently, $\partial T_c / \partial \tau_{\text{inter}}^{-1}$ approaches $-\pi/4$ for repulsive interband interaction and 0 for attractive interband pairing interaction, in agreement with our discussion in Sec. 3.2.1.

The interesting behaviors of $\partial T_c / \partial \tau_{\text{inter}}^{-1}$ take place in the vicinity of the Lifshitz transition. For the repulsive case ($\lambda_{12} < 0$), we can see a sharp increase of the magnitude of the suppression rate, despite the fact that the second band is only incipient. On the other hand, for the attractive case ($\lambda_{12} > 0$), the magnitude of the suppression rate displays a rather mild maximum when the second band crosses the Fermi level, which agrees with our numerical phase diagrams shown in Fig. 28.

So we can conclude that the fate of the evolution of T_c in the dirty system across the Lifshitz transition depends then on the competition between two opposite effects: the suppression of T_c due to the pair-breaking promoted by interband impurity scattering, and the enhancement of T_c promoted by the new electronic states that become part of the superconducting state once the second band crosses the Fermi level. The latter effect is illustrated in Fig. 33, where $\partial T_c / \partial \mu$ obtained from the asymptotic analytical solution of the clean system is shown. Generally, one expects that, for sufficiently strong disorder, and for a repulsive interband interaction, the former effect wins, such that T_c displays a maximum at the Lifshitz transition, which is indeed what we observed in the full numerical

solution of the dirty gap equations shown in Fig. 28.

3.3 Conclusions - part II

In this Chapter we investigated the evolution of the superconducting transition temperature T_c of a two-band superconductor as a function of the chemical potential μ , which controls the bands occupation. We give special attention to the limit where we are close to the bottom of the bands, so by varying μ we can go from the case where only one band crosses the Fermi level (single-band superconductivity) to the situation where both bands are populated, characterizing the regime of multiband superconductivity.

Particularly, when μ reaches the bottom of the second band which then becomes populated, making a new Fermi pocket appear in the Fermi surface, the system undergoes a so called *Lifshitz* transition, which leaves signatures in the behavior of $T_c(\mu)$. It is well known in the literature that T_c tends to increase across a Lifshitz transition, simply because of the enhancement of the system's density of states as the second band becomes populated: a larger density of states implies that more electronic states will be available for composing the superconducting condensate and as a result T_c increases.

We show, both numerically and analytically, that this is the case for 2D bands. We observe a sharp enhancement of T_c across the Lifshitz transition for both attractive and repulsive interband superconducting pairing. In a clean multiband superconductor, $T_c(\mu)$ doesn't depend on the sign of the interband pairing, which, in turn, only sets the symmetry of the resulting superconductor state: an attractive interband pairing ($\lambda_{12} > 0$) generates a state with equal sign gaps denominated s^{++} state. An repulsive interband pairing ($\lambda_{12} < 0$), on the other hand, generates an *unconventional* sign changing gaps states, the s^{+-} state.

However, recent experimental evidences show that T_c actually reduces across the Lifshitz transition of two paradigmatic examples of multiband superconductors: the SrTiO₃ and the LaAlO₃/SrTiO₃ interfaces. In these system's phase diagrams, one can see a superconducting dome, peaked at the Lifshitz transition, even without any other nearby order to compete with superconductivity. Motivated by these results, we investigated a possible origin for this curious behavior.

It so happens that residual resistivity data reveal that both STO and LAO/STO are dirty systems, so we decided to investigate the effect of *non-magnetic disorder* in a model two-band superconductor.

We show, again both analytically and numerically, that in contrast to single-band superconductors, in a multiband dilute superconductor non-magnetic disorder can suppress T_c of both s^{+-} and s^{++} states. Our asymptotic study reveals that the key for the suppression of superconductivity across the Lifshitz transition is the interband electronic

scattering promoted by the impurities, which are strongly pair-breaking. Actually, we show that what happens in the vicinity of the Lifshitz transition is a competition of two opposite effects: on the one hand, there is the tendency of increase of T_c due to the enhancement of the density of states. On the other hand, when the second band becomes populated the aforementioned interband scattering starts happening, destroying, in turn, the Cooper pairs. When disorder is strong enough, the detrimental effect of disorder wins and, as a result, T_c is reduced, generating a non-monotonic behavior of $T_c(\mu)$ across the Lifshitz transition.

Our asymptotic study also shows that the pair-breaking effect of non-magnetic disorder is stronger for a multiband superconductor with *dominant intraband pairing interactions* (λ_{11} and λ_{22}) and *subleading repulsive interband interaction* ($|\lambda_{12}| \ll \{\lambda_{11}, \lambda_{22}\}$, with $\lambda_{12} < 0$), and the theoretical phase diagram obtained in this case is in agreement with the experimental phase diagram of the LAO/STO interfaces and thin films of STO. Therefore, our work suggests an unconventional nature for the superconducting state in these systems, which is a long-standing and puzzling open question in the literature.

Another astonishing consequence of our model is a change in the symmetry of the superconducting state, from s^{+-} to s^{++} , as a function of the electronic density (n) for a fixed impurity scattering rate and for the $\lambda_{12} < 0$ case. Such result allows us to predict that in the aforementioned phase diagrams of STO and LAO/STO interfaces, we would have, at the left side of the superconducting dome (before the Lifshitz transition), an s^{+-} state, while on the right side of the dome, as n (or μ) increases, the symmetry of the state would change to s^{++} .

Interestingly, such crossover can be observed experimentally, since it leaves signatures in the spectroscopic and thermodynamic properties of the system. In particular, for densities close to the onset of such symmetry crossover, the superconducting gap in one of the bands is very small and, thus, could not be identified by some probes, which would in turn, measure a signal consistent with a single-band superconductor even though more than one band crosses the Fermi level. As a matter of fact, that is exactly what happened in a recent optical conductivity experiment performed in doped STO.

It is important to emphasize that in this thesis we focused on the case of 2D bands because the density of states of each band is a constant, and an analytic solution of the gap equations is feasible. However, in Ref. [35], we show that the same qualitative behavior described here holds for 3D bands, where the structure of a superconducting dome is more apparent. Therefore, our model can explain the features of both the phase diagrams of LAO/STO hetero-structures and bulk STO.

Bibliography

- [1] Michael R. Geller, arXiv:cond-mat/0106256 (2001).
- [2] Y. Cao, V. Fatemi, A. Demir, S. Fang, S. L. Tomarken, J. Y. Luo, J. D. Sanchez-Yamagishi, K. Watanabe, T. Taniguchi, E. Kaxiras, R. C. Ashoori, and P. Jarillo-Herrero, *Nature* **556**, 43 (2018).
- [3] Y. Cao, V. Fatemi, S. Fang, K. Watanabe, T. Taniguchi, E. Kaxiras, and P. Jarillo-Herrero, *Nature* **556**, 80 (2018).
- [4] M. Yankowitz, S. Chen, H. Polshyn, K. Watanabe, T. Taniguchi, D. Graf, A. F. Young, C. R. Dean, *Science* **363**, 1059 (2019).
- [5] M. Faraday, *Phil. Trans. R. Soc. London*, **115**, 440 (1825).
- [6] P. Atkins and J de Paula, *Atkins' Physical Chemistry* (W. H. Freeman and Company, New York, 2006), p. 391.
- [7] P. Lazzeretti, *Progress in Nuclear Magnetic Resonance Spectroscopy*, **36**, 1 (2000).
- [8] R. Hoffman, V.I. Minkin, B.K. Carpenter, *HYLE-Int. J.Philos. Chem.* **3**, 3 (1997).
- [9] Paul von Ragué Schleyer, *Chemical Reviews* **101** 1115 (2001).
- [10] K. S. Krishnan, B. C. Guha and S. Banerjee, *Phil. Trans. Roy. Soc.* **A231**, 235 (1933);
- [11] L Pauling, *J.Chem. Phys.* **4**, 637 (1936).
- [12] F. London, *C.R. Acad. Sci.* **28**, 205 (1937).
- [13] F. London, *J. Phys. Radium* **8**, 397 (1937).
- [14] F. London, *J. Chem. Phys.* **5**, 837 (1937).
- [15] K. Lonsdale, *Proc. R. Soc. A* **159**, 149 (1937).
- [16] G. Baym *Lectures on Quantum Mechanics* (W. A. Benjamin, Massachusetts), p. 498 (1973).
- [17] J.S. Waugh, R.W. Fessenden, *J. Am. Chem. Soc.* **79**, 846 (1957).
- [18] C.E. Johnson, F.A. Bovey, *J. Chem. Phys.* **29**, 1012 (1958).
- [19] B.P. Dailey, *J. Chem. Phys.* **41** 2304 (1964).

- [20] Y. Imry, *Introduction to mesoscopic physics*. (Oxford University Press, 2ed, New York 2002).
- [21] H. Bouchiat, Am. Phys. Soc.:Physics Viewpoint **1**, 7 (2008).
- [22] A. L. Fetter, J. D. Walecka *Quantum Theory of Many-Particle Systems* (McGraw-Hill, San Francisco 1971).
- [23] H. Bruus, K. Flensberg, *Many-body quantum theory in condensed matter physics: an introduction* (New York, NY: Oxford University Press 2007).
- [24] A. Y. Liu, I. I. Mazin, and J. Kortus, Phys. Rev. Lett. **87**, 087005 (2001).
- [25] M. Marz, G. Goll, W. Goldacker, and R. Lortz, Phys. Rev. B **82**, 024507 (2010).
- [26] T. Yokoya, T. Kiss, A. Chainani, S. Shin, M. Nohara, and H. Takagi, Science **294**, 2518 (2001).
- [27] H. Ding, P. Richard, K. Nakayama, K. Sugawara, T. Arakane, Y. Sekiba, A. Takayama, S. Souma, T. Sato, T. Takahashi, Z. Wang, X. Dai, Z. Fang, G. F. Chen, J. L. Luo, and N. L. Wang, EPL **83**, 47001 (2008).
- [28] A. P. Mackenzie, S. R. Julian, A. J. Diver, G. J. McMullan, M. P. Ray, G. G. Lonzarich, Y. Maeno, S. Nishizaki, and T. Fujita, Phys. Rev. Lett. **76**, 3786 (1996).
- [29] P. M. C. Rourke, M. A. Tanatar, C. S. Turel, J. Berdeklis, C. Petrovic, and J. Y. T. Wei, Phys. Rev. Lett. **94**, 107005 (2005).
- [30] G. Binnig, A. Baratoff, H.E. Hoenig, and J.G. Bednorz, Phys. Rev. Lett. **45**, 1352 (1980).
- [31] X. Lin, G. Bridoux, A. Gourgout, G. Seyfarth, S. Krämer, M. Nardone, B. Fauqué, and K. Behnia, Phys. Rev. Lett. **112**, 207002 (2014).
- [32] D. van der Marel, J. L. M. van Mechelen, and I. I. Mazin, Phys. Rev. B **84**, 205111 (2011).
- [33] A. Joshua, S. Pecker, J. Ruhman, E. Altman, and S. Ilani, Nat. Commun. **3**, 1129 (2012).
- [34] X. Lin, B. Fauqué, and K. Behnia, Science **349**, 945 (2015).
- [35] T. V. Trevisan, M. Schütt, R. M. Fernandes, Phys. Rev. Lett. **121**, 127002 (2018).
- [36] T. V. Trevisan, M. Schuett, and R. M. Fernandes, Phys. Rev. B **98**, 094514 (2018).
- [37] S. K. Maiti, Sol. State. Commun. 150, 2212 (2010).

-
- [38] C. Cohen-Tannoudji, B. Diu and F. Laloe *Quantum Mechanics* (New York, NY; Paris: John Wiley, Vol. 1, 2005).
- [39] J. Hubbard, Proc. R. Soc. A **276**, 238 (1963).
- [40] M. Schüler, M. Rösner, T. O. Wehling, A. I. Lichtenstein, and M. I. Katsnelson, Phys. Rev. Lett. **111**, 036601 (2013).
- [41] F. H. L. Essler, H. Frahm, F. Göhmann, A. Klümper and V. E. Korepin, *The One-Dimensional Hubbard Model*. United Kingdom: Cambridge University Press, 2005, 674p.
- [42] R. J. Bursill, C. Castleton, and W. Barford, Chemical Physics Letters **294**, 305 (1998).
- [43] L. Andjelković, M. Perić, M. Zlatar, S. Grubisic, M. Gruden-Pavlovic, Tetrahedron Letters **53**, 794 (2011).
- [44] E. Merzbacher *Quantum Mechanics* (John Wiley: New YorkNova York, 3 ed., 1998), 656p.
- [45] D. Bohm and D. Pines, Phys. Rev. **82**, 625 (1951).
- [46] D. Bohm and D. Pines, Phys. Rev. **85**, 338 (1952).
- [47] D. Bohm and D. Pines, Phys. Rev. **92**, 609 (1953).
- [48] R. M. Fernandes, J. T. Haraldsen, P. Wölfle, and A. V. Balatsky, Phys. Rev. B **87**, 014510 (2013).
- [49] A. V. Balatsky, I. Vekhter, Jian-Xin Zhu, Rev. Mod. Phys. **78**, 873 (2006).
- [50] A. V. Chubukov, I. Eremin, and D. V. Efremov, Phys. Rev. B **93**, 174516 (2016).
- [51] C. Bell, S. Harashima, Y. Kozuka, M. Kim, B. G. Kim, Y. Hikita, and H. Y. Hwang, Phys. Rev. Lett. **103**, 226802 (2009).
- [52] P. W. Anderson, Phys. Rev. Lett. **3**, 325 (1959).
- [53] P.B. Allen, Phys. Rev. B **17**,3725 (1978).
- [54] A. A. Golubov and I. I. Mazin, Phys. Rev. B **55**, 15146 (1997).
- [55] D. V. Efremov, M. M. Korshunov, O. V. Dolgov, A. A. Golubov, and P. J. Hirschfeld, Phys. Rev. B **84**, 180512(R) (2011).
- [56] R. D. Mattuck, *A Guide to Feynman Diagrams in the Many-body Problem* (Dover Books on Physics Series, 1992).

-
- [57] J. Rammer, *Quantum transport theory* (CRC Press, 2018).
- [58] M. Thiemann, M. H. Beutel, M. Dressel, N. R. Lee-Hone, D. M. Broun, E. Fillis-Tsirakis, H. Boschker, J. Mannhart, and M. Scheffler, arXiv:1703.04716.
- [59] D. J. Bergmann and D. Rainer, *Z. Phys.* **263**, 59 (1973).
- [60] J. Kang and R. M. Fernandes, *Phys. Rev. B* **93**, 224514 (2016).
- [61] A. A. Golubov and I. I. Mazin, *Phys. Rev. B* **55**, 15146 (1997).
- [62] Y. Wang, A. Kreisel, P. J. Hirschfeld, and V. Mishra, *Phys. Rev. B* **87**, 094504 (2013).
- [63] J. D. Jackson, *Classical electrodynamics*, 3rd edition (1998).

Appendix

APPENDIX A – Derivation of the Hubbard Hamiltonian

Here we provide a detailed derivation of both the single-band Hubbard Hamiltonian defined in Eq.(2.9), and the three-band Hubbard Hamiltonian defined in Eqs.(2.94) and (2.95), which we use in the main text of this thesis. This appendix is divided in three sections. In Sec. A.1 we derive Eq.(2.9), while in in Sec. A.2 we show how this Hamiltonian needs to be modified to account for multiple orbitals per site.

A.1 Single-band Hubbard Hamiltonian

Proposed by John Hubbard in 1963 to describe electrons correlations in narrow bands[39], the Hubbard model is the simplest model available to study *interacting* electrons in a lattice with either one orbital per site (*single-band model*) or multiple orbitals per site (*multiband model*). We first show how to derive the single-band Hubbard Hamiltonian for a 1D lattice with periodic boundary conditions.

The starting point is the complete Hamiltonian of N_e interacting electrons in first quantization, which is given by

$$\mathcal{H}_0 = \sum_{i=1}^{N_e} \left(\frac{\mathbf{p}_i^2}{2m} + V_c(\mathbf{r}_i) \right) + \frac{1}{2} \sum_{j \neq i=1}^{N_e} \frac{e^2}{|\mathbf{r}_i - \mathbf{r}_j|}. \quad (\text{A.1})$$

Here, \mathbf{p}_i and \mathbf{r}_i denote, respectively, the momentum and the position of the i -th electron of the system, while e is the elementary charge. The information about the existence of an underlying lattice enters in $V_c(\mathbf{r})$, which is the periodic generated by the lattice ions and its core electrons. Here we make an approximation by assuming that the lattice is *static*, so $V_c(\mathbf{r})$ does not change in time.

In the specific case of our rings, since here we are deriving a model only for the degrees of freedom of the π -electrons, the binding σ -electrons, frozen in the sp_2 orbitals, also contributes to $V_c(\mathbf{r})$ through a *static charge density in the σ -bonds*. This scenario changes in Sec.A.2.

The next step is to rewrite the Hamiltonian in Eq.(A.1) in second quantization

[22],

$$\begin{aligned} \hat{H}_0 &= \sum_{\sigma=\uparrow,\downarrow} \int d\mathbf{r} \hat{\psi}_\sigma^\dagger(\mathbf{r}) h(\mathbf{r}) \hat{\psi}_\sigma(\mathbf{r}) \\ &+ \frac{1}{2} \sum_{\sigma,\sigma'} \int d\mathbf{r} \int d\mathbf{r}' \hat{\psi}_\sigma^\dagger(\mathbf{r}) \hat{\psi}_{\sigma'}^\dagger(\mathbf{r}') u(\mathbf{r}, \mathbf{r}') \hat{\psi}_{\sigma'}(\mathbf{r}') \hat{\psi}_\sigma(\mathbf{r}) , \end{aligned} \quad (\text{A.2})$$

where

$$h(\mathbf{r}) \equiv \frac{\mathbf{P}^2}{2m} + V_c(\mathbf{r}) = -\frac{\hbar^2}{2m} \nabla^2 + V_c(\mathbf{r}) , \quad (\text{A.3})$$

corresponds the single-particle Hamiltonian, while

$$u(\mathbf{r}, \mathbf{r}') = \frac{e^2}{|\mathbf{r} - \mathbf{r}'|} , \quad (\text{A.4})$$

is the standard Coulomb repulsion between the electrons. Besides, $\hat{\psi}_\sigma^\dagger(\mathbf{r})$ ($\hat{\psi}_\sigma(\mathbf{r})$) is the field operator that creates (annihilates) an electron with spin σ at the position \mathbf{r} of the real space,

$$\hat{\psi}_\sigma^\dagger(\mathbf{r}) = \sum_j \varphi_j^*(\mathbf{r}) c_{j\sigma}^\dagger . \quad (\text{A.5})$$

Note that it is given in terms of the single-particle states $\varphi_j(\mathbf{r}) \equiv \langle \mathbf{r} | j \rangle$, which are the eigenstates of the single-particle Hamiltonian defined in (A.3). Moreover, the annihilation operator $\hat{\psi}_\sigma(\mathbf{r})$ is readily obtained by taking the Hermitian conjugate of Eq.(A.5).

Choosing $\varphi_j(\mathbf{r})$ to be the *Wannier wave functions*, which are centered at the position of the j -th site of the ring, we obtain the field operators in the *site basis*¹, meaning that the index j runs from one to the total number of sites N of the ring and the operator $c_{j\sigma}^\dagger$ ($c_{j\sigma}$) creates (annihilates) one electron with spin σ in the site j . Moreover, since we are dealing with a sing system, periodic boundary conditions apply, i.e. $c_{j+N\sigma}^\dagger = c_{j\sigma}^\dagger$. More details about the functional form of $\varphi_j(\mathbf{r})$ is provided later in this Appendix.

Substituting Eq.(A.5) into Eq.(A.2), we find

$$\hat{H}_0 = \sum_{i,j=1}^N \sum_{\sigma=\uparrow,\downarrow} t_{ij} c_{i\sigma}^\dagger c_{j\sigma} + \frac{1}{2} \sum_{i,j,k,l=1}^N \sum_{\sigma,\sigma'=\uparrow,\downarrow} U_{ijkl} c_{i\sigma}^\dagger c_{j\sigma'}^\dagger c_{k\sigma'} c_{l\sigma} . \quad (\text{A.6})$$

Here t_{ij} is the *hopping parameter*

$$t_{ij} \equiv \langle i | h | j \rangle = \int d\mathbf{r} \varphi_i^*(\mathbf{r}) h(\mathbf{r}) \varphi_j(\mathbf{r}) , \quad (\text{A.7})$$

¹Alternatively, we could have chosen the single-particle wave functions to be the Bloch states. In this case we would find the field operator in the Bloch bases basis. The field operators, and consequently the second-quantized Hamiltonians in the site basis and in the Bloch basis are related by a simple discrete Fourier transform.

which gives the probability amplitude of an electron to hop between the sites i and j , and

$$U_{ijkl} \equiv \langle ij | u | lk \rangle = \int d\mathbf{r} \int d\mathbf{r}' \varphi_i^*(\mathbf{r}) \varphi_j^*(\mathbf{r}) u(\mathbf{r}, \mathbf{r}') \varphi_k(\mathbf{r}') \varphi_l(\mathbf{r}) \quad (\text{A.8})$$

is the Coulomb repulsion in the site basis.

The Hamiltonian (A.6) is still very generic and complex and, in order to obtain the standard single-band Hubbard Hamiltonian, two important approximations must be done [39]. First, we should note that, for narrow orbitals, the overlap between the Wannier wave-functions centered at different sites of the ring will be negligible for sites well-separated from one another, meaning that the most significant contribution for t_{ij} comes from nearest neighbor sites, i.e.,

$$t_{ij} \approx \langle i | h | i + 1 \rangle \delta_{j,i+1} + \langle i | h | i - 1 \rangle \delta_{j,i-1} = -t (\delta_{j,i+1} + \delta_{j,i-1}) , \quad (\text{A.9})$$

where we define a uniform hopping amplitude $\langle i | h | i + 1 \rangle = \langle i | h | i - 1 \rangle \equiv -t$, (with $t > 0$). Note that a non-uniform hopping would break the discrete rotation symmetry of the rings. Furthermore the above choice of the minus sign in the definition hopping amplitude is purely for convenience. The 1D Hubbard model has a $t \rightarrow -t$ symmetry.

The second approximation consists in transforming the two-body interaction Eq.(A.8) into a purely local term, called *on-site Coulomb repulsion*,

$$\langle ij | u | lk \rangle \approx \langle ii | u | ii \rangle \delta_{j,i} \delta_{j,i} \delta_{k,i} \delta_{l,i} \equiv U \delta_{j,i} \delta_{j,i} \delta_{k,i} \delta_{l,i} , \quad (\text{A.10})$$

with $U > 0$. Therefore, substituting Eqs.(A.9) and (A.10) into Eq.(A.6), and using the fermionic anti-commutation relations,

$$\{c_{i\sigma}, c_{j\sigma'}^\dagger\} = \delta_{i,j} \delta_{\sigma,\sigma'} , \quad (\text{A.11})$$

$$\{c_{i\sigma}, c_{j\sigma'}\} = \{c_{i\sigma}^\dagger, c_{j\sigma'}^\dagger\} = 0 , \quad (\text{A.12})$$

we find the standard Hubbard Hamiltonian for a ring with N sites, N_e electrons and only one orbital per site:

$$\hat{H}_0 = -t \sum_{j=1}^N \sum_{\sigma} \left(c_{j\sigma}^\dagger c_{j+1\sigma} + \text{h.c.} \right) + U \sum_{j=1}^N \hat{n}_{j\uparrow} \hat{n}_{j\downarrow} . \quad (\text{A.13})$$

Here, ‘‘h.c.’’ denotes the Hermitian conjugate of $c_{j\sigma}^\dagger c_{j+1\sigma}$ and $\hat{n}_{j\sigma} = c_{j\sigma}^\dagger c_{j\sigma}$ is the number operator. Although the Hamiltonian (A.13) looks simple, the calculation of its energy levels and corresponding eigenstates is not a trivial task. For small enough systems, as is the case in this thesis, an exactly diagonalization of Eq.(A.13) can be done. However, for large lattice systems, an analytic solution for the Hubbard Hamiltonian exists only for 1D lattice via Bethe ansatz [41].

A.1.1 Complete energy spectrum

In Fig. 7 at Sec. 2.2.1 of this thesis, we show the energy spectrum, as function of U/t , of rings with $3 \leq N \leq 6$ sites, all of them in the half-filling regime ($N = N_e$). For those rings with $N \geq 4$ sites we show only a few of the lowest energy levels, since the complete spectrum involves too many levels and the figures end up looking a little bit confusing. Here, however, we add these figures for completeness.

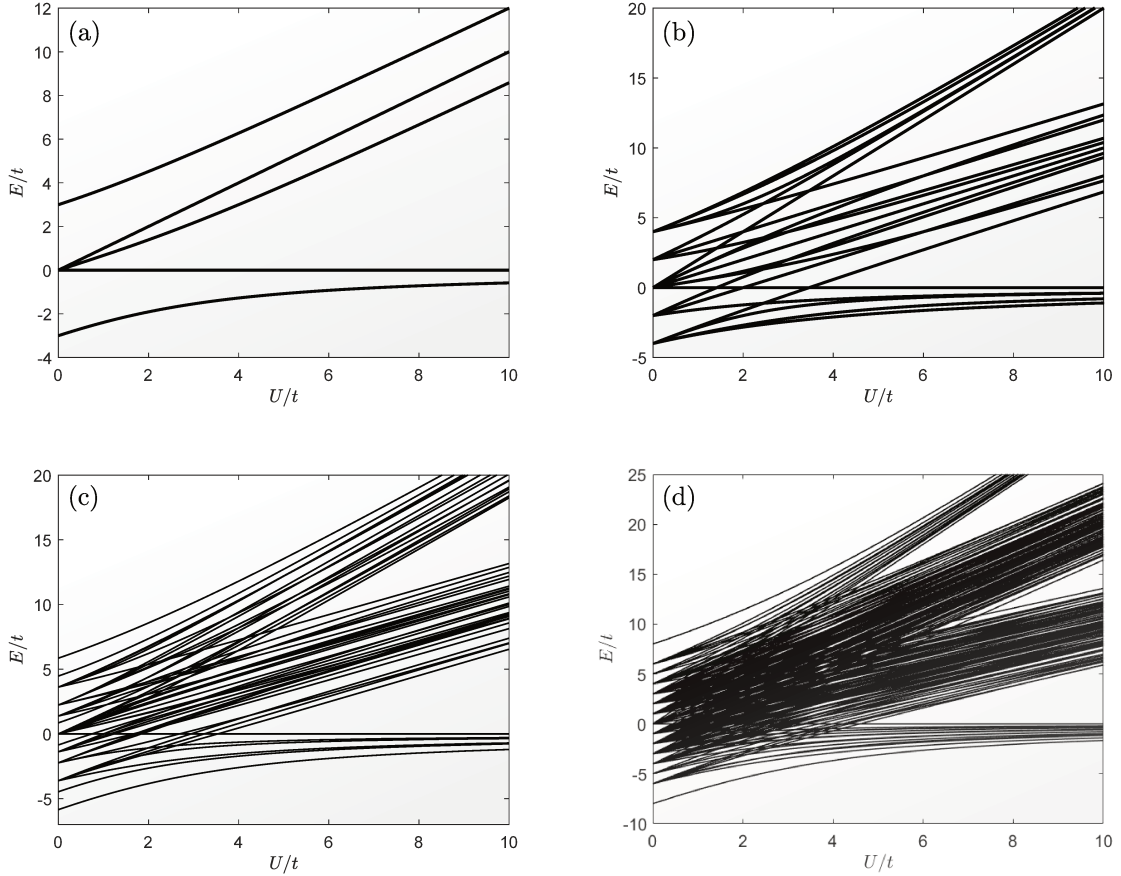


Figure 34 – **Energy spectrum of the Hubbard Hamiltonian** The panels show the energy levels of Eq.(2.9), as function of U/t for rings with (a) $N = 3$ sites, (b) $N = 4$ sites, (c) $N = 5$ sites and (d) $N = 6$ sites at the half-filling regime, i.e., $N = N_e$.

A.2 Multiband Hubbard Hamiltonian

The field operator defined in Eq.(A.5) involves only one single-particle wave function $\varphi_j(\mathbf{r})$, which describes a p_z orbital centered in the j -th site of the ring. If, on the other hand, we want to consider multiple orbitals per site, the field operator must be modified accordingly to incorporate these extra degrees of freedom. In particular for the case where we have two sp_2 orbitals and one p_z orbital per site, as illustrated in Fig. 5,

the field operator takes the form

$$\hat{\psi}_\sigma^\dagger(\mathbf{r}) = \sum_{j=1}^N \left[\varphi_j^*(\mathbf{r}) c_{j\sigma}^\dagger + \sum_{\kappa=1}^2 W_{j,\kappa}^*(\mathbf{r}) d_{j\kappa;\sigma}^\dagger \right], \quad (\text{A.14})$$

where $W_{j,\kappa}(\mathbf{r}) \equiv \langle \mathbf{r} | W_{j,\kappa} \rangle$, with $\kappa = 1$ ($\kappa = 2$), denotes the Wannier wave function of the *right* (*left*) sp_2 orbital centered in the j -th site of the ring, while $\varphi_j(\mathbf{r})$ continues to represent the Wannier correspondent to the p_z orbitals. Consistently, here $d_{j\kappa;\sigma}^\dagger$ ($d_{j\kappa;\sigma}$) creates (annihilates) one electron with spin σ in the κ -th sp_2 orbital of the j -th site of the ring, and $c_{j\sigma}^\dagger$ ($c_{j\sigma}$) creates (annihilates) one electron with spin σ at the p_z orbital of the same site. Later in this appendix, we explicit write $W_{j,\kappa}(\mathbf{r})$.

Hereafter, we treat the electrons in the p_z and sp_2 orbitals as *distinguishable* particles. This is one of the assumptions of our model which, at first glance, this might look a bit harsh. However, it is justified by separation of the energy scales of the system, as discussed in Sec.2.3.1. As a consequence the creation and annihilation operators in the sp_2 orbitals obey the following anti-commutation relations:

$$\{d_{i,\kappa\sigma}, d_{j,\gamma\sigma'}^\dagger\} = \delta_{i,j} \delta_{\kappa,\gamma} \delta_{\sigma,\sigma'}, \quad (\text{A.15})$$

$$\{d_{i,\kappa\sigma}^\dagger, d_{j,\gamma\sigma'}^\dagger\} = \{d_{i,\kappa\sigma}, d_{j,\gamma\sigma'}\} = 0, \quad (\text{A.16})$$

$$\{d_{i,\kappa\sigma}, c_{j,\sigma'}^\dagger\} = \{d_{i,\kappa\sigma}, c_{j,\sigma'}\} = 0. \quad (\text{A.17})$$

Substituting Eq.(A.14) into Eq.(A.2), we obtain $\hat{H} = \hat{H}_K + \hat{H}_{int}$, where the kinetic component,

$$\hat{H}_K = \sum_{i,j=1}^N \sum_{\sigma} \left[t_{ij} c_{i\sigma}^\dagger c_{j\sigma} + \sum_{\kappa=1}^2 \left(\bar{t}_{ij}^\kappa c_{i\sigma}^\dagger d_{j\kappa;\sigma} + h.c. \right) + \sum_{\kappa,\gamma=1}^2 \bar{t}_{ij}^{\kappa,\gamma} d_{i\kappa;\sigma}^\dagger d_{j\gamma;\sigma} \right], \quad (\text{A.18})$$

describes three processes: (a) the hopping between p_z orbitals of different sites as defined in Eq.(A.7), (b) the hopping between the p_z and sp_2 orbitals of distinct sites,

$$\bar{t}_{ij}^\kappa \equiv \langle \varphi_i | h | W_{j,\kappa} \rangle = \int d\mathbf{r} \varphi_i^*(\mathbf{r}) h(\mathbf{r}) W_{j,\kappa}(\mathbf{r}), \quad (\text{A.19})$$

and (c) the hopping between distinct sp_2 orbitals,

$$\bar{t}_{ij}^{\kappa,\gamma} \equiv \langle W_{i,\kappa} | h | W_{j,\gamma} \rangle = \int d\mathbf{r} W_{i,\kappa}^*(\mathbf{r}) h(\mathbf{r}) W_{j,\gamma}(\mathbf{r}). \quad (\text{A.20})$$

Recall that $h(\mathbf{r})$ is defined in Eq.(A.3). The interaction part of the Hamiltonian, \hat{H}_{int} , on the other hand, accounts for all possible matrix elements of the Coulomb repulsion involving (a) four p_z orbitals, (b) three p_z orbitals and one sp_2 , (c) two p_z and two sp_2 orbitals, (d) one p_z orbital and three sp_2 orbitals, and finally (d) four sp_2 orbitals. Its full

expression is very long and, since its straightforward obtained by substituting Eq.(A.14) into the interacting part of (A.2), it is unnecessary explicitly shown \hat{H}_{int} here.

Similarly as we did in Sec. A.1, we apply *Hubbard-like approximations* to simplify \hat{H} . The first one is to neglect the hopping between p_z and sp_2 orbitals. This is justified by the symmetry properties of $h(\mathbf{r})$, $\varphi_j(\mathbf{r})$ and $W_{j,\kappa}(\mathbf{r})$. Here we approximate the single-particle wave-functions as hydrogen-like orbitals,

$$\varphi_j(\mathbf{r}) = \varphi(\mathbf{r} - \mathcal{R}_j) = R_1(j)Y_1^0(\theta_j, \phi_j) , \quad (\text{A.21})$$

$$W_{j,\kappa}(\mathbf{r}) = W_\kappa(\mathbf{r} - \mathcal{R}_j) = \frac{1}{\sqrt{12\pi}}R_0(j) + 2R_1(j)\text{Re} [c_{j,\kappa}Y_1^{-1}(\theta_j, \phi_j)] , \quad (\text{A.22})$$

where \mathcal{R}_j is the position of the j -th site of the ring, already defined in Eq.(2.8), $j \equiv \mathbf{r} - \mathcal{R}_j$, with θ_j and ϕ_j denoting its polar and azimuthal angles, and $Y_l^m(\theta, \phi)$ are the spherical harmonics. Regarding the radial part of these functions

$$R_0(r) = \frac{1}{\sqrt{2a_0^3}} \left(1 - \frac{r}{2a_0}\right) e^{-r/2a_0} \quad (\text{A.23})$$

is the radial part of the wave function of an electron in the shell characterized by the principal quantum number $n = 2$ - since in the carbon atoms the valence electron are those in the $n = 2$ shell - and by the angular momentum number $l = 0$, which refers to an s -type orbital [38]. In addition,

$$R_1(\mathbf{r}) = \frac{r}{\sqrt{24a_0^5}} e^{-r/2a_0} \quad (\text{A.24})$$

is the radial part of the wave function of an electron in a shell with $n = 2$ and $l = 1$. Recall that a_0 denotes the Bohr radius. Moreover, the constants

$$c_{j,1} = \frac{1}{\sqrt{3}} e^{i(\alpha_j + 2\pi/3)} , \quad (\text{A.25})$$

$$c_{j,2} = \frac{1}{\sqrt{3}} e^{i(\alpha_j - 2\pi/3)} , \quad (\text{A.26})$$

encodes the spacial orientation of the sp_2 orbitals. Here $\alpha_j = (j - 1)2\pi/N$ is the angular position of the j -th site of the ring.

We can readily see that Eqs.(A.21) and (A.22) are *odd* and *even*, respectively, under the transformation $\theta_j \rightarrow \pi - \theta_j$, while ϕ_j remains unchanged, which corresponds to a reflection in the xy plane ($z \rightarrow -z$). That is because $Y_1^0(\pi - \theta_j, \phi_j) = -Y_1^0(\theta_j, \phi_j)$, while $Y_1^{\pm 1}(\pi - \theta_j, \phi_j) = Y_1^{\pm 1}(\theta_j, \phi_j)$. The single-particle Hamiltonian $h(\mathbf{r})$, on the other hand, is always *even* under such reflection, because the periodic potential V_c exhibits this symmetry. As a consequence the integrand in Eq.(A.19) is *odd* under xy -plane reflection, which causes \bar{t}_{ij}^κ to vanish. In the same way, the hopping between a p_z and a s hydrogen-like orbital is also zero, as we mention in Sec.2.1.

The second approximation has to do with the hopping between sp_2 orbitals, we assume that the nearest-neighbor sites give the major contribution to $\bar{t}_{ij}^{\kappa\gamma}$. Therefore, in Eq.(A.20), we only take into account the hoppings (a) between the *right* sp_2 orbital of site j and the *left* sp_2 orbital of the site $j + 1$ and (b) between the *left* sp_2 orbital of the site j and the *right* orbital of the site $j - 1$. Mathematically, such approximation is

$$\bar{t}_{ij}^{\kappa,\gamma} \approx -\tilde{t} [\delta_{j,i+1}\delta_{\kappa,1}\delta_{\gamma,2} + \delta_{j,i-1}\delta_{\kappa,2}\delta_{\gamma,1}\delta] . \quad (\text{A.27})$$

Here, we define $\langle W_{i,1} | h | W_{i+1}, 2 \rangle = \langle W_{i,2} | h | W_{i-1}, 1 \rangle \equiv -\tilde{t}$ (with $\tilde{t} > 0$), independent of the rings site. Note that, since the overlap between first neighbors sp_2 orbitals is typically larger the overlap between p_z orbitals, we have $\tilde{t} > t$.

The next set of approximation involves the interaction part of the the Hamiltonian \hat{H}_{int} . Similarly to Sec. A.1, we keep only on-site Coulomb repulsion, which, as we show in Appendix B, are those that give the leading contributions to the matrices elements of \hat{H}_{int} . Under these assumptions, the interaction part of the Hamiltonian takes the form

$$\begin{aligned} \hat{H}_{int} = & \frac{1}{2} \sum_{\sigma, \sigma'} \sum_{j=1}^N \left\{ \langle \varphi_j \varphi_j | u | \varphi_j \varphi_j \rangle c_{j\sigma}^\dagger c_{j\sigma'}^\dagger c_{j\sigma'} c_{j\sigma} \right. \\ & + \sum_{\kappa_1, \kappa_2, \kappa_3, \kappa_4} \langle W_{j, \kappa_1} W_{j, \kappa_2} | u | W_{j, \kappa_4} W_{j, \kappa_3} \rangle d_{j\kappa_1, \sigma}^\dagger d_{j\kappa_2, \sigma'}^\dagger d_{j\kappa_3, \sigma'} d_{j\kappa_4, \sigma} \\ & + 2 \sum_{\kappa} \langle \varphi_j \varphi_j | u | W_{j, \kappa} \varphi_j \rangle \left(c_{j\sigma}^\dagger c_{j\sigma'}^\dagger c_{j\sigma'} d_{j\kappa, \sigma} + \text{h.c.} \right) \\ & + 2 \sum_{\kappa_1, \kappa_2, \kappa_3} \langle W_{j, \kappa_1} W_{j, \kappa_2} | u | W_{j, \kappa_3} \varphi_j \rangle \left(d_{j\kappa_1, \sigma}^\dagger d_{j\kappa_2, \sigma'}^\dagger c_{j\sigma'} d_{j\kappa_3, \sigma} + \text{h.c.} \right) \\ & + \sum_{\kappa_1, \kappa_2} \langle \varphi_j \varphi_j | u | W_{j, \kappa_1} W_{j, \kappa_2} \rangle \left(c_{j\sigma}^\dagger c_{j\sigma'}^\dagger d_{j\kappa_2, \sigma'} d_{j\kappa_1, \sigma} + \text{h.c.} \right) \\ & + \sum_{\kappa_1, \kappa_2} \langle \varphi_j W_{j, \kappa_1} | u | W_{j, \kappa_2} \varphi_j \rangle \left(c_{j\sigma}^\dagger d_{j\kappa_1, \sigma'}^\dagger c_{j\sigma'} d_{j\kappa_2, \sigma} + \text{h.c.} \right) \\ & \left. + \sum_{\kappa_1, \kappa_2} \langle \varphi_j W_{j, \kappa_1} | u | \varphi_j W_{j, \kappa_2} \rangle \left(c_{j\sigma}^\dagger d_{j\kappa_1, \sigma'}^\dagger d_{j\kappa_2, \sigma'} c_{j\sigma} + \text{h.c.} \right) \right\} \quad (\text{A.28}) \end{aligned}$$

Note that because the Wannier wave functions in Eqs.(A.21) and (A.22) are real, the interaction matrices elements are also real and the following identities hold:

$$\langle \varphi_j \varphi_j | u | W_{j, \kappa} \varphi_j \rangle = \langle \varphi_j \varphi_j | u | \varphi_j W_{j, \kappa} \rangle , \quad (\text{A.29})$$

$$\langle W_{j, \kappa_1} W_{j, \kappa_2} | u | W_{j, \kappa_3} \varphi_j \rangle = \langle W_{j, \kappa_2} W_{j, \kappa_1} | u | \varphi_j W_{j, \kappa_3} \rangle , \quad (\text{A.30})$$

$$\langle \varphi_j \varphi_j | u | W_{j, \kappa_1} W_{j, \kappa_2} \rangle = \langle \varphi_j W_{j, \kappa_2} | u | W_{j, \kappa_1} \varphi_j \rangle , \quad (\text{A.31})$$

$$\langle \varphi_j W_{j, \kappa_1} | u | \varphi_j W_{j, \kappa_2} \rangle = \langle W_{j, \kappa_1} \varphi_j | u | W_{j, \kappa_2} \varphi_j \rangle . \quad (\text{A.32})$$

Again due to symmetry arguments, the interaction matrices elements involving only one p_z orbital or only one sp_2 are identically zero. Moreover, as we show in Appendix B for the specific case of the prototype of the benzene molecule, $\langle \varphi_j \varphi_j | u | W_{j,\kappa_1} W_{j,\kappa_2} \rangle$ is subleading and can be neglected. Thus \hat{H}_{int} can be further simplified as a contribution of only four terms ,

$$\begin{aligned} \hat{H}_{int} = \frac{1}{2} \sum_{j=1}^N \left\{ U c_{j\sigma}^\dagger c_{j\sigma'}^\dagger c_{j\sigma'} c_{j\sigma} + \tilde{U}_1 \sum_{\kappa} d_{j\kappa,\sigma}^\dagger d_{j\kappa,\sigma'}^\dagger d_{j\kappa,\sigma'} d_{j\kappa,\sigma} \right. \\ \left. + \tilde{U}_2 \sum_{\kappa} d_{j\kappa,\sigma}^\dagger d_{j\bar{\kappa},\sigma'}^\dagger d_{j\bar{\kappa},\sigma'} d_{j\kappa,\sigma} + U_c \sum_{\kappa} \left(c_{j\sigma}^\dagger d_{j\kappa,\sigma'}^\dagger d_{j\kappa,\sigma'} c_{j\sigma} + \text{h.c.} \right) \right\} \quad (\text{A.33}) \end{aligned}$$

where $\bar{\kappa} = 2$ ($\bar{\kappa} = 1$) if $\kappa = 1$ ($\kappa = 2$). In Eq.(A.33), the term proportional to U is the usual on-site Coulomb repulsion between two electrons in the p_z orbital, the same that appears in Eq.(A.13). The term proportional to \tilde{U}_1 (\tilde{U}_2), on the other hand, describes the intra-orbital (inter-orbital) on-site Coulomb repulsion between two σ electrons in the same (in different) sp_2 orbitals of the same ring site. The last term, proportional to U_c describes a density-density coupling between σ -electrons and π -electrons, as will become more evident in Eq.(A.35).

Combining Eqs.(A.18) and (A.33) and using the fermionic anti-commutation relations, we can write the three-band Hubbard Hamiltonian as $\hat{H} = \hat{H}_p + \hat{H}_{sp} + \hat{H}_c$, where \hat{H}_p is the Hubbard Hamiltonian for the degrees of freedom of the π -electrons only identical to Eq.(A.13), with the only difference that here, contrary to the case of the Appendix A.1, the σ -electrons *do not* contribute to the ring periodic potential. Besides,

$$\hat{H}_{sp} = -\tilde{t} \sum_{j=1}^N \sum_{\sigma} \left(d_{j,1\sigma}^\dagger d_{j+1,2\sigma} + d_{j,2\sigma}^\dagger d_{j-1,1\sigma} \right) + \sum_{j=1}^N \left[\tilde{U}_1 \sum_{\kappa} \hat{n}_{j,\kappa\uparrow} \hat{n}_{j,\kappa\downarrow} + \tilde{U}_2 \sum_{\sigma,\sigma'} \hat{n}_{j,1\sigma} \hat{n}_{j,2\sigma} \right] \quad (\text{A.34})$$

is the Hubbard Hamiltonian for the σ -electrons degrees of freedom, and

$$\hat{H}_c = U_c \sum_{j=1}^N \sum_{\kappa} \sum_{\sigma,\sigma'} \hat{n}_{j\sigma} \hat{n}_{j,\kappa\sigma'} \quad (\text{A.35})$$

express the coupling between these two "kinds" of electron. In Eqs.(A.34) and (A.35), we $\hat{n}_{j,\kappa\sigma} = d_{j,\kappa\sigma}^\dagger d_{j,\kappa\sigma}$ are the number operators associated with the sp_2 orbitals.

APPENDIX B – Estimation of the on-site Coulomb repulsion

In this appendix we estimate the matrix elements of the on-site Coulomb repulsion that appears in the interaction segment of the multiband Hubbard Hamiltonian we derive in Appendix A - see Eq.(A.33). Here in the ring with six sites at the half-filling regime (prototype of the benzene molecule) and, in order to be able to solve the integrals analytically, we approximate the Wannier wave functions by hydrogen-like orbitals.

Let's start by calculating the Coulomb repulsion between two π -electrons at the j -th site of the ring. Recall that such on-site interaction is characterized by the parameter

$$U \equiv \langle \varphi_j \varphi_j | u | \varphi_j \varphi_j \rangle = e^2 \int \int d\mathbf{r} d\mathbf{r}' \frac{|\varphi_j(\mathbf{r})|^2 |\varphi_j(\mathbf{r}')|^2}{|\mathbf{r} - \mathbf{r}'|}, \quad (\text{B.1})$$

where $\varphi_j(\mathbf{r})$ is the Wannier function for the p_z orbitals, which, in the localized orbital approximation takes the form of Eq.(A.21).

Making the change of variables $\mathbf{y} = \mathbf{r} - \mathcal{R}_j$ and $\mathbf{y}' = \mathbf{r}' - \mathcal{R}_j$, where \mathcal{R}_j is the position of the j -th site of the ring defined in Eq.(2.8), and using spherical Harmonics expansion [63],

$$\frac{1}{|\mathbf{y} - \mathbf{y}'|} = 4\pi \sum_{l=0}^{\infty} \sum_{m=-l}^l \frac{1}{2l+1} \frac{y_{<}^l}{y_{>}^{l+1}} Y_l^m(\theta, \phi) Y_l^{m*}(\theta', \phi'), \quad (\text{B.2})$$

we can rewrite Eq.(B.1) as

$$U = 4\pi e^2 \sum_{l=0}^{\infty} \sum_{m=-l}^l \frac{1}{2l+1} \int_0^{\infty} dy \int_0^{\infty} dy' y^2 y'^2 \frac{y_{<}^l}{y_{>}^{l+1}} R_l^2(y) R_l^2(y') I_{ang}(l, m). \quad (\text{B.3})$$

Here, $y_{<} = \min\{y, y'\}$ ($y_{>} = \max\{y, y'\}$) is the smaller (larger) of the absolute value of y and y' . Moreover θ and ϕ (θ' and ϕ') are the polar and azimuthal angles associated with the vector \mathbf{y} (\mathbf{y}'). The angular integration in Eq.(B.3),

$$I_{ang}(l, m) = \int d\Omega Y_l^m(\theta, \phi) [Y_1^0(\theta, \phi)]^2 \int d\Omega' Y_l^{m*}(\theta', \phi') [Y_1^0(\theta', \phi')]^2 \quad (\text{B.4})$$

can be calculated analytically: since ¹ $[Y_1^0(\theta, \phi)]^2 = Y_2^0(\theta, \phi)/\sqrt{5\pi} + Y_0^0(\theta, \phi)/\sqrt{4\pi}$, the orthonormality relation of the spherical Harmonics yields

$$I_{ang}(l, m) = \left(\frac{\delta_{l,2}}{5\pi} + \frac{\delta_{l,0}}{4\pi} \right) \delta_{m,0}. \quad (\text{B.5})$$

¹Another useful spherical Harmonics multiplications that we encounter in the calculation of

Therefore, substituting Eq.(B.5) into Eq.(B.3), we find

$$U = e^2 \left(\mathcal{I} [R_1^2(y), R_1^2(y'), 0] + \frac{4}{25} \mathcal{I} [R_1^2(y), R_1^2(y'), 2] \right) = \frac{501}{2560} \frac{e^2}{a_0} \approx 0.196 \frac{e^2}{a_0}, \quad (\text{B.6})$$

recalling that a_0 denotes the Bohr radius. Besides, here we define

$$\mathcal{I} [F_1(y), F_2(y'), l] = \int_0^\infty dy \int_0^\infty dy' y^2 y'^2 \frac{y^l}{y^{l+1}} F_1(y) F_2(y') \quad (\text{B.7})$$

$$= \int_0^\infty dy \int_0^y dy' \frac{y'^{l+2}}{y^{l-1}} F_1(y) F_2(y') + \int_0^\infty dy \int_y^\infty dy' \frac{y'^{l+2}}{y'^{l-1}} F_1(y) F_2(y'), \quad (\text{B.8})$$

for any functions $F_1(y)$ and $F_2(y')$ of y and y' , respectively.

Let's turn to the interaction matrix elements in Eq.(A.33). The procedure is analogous to what we just shown to calculate U , so we skip the intermediary steps. Here, however, we have an explicit dependence of the Wannier wave functions on the sites positions. Such dependence occurs via the constants $c_{j,\kappa}$ - see Eqs.(A.22), (A.25) and (A.26). Therefore hereafter the focus is in the prototype of the benzene molecule ($N = 6$).

As we mention in Appendix A,

$$\langle \varphi_j \varphi_j | u | W_{j,\kappa} \varphi_j \rangle = e^2 \int \int d\mathbf{r} d\mathbf{r}' \frac{\varphi_j^*(\mathbf{r}) W_{j,\kappa}(\mathbf{r}) |\varphi_j(\mathbf{r}')|^2}{|\mathbf{r} - \mathbf{r}'|} = 0, \quad (\text{B.9})$$

for the localized orbital approximation, Eqs.(A.21) and (A.22). That is simply because from the angular over θ and ϕ we find contributions as

$$\int d\Omega Y_l^m(\theta, \phi) Y_1^0(\theta, \phi) = \delta_{l,1} \delta_{m,0} \quad (\text{B.10})$$

and

$$\begin{aligned} \int d\Omega Y_l^m(\theta, \phi) Y_1^0(\theta, \phi) Y_1^{\pm 1}(\theta, \phi) &= \sqrt{\frac{3}{20\pi}} \int d\Omega Y_l^m(\theta, \phi) Y_2^{\pm 1}(\theta, \phi) \\ &= \sqrt{\frac{3}{20\pi}} (-1)^m \delta_{l,2} \delta_{m,\pm 1}, \end{aligned} \quad (\text{B.11})$$

while from the angular integral over θ' and ϕ' we find a different set of Kronecker deltas

$$\int d\Omega' [Y_l^m(\theta', \phi')]^* [Y_1^0(\theta, \phi)]^2 = \frac{1}{\sqrt{5}} \delta_{l,2} \delta_{m,0} + \frac{1}{\sqrt{4\pi}} \delta_{l,0} \delta_{m,0}. \quad (\text{B.12})$$

this Appendix: $Y_1^0(\theta, \phi) Y_1^{\pm 1}(\theta, \phi) = \sqrt{\frac{3}{20\pi}} Y_2^{\pm 1}(\theta, \phi)$, $Y_1^{\pm 1}(\theta, \phi) Y_1^{\pm 1}(\theta, \phi) = \sqrt{\frac{3}{10\pi}} Y_2^{\pm 2}(\theta, \phi)$ and $Y_1^1(\theta, \phi) Y_1^{-1}(\theta, \phi) = \frac{1}{\sqrt{20\pi}} Y_2^0(\theta, \phi) - \frac{1}{\sqrt{4\pi}} Y_0^0(\theta, \phi)$.

Since these different angular integrals appear as a product in the matrix element Eq.(B.9), the result is identically zero, for all κ . Similarly, $\langle W_{j,\kappa_1} W_{j,\kappa_2} |u| W_{j,\kappa_3} \varphi_j \rangle = 0$ for all κ_1, κ_2 and κ_3 .

Now, concerning

$$\langle \varphi_j \varphi_j |u| W_{j,\kappa_1} W_{j,\kappa_2} \rangle = \langle \varphi_j W_{j,\kappa_2} |u| W_{j,\kappa_2} \varphi_j \rangle = e^2 \int \int d\mathbf{r} d\mathbf{r}' \frac{\varphi_j(\mathbf{r}) \varphi_j(\mathbf{r}') W_{j,\kappa_1}(\mathbf{r}) W_{j,\kappa_2}(\mathbf{r}')}{|\mathbf{r} - \mathbf{r}'|}, \quad (\text{B.13})$$

we can write it in a matrix form:

$$\langle \varphi_j \varphi_j |u| W_{j,\kappa_1} W_{j,\kappa_2} \rangle \equiv (M_1)_{\kappa_1, \kappa_2}, \quad (\text{B.14})$$

where

$$(M_1)_{\kappa_1, \kappa_2} = e^2 \left\{ \frac{1}{9} \mathcal{I} [R_0(y) R_1(y), R_0(y') R_1(y'), 1] + \frac{6}{25} \text{Re} [(c_{j,\kappa_1})^* c_{j,\kappa_2}] \mathcal{I} [R_1^2(y), R_1^2(y'), 2] \right\}, \quad (\text{B.15})$$

and, again, the radial integrals can be calculated analytically. Interestingly, the dependence on j of $(c_{j,\kappa_1})^* c_{j,\kappa_2}$ vanishes and the resulting matrix is *site independent*:

$$M_1 = \frac{e^2}{a_0} \begin{pmatrix} \frac{43}{2560} & \frac{1}{160} \\ \frac{1}{160} & \frac{43}{2560} \end{pmatrix} \approx \frac{e^2}{a_0} \begin{pmatrix} 0.017 & 0.006 \\ 0.006 & 0.017 \end{pmatrix}. \quad (\text{B.16})$$

Similarly,

$$\langle \varphi_j W_{j,\kappa_1} |u| \varphi_j W_{j,\kappa_2} \rangle = e^2 \int \int d\mathbf{r} d\mathbf{r}' \frac{\varphi_j^2(\mathbf{r}) W_{i,\kappa_1}^\alpha(\mathbf{r}') W_{i,\kappa_2}(\mathbf{r}')}{|\mathbf{r} - \mathbf{r}'|} \equiv (M_2)_{\kappa_1, \kappa_2}, \quad (\text{B.17})$$

with

$$(M_2)_{\kappa_1, \kappa_2} = e^2 \left\{ \frac{1}{3} \mathcal{I} [R_1^2(y), R_0^2(y'), 0] + \frac{4}{25} \text{Re} [c_{j,\kappa_1} (c_{j,\kappa_2})^*] \mathcal{I} [R_1^2(y), R_1^2(y'), 2] \right. \\ \left. - 2 \text{Re} [c_{j,\kappa_1} (c_{j,\kappa_2})^*] \mathcal{I} [R_1^2(y), R_1^2(y'), 0] \right\}, \quad (\text{B.18})$$

which in turn results in

$$M_2 = \frac{e^2}{a_0} \begin{pmatrix} \frac{1309}{7680} & -\frac{1}{240} \\ -\frac{1}{240} & \frac{1309}{7680} \end{pmatrix} \approx \frac{e^2}{a_0} \begin{pmatrix} 0.170 & -0.004 \\ -0.004 & 0.170 \end{pmatrix}. \quad (\text{B.19})$$

The most complicated matrix element is

$$\langle W_{j,\kappa_1} W_{j,\kappa_2} |u| W_{j,\kappa_3} W_{j,\kappa_4} \rangle = e^2 \int \int d\mathbf{r} d\mathbf{r}' \frac{W_{j,\kappa_1}(\mathbf{r}) W_{j,\kappa_3}(\mathbf{r}) W_{j,\kappa_2}(\mathbf{r}') W_{j,\kappa_4}(\mathbf{r}')}{|\mathbf{r} - \mathbf{r}'|} \equiv (M_3)_{m,n}, \quad (\text{B.20})$$

which can also be written in a matrix form if we define the basis $\{|11\rangle, |12\rangle, |21\rangle, |22\rangle\}$, in this order and identify $(M_3)_{1,2} = \langle 11 | M_3 | 12 \rangle \equiv \langle W_{j,1} W_{j,1} | u | W_{j,1} W_{j,2} \rangle$. Therefore,

$$\begin{aligned} \langle \kappa_1 \kappa_2 | M_3 | \kappa_3 \kappa_4 \rangle = e^2 \left\{ \frac{1}{9} \mathcal{I} [R_0^2(y), R_0^2(y'), 0] + \frac{2Re [c_{j,\kappa_2} (c_{j,\kappa_3})^*]}{3} \mathcal{I} [R_0^2(y), R_1^2(y'), 0] \right. \\ + \frac{2Re [c_{j,\kappa_1} (c_{j,\kappa_4})^*]}{3} \mathcal{I} [R_1^2(y), R_0^2(y'), 0] \\ + 4Re [c_{j,\kappa_2} (c_{j,\kappa_3})^*] Re [c_{j,\kappa_1} (c_{j,\kappa_4})^*] \mathcal{I} [R_1^2(y), R_1^2(y'), 0] \\ + \frac{2Re [(c_{j,\kappa_1} + c_{j,\kappa_4}) (c_{j,\kappa_2} + c_{j,\kappa_3})^*]}{9} \mathcal{I} [R_0(y) R_1(y), R_0(y') R_1(y'), 1] \\ + \frac{4Re [(c_{j,\kappa_1} c_{j,\kappa_4}) (c_{j,\kappa_2} c_{j,\kappa_3})^*]}{25} \mathcal{I} [R_1^2(y), R_1^2(y'), 2] \\ \left. + \frac{4Re [c_{j,\kappa_2} (c_{j,\kappa_3})^*] Re [c_{j,\kappa_1} (c_{j,\kappa_4})^*]}{25} \mathcal{I} [R_1^2(y), R_1^2(y'), 2] \right\}, \quad (\text{B.21}) \end{aligned}$$

and we find

$$M_3 = \frac{e^2}{a_0} \begin{pmatrix} \frac{4649}{23040} & -\frac{13}{5760} & -\frac{13}{5760} & \frac{287}{23040} \\ \frac{13}{5760} & \frac{3587}{23040} & \frac{287}{23040} & -\frac{13}{5760} \\ -\frac{13}{5760} & \frac{287}{23040} & \frac{3587}{23040} & -\frac{13}{5760} \\ -\frac{287}{23040} & -\frac{13}{5760} & -\frac{13}{5760} & \frac{4649}{23040} \end{pmatrix} \approx \frac{e^2}{a_0} \begin{pmatrix} 0.202 & -0.002 & -0.002 & 0.012 \\ -0.002 & 0.156 & 0.012 & -0.002 \\ -0.002 & 0.012 & 0.156 & -0.002 \\ 0.012 & -0.002 & -0.002 & 0.202 \end{pmatrix}. \quad (\text{B.22})$$

Comparing Eqs.(B.16), (B.19) and (B.22) we can readily see that their *diagonal* elements are the *dominant ones*. Moreover, the diagonal elements of M_1 are much smaller than those of M_2 and M_3 , and also much smaller than U . As a consequence, we can completely neglect M_1 .

Neglecting both M_1 and the off-diagonal elements of M_2 and M_3 , Eq.(A.28) reduces to Eq.(A.33), where

$$\tilde{U}_1 = \langle W_{j,\kappa} W_{j,\kappa} | u | W_{j,\kappa} W_{j,\kappa} \rangle = \langle 11 | M_3 | 11 \rangle = \langle 22 | M_3 | 22 \rangle \approx 0.202 \frac{e^2}{a_0}, \quad (\text{B.23})$$

$$\tilde{U}_2 = \langle W_{j,\kappa} W_{j,\bar{\kappa}} | u | W_{j,\kappa} W_{j,\bar{\kappa}} \rangle = \langle 12 | M_3 | 12 \rangle = \langle 21 | M_3 | 21 \rangle \approx 0.156 \frac{e^2}{a_0}, \quad (\text{B.24})$$

$$U_c = \langle \varphi_j W_{j,\kappa} | u | \varphi_j W_{j,\kappa} \rangle = \langle 11 | M_2 | 11 \rangle = \langle 22 | M_2 | 22 \rangle \approx 0.170 \frac{e^2}{a_0}, \quad (\text{B.25})$$

are all of the same order of the π -electrons on-site Coulomb repulsion. Recall that, consistently with the notation we used before, $\bar{\kappa} = 1$ ($\bar{\kappa} = 2$) if $\kappa = 2$ ($\kappa = 1$). Similar results holds for rings with $N \neq 6$.

Finding estimations for the hopping parameter between p_z orbitals (t) and sp_2 orbitals (\tilde{t}) is a much more complex task for two reasons: (a) first, we need the precise form of the periodic potential and (b) the integrals we need to solve involves Wannier functions centered at different sites, which makes the changes of variables we introduced in this Appendix, and also the subsequent analytic approach unfeasible. Therefore, we do not provide estimations for neither t nor \tilde{t} . For the purposes of this thesis, we use, when dealing with the prototype of the benzene molecule, the values $t = 2.54eV$ and $U/t = 1.2$, obtained by the authors in Refs.[40, 42]. We also keep in mind that $\tilde{t} > t$, since the overlap between neighbors sp_2 orbitals is larger than the overlap between p_z orbitals. In most of the calculations shown in this work, we are careful to present the physical observables in units of t and/or \tilde{t} .

APPENDIX C – Matrix element of \mathbf{P} in the site basis

In this Appendix we derive the approximate expression for the matrix element of the electronic momentum \mathbf{P} , in the site basis, shown in Eq.(2.81).

The first thing we should note is that $\mathbf{V} \equiv \mathbf{P}/m$, where m denotes the electron mass, is simply the electron *velocity operator*, which is related to the system's single-particle Hamiltonian through the commutator

$$\mathbf{V} = \frac{1}{i\hbar} [\mathbf{R}, h] . \quad (\text{C.1})$$

Here, we denote by \mathbf{R} the electron position operator and we recall that the single particle Hamiltonian, in coordinate representation, is given by Eq.(A.3).

Calculating the expected value of Eq.(C.1) in the single-particle Wannier wave functions $\varphi_j(\mathbf{r}) = \langle \mathbf{r} | \varphi_j \rangle$, we obtain

$$\left\langle j_1 \left| \frac{1}{i\hbar} [\mathbf{R}, h] \right| j_2 \right\rangle = \frac{1}{m} \langle j_1 | \mathbf{P} | j_2 \rangle = \frac{1}{i\hbar} (\langle j_1 | \mathbf{R}h | j_2 \rangle - \langle j_1 | h\mathbf{R} | j_2 \rangle) . \quad (\text{C.2})$$

Now, inserting the closure relation

$$\mathbb{1} = \sum_{j=1}^N |j\rangle \langle j| \quad (\text{C.3})$$

between the \mathbf{R} and h operators on the right-hand side of Eq.(C.2) and approximating the position expected values as

$$\langle j_1 | \mathbf{R} | j_2 \rangle \approx \mathcal{R}_{j_2} \langle j_1 | j_2 \rangle = \mathcal{R}_{j_2} \delta_{j_1, j_2} , \quad (\text{C.4})$$

which is justified by the fact that the Wannier function $\varphi_j(\mathbf{r})$ is localized about the j -th site of the ring, whose position we denote by \mathcal{R}_j , we readily find

$$\frac{1}{m} \langle j_1 | \mathbf{P} | j_2 \rangle = \frac{1}{i\hbar} (\mathcal{R}_{j_1} - \mathcal{R}_{j_2}) \langle j_1 | h | j_2 \rangle . \quad (\text{C.5})$$

Finally, recalling that $\langle j_1 | h | j_2 \rangle = t_{j_1, j_2}$ gives the hopping between the sites j_1 and j_2 , which, in the nearest-neighbor approximation simplifies to

$$\langle j_1 | h | j_2 \rangle \approx -t \delta_{j_2, j_1 \pm 1} , \quad (\text{C.6})$$

we obtain Eq.(2.81):

$$\langle j_1 | \mathbf{P} | j_2 \rangle = -\frac{mt}{i\hbar} (\mathcal{R}_{j_1} - \mathcal{R}_{j_2}) \delta_{j_2, j_1 \pm 1} . \quad (\text{C.7})$$

APPENDIX D – Breit-Darwin Hamiltonian in second quantization

In this Appendix, for the purpose of comparison with our effective momentum-momentum interaction \mathcal{W}_{eff} , we derive the expression for the Breit-Darwin interaction in the Second Quantization formalism.

The Breit-Darwin Hamiltonian is a *relativistic correction* to the Coulomb repulsion of a system of N_e interacting electrons [63]. Roughly speaking, an electron moving with a velocity \mathbf{v} , generates a magnetic field, which is felt by another electron in this system through a Lorentz force. The Hamiltonian describing such collective interaction is

$$\mathcal{H}_{BD} = -\frac{1}{2c^2} \iint d\mathbf{r}d\mathbf{r}' \mathbf{J}(\mathbf{r}) \cdot \overleftrightarrow{\mathcal{G}}(\mathbf{r} - \mathbf{r}') \cdot \mathbf{J}(\mathbf{r}') . \quad (\text{D.1})$$

Note that Eq.(D.1) is a very weak interaction proportional to v^2/c^2 , where c is the light speed, justifying the denomination of relativistic correction. Our effective momentum-momentum interaction, on the other hand, having a completely different origin than \mathcal{H}_{BD} is a much larger magnitude, as we discuss in Sec. 2.3.4.

In Eq.(D.1), $\mathbf{J}(\mathbf{r})$ is the electric current operator, which in coordinate representation takes the form

$$\mathbf{J}(\mathbf{r}) = \frac{\hbar}{2mi} \sum_{j=1}^{N_e} [\nabla_j \delta(\mathbf{r} - \mathbf{r}_j) + \delta(\mathbf{r} - \mathbf{r}_j) \nabla_j] . \quad (\text{D.2})$$

Here ∇_j indicates the gradient with respect to the position \mathbf{r}_j of the j -th electron of the system, while N_e denotes the total number of electrons. Moreover, $\overleftrightarrow{\mathcal{G}}$ is a tensor, whose components are

$$G_{\mu\nu}(\mathbf{r} - \mathbf{r}') = \frac{e^2}{2} \left[\frac{\delta_{\mu,\nu}}{|\mathbf{r} - \mathbf{r}'|} + \frac{(r_\mu - r'_\mu)(r_\nu - r'_\nu)}{|\mathbf{r} - \mathbf{r}'|^3} \right] , \quad (\text{D.3})$$

with $\mu, \nu = x, y, z$.

There are two ways of deriving the second quantized expression of \mathcal{H}_{BD} : (a) we can second-quantize the the current operator in Eq.(D.2) and substitute the resulting expression into Eq.(D.1) imposing normal ordering of the creation and annihilation fermionic operators in order to avoid non-physical one-body terms, which would appear just as a consequence of the anti-commutation relations. The other option (b) is to

substitute Eq.(D.2) into Eq.(D.1) and second-quantize the resulting full two-body operator. We verified that both approaches give exactly the same result and here, for simplicity, we follow the procedure (a), since it is the simplest one.

As any other one-body operator, the second-quantized form of Eq.(D.2) is

$$\hat{\mathbf{J}}(\mathbf{r}) = \frac{\hbar}{2mi} \sum_{\sigma=\uparrow,\downarrow} \int d^3r' \hat{\psi}_\sigma^\dagger(\mathbf{r}') [\nabla' \delta(\mathbf{r} - \mathbf{r}') + \delta(\mathbf{r} - \mathbf{r}') \nabla'] \hat{\psi}_\sigma(\mathbf{r}') , \quad (\text{D.4})$$

where ∇' denotes the gradient with respect to \mathbf{r}' , and $\hat{\psi}_\sigma^\dagger(\mathbf{r})$ ($\hat{\psi}_\sigma(\mathbf{r})$) is the field operator that creates (annihilates) one electron with spin σ in the p_z orbital of the j -th site of the ring, as defined in Eq.(A.5). Note that here we are considering only one p_z orbital per site instead of the full three-orbital model. That is simply because we want to compare the Breit-Darwin interaction with the effective interaction \mathcal{W}_{eff} we derived in Sec. 2.3.3, which is an effective interaction between the π -electrons only.

Substituting Eq.(A.5) into Eq.(D.4), we find

$$\hat{\mathbf{J}}(\mathbf{r}) = \frac{\hbar}{2mi} \sum_{i,j=1}^N \sum_{\sigma} [\varphi_i^*(\mathbf{r}) (\nabla \varphi_j(\mathbf{r})) - \varphi_j(\mathbf{r}) (\nabla \varphi_i^*(\mathbf{r}))] c_{i\sigma}^\dagger c_{j\sigma} , \quad (\text{D.5})$$

where we used the integration by parts

$$\begin{aligned} \int d\mathbf{r}' f(\mathbf{r}') \nabla' [\delta(\mathbf{r} - \mathbf{r}') g(\mathbf{r}')] &= \int d\mathbf{r}' \nabla' [\delta(\mathbf{r} - \mathbf{r}') f(\mathbf{r}') g(\mathbf{r}')] \\ &\quad - \int d\mathbf{r}' \delta(\mathbf{r} - \mathbf{r}') g(\mathbf{r}') [\nabla' f(\mathbf{r}')] = -g(\mathbf{r}) \nabla f(\mathbf{r}) . \end{aligned} \quad (\text{D.6})$$

Now, substituting Eq.(D.5) into Eq.(D.1), and asking for the normal ordering of the fermionic operators, i.e. [22]

$$: c_{i\sigma}^\dagger c_{j\sigma} c_{k\sigma'}^\dagger c_{l\sigma'} : = c_{i\sigma}^\dagger c_{k\sigma'}^\dagger c_{l\sigma'} c_{j\sigma} , \quad (\text{D.7})$$

we readily obtain

$$\hat{H}_{BD} = \frac{\hbar^2}{8m^2c^2} \sum_{\mu,\nu} \sum_{i,j,k,l} \sum_{\sigma,\sigma'} (A_{ijkl} + B_{ijkl} - C_{ijkl} - D_{ijkl}) c_{i\sigma}^\dagger c_{k\sigma'}^\dagger c_{l\sigma'} c_{j\sigma} . \quad (\text{D.8})$$

with ¹

$$A_{ijkl} = \iint d\mathbf{r}d\mathbf{r}' \varphi_i^*(\mathbf{r}) (\partial_\mu \varphi_j(\mathbf{r})) G_{\mu\nu}(\mathbf{r} - \mathbf{r}') \varphi_k^*(\mathbf{r}') (\partial'_\nu \varphi_l(\mathbf{r}')) , \quad (\text{D.9})$$

$$B_{ijkl} = \iint d\mathbf{r}d\mathbf{r}' \varphi_j(\mathbf{r}) (\partial_\mu \varphi_i^*(\mathbf{r})) G_{\mu\nu}(\mathbf{r} - \mathbf{r}') \varphi_l(\mathbf{r}') (\partial'_\nu \varphi_k^*(\mathbf{r}')) , \quad (\text{D.10})$$

$$C_{ijkl} = \iint d\mathbf{r}d\mathbf{r}' \varphi_i^*(\mathbf{r}) (\partial_\mu \varphi_j(\mathbf{r})) G_{\mu\nu}(\mathbf{r} - \mathbf{r}') \varphi_l(\mathbf{r}') (\partial'_\nu \varphi_k^*(\mathbf{r}')) , \quad (\text{D.11})$$

$$D_{ijkl} = \iint d\mathbf{r}d\mathbf{r}' \varphi_j(\mathbf{r}) (\partial_\mu \varphi_i^*(\mathbf{r})) G_{\mu\nu}(\mathbf{r} - \mathbf{r}') \varphi_k^*(\mathbf{r}') (\partial'_\nu \varphi_l(\mathbf{r}')) . \quad (\text{D.12})$$

Note that Eq.(2.46) is equivalent to

$$A_{ijkl} = -\frac{1}{\hbar^2} \left\langle ik \left| \hat{G}_{\mu\nu}(\mathbf{X}_1, \mathbf{X}_2) \hat{P}_\mu^{(1)} \hat{P}_\nu^{(2)} \right| jl \right\rangle . \quad (\text{D.13})$$

The superscript index 1 (2) in the momentum operator denote that it acts in the first (second) entrance of the ket $|i, j\rangle = |i\rangle \otimes |j\rangle$, where $|i\rangle$ which in coordinate representation gives the Wannier function $\varphi_i(\mathbf{r})$. Eq.(D.13) is easy to show: first recognizing that

$$\partial_\mu \varphi_{i,\alpha}(\mathbf{r}) = \frac{i}{\hbar} \left\langle \mathbf{r} \left| \hat{P}_\mu \right| i\alpha \right\rangle , \quad (\text{D.14})$$

$$\partial_\mu \varphi_{i,\alpha}^*(\mathbf{r}) = -\frac{i}{\hbar} \left\langle i\alpha \left| \hat{P}_\mu \right| \mathbf{r} \right\rangle , \quad (\text{D.15})$$

we can rewrite Eq.(D.9) as

$$\begin{aligned} A_{ijkl} &= \iint d\mathbf{r}d\mathbf{r}' G_{\mu\nu}(\mathbf{r} - \mathbf{r}') \langle \mathbf{r} | P_\mu | j \rangle \langle \mathbf{r}' | P_\nu | l \rangle \langle i | \mathbf{r} \rangle \langle k | \mathbf{r}' \rangle \\ &= \iint d\mathbf{r}d\mathbf{r}' G_{\mu\nu}(\mathbf{r} - \mathbf{r}') \langle \mathbf{r}\mathbf{r}' | P_\mu^{(1)} P_\nu^{(2)} | jl \rangle \langle ik | \mathbf{r}\mathbf{r}' \rangle . \end{aligned} \quad (\text{D.16})$$

Moreover, $G_{\mu\nu}(\mathbf{r} - \mathbf{r}')$ can be seen as the coordinate representation of the Hermitian operator $\hat{G}_{\mu\nu}(\mathbf{X}_1, \mathbf{X}_2)$, where \mathbf{X}_1 (\mathbf{X}_2) is the position operator of the particle 1 (particle 2), i.e.,

$$G_{\mu\nu}(\mathbf{r} - \mathbf{r}') \langle ik | \mathbf{r}\mathbf{r}' \rangle = \left\langle ik \left| \hat{G}_{\mu\nu}(\mathbf{X}_1 - \mathbf{X}_2) \right| \mathbf{r}\mathbf{r}' \right\rangle . \quad (\text{D.17})$$

Therefore, substituting Eq.(D.17) into Eq.(D.16) and using the closure relation

$$\mathbb{1} = \iint d^3\mathbf{r}' |\mathbf{r}\mathbf{r}'\rangle \langle \mathbf{r}\mathbf{r}'| ,$$

we recover Eq.(D.13).

¹Hereafter we use the notation $\nabla = \sum_\mu \frac{\partial}{\partial r_\mu} \hat{e}_\mu = \sum_\mu \partial_\mu \hat{e}_\mu$ and $\nabla' = \sum_\mu \frac{\partial}{\partial r'_\mu} \hat{e}_\mu = \sum_\mu \partial'_\mu \hat{e}_\mu$.

Correspondingly, Eqs.(D.10)-(D.12) are equivalent to

$$B_{ijkl} = -\frac{1}{\hbar^2} \left\langle ik \left| \hat{P}_\mu^{(1)} \hat{P}_\nu^{(2)} \hat{G}_{\mu\nu}(\mathbf{X}_1, \mathbf{X}_2) \right| jl \right\rangle, \quad (\text{D.18})$$

$$C_{ijkl} = \frac{1}{\hbar^2} \left\langle ik \left| \hat{P}_\nu^{(2)} \hat{G}_{\mu\nu}(\mathbf{X}_1, \mathbf{X}_2) \hat{P}_\mu^{(1)} \right| jl \right\rangle, \quad (\text{D.19})$$

$$D_{ijkl} = \frac{1}{\hbar^2} \left\langle ik \left| \hat{P}_\mu^{(1)} \hat{G}_{\mu\nu}(\mathbf{X}_1, \mathbf{X}_2) \hat{P}_\nu^{(2)} \right| jl \right\rangle. \quad (\text{D.20})$$

Now, note that the set $\{|ij\rangle\}$ constitutes an orthonormal basis, with closure relation

$$\mathbb{1} = \sum_{i,j=1}^N |ij\rangle \langle ij|. \quad (\text{D.21})$$

So inserting identities Eq.(D.21) between the momentum operators and $\hat{G}_{\mu,\nu}$ in Eq.(D.13) and Eqs.(D.18)-(D.20), and approximating the matrices elements of $\hat{G}_{\mu,\nu}$ by a purely local term, i.e.

$$\left\langle ij \left| \hat{G}_{\mu\nu}(\mathbf{X}_1 - \mathbf{X}_2) \right| kl \right\rangle \approx \left\langle ii \left| \hat{G}_{\mu\nu}(\mathbf{X}_1 - \mathbf{X}_2) \right| ii \right\rangle \delta_{i,j} \delta_{i,k} \delta_{i,l}, \quad (\text{D.22})$$

where we define $T_{\mu\nu}^{(i)} \equiv \left\langle ii \left| \hat{G}_{\mu\nu}(\mathbf{X}_1 - \mathbf{X}_2) \right| ii \right\rangle$, those matrices elements simplify to

$$A_{ijkl} = -\frac{1}{\hbar^2} T_{\mu\nu}^{(i)} \left\langle i \left| \hat{P}_\mu \right| j \right\rangle \left\langle i \left| \hat{P}_\nu \right| l \right\rangle \delta_{i,k} = -\frac{1}{\hbar^2} \langle i | \mathbf{P} | j \rangle \cdot \overleftarrow{T}^{(i)} \cdot \langle i | \mathbf{P} | l \rangle \delta_{k,i}, \quad (\text{D.23})$$

$$B_{ijkl} = -\frac{1}{\hbar^2} T_{\mu\nu}^{(j)} \left\langle i \left| \hat{P}_\mu \right| j \right\rangle \left\langle k \left| \hat{P}_\nu \right| j \right\rangle \delta_{j,l} = -\frac{1}{\hbar^2} \langle i | \mathbf{P} | j \rangle \cdot \overleftarrow{T}^{(j)} \cdot \langle k | \mathbf{P} | j \rangle \delta_{j,l}, \quad (\text{D.24})$$

$$C_{ijkl} = \frac{1}{\hbar^2} T_{\mu\nu}^{(i)} \left\langle i \left| \hat{P}_\mu \right| j \right\rangle \left\langle k \left| \hat{P}_\nu \right| i \right\rangle \delta_{i,l} = \frac{1}{\hbar^2} \langle i | \mathbf{P} | j \rangle \cdot \overleftarrow{T}^{(i)} \cdot \langle k | \mathbf{P} | i \rangle \delta_{i,l}, \quad (\text{D.25})$$

$$D_{ijkl} = \frac{1}{\hbar^2} T_{\mu\nu}^{(j)} \left\langle i \left| \hat{P}_\mu \right| j \right\rangle \left\langle j \left| \hat{P}_\nu \right| l \right\rangle \delta_{j,k} = \frac{1}{\hbar^2} \langle i | \mathbf{P} | j \rangle \cdot \overleftarrow{T}^{(j)} \cdot \langle j | \mathbf{P} | l \rangle \delta_{k,j}. \quad (\text{D.26})$$

We can further simplify the previous equations using the nearest-neighbor approximation for the momentum matrix elements, Eq.(2.81). In this case, substituting Eq.(2.81) into Eqs.(D.23)-(D.26) and plugging the resulting expressions back into Eq.(D.18), we find, after a few change of variables,

$$\begin{aligned} \hat{H}_{BD} = \frac{1}{8m^2c^2} \left(\frac{mt}{\hbar} \right)^2 \sum_{j=1}^N \sum_{\sigma,\sigma'} \left[(\mathcal{R}_j - \mathcal{R}_{j+1}) \cdot \overleftarrow{T}^{(i)} \cdot (\mathcal{R}_j - \mathcal{R}_{j+1}) \hat{C}_j^{(1)} \right. \\ \left. + (\mathcal{R}_j - \mathcal{R}_{j+1}) \cdot \overleftarrow{T}^{(i)} \cdot (\mathcal{R}_j - \mathcal{R}_{j-1}) \hat{C}_j^{(2)} \right. \\ \left. (\mathcal{R}_j - \mathcal{R}_{j-1}) \cdot \overleftarrow{T}^{(i)} \cdot (\mathcal{R}_j - \mathcal{R}_{j+1}) \hat{C}_j^{(3)} \right. \\ \left. (\mathcal{R}_j - \mathcal{R}_{j-1}) \cdot \overleftarrow{T}^{(i)} \cdot (\mathcal{R}_j - \mathcal{R}_{j-1}) \hat{C}_j^{(4)} \right], \quad (\text{D.27}) \end{aligned}$$

with

$$\hat{C}_j^{(1)} = \left(c_{j\sigma}^\dagger c_{j\sigma'}^\dagger c_{j+1\sigma'} c_{j+1\sigma} + \text{h.c.} \right) - \left(c_{j\sigma}^\dagger c_{j+1\sigma'}^\dagger c_{j\sigma'} c_{j+1\sigma} + \text{h.c.} \right), \quad (\text{D.28})$$

$$\hat{C}_j^{(2)} = \left(c_{j\sigma}^\dagger c_{j\sigma'}^\dagger c_{j-1\sigma'} c_{j+1\sigma} + \text{h.c.} \right) - \left(c_{j\sigma}^\dagger c_{j-1\sigma'}^\dagger c_{j\sigma'} c_{j+1\sigma} + \text{h.c.} \right), \quad (\text{D.29})$$

$$\hat{C}_j^{(3)} = \left(c_{j\sigma}^\dagger c_{j\sigma'}^\dagger c_{j+1\sigma'} c_{j-1\sigma} + \text{h.c.} \right) - \left(c_{j\sigma}^\dagger c_{j+1\sigma'}^\dagger c_{j\sigma'} c_{j-1\sigma} + \text{h.c.} \right), \quad (\text{D.30})$$

$$\hat{C}_j^{(4)} = \left(c_{j\sigma}^\dagger c_{j\sigma'}^\dagger c_{j-1\sigma'} c_{j-1\sigma} + \text{h.c.} \right) - \left(c_{j\sigma}^\dagger c_{j-1\sigma'}^\dagger c_{j\sigma'} c_{j-1\sigma} + \text{h.c.} \right). \quad (\text{D.31})$$

D.1 Estimation of $\overleftrightarrow{T}^{(i)}$

Similarly to what we do in Appendix B, we can estimate $\overleftrightarrow{T}^{(i)}$. Substituting Eq.(D.3) into Eq.(D.22), we realize that we can separate $T_{\mu\nu}^{(i)}$ into two components: $\overleftrightarrow{T}^{(i)} = P_i \mathbb{1} + \overleftrightarrow{Q}^{(i)}$, where

$$P_i = \frac{e^2}{2} \iint d\mathbf{r} d\mathbf{r}' \frac{|\varphi_i(\mathbf{r})|^2 |\varphi_i(\mathbf{r}')|^2}{|\mathbf{r} - \mathbf{r}'|}, \quad (\text{D.32})$$

and

$$\begin{aligned} \overleftrightarrow{Q}^{(i)} &= \frac{e^2}{2} \iint d\mathbf{r} d\mathbf{r}' \frac{(\mathbf{r} - \mathbf{r}') (\mathbf{r} - \mathbf{r}')}{|\mathbf{r} - \mathbf{r}'|^3} |\varphi_i(\mathbf{r})|^2 |\varphi_i(\mathbf{r}')|^2 \\ &= e^2 \iint d\mathbf{r} d\mathbf{r}' \frac{\mathbf{r} (\mathbf{r} - \mathbf{r}')}{|\mathbf{r} - \mathbf{r}'|^3} |\varphi_i(\mathbf{r})|^2 |\varphi_i(\mathbf{r}')|^2. \end{aligned} \quad (\text{D.33})$$

Comparing Eq.(D.32) with Eq.(B.1), we readily find that $P_i = U/2$. Moreover, using a localized approximation for the p_z orbitals, i.e., assuming that $\varphi_j(\mathbf{r})$ has the functional form of Eq.(A.21), we can move on to calculate the tensor $\overleftrightarrow{Q}^{(i)}$.

In the same way as in Sec. B we start with the change of variables $\mathbf{y} = \mathbf{r} - \mathcal{R}_i$ and $\mathbf{y}' = \mathbf{r}' - \mathcal{R}_i$, recalling that \mathcal{R}_i denotes the ring's i -th site position. Thus Eq.(D.33) reduces to

$$\overleftrightarrow{Q}^{(i)} \iint d\mathbf{y} d\mathbf{y}' \frac{\mathbf{y} (\mathbf{y} - \mathbf{y}')}{|\mathbf{y} - \mathbf{y}'|^3} |\varphi(\mathbf{y})|^2 |\varphi(\mathbf{y}')|^2. \quad (\text{D.34})$$

Now, recalling that

$$\nabla \left(\frac{1}{|\mathbf{y} - \mathbf{y}'|} \right) = -\frac{\mathbf{y} - \mathbf{y}'}{|\mathbf{y} - \mathbf{y}'|^3}, \quad (\text{D.35})$$

and using into the expansion in spherical harmonics defined in Eq.(B.2) we can rewrite Eq.(D.34) as

$$\overleftrightarrow{Q}^{(i)} = -4\pi e^2 \sum_{l=0}^{\infty} \sum_{m=-l}^l \frac{1}{(2l+1)} \iint d\mathbf{y} d\mathbf{y}' |\varphi(\mathbf{y})|^2 |\varphi(\mathbf{y}')|^2 [Y_l^m(\theta', \phi')]^* \mathbf{y} \nabla \left(\frac{y_{>}^l}{y_{<}^{l+1}} Y_l^m(\theta, \phi) \right). \quad (\text{D.36})$$

The angular integral associated with \mathbf{y}' can be readily calculated using the spherical harmonics orthonormality,

$$\begin{aligned} I_{ang}(y') &\equiv \int d\Omega' |\varphi(\mathbf{y}')|^2 [Y_l^m(\theta', \phi')]^* \\ &= R_1^2(y') \left[\frac{1}{\sqrt{5\pi}} \delta_{l,2} \delta_{m,0} + \frac{1}{\sqrt{4\pi}} \delta_{l,0} \delta_{m,0} \right], \end{aligned} \quad (\text{D.37})$$

and if we write the gradient ∇ explicit in terms of spherical coordinates,

$$\nabla = \frac{\partial}{\partial y} \hat{y} + \frac{1}{y} \frac{\partial}{\partial \theta} \hat{\theta} + \frac{1}{y \sin \theta} \frac{\partial}{\partial \phi} \hat{\phi}, \quad (\text{D.38})$$

Eq.(D.36) becomes

$$\begin{aligned} \overleftrightarrow{Q}^{(i)} &= -4\pi e^2 \sum_{l=0}^{\infty} \sum_{m=-l}^l \frac{1}{(2l+1)} \int_0^{\infty} dy' y'^2 I_{ang}(y') \left[\int_0^{\infty} dy y^3 \frac{\partial}{\partial y} \left(\frac{y_{<}^l}{y_{>}^{l+1}} \right) \int d\Omega \varphi_{\alpha}^*(y) \varphi_{\gamma}(y) Y_l^m(\theta, \phi) \hat{y} \hat{y} \right. \\ &\quad + \int_0^{\infty} dy y^2 \frac{y_{<}^l}{y_{>}^{l+1}} \int d\Omega \varphi_{\alpha}^*(y) \varphi_{\gamma}(y) \left(\frac{\partial}{\partial \theta} Y_l^m(\theta, \phi) \right) \hat{y} \hat{\theta} \\ &\quad \left. + \int_0^{\infty} dy y^2 \frac{y_{<}^l}{y_{>}^{l+1}} \int d\Omega \varphi_{\alpha}^*(y) \varphi_{\gamma}(y) \frac{1}{\sin \theta} \left(\frac{\partial}{\partial \phi} Y_l^m(\theta, \phi) \right) \hat{y} \hat{\phi} \right]. \end{aligned} \quad (\text{D.39})$$

Here,

$$\hat{y} \hat{y} = \begin{pmatrix} \sin^2 \theta \cos^2 \phi & \sin^2 \theta \sin \phi \cos \phi & \sin \theta \cos \theta \cos \phi \\ \sin^2 \theta \sin \phi \cos \phi & \sin^2 \theta \sin^2 \phi & \sin \theta \cos \theta \sin \phi \\ \sin \theta \cos \theta \cos \phi & \sin \theta \cos \theta \sin \phi & \cos^2 \theta \end{pmatrix}, \quad (\text{D.40})$$

$$\hat{y} \hat{\theta} = \begin{pmatrix} \sin \theta \cos \theta \cos^2 \phi & \sin \theta \cos \theta \sin \phi \cos \phi & -\sin^2 \theta \cos \phi \\ \sin \theta \cos \theta \sin \phi \cos \phi & \sin \theta \cos \theta \sin^2 \phi & -\sin^2 \theta \sin \phi \\ \cos^2 \theta \cos \phi & \cos^2 \theta \sin \phi & -\sin \theta \cos \theta \end{pmatrix}, \quad (\text{D.41})$$

and

$$\hat{y} \hat{\phi} = \begin{pmatrix} -\sin \theta \sin \phi \cos \phi & \sin \theta \cos^2 \phi & 0 \\ -\sin \theta \sin^2 \phi & \sin \theta \sin \phi \cos \phi & 0 \\ -\cos \theta \sin \phi & \cos \theta \cos \phi & 0 \end{pmatrix}. \quad (\text{D.42})$$

Despite Eq.(D.39) looks complicated, we can calculate it analytically, obtaining

$$\overleftrightarrow{Q}^{(i)} = \frac{e^2}{a_0} \begin{pmatrix} \frac{993}{35840} & 0 & 0 \\ 0 & \frac{993}{35840} & 0 \\ 0 & 0 & \frac{1521}{35840} \end{pmatrix}, \quad (\text{D.43})$$

and, consequently

$$\overleftrightarrow{T}^{(i)} = \frac{e^2}{a_0} \begin{pmatrix} \frac{225}{1792} & 0 & 0 \\ 0 & \frac{225}{1792} & 0 \\ 0 & 0 & \frac{1257}{8960} \end{pmatrix} \approx U \begin{pmatrix} 0.64 & 0 & 0 \\ 0 & 0.64 & 0 \\ 0 & 0 & 0.72 \end{pmatrix}. \quad (\text{D.44})$$

Because of the matrix structure of $\overleftrightarrow{T}^{(i)}$, it readily follows that

$$(\mathcal{R}_j - \mathcal{R}_{j+1}) \cdot \overleftrightarrow{T}^{(i)} \cdot (\mathcal{R}_j - \mathcal{R}_{j+1}) = (\mathcal{R}_j - \mathcal{R}_{j-1}) \cdot \overleftrightarrow{T}^{(i)} \cdot (\mathcal{R}_j - \mathcal{R}_{j-1}) \approx 0.64a^2U, \quad (\text{D.45})$$

$$(\mathcal{R}_j - \mathcal{R}_{j+1}) \cdot \overleftrightarrow{T}^{(i)} \cdot (\mathcal{R}_j - \mathcal{R}_{j-1}) = (\mathcal{R}_j - \mathcal{R}_{j-1}) \cdot \overleftrightarrow{T}^{(i)} \cdot (\mathcal{R}_j - \mathcal{R}_{j+1}) \approx -0.64a^2U \cos\left(\frac{2\pi}{N}\right). \quad (\text{D.46})$$

Finally, substituting Eqs.(D.45) and (D.46) into Eq.(D.27) and recollecting the terms, we obtain

$$\begin{aligned} \hat{H}_{BD} = & \frac{0.64U(at)^2}{4c^2\hbar^2} \sum_{j=1}^N \sum_{\sigma,\sigma'} \left[(c_{j\sigma}^\dagger c_{j\sigma'}^\dagger c_{j+1\sigma'} c_{j+1\sigma} + \text{h.c.}) - (c_{j+1\sigma}^\dagger c_{j\sigma'}^\dagger c_{j+1\sigma'} c_{j\sigma} + \text{h.c.}) \right. \\ & \left. - \cos\left(\frac{2\pi}{N}\right) (c_{j+1\sigma}^\dagger c_{j-1\sigma'}^\dagger c_{j\sigma'} c_{j\sigma} + \text{h.c.}) + \cos\left(\frac{2\pi}{N}\right) (c_{j\sigma}^\dagger c_{j-1\sigma'}^\dagger c_{j-2\sigma'} c_{j-1\sigma} + \text{h.c.}) \right]. \quad (\text{D.47}) \end{aligned}$$

Four different processes contributes to \hat{H}_{BD} , two "bubbles" and two extended processes, as illustrated in Fig. 35.

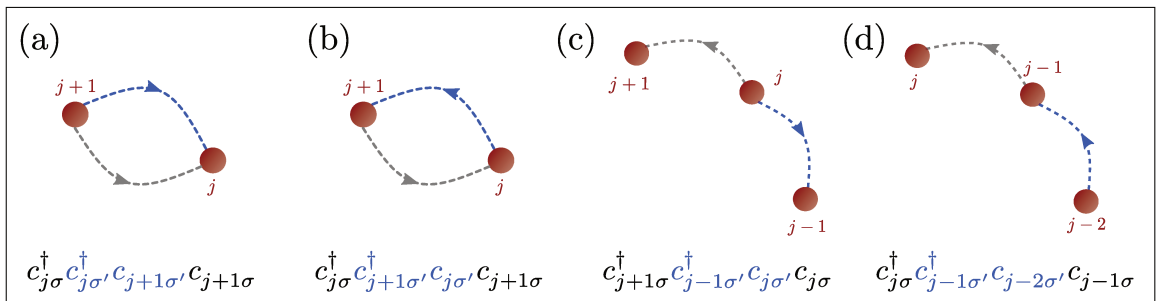


Figure 35 – **Breit-Darwin interaction.** Illustration of the four types of two-body processes that appear in the second-quantized Breit-Darwin interaction Eq.(D.47). (a) $c_{j\sigma}^\dagger c_{j\sigma'}^\dagger c_{j+1\sigma'} c_{j+1\sigma}$ and (b) $c_{j+1\sigma}^\dagger c_{j\sigma'}^\dagger c_{j+1\sigma'} c_{j\sigma}$ are the two "Bubble-type" terms, while (c) $c_{j+1\sigma}^\dagger c_{j-1\sigma'}^\dagger c_{j\sigma'} c_{j\sigma}$ and (d) $c_{j\sigma}^\dagger c_{j-1\sigma'}^\dagger c_{j-2\sigma'} c_{j-1\sigma}$ are the extended terms. The Hermitian conjugate of (a)-(d) just reverse the direction of the arrows.

APPENDIX E – Matsubara sums for the clean case

Here we provided a detailed derivation of the the analytic expressions for the matrix elements of \hat{A}_{clean} defined in Eqs.(3.20) and (3.21). This Appendix is reproduced from Ref. [36].

Deriving an analytic expression for the matrix elements $\left(\hat{A}_{\text{clean}}\right)_{ij}$ involves calculating, analytically, Matsubara sums of the type

$$\sum_n \frac{1}{\omega_n} \arctan\left(\frac{y}{\omega_n}\right) = \frac{\text{sign}(y)}{T_c} s_1\left(\frac{|y|}{T_c}\right), \quad (\text{E.1})$$

where the quantity y can assume the values Ω_0 , $W_1 = -\mu$ or $W_2 = -\mu + \varepsilon_0$, and

$$s_1(|x|) \equiv 2 \sum_{n=0}^{\infty} \frac{1}{(2n+1)\pi} \arctan\left(\frac{|x|}{(2n+1)\pi}\right). \quad (\text{E.2})$$

We calculate an approximate expression for $s_1(|x|)$, taking advantage of the asymptotic behavior of $\arctan\left(\frac{|x|}{(2n+1)\pi}\right)$ in two regimes: $|x| \ll 1$ and $|x| \gg 1$. If $|x| \ll 1$, $\frac{|x|}{(2n+1)\pi} \ll 1$ for all n , and a Taylor expansion of $\arctan\left(\frac{|x|}{(2n+1)\pi}\right)$ leads to

$$s_1(|x| \ll 1) = 2 \sum_{l=0}^{\infty} \frac{(-1)^l \zeta(2l+2) [2^{2l+2} - 1]}{(2l+1)(2\pi)^{2l+2}} |x|^{2l+1}, \quad (\text{E.3})$$

where we used the fact that

$$\sum_{n=0}^{\infty} \frac{1}{[(2n+1)\pi]^k} = \frac{(2^k - 1) \zeta(k)}{(2\pi)^k}, \quad (\text{E.4})$$

with integer $k \geq 2$ and $\zeta(k)$ denoting the Riemann zeta function. The leading term is clearly the $l = 0$:

$$s_1(|x| \ll 1) \sim \frac{|x|}{4}. \quad (\text{E.5})$$

On the other hand, if $|x| \gg 1$, $\frac{|x|}{(2n+1)\pi} \gg 1$ for small values of n , but the ratio decreases with increasing n , until it eventually behaves as $\frac{|x|}{(2n+1)\pi} \ll 1$ for large

enough n . Denoting by N^* the value of n such that $(2N^* + 1)\pi = |x|$, i.e. $N^* = \frac{|x|}{2\pi} - \frac{1}{2}$, we approximate $\arctan\left(\frac{|x|}{(2n+1)\pi}\right)$ by its Taylor expansion in powers of $1/|x|$ when $0 < n < N^*$, and by its Taylor expansion in powers of $|x|$ when $N^* + 1 < n < \infty$. The result is

$$s_1(|x| \gg 1) = \sum_{n=0}^{N^*} \frac{1}{2n+1} - 2 \sum_{l=0}^{\infty} \frac{(-1)^l}{(2l+1)|x|^{2l+1}} \sum_{n=0}^{N^*} [(2n+1)\pi]^{2l} + 2 \sum_{l=0}^{\infty} \frac{(-1)^l |x|^{2l+1}}{(2l+1)} \sum_{n=N^*+1}^{\infty} \frac{1}{[(2n+1)\pi]^{2l+2}}. \quad (\text{E.6})$$

The sums over n that appear in Eq.(E.6) can be evaluated analytically:

$$\sum_{n=0}^{N^*} \frac{1}{[(2n+1)\pi]^k} = \begin{cases} \frac{(2^k - 1)\zeta(k)}{(2\pi)^k} + \frac{1}{(2\pi)^k (|k| + 1)} B_{|k|+1}\left(1 + \frac{|x|}{2\pi}\right), & \text{if } k \leq 0 \\ \frac{1}{2\pi} \left[\psi\left(1 + \frac{|x|}{2\pi}\right) - \psi\left(\frac{1}{2}\right) \right], & \text{if } k = 1, \\ \frac{(2^k - 1)\zeta(k)}{(2\pi)^k} - \frac{1}{(k-1)!} \left(\frac{-1}{2\pi}\right)^k \psi^{(k-1)}\left(1 + \frac{|x|}{2\pi}\right), & \text{if } k > 1 \end{cases} \quad (\text{E.7})$$

and

$$\sum_{n=N^*+1}^{\infty} \frac{1}{[(2n+1)\pi]^k} = \frac{1}{(k-1)!} \left(\frac{-1}{2\pi}\right)^k \psi^{(k-1)}\left(1 + \frac{|x|}{2\pi}\right), \quad \text{if } k \geq 2, \quad (\text{E.8})$$

where $\psi^{(k)}(x)$, $\psi(x) = \psi^{(0)}(x)$ and $B_k(x)$ are, respectively, the polygamma function of k -th order, the digamma function, and the Bernoulli polynomials. In the limit $|x| \gg 1$, a Taylor expansion, up to order $\mathcal{O}\left(\frac{1}{|x|^k}\right)$ leads to:

$$\sum_{n=0}^{N^*} \frac{1}{[(2n+1)\pi]^k} \sim \begin{cases} \frac{1}{2\pi} \ln(\kappa|x|), & \text{if } k = 1 \\ \frac{(2^k - 1)\zeta(k)}{(2\pi)^k} - \frac{1}{2\pi(k-1)|x|^{k-1}}, & \text{if } k \leq 0 \text{ or } k > 1 \end{cases}, \quad (\text{E.9})$$

and

$$\sum_{n=N^*+1}^{\infty} \frac{1}{[(2n+1)\pi]^k} \sim \frac{1}{2\pi(k-1)|x|^{k-1}}, \quad \text{if } k \geq 2. \quad (\text{E.10})$$

Here, we defined the constant $\kappa = 2e^\gamma/\pi \approx 1.13$, with γ denoting Euler's constant.

Substituting Eqs.(E.9) and (E.10) into Eq.(E.6), we find that its second and third terms result in the same constant $\sum_{l=0}^{\infty} \frac{(-1)^l}{\pi(2l+1)^2} = \frac{\mathcal{C}}{\pi}$ ($\mathcal{C} \approx 0.92$ is the Catalan's constant), differing only by a minus sign. Thus, they cancel out, and we obtain:

$$s_1(|x| \gg 1) \sim \frac{1}{2} \ln(\kappa|x|). \quad (\text{E.11})$$

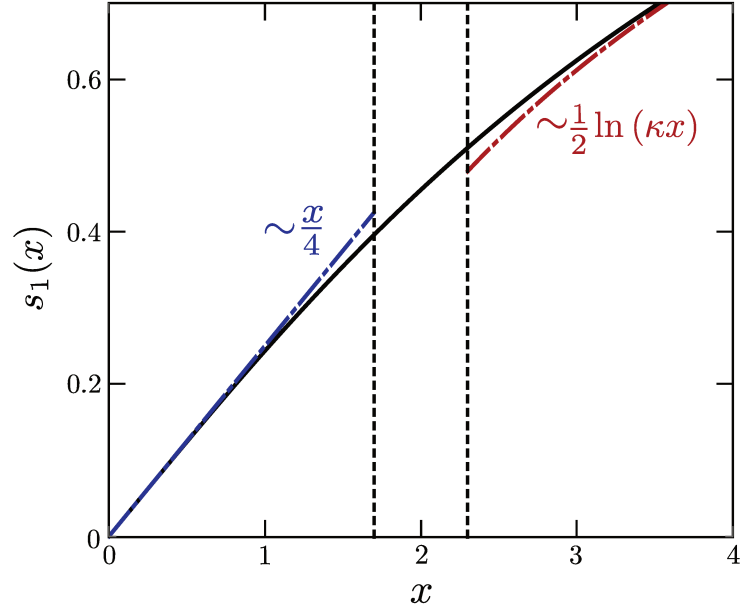


Figure 36 – Numerical and asymptotic solutions for the Matsubara sum (E.2). The dot-dashed blue and red lines are the asymptotic solutions for $|x| \ll 1$ and $|x| \gg 1$, while the solid line is the numerical result. The dashed vertical lines delimit the region where the asymptotic approximation begins to fail.

To summarize, combining Eqs.(E.5) and (E.11), we have

$$s_1(|x|) \sim \begin{cases} \frac{|x|}{4}, & \text{if } |x| \ll 1 \\ \frac{1}{2} \ln(\kappa|x|), & \text{if } |x| \gg 1 \end{cases}. \quad (\text{E.12})$$

Note that $s_1(|x| \rightarrow 1^+) \neq s_1(|x| \rightarrow 1^-)$. This is because the asymptotic approach we described begins to fail for $|x|$ of order one, as we can see in Fig.36. As a consequence, the asymptotic expressions for $T_c(\mu)$ deviate from the numeric results when μ approaches the boundaries μ_1^* , μ_2^* and μ_3^* of the regions of the phase diagram illustrated in Fig. 24. At these points, either $|W_1|$ or $|W_2|$ becomes of the order of T_c .

APPENDIX F – Matsubara sums for the dirty case

Here we provided a detailed derivation of the the analytic expressions for the matrix elements of \hat{A}_{dirty} defined in Eq.(3.64). This Appendix is reproduced from Ref. [36].

In the case of a dirty two-band superconductor, there are two distinct types of Matsubara sums that we need to calculate for $\delta\hat{A}$, as shown in Eq. (3.64). The first are sums of the type:

$$\sum_n \frac{1}{\omega_n} \arctan\left(\frac{y_1}{\omega_n}\right) \frac{y_2}{y_2^2 + \omega_n^2} \frac{\text{sign}(y_1 y_2)}{T_c^2} s_2\left(\frac{|y_1|}{T_c}, \frac{|y_2|}{T_c}\right), \quad (\text{F.1})$$

where we define:

$$s_2(|x_1|, |x_2|) \equiv 2 \sum_{n=0}^{\infty} \frac{1}{(2n+1)\pi} \arctan\left(\frac{|x_1|}{(2n+1)\pi}\right) \frac{|x_2|}{|x_2|^2 + [(2n+1)\pi]^2}. \quad (\text{F.2})$$

The other sum is

$$\sum_n \frac{1}{\omega_n^2} \arctan\left(\frac{y_1}{\omega_n}\right) \arctan\left(\frac{y_2}{\omega_n}\right) = \frac{\text{sign}(y_1 y_2)}{T_c^2} s_3\left(\frac{|y_1|}{T_c}, \frac{|y_2|}{T_c}\right), \quad (\text{F.3})$$

where we define:

$$s_3(|x_1|, |x_2|) \equiv 2 \sum_{n=0}^{\infty} \frac{1}{[(2n+1)\pi]^2} \arctan\left(\frac{|x_1|}{(2n+1)\pi}\right) \arctan\left(\frac{|x_2|}{(2n+1)\pi}\right). \quad (\text{F.4})$$

In these expressions, both y_1 and y_2 can assume the values $\Omega_0 = \Lambda$, $W_1 = -\mu$, or $W_2 = -\mu + \varepsilon_0$.

To proceed with the calculation of (F.2) and (F.4), we use an asymptotic approach similar to that described in Appendix E. In each of the four regions of the two-dimensional parameter space $|x_1| \times |x_2|$ bounded by the lines $|x_1| = 1$ and $|x_2| = 1$ (see Fig.37), we substitute $\arctan\left(\frac{|x_i|}{(2n+1)\pi}\right)$ and $\frac{|x_i|}{|x_i|^2 + [(2n+1)\pi]^2}$ by their Taylor expansions in powers of $|x_i|$ if $|x_i| \ll 1$, or $1/|x_i|$ if $|x_i| \gg 1$.

When $|x_i| \gg 1$ we decompose the sums over n into two contributions,

$$\sum_{n=0}^{\infty} f(n) = \sum_{n=0}^{N_i^*} f(n) + \sum_{n=N_i^*+1}^{\infty} f(n), \quad (\text{F.5})$$

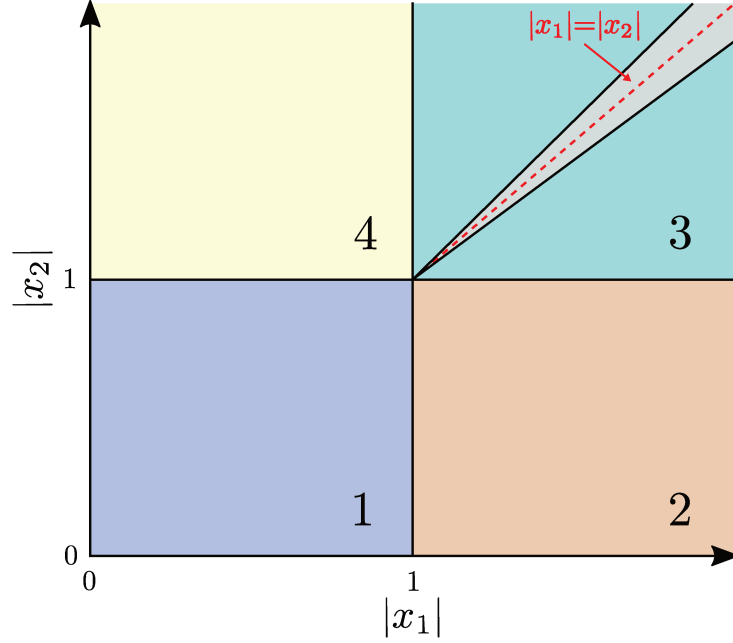


Figure 37 – Different regions of the two-dimensional parameter space $|x_1| \times |x_2|$ in which the analytic expansions are performed. In region 3, the silver area around the line $|x_1| = |x_2|$ indicates the region where the approximations lose precision, since the neglected terms of order $\mathcal{O}\left(\frac{1}{|x_j|} \left(\frac{|x_{<|}}{|x_{>|}}\right)^2\right)$, $j = 1, 2$, become more important.

where $f(n)$ denotes any function of n . As in Appendix E, $N_i^* = \frac{|x_i|}{2\pi} - \frac{1}{2}$ is defined such that $(2N_i^* + 1)\pi = |x_i|$. When both $|x_1| \gg 1$ and $|x_2| \gg 1$, on the other hand, the decomposition is such that

$$\sum_{n=0}^{\infty} f(n) = \sum_{n=0}^{N_{<}^*} f(n) + \sum_{n=N_{<}^*+1}^{N_{>}^*} f(n) + \sum_{n=N_{>}^*+1}^{\infty} f(n), \quad (\text{F.6})$$

with $N_{<}^* = \min\{N_1^*, N_2^*\}$ and $N_{>}^* = \max\{N_1^*, N_2^*\}$. Therefore, besides the sums already calculated in Eqs. (E.4), (E.9) and (E.10), we also need, for $|x_i| \gg 1$,

$$\sum_{n=N_1^*}^{N_2^*} \frac{1}{[(2n+1)\pi]^k} \sim \begin{cases} \frac{1}{2\pi} \ln\left(\frac{|x_2|}{|x_1|}\right), & \text{if } k = 1 \\ \frac{1}{2\pi(k-1)} \left[\frac{1}{|x_1|^{k-1}} - \frac{1}{|x_2|^{k-1}} \right], & \text{if } k \leq 0 \text{ or } k > 1 \end{cases}. \quad (\text{F.7})$$

After a straightforward calculation, we then find the following asymptotic approximations for (F.2) and (F.4) in each of the four asymptotic regions of the $(|x_1|, |x_2|)$

plane:

$$s_2(|x_1|, |x_2|) \approx \begin{cases} 0, & \text{if } |x_1|, |x_2| \ll 1 \\ \kappa' |x_2|, & \text{if } |x_1| \gg 1, |x_2| \ll 1 \\ \frac{1}{2|x_2|} \ln(\kappa |x_{<}|) - \frac{|x_1|}{2|x_{>}|^2} + \frac{|x_2| \theta(|x_1| - |x_2|)}{4|x_1|^2}, & \text{if } |x_1|, |x_2| \gg 1 \\ 0, & \text{if } |x_1| \ll 1, |x_2| \gg 1 \end{cases}, \quad (\text{F.8})$$

and

$$s_3(|x_1|, |x_2|) \approx \begin{cases} 0, & \text{if } |x_1|, |x_2| \ll 1 \\ \kappa' |x_2|, & \text{if } |x_1| \gg 1, |x_2| \ll 1 \\ \frac{\pi^2}{16} - \frac{(|x_1| + |x_2|)}{2|x_1||x_2|} \ln(\kappa |x_{<}|) - \frac{1}{2|x_{<}|} + \frac{|x_{<}|}{2|x_{>}|^2}, & \text{if } |x_1|, |x_2| \gg 1 \\ \kappa' |x_1|, & \text{if } |x_1| \ll 1, |x_2| \gg 1 \end{cases}. \quad (\text{F.9})$$

Here, we defined the constant $\kappa' = \frac{7\zeta(3)}{8\pi^2} \approx 0.11$ and defined $|x_{<}| = \min\{|x_1|, |x_2|\}$ and $|x_{>}| = \max\{|x_1|, |x_2|\}$. Recall that $\zeta(x)$ is the zeta function, $\theta(x)$ is the Heaviside step function and $\kappa \approx 1.13$ is the constant defined in Appendix E.

It is important to note that we treat the approximations we use during the derivation of Eqs.(F.8) and (F.9) consistently: in all the four regions of the parameter space shown in Fig.37, we kept only terms up to order $\mathcal{O}(|x|^2)$, with $|x| \ll 1$. Note that there is a small sliver region around $|x_1| = |x_2|$ in region 3 where this approximation loses precision as compared to the other regions of the $(|x_1|, |x_2|)$ plane.

The matrix elements of $\delta\hat{A}$, defined in Eq. (3.64), are given by combinations of (F.8) and (F.9). In each region of the phase diagram shown in Fig.24, the leading contributions yield for R_1 :

$R_1 \sim$

$$\left\{ \begin{array}{ll} \frac{\Omega_0 + \mu - \varepsilon_0}{2\Omega_0^2} + \frac{1}{2\Omega_0} \ln \left(\frac{\varepsilon_0 - \mu}{\Omega_0} \right), & \text{region I} \\ \frac{4\Omega_0 + \mu - 2\varepsilon_0}{4\Omega_0^2} + \frac{\mu \theta(\varepsilon_0 - 2\mu)}{4(\varepsilon_0 - \mu)^2} - \frac{\varepsilon_0 - \mu}{2W_{>}^2} + \frac{1}{2\Omega_0} \ln \left(\frac{\varepsilon_0 - \mu}{\Omega_0} \right) - \frac{1}{2\mu} \ln \left(\frac{\mu}{W_{<}} \right), & \text{region II} \\ \frac{4\Omega_0 - \mu}{4\Omega_0^2} - \frac{1}{2\mu} \ln \left(\frac{\kappa\mu}{T_c} \right) + \frac{1}{2\Omega_0} \ln \left(\frac{\kappa\Omega_0}{T_c} \right), & \text{region III} \\ \frac{4\Omega_0 + \mu - 2\varepsilon_0}{4\Omega_0^2} + \frac{\mu - \varepsilon_0}{2\mu^2} - \frac{1}{2\mu} \ln \left(\frac{\kappa^2\mu(\mu - \varepsilon_0)}{T_c^2} \right) - \frac{1}{2\Omega_0} \ln \left(\frac{\kappa^2\Omega_0(\mu - \varepsilon_0)}{T_c^2} \right), & \text{region IV} \end{array} \right. \quad (\text{F.10})$$

For R_2 , we find:

$R_2 \sim$

$$\left\{ \begin{array}{ll} \frac{\varepsilon_0 - \mu}{4\Omega_0^2} + \frac{1}{2(\varepsilon_0 - \mu)} \ln \left(\frac{\kappa(\varepsilon_0 - \mu)}{T_c} \right) - \frac{1}{2\Omega_0} \ln \left(\frac{\kappa\Omega_0}{T_c} \right), & \text{region I} \\ \frac{\mu + \varepsilon_0}{4\Omega_0^2} - \frac{\mu}{2W_{>}^2} + \frac{(\varepsilon_0 - \mu) \theta(2\mu - \varepsilon_0)}{4\mu^2} + \frac{1}{2(\varepsilon_0 - \mu)} \ln \left(\frac{\kappa^2(\varepsilon_0 - \mu)W_{<}}{T_c^2} \right) - \frac{1}{2\Omega_0} \ln \left(\frac{\kappa^2\mu\Omega_0}{T_c^2} \right), & \text{region II} \\ \frac{\Omega_0 + \mu}{2\Omega_0^2} + \frac{2\kappa'(\varepsilon_0 - \mu)}{T_c^2} - \frac{1}{2\Omega_0} \ln \left(\frac{\kappa^2\mu\Omega_0}{T_c^2} \right), & \text{region III} \\ \frac{\mu + \varepsilon_0}{4\mu^2} + \frac{\mu + \varepsilon_0 + 4\Omega_0}{4\Omega_0^2} - \frac{1}{2\Omega_0} \ln \left(\frac{\kappa^2\Omega_0\mu}{T_c^2} \right) - \frac{1}{\mu - \varepsilon_0} \ln \left(\frac{\kappa(\mu - \varepsilon_0)}{T_c} \right), & \text{region IV} \end{array} \right. \quad (\text{F.11})$$

and for S :

$S \sim$

$$\left\{ \begin{array}{ll} \frac{1}{2(\varepsilon_0 - \mu)} - \frac{\varepsilon_0 - \mu}{2\Omega_0^2} + \frac{1}{2(\varepsilon_0 - \mu)} \ln \left(\frac{\kappa(\varepsilon_0 - \mu)}{T_c} \right) - \frac{1}{2\Omega_0} \ln \left(\frac{\kappa\Omega_0^2}{(\varepsilon_0 - \mu)T_c} \right), & \text{region I} \\ \frac{2\mu - \varepsilon_0}{2\mu(\varepsilon_0 - \mu)} - \frac{\varepsilon_0 - 2\mu}{2\Omega_0^2} + \frac{1}{2W_{<}} - \frac{W_{<}}{2W_{>}^2} + \frac{\varepsilon_0}{2\mu(\varepsilon_0 - \mu)} \ln \left(\frac{\kappa W_{<}}{T_c} \right) - \frac{1}{2\mu} \ln \left(\frac{\kappa\mu}{T_c} \right) + \frac{1}{2(\varepsilon_0 - \mu)} \ln \left(\frac{\kappa(\varepsilon_0 - \mu)}{T_c} \right) - \frac{1}{2\Omega_0} \ln \left(\frac{\kappa^2\Omega_0^2\mu}{(\varepsilon_0 - \mu)T_c^2} \right), & \text{region II} \\ \frac{\pi^2}{8T_c} - \frac{2\kappa'(\varepsilon_0 - \mu)}{T_c^2} - \frac{1}{2\mu} + \frac{\mu}{2\Omega_0^2} - \frac{1}{2\mu} \ln \left(\frac{\kappa\mu}{T_c} \right) - \frac{1}{2\Omega_0} \ln \left(\frac{\kappa^3\Omega_0^2\mu}{T_c^3} \right), & \text{region III} \\ \frac{\pi^2}{4T_c} - \frac{1}{\mu - \varepsilon_0} - \frac{\varepsilon_0}{2\mu^2} + \frac{2\mu - \varepsilon_0}{2\Omega_0^2} - \frac{1}{2\Omega_0} \ln \left(\frac{\kappa^4\Omega_0^2\mu(\mu - \varepsilon_0)}{T_c^4} \right) - \frac{1}{2\mu} \ln \left(\frac{\kappa^2\mu(\mu - \varepsilon_0)}{T_c^2} \right) - \frac{1}{\mu - \varepsilon_0} \ln \left(\frac{\kappa(\mu - \varepsilon_0)}{T_c} \right), & \text{region IV} \end{array} \right. \quad (\text{F.12})$$

where, $W_{<} \equiv \min\{|W_1|, |W_2|\}$ and $W_{>} \equiv \max\{|W_1|, |W_2|\}$. The order of the terms in the expressions for R_1 , R_2 and S are also consistent with those in Eqs.(F.8) and (F.9).